

MEASUREMENT OF STRANGENESS
PRODUCTION IN γp INTERACTIONS AT HERA
WITH THE H1 DETECTOR

Dissertation
zur Erlangung des Doktorgrades
des Fachbereiches Physik
der Universität Hamburg

vorgelegt von
KAREN JOHANNSEN ✓
aus
SCHENEFELD

Hamburg

1996

MEASUREMENT OF STRANGENESS
PRODUCTION IN VP INTERACTIONS AT HERA
WITH THE H1 DETECTOR

Dissertation
zur Erlangung des Doktorgrades
des Fachbereiches Physik
der Universität Hamburg

vorgelegt von
KAREN JOHANNSEN
aus
SCHNEEFELD

Gutachter der Dissertation:

Prof. Dr. V. Blobel
Prof. Dr. G. Kramer

Gutachter der Disputation:

Prof. Dr. V. Blobel
Prof. Dr. J. B. Dainton

Datum der Disputation:

26. März 1996

Sprecher des Fachbereiches und

Vorsitzender des Promotionsausschusses: Prof. Dr. B. Kramer

Abstract

In this study, strangeness production, specifically the production of K^0 mesons, is investigated in γp interactions at a center of mass energy of $W \approx 160 - 240 \text{ GeV}$. The data taken with the H1 experiment in 1994 corresponds to an integrated luminosity of $L = 1395 \text{ nb}^{-1}$ and allows to measure the differential K^0 -production cross-section both as a function of the transverse momentum p_t and the pseudorapidity η in the kinematic range $0.5 < p_t < 5.0 \text{ GeV}/c$ and $|\eta| < 1.3$. In addition, the dependence on the rapidity y^* measured in the center of mass of the γp system is investigated. The results are found to be broadly consistent with predictions from *leading order* and *next-to-leading-order* calculations. Furthermore, the measurement of the K/π ratio is presented; K^* and Λ production and the W dependence of the K^0 cross-section are discussed.

Kurzfassung

In dieser Arbeit wird die Produktion von Strangeness, insbesondere die von K^0 -Mesonen, in Photoproduktionsereignissen in einem Bereich der Schwerpunktsenergie von $W \approx 160 - 240 \text{ GeV}$ untersucht. Mit den im Jahr 1994 genommenen Daten des H1-Experimentes, die einer integrierten Luminosität von $L = 1395 \text{ nb}^{-1}$ entsprechen, werden die differentiellen K^0 -Produktionswirkungsquerschnitte sowohl in Abhängigkeit des Transversalimpulses p_t als auch der Pseudorapidity η im kinematischen Bereich von $0.5 < p_t < 5.0 \text{ GeV}/c$ und $|\eta| < 1.3$ gemessen. Zusätzlich wird die Abhängigkeit von der im Schwerpunkt des γp -Systems gegebenen Rapidität y^* bestimmt. Alle Ergebnisse werden mit QCD-Vorhersagen, die auf *leading order* und *next-to-leading-order* Rechnungen basieren, verglichen und sind mit diesen verträglich. In der Arbeit werden darüber hinaus erste Studien über verwandte Themenbereiche wie die Messung des K/π -Verhältnisses, die K^* - und Λ -Produktion sowie die Messung der W -Abhängigkeit des K^0 -Wirkungsquerschnittes diskutiert.

Contents

Introduction	4
1 Photoproduction at HERA	6
1.1 Kinematics	7
1.2 The photoproduction cross section	8
1.3 The various photoproduction processes	10
1.4 Production of heavy flavors	13
1.5 Photoproduction Monte Carlos	14
1.5.1 PHOJET	14
1.5.2 PYTHIA5.7	15
2 Strangeness in γp interactions	16
2.1 The K mesons	16
2.1.1 Characteristic particle properties	16
2.1.2 Kinematics of the decay $K_S^0 \rightarrow \pi^- \pi^+$	17
2.2 The K^0 -production cross section	20
2.3 Strangeness from the fragmentation process	21
2.3.1 Fragmentation models	21
2.3.2 Multiple Interactions	24
2.3.3 Strangeness suppression	24
2.3.4 The hadronic final state	27
2.3.5 K^0 from hadronic decays	30
2.3.6 Fragmentation functions	33
2.4 Strangeness from the hard subprocess	34
2.5 Strangeness production in photon-gluon fusion	34
3 The H1 experiment at HERA	37
3.1 The ep collider HERA	37
3.2 The H1 detector	37
3.3 The central tracking chambers	39
3.3.1 The central jet chamber	40
3.3.2 The H1 calorimeter	42
3.3.3 The luminosity system	42
3.4 The H1 trigger	43
3.4.1 The central trigger logic (CTL)	45
3.4.2 The L4 filter farm	45
3.5 The H1 reconstruction	46
3.5.1 Track reconstruction with the central jet chamber	46

3.5.2	Reconstruction of V^0 decays	48
4	Determination of the K^0 cross sections	53
4.1	The data sample	54
4.2	Event selection on L1	54
4.2.1	Acceptance and efficiency of the electron tagger	55
4.2.2	Acceptance and efficiency of the DCR Φ trigger	57
4.3	Event selection on L4 and L5	60
4.4	The track efficiency	62
4.4.1	Single track reconstruction efficiency	62
4.4.2	Basic track selection cuts	64
4.4.3	Performance of the <i>CJC</i> in 1994	64
4.5	K_S^0 -reconstruction efficiency	68
4.5.1	The K_S^0 generator for the <i>CJC</i>	69
4.5.2	The geometric acceptance of the <i>CJC</i>	71
4.5.3	Improving the signal-to-background ratio	72
4.5.4	The misalignment of the <i>CJC</i>	82
4.5.5	The K_S^0 signal and the determination of the signal-to-background ratio	82
4.5.6	Inefficiencies related to the <i>CJC</i> performance	83
4.5.7	V^0 -finder efficiency	92
4.6	The luminosity measurement	93
4.6.1	Correction for proton satellite bunches	95
4.7	Background from non- <i>ep</i> interactions	95
4.8	Systematic uncertainties	96
4.8.1	Systematic uncertainties related to the K_S^0 selection	96
4.8.2	Summary of systematic uncertainties	97
4.9	Fully corrected cross sections	100
4.9.1	$d^2\sigma/dp_t^2 d\eta$ for $ \eta < 1.3$	102
4.9.2	$d\sigma/d\eta$ for $0.5 < p_t < 5.0 \text{ GeV}/c$	103
4.9.3	$d\sigma/d\eta$ for various p_t ranges	104
4.9.4	$d^2\sigma/dp_t^2 dy_{rap}^*$ for $ \eta < 1.3$	105
4.9.5	$d\sigma/dy_{rap}^*$ for $0.5 < p_t < 5.0 \text{ GeV}/c$ and $ \eta < 1.3$	106
5	Discussion of results	107
5.1	Comparison to the 1993 measurement	107
5.2	Comparison to NLO calculations	107
5.3	Comparison to QCD-based generators	110
5.3.1	PYTHIA 5.7	110
5.3.2	PHOJET	110
5.4	Measurement of the K/π ratio	115
5.4.1	The inclusive charged-particle cross section in photoproduction	115
5.4.2	The K/π ratio	118
5.5	Outlook	119
5.5.1	Reconstruction of K^* decays	119
5.5.2	Λ production	120
5.5.3	The energy dependence of the K^0 -production cross section	122

Introduction

The basic model used in elementary particle physics is the standard model which has been successful in describing the majority of all observed phenomena. In this model the fundamental constituents of matter are leptons and quarks and the interactions between them are mediated by bosons. The electromagnetic force is mediated by photons while weak and strong interactions are related to the exchange of W^\pm/Z -bosons and gluons. The concepts behind the standard model are based on symmetries and gauge principles.

All leptons and quarks can be grouped into three families (leptons: $(e^-, \nu_e), (\mu^-, \nu_\mu), (\tau^-, \nu_\tau)$, quarks: $(d, u), (s, c), (b, t)$). Since quarks are not observed as free particles, the final state of a high-energy collision contains leptons and hadrons, the latter ones consisting of either $q\bar{q}$ -pairs (*mesons*) or three quarks (*baryons*).

With increasing beam energies the hadronic final state of an interaction gets rather complex; in addition to stable hadrons containing light quarks particles containing heavy quarks are produced. The composition of the hadronic final state depends on the one hand on the structure of the incoming particles and on the other hand on the mechanisms which determine the formation of hadrons during the fragmentation.

By investigating inclusive strangeness production one can study the fragmentation of quarks and gluons into hadrons and furthermore the suppression of strange quarks relative to light quarks (d, u) . In this analysis the main focus is on inclusive K^0 production since, in contrast to charged kaons, neutral kaons can easily be identified through their decay into two charged pions.

The results can be compared both to next-to-leading-order QCD calculations where the fragmentation is parameterized by fragmentation functions or to leading order calculations as they are used in Monte-Carlo generators like PYTHIA or PHOJET in combination with a phenomenological fragmentation model like JETSET. A better understanding of the fragmentation process is necessary if one wants to isolate strangeness from the hard subprocesses or the quark and gluon sea of the proton or the photon.

The thesis is organized as follows:

The first two chapters give an overview of the underlying basic theory of K^0 production in γp interactions. Chapter 1 gives a summary on photoproduction at HERA, while chapter 2 concentrates on K^0 production. Here the decay mode $K_S^0 \rightarrow \pi^- \pi^+$ and the various sources of strangeness are discussed. The main focus is on strangeness from the fragmentation process. Using the generator PYTHIA in combination with JETSET studies on the composition of the hadronic final state are performed.

The experimental part of the analysis starts with a description of the H1 experiment at HERA in chapter 3. The detector components relevant to this analysis and

the technical aspects of the K_S^0 reconstruction are explained.

In chapter 4 the measurement of the differential K^0 production cross sections as functions of the transverse momentum p_t and (pseudo)rapidity y (η) in the kinematic range $0.5 < p_t < 5.0 \text{ GeV}/c$ and $|\eta| < 1.3$ is discussed. First, the data sample under investigation is described followed by a discussion of the various acceptance and efficiency corrections needed to determine the final differential cross sections. In this analysis these corrections were factorized, each contribution being studied independently. The attempt was made to be as much independent from a Monte Carlo simulation as possible and to get most corrections from data itself. To calculate the losses due to the limited acceptance of the central tracking chamber (*CJC*) and due to cuts applied in order to improve the signal-to-background ratio, the geometry of the *CJC* was modeled; this allowed to calculate a p_t and η dependent weight for each reconstructed K_S^0 . The efficiency of the trigger and other event selection steps have been studied by an independent reference trigger and unbiased events samples.

The physics results are discussed in the subsequent chapter 5 where, in addition, an outlook on what would be possible with higher statistics is given. Chapter 6 will present a summary.

Chapter 1

Photoproduction at HERA

The ep collisions at the electron-proton collider HERA open a new domain of physics, since for the first time the achievable center-of-mass energy is as high as 314 GeV . This corresponds to an increase of about one order of magnitude compared to previous fixed target experiments.

Depending on the squared momentum transfer Q^2 between electron and proton different interaction models exist to describe the dominating physical processes.

In the standard model, processes at high Q^2 are usually described by models of electro-weak electron-parton scattering. Apart from the photon the mediating particles in this case are the vector bosons W^\pm and Z^0 for charged and neutral currents, respectively; the involved partons, the constituents of the proton, can be regarded as quasi-free.

The analysis of deep-inelastic-scattering processes (DIS) is mainly used to measure the proton structure function, particularly as the kinematic region accessible is much larger, both in Q^2 and in x , as in former experiments.

If Q^2 is smaller than the squared mass of the W - or Z -boson, the only remaining significant contribution is given by the electromagnetic current mediated by the exchange of a virtual photon. With decreasing Q^2 the virtuality of the photon decreases and at $Q^2 \approx 0$ the mediating photon can be considered as quasi-real. This kinematic range corresponds to *photoproduction* and here the largest rates of ep interactions are measured. The analysis of these photoproduction events can help to reveal the nature of the photon and its constituents (parton density); it also allows an alternative approach to the measurement of the parton densities in the proton.

To classify photoproduction events one usually distinguishes between diffractive and non-diffractive processes. Diffractive processes include elastic γp scattering, double-diffractive dissociation ($\gamma p \rightarrow X + Y$) and single-diffractive dissociation ($\gamma p \rightarrow Xp$ and $\gamma p \rightarrow VX$, where V corresponds to a vector meson). Non-diffractive photoproduction is usually divided into "soft" and "hard" interactions depending on the transverse energy in the events. The various contributing processes are discussed in section 1.3.

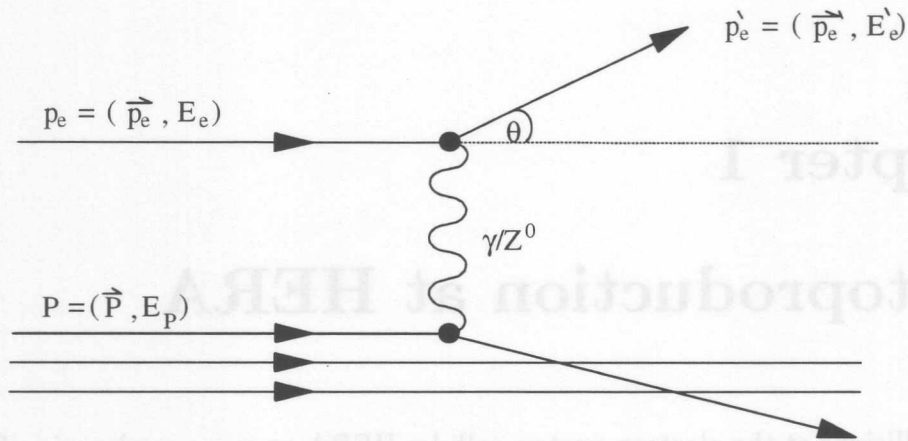


Figure 1.1: Kinematics of deep-inelastic electron-proton scattering

1.1 Kinematics

The basic kinematic variables are introduced by means of the Feynman diagram of deep-inelastic electron-proton scattering in figure 1.1. Since the square of the center of mass energy, given by

$$s \equiv (p_e + P)^2 \approx 4E_e E_P \quad (1.1)$$

(with p_e and P the 4-vectors of the incoming electron and proton, respectively), is a constant, the kinematics of inclusive scattering can be completely described by two independent variables. The common choice is a combination of the negative squared momentum transfer

$$Q^2 \equiv -q^2 = -(p_e - p'_e)^2 \approx 4E_e E'_e \sin^2 \frac{\theta}{2}, \quad (1.2)$$

where θ is the scattering angle between the incoming (p_e) and the outgoing electron (p'_e), and one of the two dimensionless Bjorken scaling variables x or y . The inelasticity or relative energy transfer y is defined by

$$y \equiv \frac{P \cdot q}{P \cdot p_e} \approx 1 - \frac{E'_e}{E_e} \cos^2 \frac{\theta}{2} \quad (1.3)$$

and the Bjorken scaling variable x by

$$x \equiv \frac{Q^2}{2P \cdot q}. \quad (1.4)$$

In the approximations above, the electron and the proton masses are neglected.

At HERA the term photoproduction refers to all processes mediated by the exchange of quasi-real photons (i.e. $Q^2 \approx 0$). In this case, the electron is scattered at a very small angle and relation 1.3 for y can be approximated by

$$y \approx 1 - \frac{E'_e}{E_e} = \frac{E_e - E'_e}{E_e} = \frac{E_\gamma}{E_e}, \quad (1.5)$$

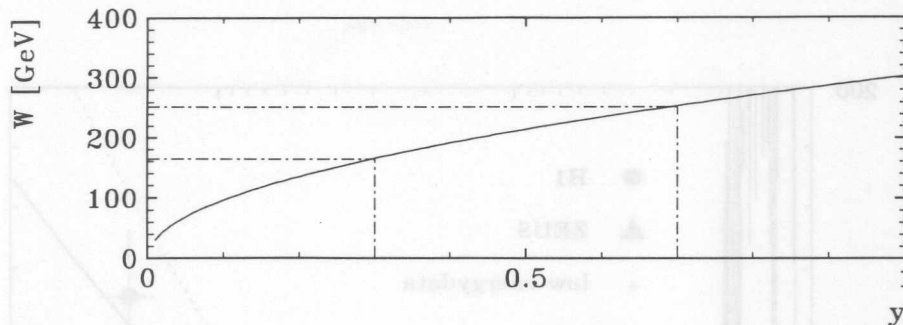


Figure 1.2: W in photoproduction as a function of y ; in addition the accessible kinematic range of the H1 experiment, in which the scattered electron can be precisely measured, is indicated.

where E_γ is the energy of the photon. A precise measurement of the energy of the scattered electron E'_e is therefore sufficient to reconstruct the kinematics of such events. The center-of-mass energy of the photon-proton system is given by:

$$W_{\gamma p} = \sqrt{s_{\gamma p}} \approx 2\sqrt{yE_e E_P} \quad (1.6)$$

Given the beam energies of $E_e = 27.6 \text{ GeV}$ and $E_P = 820 \text{ GeV}$ the dependence of W on y is shown in figure 1.2. The average value of W in photoproduction is $\approx 200 \text{ GeV}$ while the accessible kinematic range, in which the scattered electron can be precisely measured, is limited to $0.3 < y < 0.7$ (see section 4.2.1).

1.2 The photoproduction cross section

The differential cross section for inelastic ep scattering $ep \rightarrow e'\gamma p$ mediated by a virtual photon can be written as

$$\frac{d^2\sigma_{ep}}{dydQ^2} = \frac{\alpha}{2\pi} \frac{1}{Q^2} \{A(y, Q^2) \sigma_{\gamma^*p}^T(y, Q^2) + B(y, Q^2) \sigma_{\gamma^*p}^L(y, Q^2)\} \quad (1.7)$$

where $\sigma_{\gamma^*p}^T$ and $\sigma_{\gamma^*p}^L$ are the cross sections for transversely and longitudinally polarized virtual photons and A and B kinematic factors [1]. For very small Q^2 ($Q^2 \rightarrow 0$) one can neglect the longitudinal polarized component in which case

$$\sigma_{\gamma^*p}^T \rightarrow \sigma_{\gamma p}, \quad \sigma_{\gamma^*p}^L \rightarrow 0$$

If the exchanged photon is real, equation 1.7 can be simplified by applying the Weizsäcker-Williams approximation (WWA [2]). In this approximation the cross section for electroproduction is factorized into the "real" photon-proton cross section $\sigma_{\gamma p}^{total}$ depending on $W_{\gamma p}^2 = ys$ and the "photon-flux" resulting from the process $e \rightarrow e'\gamma$ at the electron-vertex. This flux is given by

$$F(y, Q^2) = \frac{\alpha}{2\pi Q^2} \left(\frac{1 + (1-y)^2}{y} - \frac{2(1-y)}{y} \cdot \frac{Q_{min}^2}{Q^2} \right)$$

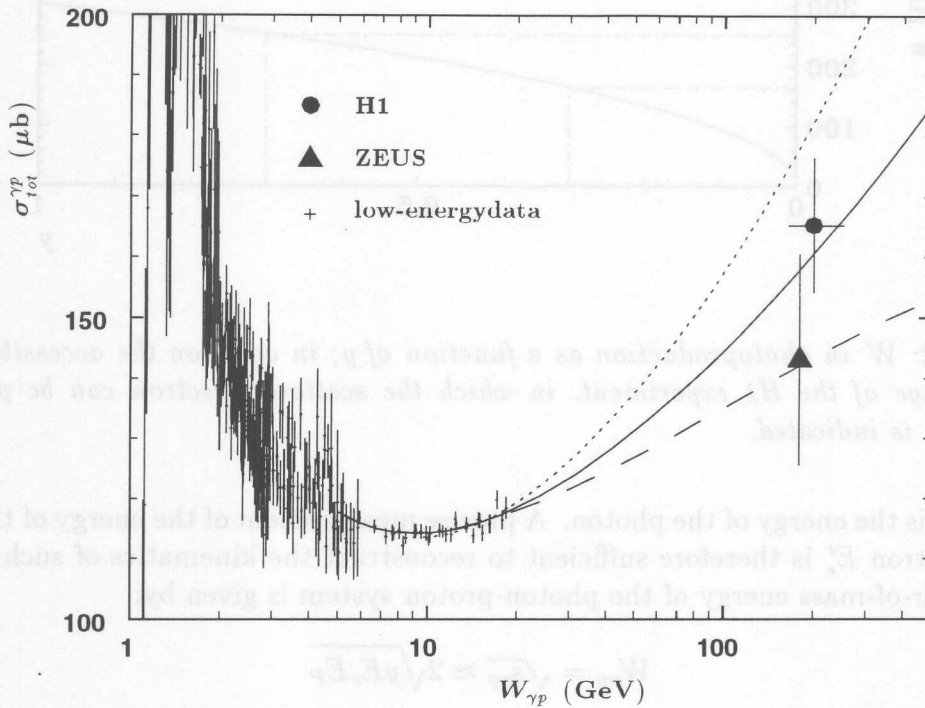


Figure 1.3: Total photoproduction cross section as a function of $W_{\gamma p}$. In addition the DL prediction [4] from a fit to hadron-hadron and low energy data (solid line) and the Regge-type ALLM cross section parameterization [7] (dashed) are shown. The dotted line corresponds to the DL parameterization after including recent results from CDF [8].

where Q_{min}^2 is the minimum photon virtuality defined by $Q_{min}^2 = (m_e y)^2 / (1 - y)$. The relation with the total photoproduction cross section yields the total differential ep cross section as a function of the square of the center-of-mass energy s :

$$\frac{d^2 \sigma_{ep}(s)}{dQ^2 dy} = \sigma_{\gamma p}^{tot}(ys) \cdot (1 - \delta_{RC}) \cdot F(y, Q^2)$$

where the factor $(1 - \delta_{RC})$ is taking into account QED radiative corrections to the ep Born cross section. In the kinematic range under study the WWA is assumed to be a very good approximation [3]. With the 94 data taken with the H1 detector the total photoproduction cross section at $W_{\gamma p} = 200 \text{ GeV}$ was measured to be [5]

$$\sigma_{\gamma p}^{tot}(W_{\gamma p}) = 165.3 \pm 2.3(\text{stat.}) \pm 10.9(\text{syst.}) \mu\text{b}$$

As has been shown by A. Donnachie and P. V. Landshoff [4] it is possible to parameterize all hadron total cross sections in a very convenient way by

$$\sigma^{tot} = X s^\epsilon + Y s^{-\eta} \quad (1.8)$$

where the exponents ϵ and η are expected to be constants, X and Y are process dependent parameters and s is the square of the available center-of-mass energy; the

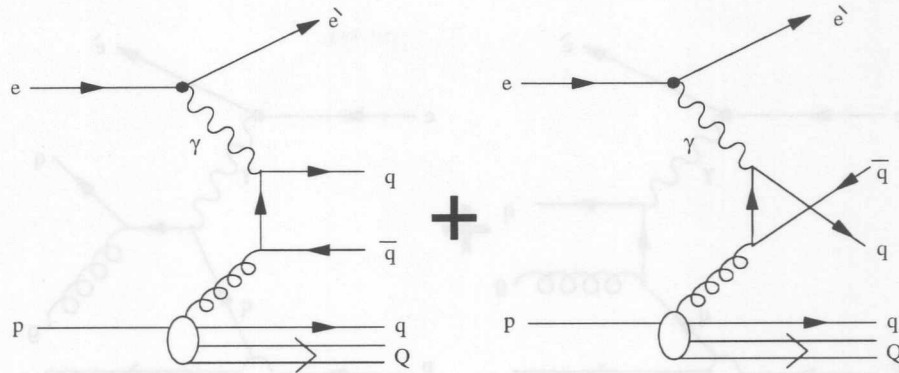


Figure 1.4: Feynman diagram of photon-gluon fusion (PGF), $\gamma g \rightarrow q\bar{q}$

fit parameters are $\epsilon = 0.08$ and $\eta = 0.45$. The first term is associated with processes due to a Pomeron exchange, the second term to processes with ρ , ω , f or a exchange. Fig. 1.3 shows the experimental results from H1 and ZEUS ([5, 6]) of the measurement of the total photoproduction cross section as a function of W . In addition results from low energy data, a Regge-type parameterization (ALLM,[7]) and two predictions from fits to hadron-hadron and low-energy data based on relation 1.8 are given ([4, 8]).

1.3 The various photoproduction processes

In this section, a phenomenological description of the various non-diffractive photoproduction processes contributing predominantly to the total photoproduction cross section is given. In addition some ideas on the treatment of the photon structure [9] as implemented in PYTHIA are explained.

The complexity of photoproduction processes arises from the dual nature of the photon since it can behave like a point-like elementary particle on the one hand and shows hadron-like properties on the other hand. Depending on how the photon couples to the proton a distinction is made between *direct* and *resolved* processes.

In direct processes, such as photon-gluon fusion (PGF) and QCD-Compton scattering, the bare photon couples directly to a quark or gluon of the proton, in the latter case via a $q\bar{q}$ pair (see fig. 1.4 and 1.5). In both cases events with jets having a rather large transverse momentum can be produced. Processes of photon-gluon fusion also yield the dominant contribution to the production of heavy c and b quarks (see section 1.4). The analysis of photon-gluon fusion events allows an alternative approach to measure the gluon structure function of the proton ([10]).

In non-direct processes the photon can be described by a $q\bar{q}$ fluctuation (fig. 1.6). In this case, where the VMD model is applicable, the $q\bar{q}$ fluctuation can be regarded as a superposition of various vector meson states, and the coupling is entirely described by the vector meson component $\gamma \rightarrow V$. This phenomenological approach where no perturbative theory is possible was successfully used for the interpretation of photoproduction processes with events having low transverse momentum p_t , but it is not sufficient to describe the events with larger transverse momentum as they are observed at HERA. For those it is necessary to consider the additional third component, the anomalous one. The anomalous component of the photon allows direct

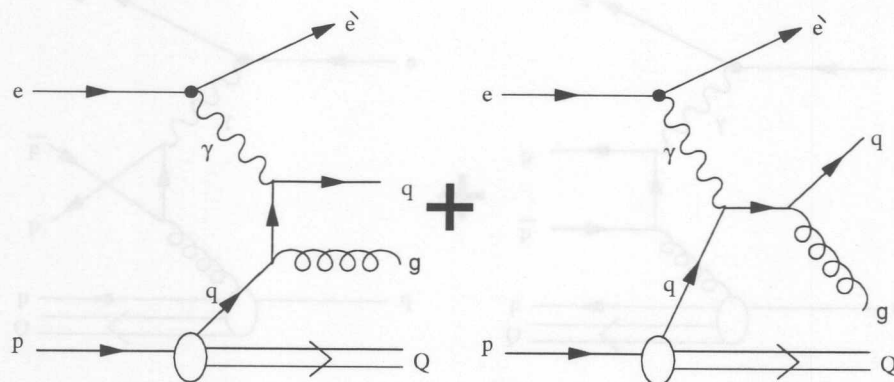


Figure 1.5: Feynman diagram of QCD-Compton scattering, $\gamma q \rightarrow gq$

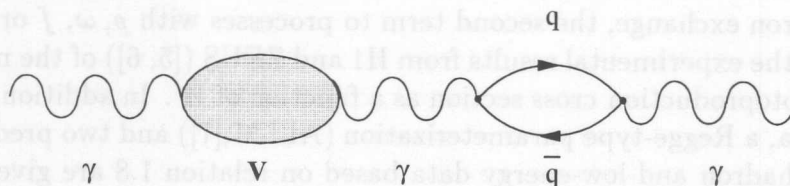


Figure 1.6: Fluctuation of a photon into a $q\bar{q}$ pair. Fluctuations with low virtuality lead to intermediate vector meson states, while at higher transverse momenta the $q\bar{q}$ fluctuation can be treated using perturbation theory.

interactions between one of the quarks of the $q\bar{q}$ fluctuation or an emitted hard gluon and a constituent of the proton; this usually leads to an event having two jets with high transverse momentum.

The Feynman diagrams of some processes, where the anomalous component is involved, are shown in figure 1.7. For the sake of simplicity, the incoming proton, the electron-photon vertex and the $q\bar{q}$ fluctuation with the γ remnant are omitted.

Both anomalous and direct processes contribute to the production of events with large transverse momentum, but they may be disentangled by the existence of a so-called photon-remnant jet. While one parton originating from the $q\bar{q}$ fluctuation takes part in the hard interaction, the remaining one continues to move along the electron direction. During the hadronization of this spectator particle a photon-remnant jet can be produced which is usually visible outside the beam-pipe and leads to a significant energy deposit in the electron direction. In direct processes the energy deposited in this area is much lower.

Common to all three types of non-diffractive photoproduction is the formation of a proton-remnant jet.

The introduction of an anomalous photon component leads to a picture where the photon is treated as a superposition of three different states, namely the *bare* photon $|\gamma\rangle$, the vector meson component $|V\rangle$ and the anomalous component $|q\bar{q}\rangle$ [9]:

$$|\gamma\rangle = \sqrt{Z_3}|\gamma_b\rangle + \sum_{V=\rho^0,\omega,\phi} \frac{e}{f_V}|V\rangle + \frac{e}{f_{q\bar{q}}}|q\bar{q}\rangle,$$

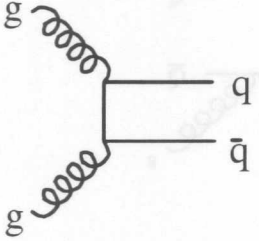
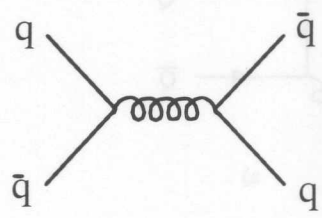
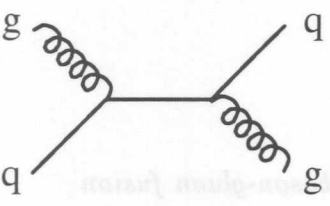
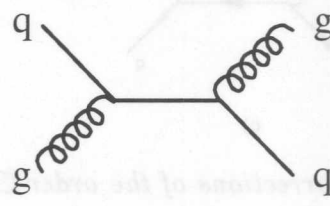
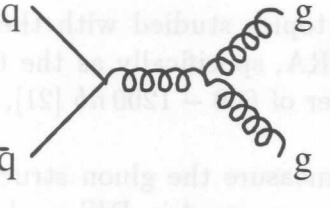
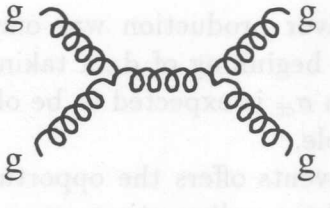
resolved photon		final state
 <p>gluon-gluon-fusion</p>	 <p>quark-antiquark-annihilation</p>	$q\bar{q}$
 <p>quark-gluon-scattering</p>	 <p>quark-gluon-scattering</p>	qg
 <p>quark-antiquark-annihilation</p>	 <p>gluon-gluon-scattering</p>	gg

Figure 1.7: Processes described by the anomalous photon component (lowest order perturbation theory)

with the normalization

$$Z_3 = 1 - \sum_{V=\rho^0, \omega, \phi} \left(\frac{e}{f_V} \right)^2 - \left(\frac{e}{f_{q\bar{q}}} \right)^2;$$

the factors $(e/f_V)^2$ and $(e/f_{q\bar{q}})^2$ give the probabilities for the processes $\gamma \rightarrow V$ and $\gamma \rightarrow q\bar{q}$, respectively.

Depending on the total transverse momentum p_t or the transverse energy flow E_t one distinguishes between "hard" and "soft" photoproduction. *Soft* photoproduction is usually associated with the energy range of $E_t < 5 \text{ GeV}$ and well described by the VMD model, whereas for E_t above 10 GeV , corresponding to *hard* photoproduction, the dominant contributions are given by processes of the direct and the anomalous photon. In the intermediate range, a mixture of the various models has to be used.

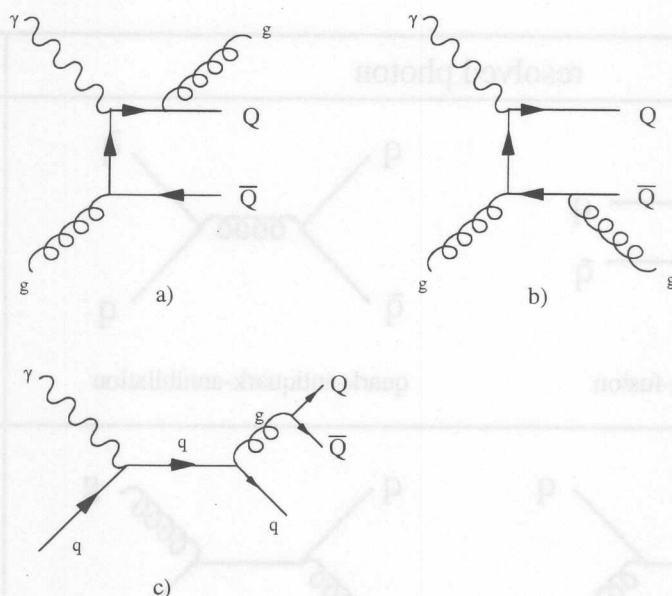


Figure 1.8: Corrections of the order $\mathcal{O}(\alpha_s)$ to boson-gluon fusion

1.4 Production of heavy flavors

The study of heavy flavor production was one of the topics studied with the H1 detector right from the beginning of data taking at HERA, specifically as the total production cross section $\sigma_{c\bar{c}}$ is expected to be of the order of $600 - 1200 \text{ nb}$ [21], and is therefore non-negligible.

Analysis of charm events offers the opportunity to measure the gluon structure function of the proton by an alternative approach to the one used in DIS, and also exclusive charm decays (mainly D mesons) can be investigated.

The dominant contribution for the production of heavy quarks originates from photon-gluon fusion (see fig. 1.4). In principle there could be additional contributions, where instead of a photon a Z^0 occurs as the mediating boson or a Z^0/γ interference, but at $Q \approx 0$ these processes are negligible.

Non-negligible are the contributions originating from the corrections of $\mathcal{O}(\alpha_s)$

$$\gamma g \rightarrow Q\bar{Q}g$$

$$\gamma q \rightarrow Q\bar{Q}q$$

with the corresponding Feynman diagrams shown in figure 1.8 and processes of order $\mathcal{O}(\alpha_s^2)$ like gluon-gluon fusion and quark-antiquark annihilation described by the anomalous photon (see fig. 1.7).

How the various processes contribute to the total production cross section is shown in figure 1.9 taking $b\bar{b}$ production as an example; for $c\bar{c}$ production the relative contributions are comparable. The numerical value of the production cross section depends on the parameterizations used for the gluon structure function $G(x_g, Q^2)$ and the photon structure function F_2^γ ; additional parameters are the mass of the produced heavy quarks ($m_c = 1.5 - 1.8 \text{ GeV}/c^2$), the QCD-scaling variable Λ and the number of flavors entering the calculation of α_s .

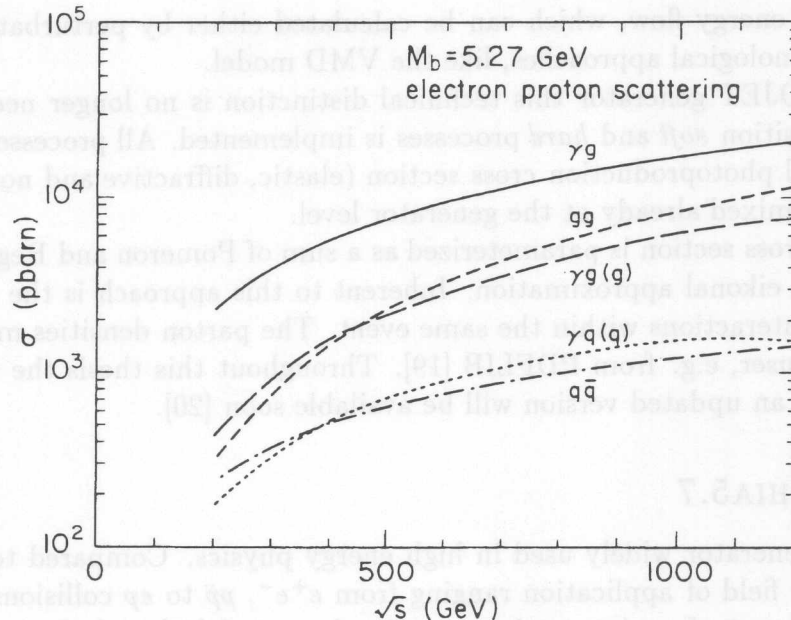


Figure 1.9: Contributions of the various subprocesses to $b\bar{b}$ production [13]

Apart from boson-gluon fusion, charmed quarks can originate from charged current interactions in deep inelastic scattering, but this contribution is negligible. (The reason is the small transition probability between light and heavy quarks given by the Kobayashi-Maskawa matrix: $|V_{cd}| = 0.204 \pm 0.017$, [12]).

1.5 Photoproduction Monte Carlos

The results of the present analysis are compared with the predictions of two different photoproduction Monte Carlos, PHOJET[14] and PYTHIA5.7[15].

Both models use string fragmentation as it is implemented in JETSET7.4 (see section 2.3.1) for the fragmentation process and IJRAY [16] for the calculation of the photon flux at the electron vertex.

The basic underlying concepts of the two Monte Carlo generators are briefly outlined in the next subsection; for more comprehensive information the corresponding manuals and papers should be addressed.

1.5.1 PHOJET

PHOJET is a Monte Carlo program set up particularly to generate γp interactions as they are observed at HERA. The main ideas are based on the Dual Parton Model (DPM, [17]) and the generator itself is similar to DTUJET [18] which describes hadronic collisions.

One of the conceptual differences between PHOJET and other generators such as PYTHIA is the unified treatment of *hard* and *soft* interactions. As explained in section 1.3 the terms *hard* and *soft* photoproduction apply to different kinematic ranges of

the transverse energy flow, which can be calculated either by perturbative QCD or more phenomenological approaches, like the VMD model.

In the PHOJET generator this technical distinction is no longer needed since a continuous transition *soft* and *hard* processes is implemented. All processes contributing to the total photoproduction cross section (elastic, diffractive and non-diffractive processes) are mixed already at the generator level.

The total cross section is parameterized as a sum of Pomeron and Reggeon amplitudes using an eikonal approximation. Inherent to this approach is the existence of multiparticle interactions within the same event. The parton densities may be freely chosen by the user, e.g. from PDFLIB [19]. Throughout this thesis the version 1.03 has been used; an updated version will be available soon [20].

1.5.2 PYTHIA5.7

PYTHIA is a generator widely used in high energy physics. Compared to PHOJET, it offers a wide field of application ranging from e^+e^- , $p\bar{p}$ to ep collisions. Recently, a special treatment of γp interactions was implemented [15] and the results of the present analysis will be compared to these predictions.

In PYTHIA all processes are described in terms of so-called "2 \rightarrow 2" processes, which can be calculated in leading order QCD using matrix elements. The "2 \rightarrow 2" processes refer in this model to the hard subprocess at the parton level.

The new feature of PYTHIA¹ allows to generate a standard mixture of minimum bias events with all contributing photon components (VMD, direct and anomalous) as well as the elastic and diffractive components of the VMD part included. The assignment of a certain "2 \rightarrow 2" process to one of the above mentioned classes is based on the virtuality of the $q\bar{q}$ fluctuation of the photon. For the proton and the VMD part of the photon it is possible to choose between different parameterizations given by the PDFLIB, for the other photon components an internal parameterization is used [9].

¹The corresponding steering parameter is $\text{MSTP}(14) = 10$.

Chapter 2

Strangeness in γp interactions

In γp interactions at HERA the majority of strange particles (e.g. K^0, K^*, Λ) is produced during the fragmentation of quarks and gluons into hadrons; additional contributions originate from the intrinsic strangeness content of the proton or the photon and photon-gluon fusion processes such as $\gamma g \rightarrow s\bar{s}$ and $\gamma g \rightarrow c\bar{c}$, where in the latter case strange particles originate from the decay of charmed mesons and baryons. Concentrating on K^0 mesons, the following sections give a brief overview of the production characteristics related to the different sources of strangeness and the calculation of the K^0 -production cross section.

2.1 The K mesons

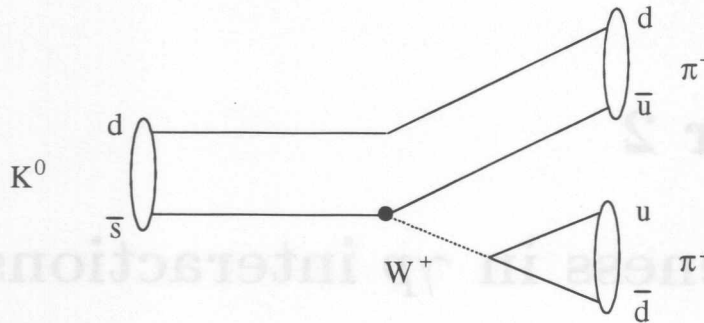
To begin with some characteristic particle properties and the kinematics of the decay into two charged pions are discussed.

2.1.1 Characteristic particle properties

K mesons, or kaons, are the lightest mesons that contain one s quark and therefore have strangeness $|S| = 1$. One distinguishes between pseudo-scalar mesons (K) with a total spin of $s = 0$ and vector mesons (K^*) with $s = 1$, depending on the orientation the spins of the two quarks have with respect to each other. Both kinds of mesons can be arranged in isospin doublets. The isospin doublet of the pseudo scalar mesons is shown in table 2.1.

S	I_3	
	$+\frac{1}{2}$	$-\frac{1}{2}$
+1	$K^+ (u\bar{s})$	$K^0 (d\bar{s})$
-1	$\bar{K}^0 (\bar{d}s)$	$K^- (\bar{u}s)$

Table 2.1: Isospin doublet of the pseudo scalar K mesons


 Figure 2.1: Quark-flow diagram of the K_S^0 decay

The kaons observed in the laboratory are linear combinations of the K^0 and the \bar{K}^0 :

$$\begin{aligned} |K_1\rangle &= \frac{1}{\sqrt{2}}(|K^0\rangle + |\bar{K}^0\rangle), & CP &= +1, \\ |K_2\rangle &= \frac{1}{\sqrt{2}}(|K^0\rangle - |\bar{K}^0\rangle), & CP &= -1 \end{aligned}$$

where

$$\begin{aligned} CP|K_1\rangle &\rightarrow |K_1\rangle \\ CP|K_2\rangle &\rightarrow -|K_2\rangle \end{aligned}$$

The eigenstate $|K_1\rangle$ corresponds to the short-lived component K_S^0 ($\tau = 8.92 \cdot 10^{-11}$ s) the eigenstate $|K_2\rangle$ to the long-lived component K_L^0 ($\tau = 5.17 \cdot 10^{-8}$ s). The mass of both particles is $m = 497.671 \text{ MeV}/c^2$ and assuming CP -invariance their contribution to K^0 and \bar{K}^0 is 50% each.

The dominant decay channels of the K_S^0 are

$$K_S^0 \rightarrow \begin{cases} \pi^- \pi^+ & 68.61\% \pm 0.28 \\ \pi^0 \pi^0 & 31.39\% \pm 0.28 \end{cases}$$

(see also fig. 2.1). The K_L^0 decays mainly into three pions ($3\pi^0$ or $\pi^- \pi^+ \pi^0$) or semileptonically into $\pi^+ \mu^- \nu$ or $\pi^+ e^- \nu$, respectively.

Given the K_S^0 life-time, the mean decay length is $c\tau = 2.675 \text{ cm}$ resulting in secondary vertices which are usually significantly separated from the primary interaction vertex. For the fraction N/N_0 of K_S^0 decays having a decay length larger than a given value d the relation 2.1 holds:

$$N(d, p_0) = N_0 \cdot \exp\left(-\frac{m_0 d}{c\tau p_0}\right) \quad (2.1)$$

with d being the distance between the primary and the secondary vertices and p_0 the total momentum of the decaying K^0 (see also figure 2.2).

2.1.2 Kinematics of the decay $K_S^0 \rightarrow \pi^- \pi^+$

Experimentally, K^0 particles are identified through their decay channel

$$K_S^0 \rightarrow \pi^- \pi^+.$$

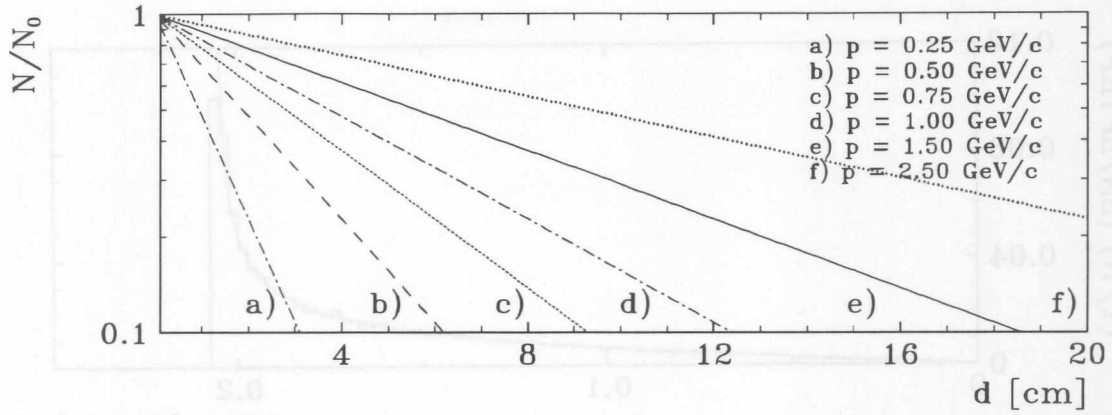
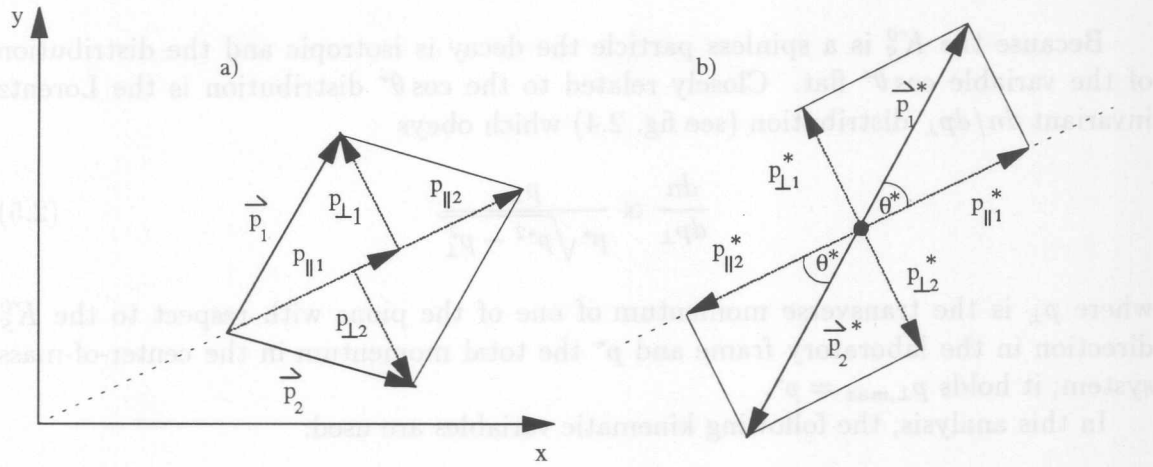


Figure 2.2: Decay length distribution for various momenta


 Figure 2.3: Kinematic variables associated with the K_S^0 decay, (a) laboratory frame, (b) cms of the K_S^0 (b).

Therefore in the following section the kinematics and the topology of this decay mode are discussed. In the center-of-mass system (*cms*) the relations

$$\begin{aligned} E^* &= \frac{m_0}{2} \\ p^* &= \sqrt{\frac{m_0^2}{4} - m_\pi^2} = 0.206 \text{ GeV}/c \end{aligned} \quad (2.2)$$

hold for the energy and the momentum of the two pions. In addition, the longitudinal and transverse momentum components of the two pions are given by

$$\begin{aligned} p_{\perp 1}^* &= p^* \sin \theta^* = -p_{\perp 2}^* \\ p_{\parallel 1}^* &= p^* \cos \theta^* = -p_{\parallel 2}^* \end{aligned} \quad (2.3)$$

where θ^* is the angle between the direction of the K_S^0 and the decay pions (fig. 2.3). A Lorentz transformation along the direction of flight of the K_S^0 yields the following relations in the laboratory system (see fig. 2.3).

$$\begin{aligned} p_{\perp 1,2} &= p_{\perp \pi 1,2}^* \\ p_{\parallel 1,2} &= \frac{p_0}{2} \pm \frac{E_0}{m_0} p^* \cos \theta^* \end{aligned} \quad (2.4)$$

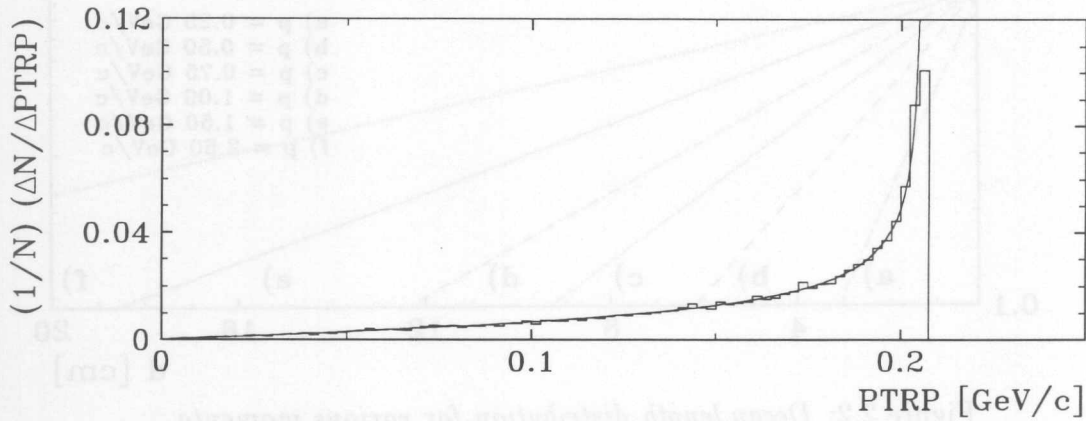


Figure 2.4: p_{\perp} distribution for simulated K_S^0 decays ($p_{\perp} = PTRP$).

Because the K_S^0 is a spinless particle the decay is isotropic and the distribution of the variable $\cos \theta^*$ flat. Closely related to the $\cos \theta^*$ distribution is the Lorentz invariant dn/dp_{\perp} distribution (see fig. 2.4) which obeys

$$\frac{dn}{dp_{\perp}} \propto \frac{p_{\perp}}{p^* \sqrt{p^{*2} - p_{\perp}^2}} \quad (2.5)$$

where p_{\perp} is the transverse momentum of one of the pions with respect to the K_S^0 direction in the laboratory frame and p^* the total momentum in the center-of-mass system; it holds $p_{\perp, max} = p^*$.

In this analysis, the following kinematic variables are used:

p_t , the transverse momentum in the laboratory frame of the K_S^0 which is measured with respect to the beam axis. Since in photoproduction the photon moves nearly parallel to the incoming electron, this is also the transverse momentum with respect to the direction of the γp center-of-mass system.

η , the pseudorapidity which is defined by

$$\eta = \frac{1}{2} \ln \left(\frac{p + p_z}{p - p_z} \right) = \frac{1}{2} \ln \left(\frac{1 + \cos \theta}{1 - \cos \theta} \right) \quad (2.6)$$

where p is the total momentum of the K_S^0 , p_z the momentum component parallel to the beam axis and θ the angle between the K_S^0 and the incoming proton ($p_z = p \cos \theta$).

y_{rap} , the rapidity which is defined by

$$y_{rap} = \frac{1}{2} \ln \left(\frac{E + p_z}{E - p_z} \right) \quad (2.7)$$

where E is the total energy of the K_S^0 ($y_{rap} \approx \eta$ when $E \gg m_{K_S^0}$).

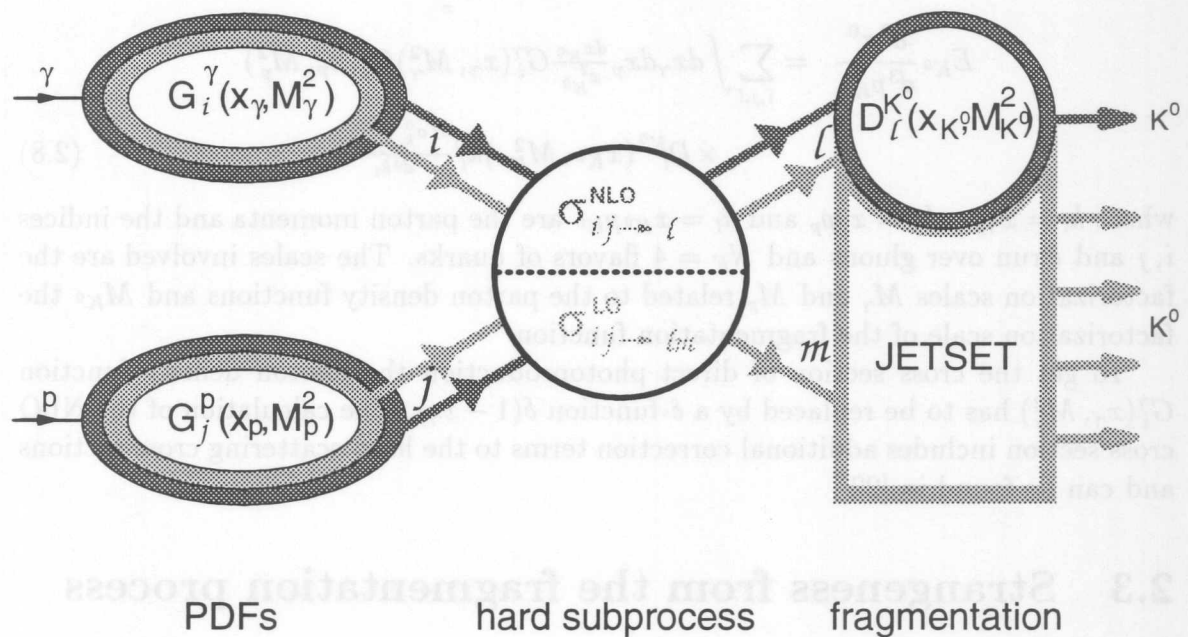


Figure 2.5: Parameters and functions involved in the cross section calculation. ($\sigma_{ij \rightarrow l}^{NLO}$ and $\sigma_{ij \rightarrow lk}^{LO}$ are the cross sections of the processes $ij \rightarrow l$ and $ij \rightarrow lk$ in next-to-leading-order and leading-order, respectively).

2.2 The K^0 -production cross section

The expected K^0 -production cross section can be estimated by means of theoretical QCD calculations or by using Monte Carlo generators like PYTHIA or PHOJET. Since strangeness can originate from various sources the main ingredients needed for a cross section calculation are the parton density functions $G_i^\gamma(x_\gamma, M_\gamma^2)$ and $G_j^p(x_p, M_p^2)$ of the photon and the proton respectively, the cross sections of the so-called hard scattering processes, $\sigma_{k_i k_j \rightarrow k_l}$ or $\sigma_{k_i k_j \rightarrow k_l k_m}$ and a formalism which eventually allows to describe the formation of hadrons during the fragmentation (see fig. 2.5). The QCD based calculations [22] include explicitly *next-to-leading-order* (NLO) corrections to the hard scattering cross sections $\sigma_{k_i k_j \rightarrow k_l}$ while in the generators the calculation of the hard subprocess is based on *leading-order* (LO) matrix elements only. These cross sections usually describe a "2 \rightarrow 2" process $\sigma_{k_i k_j \rightarrow k_l k_m}$ and the needed perturbative corrections are taken into account by initial and final state parton showers.

In addition, two completely different approaches are used to describe the formation of hadrons during the fragmentation step. The theoretical calculations are based on fragmentation functions $D_l^h(x_h, M_h^2)$ which give the probability that out of a certain parton l originating from the hard scattering subprocess a hadron h is formed (see section 2.3.6).

In the generators the partons resulting from the hard subprocess and the final state parton shower are fragmented by the JETSET algorithm (see section 2.3.1).

To leading order, the covariant form of the resolved contribution to the K^0 -production cross section for $\gamma(p_\gamma)p(p_p) \rightarrow K^0(p_{K^0})X$ is given by

$$E_{K^0} \frac{d^3\sigma^0}{d^3p_{K^0}} = \sum_{i,j,l} \int dx_\gamma dx_p \frac{dx_{K^0}}{x_{K^0}^2} G_i^\gamma(x_\gamma, M_\gamma^2) G_j^p(x_p, M_p^2) \times D_l^{K^0}(x_{K^0}, M_{K^0}^2) k_l^0 \frac{d^3\sigma_{k_i k_j \rightarrow k_l}^0}{d^3k_l} \quad (2.8)$$

where $k_i = x_\gamma p_\gamma$, $k_j = x_p p_p$ and $k_l = x_{K^0} p_{K^0}$ are the parton momenta and the indices i, j and l run over gluons and $N_F = 4$ flavors of quarks. The scales involved are the factorization scales M_γ and M_p related to the parton density functions and M_{K^0} the factorization scale of the fragmentation function.

To get the cross section of direct photoproduction the photon density function $G_i^\gamma(x_\gamma, M_\gamma^2)$ has to be replaced by a δ -function $\delta(1 - x_\gamma)$. The calculation of the NLO cross section includes additional correction terms to the hard scattering cross sections and can be found in [22].

2.3 Strangeness from the fragmentation process

The majority of strange particles is produced during the fragmentation process where partons originating from the hard subprocess are turned into hadrons. In most generators this process is simulated using a phenomenological approach while theoretical calculations are based on measured fragmentation functions.

The following sections give a brief overview on current fragmentation models and the characteristic behavior of the fragmentation functions. In addition strangeness suppression in fragmentation is discussed.

2.3.1 Fragmentation models

During the fragmentation of quarks and gluons into hadrons one usually distinguishes between two successive phases depending on the current momentum transfer Q^2 . At high Q^2 , in addition to those quarks and gluons coming from the primary interaction, further quarks and gluons can be produced, either by gluon radiation or by processes like $g \rightarrow q\bar{q}$. Due to the high Q^2 all these processes can be calculated by means of perturbative QCD using matrix elements and the model of parton showers [31]. With decreasing Q^2 (Q^2 typically $< 1 \text{ GeV}^2$) and therefore increasing α_s , this is no longer possible, and one has to use phenomenological models for the final creation of colorless objects.

Throughout this analysis the model of string fragmentation as it is implemented in JETSET7.4 [23] has been used for comparison with the data and is described below. Other models such as independent fragmentation (IF), which actually is one of the oldest approaches and dates back to the early seventies, and cluster fragmentation [29] are only outlined.

String fragmentation JETSET7.4

The fragmentation model as it is implemented in JETSET7.4 is regarded as one of the most successful ones and used in several generators. The starting point for the fragmentation is the color field formed between the quark and anti-quark of a $q\bar{q}$

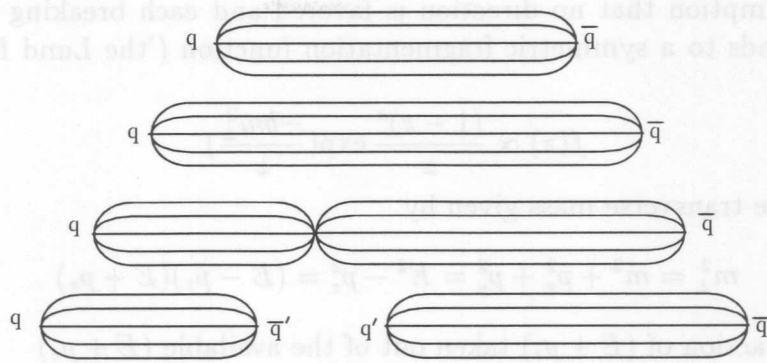


Figure 2.6: *The breaking of a string into a meson and a remaining string*

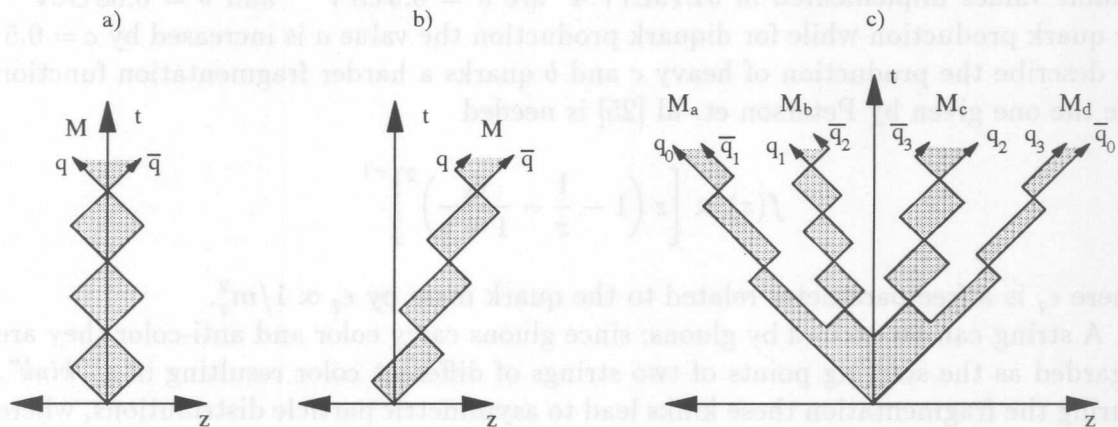


Figure 2.7: *Space-time diagram of string fragmentation. Oscillation of a $q\bar{q}$ pair without breaking of the string in the cms (a) and in an accelerated system (b). c) String fragmentation of a $q\bar{q}$ pair into four mesons.*

pair. This color-neutral object is called a string; the masses of the partons and the transverse extension are neglected. Assuming a constant energy density κ , the partons are allowed to move within a linearly increasing potential while the total energy of the string is proportional to its longitudinal extension. This assumption reflects the theoretical expectation from QCD that partons are confined.

In this model, hadrons are formed by an iterative procedure where a string breaks into two new strings or a meson and a remaining string (see fig. 2.6); the development in time is illustrated in figure 2.7.

First the quark and the anti-quark of the initial $q_0\bar{q}_0$ system move in opposite directions while the energy of the string increases continuously. By producing a new quark-antiquark pair $q_1\bar{q}_1$ the string breaks or splits into two new systems $q_0\bar{q}_1$ and $q_1\bar{q}_0$ resulting in an energetically much more favorable situation. This process is repeated as long as the potential energy in the string is large enough to create a new $q\bar{q}$ pair.

The distribution of the initial energy between the two new systems is not inherently given by the model but has to be defined externally. In the string fragmentation

model the assumption that no direction is favored and each breaking of a string is independent leads to a symmetric fragmentation function ('the Lund fragmentation function' [24])

$$f(z) \propto \frac{(1-z)^a}{z} \exp\left(\frac{-bm_{\perp}^2}{z}\right)$$

where m_{\perp} is the transverse mass given by

$$m_{\perp}^2 = m^2 + p_x^2 + p_y^2 = E^2 - p_z^2 = (E - p_z)(E + p_z)$$

and z the fraction of $(E + p_z)$ taken out of the available $(E + p_z)$

$$(E + p_z)_{new} = (1-z)(E + p_z)_{old}$$

The parameters a and b are determined from experimental measurements. The default values implemented in JETSET7.4¹ are $a = 0.3 \text{ GeV}^{-2}$ and $b = 0.58 \text{ GeV}^{-2}$ for quark production while for diquark production the value a is increased by $c = 0.5$. To describe the production of heavy c and b quarks a harder fragmentation function like the one given by Peterson et. al [25] is needed

$$f(z) \propto \left[z \left(1 - \frac{1}{z} - \frac{\epsilon_q}{1-z} \right)^2 \right]^{-1}$$

where ϵ_q is a free parameter related to the quark mass by $\epsilon_q \propto 1/m_q^2$.

A string can be excited by gluons; since gluons carry color and anti-color they are regarded as the starting points of two strings of different color resulting in a "kink". During the fragmentation these kinks lead to asymmetric particle distributions, where the particle density between the quark-gluon system is much higher than between the quark-antiquark system ("string effect").

Independent fragmentation

The model of independent fragmentation [28] was successfully used to describe experimental results from PETRA and PEP. Like in string fragmentation, hadrons are produced iteratively. The basic idea however is that each parton initiates an independent fragmentation process. Starting with one quark q_0 having energy E_0 a new quark-antiquark pair can be produced in the color field of q_0 where the combination $q_0\bar{q}_1$ leads to the formation of a meson carrying an energy fraction $z E_0$ (see fig. 2.8). This process is repeated until the available energy no longer allows the creation of a new $q\bar{q}$ pair; the remaining quark is either completely neglected or combined with another remaining quark forming a new hadron. To describe the energy splitting between the produced meson and the remaining quark the same fragmentation functions as discussed for the string model can be used; the original one however being the parameterization by Feynman and Field [26]. The fragmentation of gluons is treated by their decay into two quarks.

Though the model of independent fragmentation was successfully used, not all effects observed in data could be described, in particular the string effect. In addition, the model respects neither Lorentz invariance nor momentum and energy conservation.

¹The corresponding steering parameters are PARJ(41) for a, PARJ(42) for b and PARJ(45) for c.

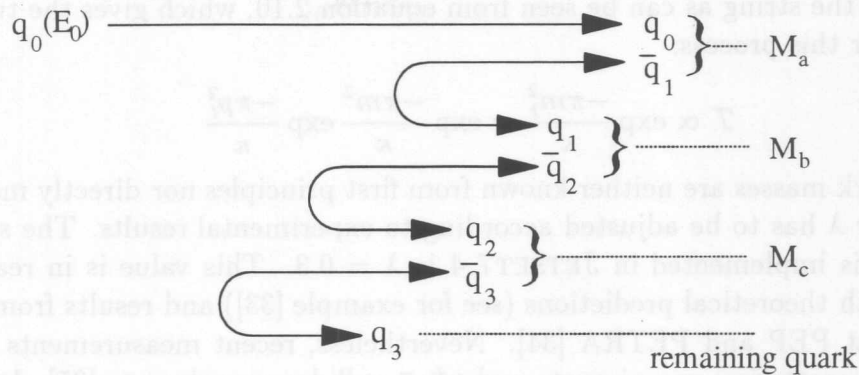


Figure 2.8: Independent fragmentation of a single quark

Cluster fragmentation

The model of cluster fragmentation allows a rather simple description of hadron production distinguishing between three successive phases. First, all existing gluons are split into quark-antiquark pairs. Then, during a so-called preconfinement phase, colorless clusters are formed from adjoining quarks and antiquarks. Finally, the fragmentation into hadrons is described by an isotropic two-body decay of the cluster under consideration. Similar to the string and independent fragmentation models, additional quark-antiquark and diquark-antidiquark pairs are created.

2.3.2 Multiple Interactions

In hadron-hadron interactions it is assumed that, in addition to the hard subprocess, which can be calculated by means of QCD, additional interactions can take place between several partons. Due to the hadronic component of the photon, this scenario of *multiple interactions* can also be applied to γp interactions, and will predominantly contribute at low p_t to the overall activity of an event. While the PYTHIA generator allows to switch off multiple interactions these are inherent to the PHOJET generator.

2.3.3 Strangeness suppression

During the fragmentation process, different flavors are produced with different probabilities, which leads to a suppression of strange hadrons with respect to non-strange particles.

Phenomenologically this is described by a so-called strangeness suppression factor λ that gives the ratio between the two probabilities $P(s\bar{s})$ and $P(u\bar{u})$ for producing a $s\bar{s}$ or $u\bar{u}$ pair, respectively,

$$\lambda = \frac{P(s\bar{s})}{P(u\bar{u})} = \frac{P(s\bar{s})}{P(d\bar{d})}. \quad (2.9)$$

Since it is assumed that there is no difference between u - and d -quarks the relation also holds with respect to d -quarks.

Physically strangeness suppression is related to the mass difference between s - and u -quarks. The higher mass of the strange quark reduces the probability to create a

$s\bar{s}$ pair out of the string as can be seen from equation 2.10, which gives the tunneling probability for this process:

$$\mathcal{T} \propto \exp \frac{-\pi m_t^2}{\kappa} = \exp \frac{-\pi m^2}{\kappa} \exp \frac{-\pi p_t^2}{\kappa} \quad (2.10)$$

Since the quark masses are neither known from first principles nor directly measured, the parameter λ has to be adjusted according to experimental results. The standard value² which is implemented in JETSET7.4 is $\lambda = 0.3$. This value is in reasonable agreement with theoretical predictions (see for example [33]) and results from former experiments at PEP and PETRA [34]. Nevertheless, recent measurements on λ in deep inelastic scattering experiments and e^+e^- collider experiments [35] claim that the standard setting of $\lambda = 0.3$ overestimates the K^0 -yield, while results from $p\bar{p}$ collider experiments even suggest a λ -value of about 0.5 [36].

A statement about strangeness suppression during fragmentation can be achieved by either comparing global Monte Carlo predictions for different λ -values with measurements from data, e.g. the K_S^0 -production cross section, or by exploiting certain ratios between strange and non-strange particle production cross sections; an alternative method which is model-independent and based on electroweak asymmetries in $q\bar{q}$ production has been proposed recently for the experiments at LEP [37].

A simulation for HERA kinematics using PYTHIA5.7 shows the expected effect on the K_S^0 -production cross section (fig. 2.9). Varying λ from 0.2 to 0.3 leads to an increase of the cross section of the order of 30%. In addition, the predictions for $\lambda = 0$ are shown; in this case no strange quarks can be produced during the fragmentation process. The fact that the remaining K_S^0 -production cross section is non-negligible, particularly at higher p_t , is a strong indication for strangeness originating from the hard subprocess or even the intrinsic strangeness of the photon or the proton. This will be discussed in section 2.4. The approach relying on ratios between strange and non-strange particles suggests a more straightforward access to the strangeness suppression factor. Some basic ideas and related experimental problems are briefly discussed in the following section (see also [38]).

The measurement of K/π

In this analysis, the ratio between neutral kaons and all charged particles from the primary interaction vertex is measured³.

Working on the very naïve assumptions that:

- during the fragmentation only (pseudo scalar) mesons are produced,
- the recombination of quarks into mesons is flavor independent and
- flavors from leading partons, i.e. partons from the hard subprocess, can be neglected,

the expected ratio can easily be calculated as a function of λ :

$$R(\lambda) = \frac{N_{K^0}}{N^+ + N^-} \approx \frac{P(K^0/\bar{K}^0)}{P(K^\pm) + P(\pi^\pm)} = \frac{\lambda}{1 + \lambda} \quad (2.11)$$

²The corresponding steering parameter is PARJ(2).

³Since no particle identification could be performed, no distinction between charged pions and charged kaons has been made.

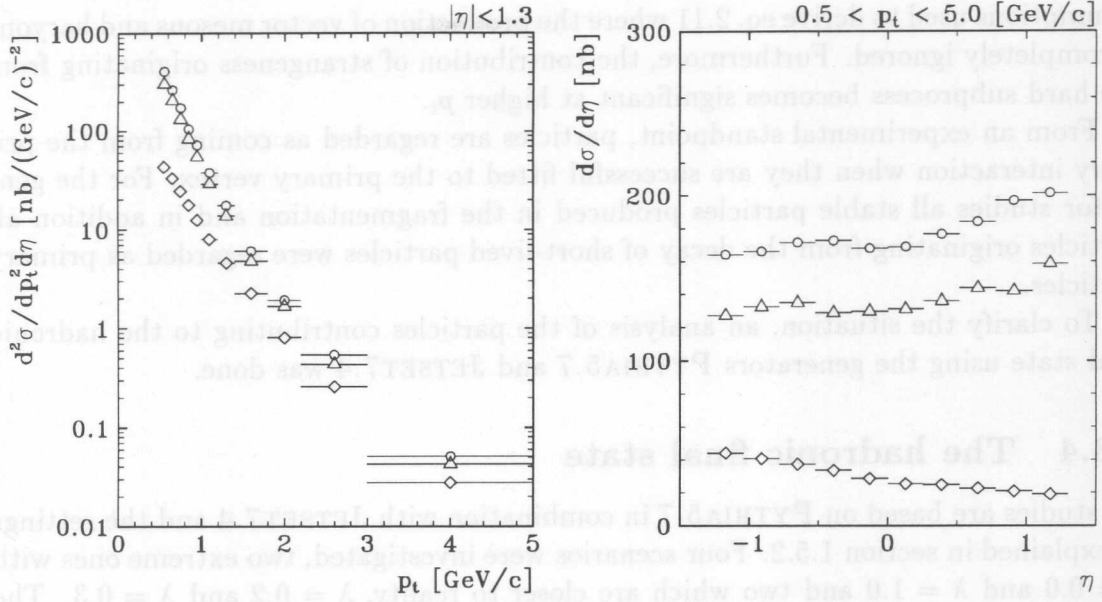


Figure 2.9: The expected K^0 -production cross sections as a function of p_t and η for various strangeness suppression factors λ ($\lambda = 0.0$: \diamond , $\lambda = 0.2$: \triangle and $\lambda = 0.3$: \circ); the generator used is PYTHIA.

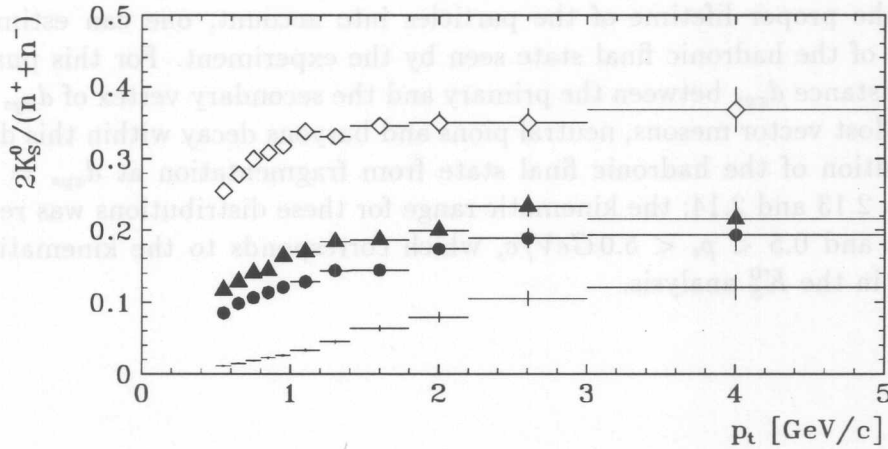


Figure 2.10: Prediction for the K/π ratio for various λ using PYTHIA5.7 (+ : $\lambda = 0$, \bullet : $\lambda = 0.2$, \triangle : $\lambda = 0.3$, \diamond : $\lambda = 1.0$).

where $P(K^0/\bar{K}^0)$, $P(K^\pm)$ and $P(\pi^\pm)$ are the probabilities to form a certain kaon or pion from the quarks produced during the fragmentation. In the measurement, the number of K^0 is assumed to be twice the number of K_S^0 . For this scenario the ratio should vary between 0 for $\lambda = 0$ and 0.5 for $\lambda = 1$. In fig. 2.10 various predictions from JETSET7.4 for different strangeness suppression factors are shown. In addition to a significant decrease of the ratio R at low p_t due to smaller phase-space available for the production of K_S^0 compared to pions, these predictions are systematically lower than the estimates given by equation 2.11. This is of course related to the very naive

assumptions used to derive eq. 2.11 where the production of vector mesons and baryons is completely ignored. Furthermore, the contribution of strangeness originating from the hard subprocess becomes significant at higher p_t .

From an experimental standpoint, particles are regarded as coming from the primary interaction when they are successfully fitted to the primary vertex. For the generator studies all stable particles produced in the fragmentation and in addition all particles originating from the decay of short-lived particles were regarded as primary particles.

To clarify the situation, an analysis of the particles contributing to the hadronic final state using the generators PYTHIA5.7 and JETSET7.4 was done.

2.3.4 The hadronic final state

All studies are based on PYTHIA5.7 in combination with JETSET7.4 and the settings as explained in section 1.5.2. Four scenarios were investigated, two extreme ones with $\lambda = 0.0$ and $\lambda = 1.0$ and two which are closer to reality, $\lambda = 0.2$ and $\lambda = 0.3$. The various contributions of charged and non-charged particles are shown in fig. 2.11 and 2.12. A rather large fraction of the produced charged particles are stable or long-lived mesons (e.g. K^\pm , π^\pm) and baryons while the rest is composed of short-living vector mesons and resonances that can further decay. For neutral particles the situation is different. Apart from the stable neutron and the K^0 s that go into K_L^0 , all particles have a short lifetime and decay.

Taking the proper lifetime of the particles into account, one can estimate the composition of the hadronic final state seen by the experiment. For this purpose, a cut on the distance d_{xyz} between the primary and the secondary vertex of $d_{xyz} < 1 \text{ cm}$ is applied. Most vector mesons, neutral pions and baryons decay within this distance. The composition of the hadronic final state from fragmentation at $d_{xyz} = 1 \text{ cm}$ is shown in fig. 2.13 and 2.14; the kinematic range for these distributions was restricted to $|\eta| < 1.3$ and $0.5 < p_t < 5.0 \text{ GeV}/c$, which corresponds to the kinematic range investigated in the K_S^0 analysis.

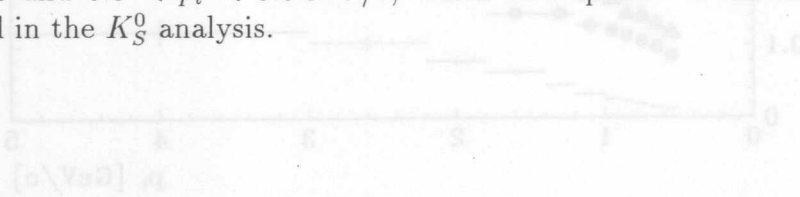


Figure 2.10: Prediction for the R/π ratio for various λ using PYTHIA5.7. ($\lambda = 0.0$: \square , $\lambda = 0.2$: \triangle , $\lambda = 0.3$: \circ , $\lambda = 1.0$: \times .)

where $P(K^0/\bar{K}^0)$, $P(K^\pm)$ and $P(\pi^\pm)$ are the probabilities to form a certain hadron from the quarks produced during the fragmentation. In the measurement, the number of K^0 is assumed to be twice the number of \bar{K}^0 . For this scenario the ratio should vary between 0 for $\lambda = 0$ and 0.5 for $\lambda = 1$. In fig. 2.10 various predictions from JETSET7.4 for different strangeness suppression factors are shown. In addition to a significant decrease of the ratio R at low p_t due to smaller phase space available for the production of K_S^0 compared to pions, these predictions are systematically lower than the estimates given by equation 2.11. This is of course related to the very naive

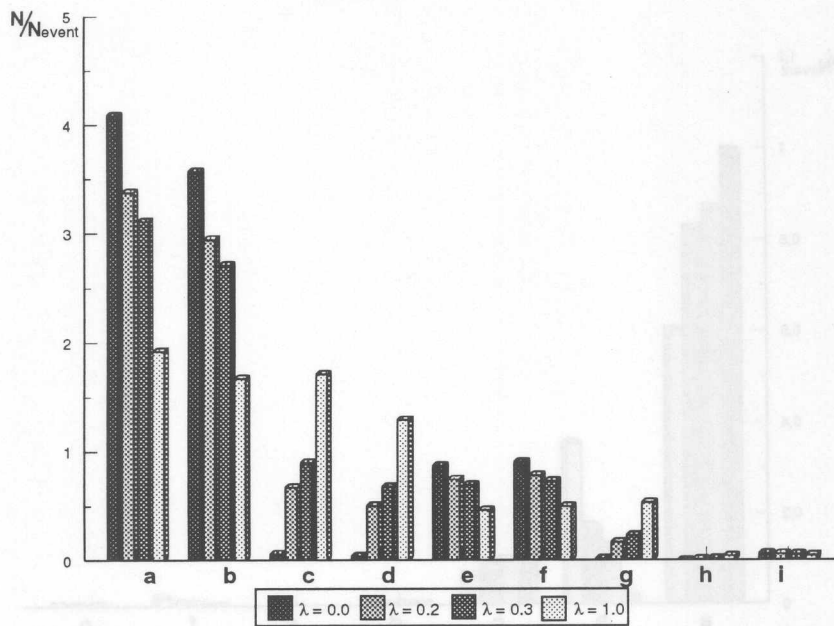


Figure 2.11: Composition of the hadronic final state from fragmentation (charged particles): a) π^\pm , b) ρ^\pm , c) $K^{*\pm}$, d) K^\pm , e) p^\pm , f) light baryons (d,u), g) heavy baryons (s,c,b), h) $D_s^{*\pm}, D_s^\pm$, i) $D^{*\pm}, D^\pm$.

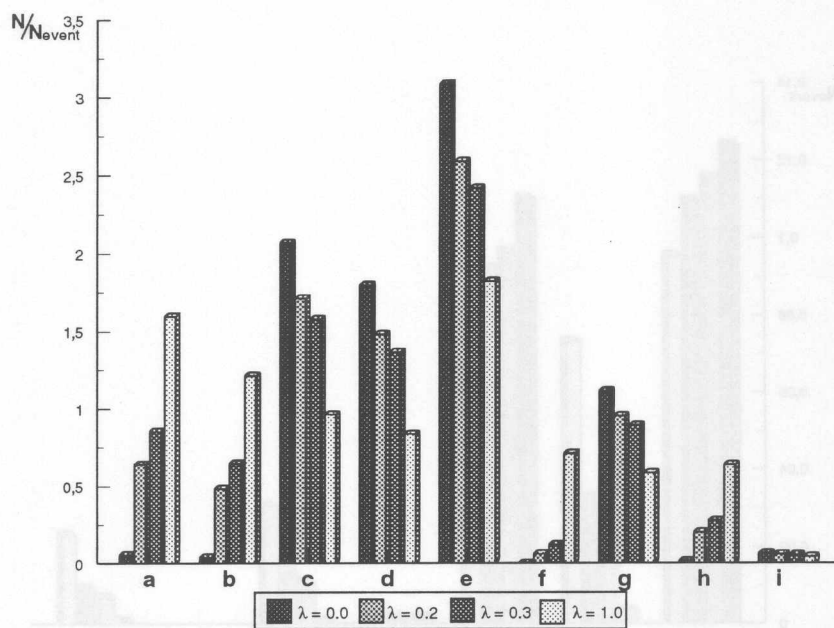


Figure 2.12: Composition of the hadronic final state from fragmentation (neutral particles): a) K^{*0} , b) K^0 , c) π^0 , d) ρ^0 , e) ω, η, η' , f) ϕ , g) light baryons (d,u), h) heavy baryons (s,c,b), i) D^{*0}, D^0 .

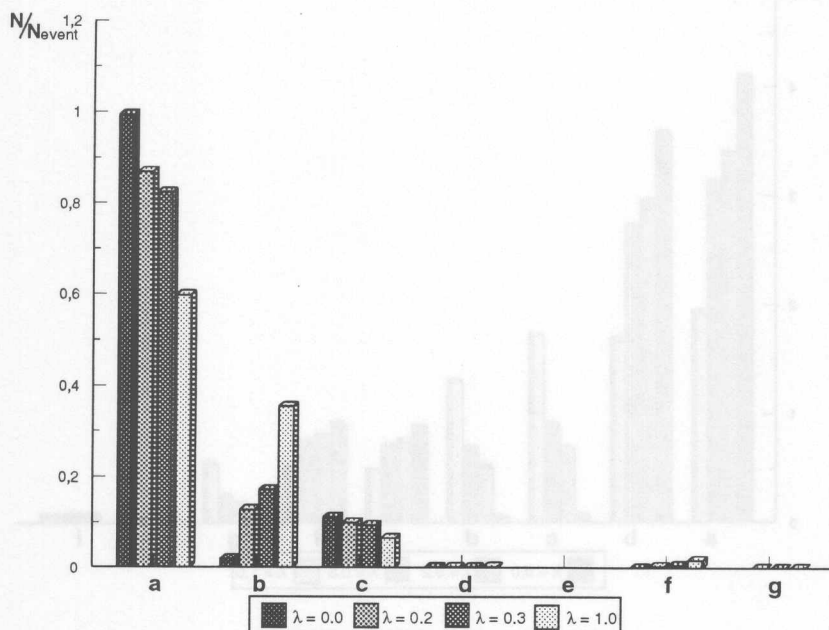


Figure 2.13: Stable particles in the kinematic range $|\eta| < 1.3$, $0.5 < p_t < 5.0 \text{ GeV}/c$ (charged particles): a) π^\pm , b) K^\pm , c) p/\bar{p} , d) e^\pm, μ^\pm, τ^\pm , e) D^+ , f) light baryons, g) heavy baryons.

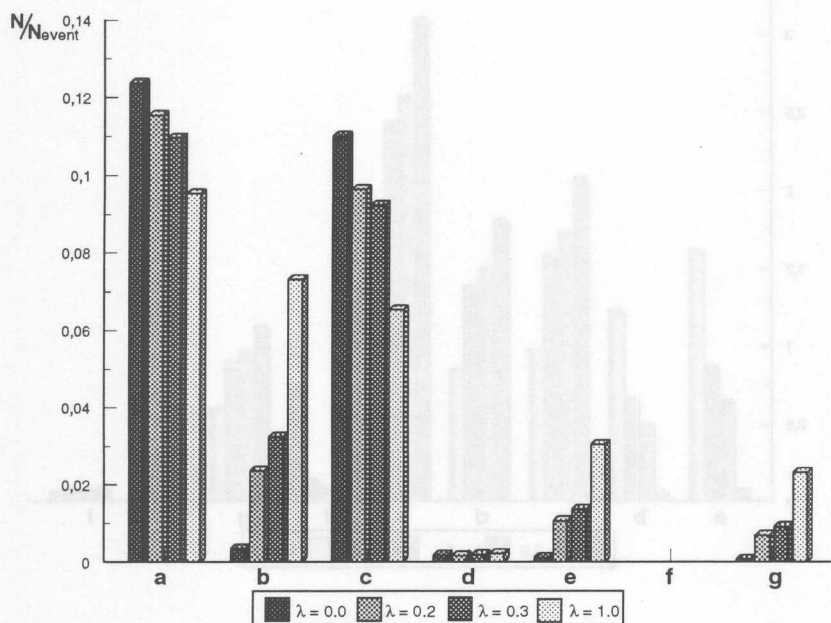


Figure 2.14: Stable particles in the kinematic range $|\eta| < 1.3$, $0.5 < p_t < 5.0 \text{ GeV}/c$ (neutral particles): a) γ , b) K_L^0 , c) n , d) ν_e, ν_μ, ν_τ , e) K_S^0 , f) D^0 , g) baryons.

Comparing the results for various strangeness suppression factors leads to the following results. As expected, the amount of strange particles increases significantly with increasing λ . But for the simple reasons that strangeness can also originate from other processes, that not only mesons are produced but also baryons and that a large fraction of the particles produced in fragmentation have very short lifetimes and decay, the number of observed strange particles is not simply scaled by the strangeness suppression factor λ . This holds particularly for the number of K^0 .

The next section describes where the K^0 s measured in the experiment are expected to originate from.

2.3.5 K^0 from hadronic decays

In the previous section it has been shown that during fragmentation a large contribution of heavier baryons and vector mesons is produced which can decay into lighter pseudoscalar mesons like K^+/K^- , K^0/\bar{K}^0 , π^+/π^- , or gammas ($\pi^0 \rightarrow \gamma\gamma$). It is therefore interesting to study where the K^0 s come from.

In the following section it is distinguished between K^0 s originating from the string fragmentation, either directly or via a K^* decay (see below), K^0 s originating from charm decays (see section 2.5), K^0 s originating from ϕ decays ($\phi \rightarrow K_S^0 K_L^0$, BR=34.4%) and K^0 s produced in diffractive events.

In fig. 2.15 and 2.16 the η and p_t distributions for the various K^0 s are shown. Since the kinematic range of the current analysis is restricted to particles with $\eta < |1.3|$ and $p_t > 0.5 \text{ GeV}/c$, these cuts have been applied to the generated particles, too. For all λ scenarios (except $\lambda = 0.0$) the dominant source of K^0 is the fragmentation process. The amount of K^0 coming directly from the string fragmentation and the amount of K^0 from K^* decays is about the same. The two η distributions do not show any significant differences, the same holds for the p_t distributions, except for the very low- p_t range; there might be an indication that the p_t distribution of K^0 from K^* decays is slightly softer.

The third important contribution is formed by K^0 s from charm decays. Charmed mesons are not produced during the fragmentation but only during the hard subprocess, the dominant process being photon-gluon fusion (see section 2.5). This explains the different shape of the η distribution (K^0 s from charm decays are predominantly expected in the backward hemisphere of the detector) and that this contribution is not sensitive to λ . The p_t -spectrum of K^0 s from charm decays is much harder than that of K^0 s originating from the fragmentation process.

K^0 originating from K^* decays

Nearly 50% of the K^0 s originating from fragmentation are K^* decay products. The arrangement of the K^* mesons within an isospin doublet is analogous to the one of the pseudoscalar kaons (see table 2.1). Having a mass of $m_{K^*} = 0.892 \text{ GeV}/c^2$, the K^* s are much heavier than the pseudoscalar kaons.

They decay nearly exclusively via a strong interaction into a kaon and a pion

$$K^{*+} \rightarrow \begin{cases} K^0 \pi^+ & 66.6 \% \\ K^+ \pi^0 & 33.3 \% \end{cases}$$

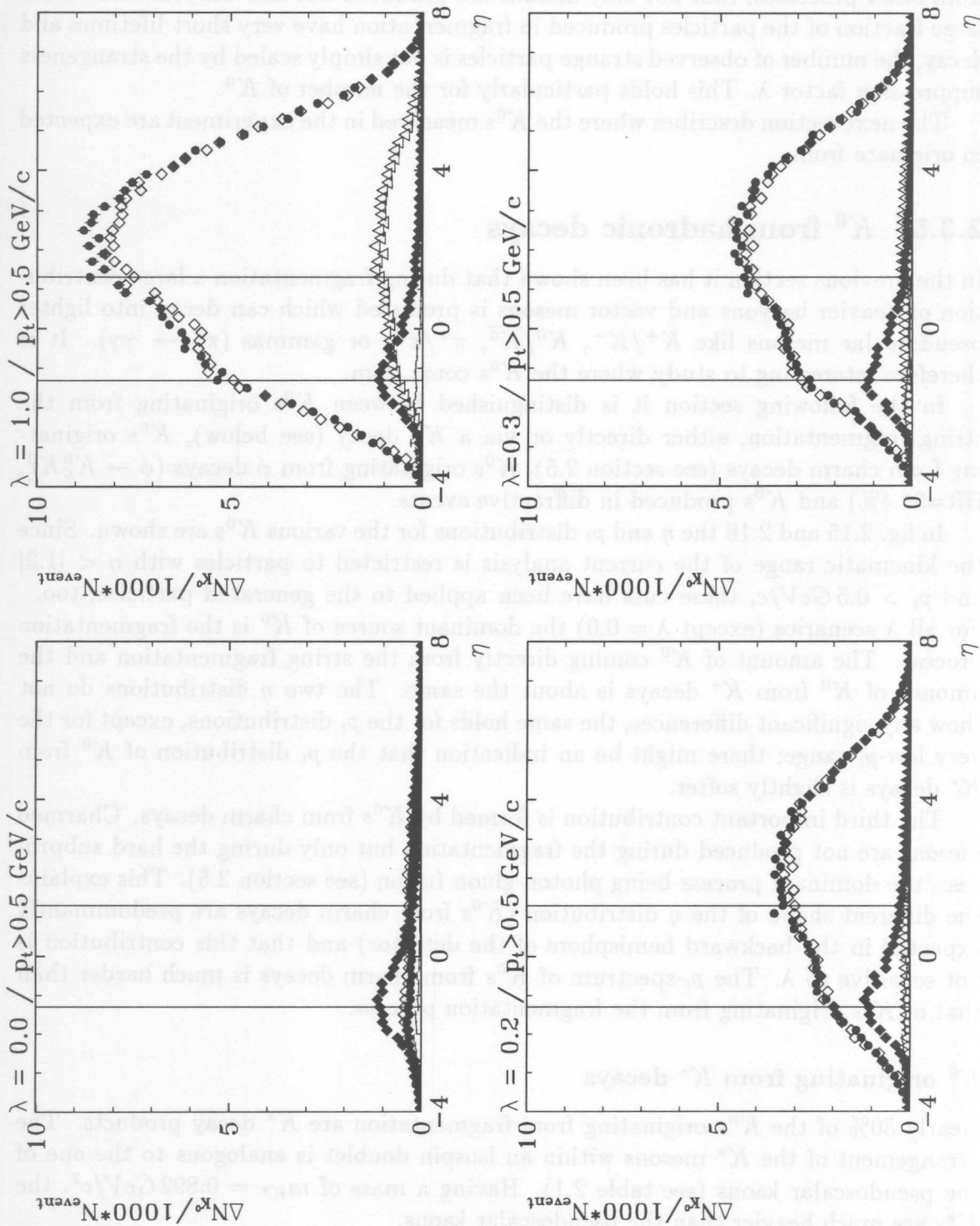


Figure 2.15: η distributions of K^0 produced in γp interactions. \bullet : K^0 directly from the string, \diamond : K^0 via K^* decay from the string, filled \diamond : K^0 from charm decays, \triangle : K^0 from ϕ decays, + other origins; the pseudorapidity range indicated by two vertical lines corresponds to the range $|\eta| < 1.3$ which can be investigated using the CJC.

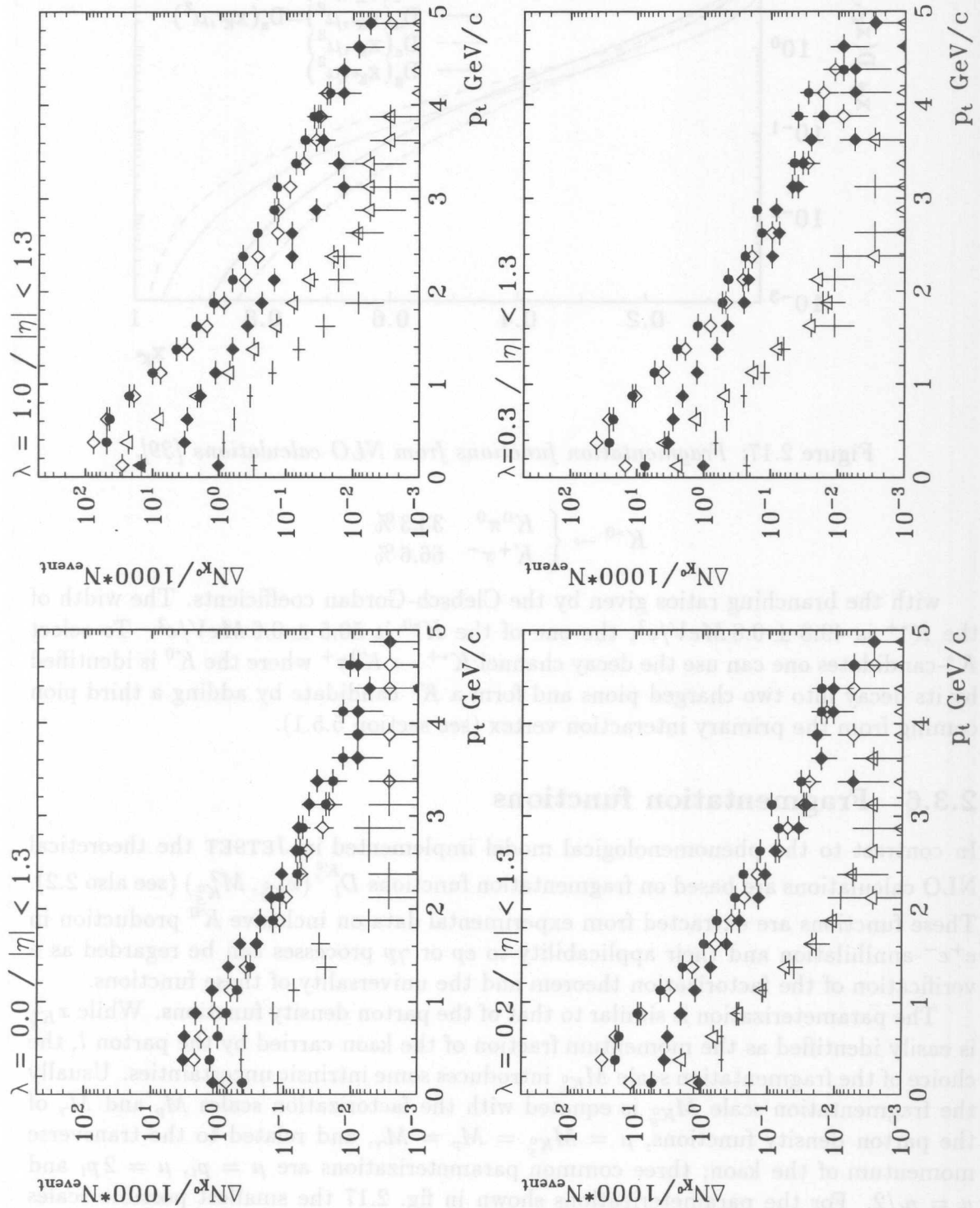


Figure 2.16: p_t distributions of K^0 produced in γp interactions. \bullet : K^0 directly from the string, \diamond : K^0 via K^* decay from the string, filled \diamond : K^0 from charm decays, \triangle : K^0 from ϕ decays, + other origins.

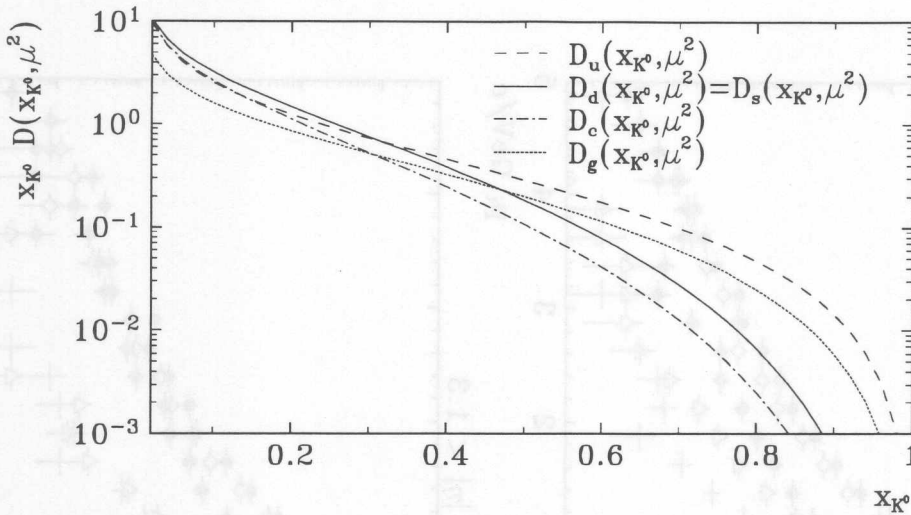


Figure 2.17: Fragmentation functions from NLO calculations [39].

$$K^{*0} \rightarrow \begin{cases} K^0 \pi^0 & 33.3\% \\ K^+ \pi^- & 66.6\% \end{cases}$$

with the branching ratios given by the Clebsch-Gordan coefficients. The width of the K^{*+} is $49.8 \pm 0.8 \text{ MeV}/c^2$, the one of the K^{*0} is $50.5 \pm 0.6 \text{ MeV}/c^2$. To select K^* -candidates one can use the decay channel $K^{*+} \rightarrow K^0 \pi^+$ where the K^0 is identified by its decay into two charged pions and form a K^* candidate by adding a third pion coming from the primary interaction vertex (see section 5.5.1).

2.3.6 Fragmentation functions

In contrast to the phenomenological model implemented in JETSET the theoretical NLO calculations are based on fragmentation functions $D_i^{K^0}(x_{K_S^0}, M_{K_S^0}^2)$ (see also 2.2). These functions are extracted from experimental data on inclusive K^0 production in e^+e^- -annihilation and their applicability to ep or γp processes can be regarded as a verification of the factorization theorem and the universality of these functions.

The parameterization is similar to that of the parton density functions. While $x_{K_S^0}$ is easily identified as the momentum fraction of the kaon carried by the parton l , the choice of the fragmentation scale $M_{K_S^0}$ introduces some intrinsic uncertainties. Usually the fragmentation scale $M_{K_S^0}$ is equated with the factorization scales M_p and M_γ of the parton density functions, $\mu = M_{K_S^0} = M_p = M_\gamma$, and related to the transverse momentum of the kaon; three common parameterizations are $\mu = p_t$, $\mu = 2p_t$ and $\mu = p_t/2$. For the parameterizations shown in fig. 2.17 the smallest possible scales were chosen; for u, d and s -quarks this is $\mu = \sqrt{2} \text{ GeV}/c$ and for c quarks one sets $\mu = m(\eta_c)$, the mass of the η_c .

2.4 Strangeness from the hard subprocess

Strangeness can originate from the intrinsic strangeness of the proton and/or the photon or the hard subprocess. For the photon, the intrinsic strangeness is given by the resolved component of the photon, which in PYTHIA is described by the VMD model and the anomalous part of the photon. The intrinsic strangeness of the proton is related to the strange sea-quarks.

The probability to get strangeness from the photon or the proton is given by the parton density functions (PDFs) $G_i^\gamma(x_\gamma, M_\gamma^2)$ and $G_j^p(x_p, M_p^2)$ where x_γ and x_p are the momentum fractions carried by the corresponding parton and M_γ^2 and M_p^2 the factorization scales. Fig. 2.18 shows various parameterizations of the strangeness distribution functions, the parameterization currently used in Monte Carlo and NLO calculations are those of GRV[40] both for the photon and the proton⁴. In γp interactions as observed at HERA most events are expected to have scaling variables in the range $0.003 < x_p < 0.3$ and $x_\gamma > 0.003$, (see fig. 2.19) and according to predictions by PYTHIA5.7, the fraction of events with strangeness from the photon in resolved events is expected to be about $\approx 0.02\%$, while strangeness from the proton is with $\approx 0.017\%$ even more suppressed. In addition strange quarks can be produced directly in the hard subprocess (see for example fig. 1.7), where the dominant process is photon-gluon fusion. From the distributions shown in the previous section for $\lambda = 0$, it is obvious that contributions from these processes might become important at higher p_t .

2.5 Strangeness production in photon-gluon fusion

Photon-gluon fusion is the dominant process for production of heavy flavors at HERA. Since a large fraction of charmed mesons decays into neutral kaons

$$\begin{aligned} D^\pm &\rightarrow K^0 X + \overline{K}^0 X && (59 \pm 7)\% \\ D^0 &\rightarrow K^0 X + \overline{K}^0 X && (42 \pm 5)\% \end{aligned}$$

the reconstruction of these decays can be useful for an enhancement of events containing charm.

Of special interest is the decay channel $D^0 \rightarrow \overline{K}^0 \pi^+ \pi^-$, where one has to distinguish between the direct mode

$$\begin{aligned} D^0 &\rightarrow \overline{K}^0 \pi^+ \pi^- && (1.8 \pm 0.50)\% \\ &\mapsto \pi^+ \pi^- && 0.5 \cdot (68.61 \pm 0.28)\% \end{aligned}$$

and the K^* -resonance-mode

$$\begin{aligned} D^0 &\rightarrow K^{*-} \pi^+ && \approx 0.05\% \\ &\mapsto \overline{K}^0 \pi^- && 66.67\% \\ &\mapsto \pi^- \pi^+ && 0.5 \cdot (68.61 \pm 0.28)\% \end{aligned}$$

The standard method to eventually identify charm events is given by the D^* -tagging [41]. This traditional method utilizes the decay

$$D^{*+} \rightarrow D^0 \pi^+ \quad (55 \pm 4)\%,$$

⁴In case PYTHIA5.7 is used with the new option generating a mixture of all γp -subprocesses an internal parameterization is chosen for the photon structure function.

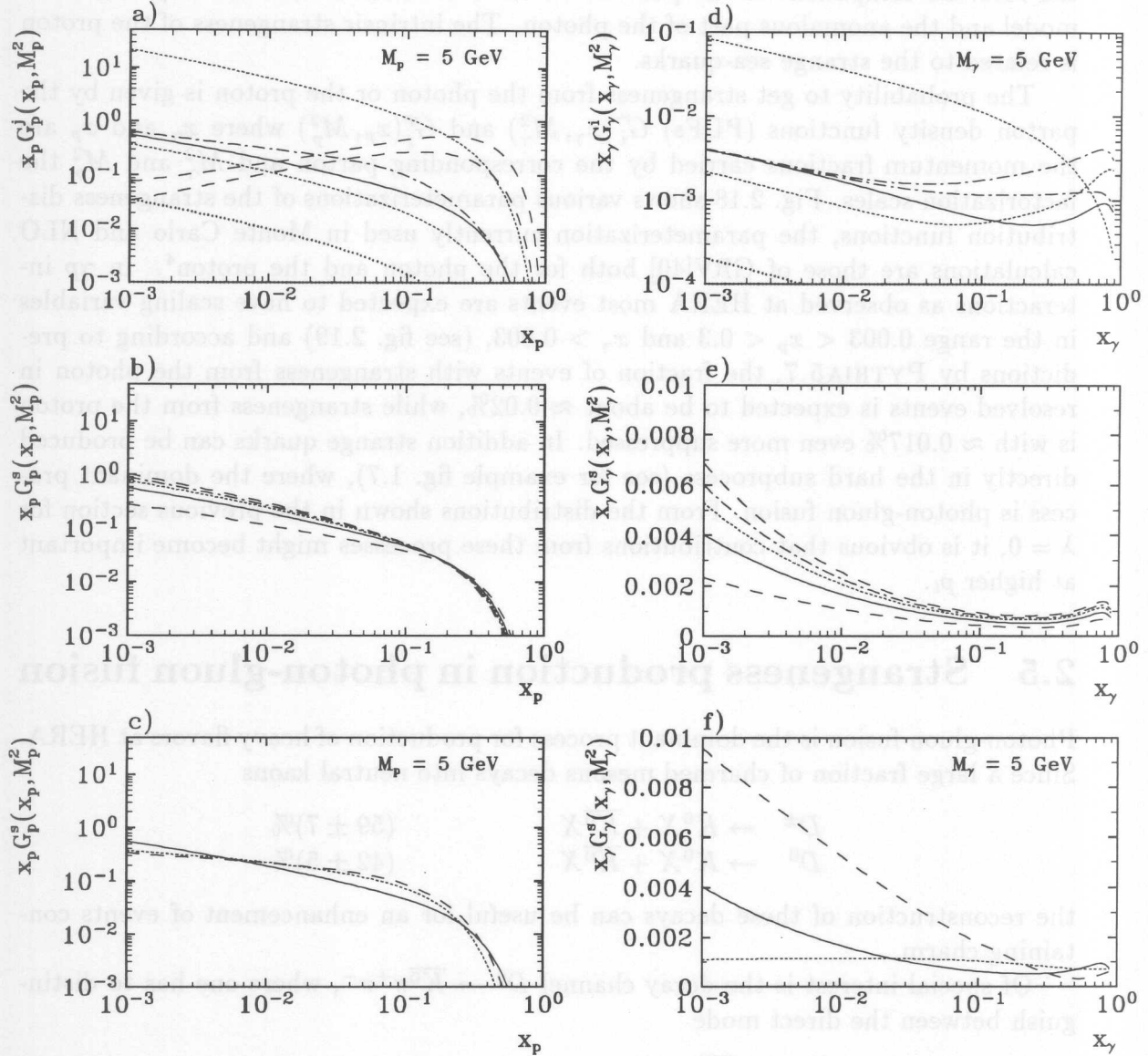


Figure 2.18: Parton density distributions of the proton (right) and the photon (left). Fig.a/d) show the density distribution of the gluon (upper dotted curve) and various flavors (dashed: u and d valence quarks, solid: s quark, dashed-dotted: u and d sea quarks, lower dotted curve: c quarks). Fig. b/e) show the strangeness distribution for various values of the factorization scale M_p/M_γ , $M = 2, 5, 10, 15$ and 25GeV (the larger M the larger the strangeness density). In Fig. c/f) the GRV-parameterization (solid curve) is compared against two other parameterizations (proton: CTEQ (dashed), MRS S0 (dotted), photon: LAC-G (dashed), DG (dotted) [19] and references given there)

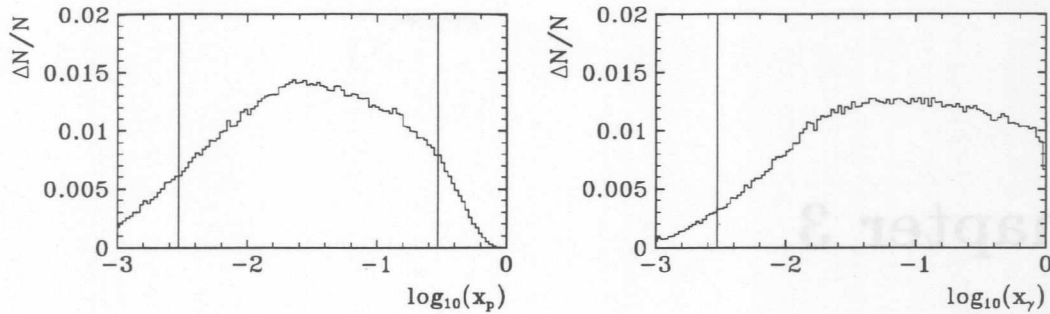


Figure 2.19: Distribution of the scaling variables x_γ and x_p for γp interactions as predicted by PYTHIA

but in this case not the actual D^* signal is investigated but the corresponding mass-difference

$$\Delta M = M(D^0 \pi^+) - M(D^0)$$

between the reconstructed D^* ($m_{D^*} = 2010.1 \pm 0.6 \text{ MeV}/c^2$) and the D^0 ($m_{D^0} = 1864.5 \pm 0.5 \text{ MeV}/c^2$); due to the given kinematic, this mass difference of $\Delta M = 145.44 \text{ MeV}/c^2$ can be measured much more accurately than the mass of the D^* .

3.2 The H1 detector

Throughout this work, the H1 coordinate system is defined as a right-handed one where x is along the proton-beam direction, y points upward and z is horizontal.

Chapter 3

The H1 experiment at HERA

In this chapter the H1 experiment at HERA is described. The emphasis is on the detector components used in this analysis. In addition, some details of the trigger system and the event reconstruction are explained.

3.1 The ep collider HERA

The ep collider HERA (*Hadron Elektron Ring Anlage*) was put into operation in 1991, and it is the first machine allowing electron-proton collisions at a center-of-mass energy of $\sqrt{s} = 314 \text{ GeV}$. It consists of two independent accelerators of 6336 m in circumference each. The maximal energy is 30 GeV for electrons (or positrons) and 820 GeV for protons. Operating under optimal conditions, the maximal luminosity which can be achieved is $\mathcal{L} = 1.5 \cdot 10^{31} \text{ cm}^{-2} \text{ s}^{-1}$.

Fig. 3.1 shows the experimental site in Hamburg. The accelerators DESY and PETRA are used as pre-accelerator and injection system, respectively. The experiments H1 and ZEUS are located in the North hall and in the South hall. The West hall houses the infrastructure needed to operate HERA and the East hall will be used for experiments with polarized electrons or positrons.

In both beams the maximal number of bunches is 210 and the time difference between two bunch crossings is 96 ns ; some additional parameters are listed in table 3.1. In contrast to the design value, there were only 153 colliding bunch sequences filled in 1994; in addition, 32 bunches had no collision partners. These pilot bunches (17 proton bunches and 15 positron bunches) can be used to estimate the background from interactions of the electron or proton beam with the residual gas which consists mainly of hydrogen and carbon monoxide at a gas pressure of $\approx 1 - 2 \cdot 10^{-9} \text{ mbar}$. Apart from a reduced number of filled bunch sequences, only a fraction of the design currents could be achieved. Therefore the maximal measured luminosity amounted only to $\mathcal{L} = 2.5 \cdot 10^{30} \text{ cm}^{-2} \text{ s}^{-1}$ which corresponds to $\approx 17\%$ of the design value. The length of the interaction region which is related to the longitudinal extension of the electron and proton bunches is about 40 cm (see fig. 3.2).

3.2 The H1 detector

Throughout this work, the H1 coordinate system is defined as a right-handed one where z is along the proton-beam direction, y points upward and x is horizontal.

	design parameters		1994		units
	p-ring	e-ring	p-ring	e-ring	
ep <i>c.m.s</i> energy	314		301		GeV
Q_{max}^2	98400		90528		GeV ² /c ²
peak luminosity	$1.5 \cdot 10^{31}$		$2.5 \cdot 10^{30}$		cm ⁻² s ⁻¹
energy	820	30	820	27.6	GeV
bending radius of dipoles	588	608	588	608	m
magnetic bending field	4.64	0.165	4.64	0.165	T
circumference	6336		6336		m
number of bunch buckets	210		153		-
circulating currents	163	58	35	25	mA
time between bunch crossings	96		96		ns

Table 3.1: Characteristic parameters of the ep collider HERA [45]

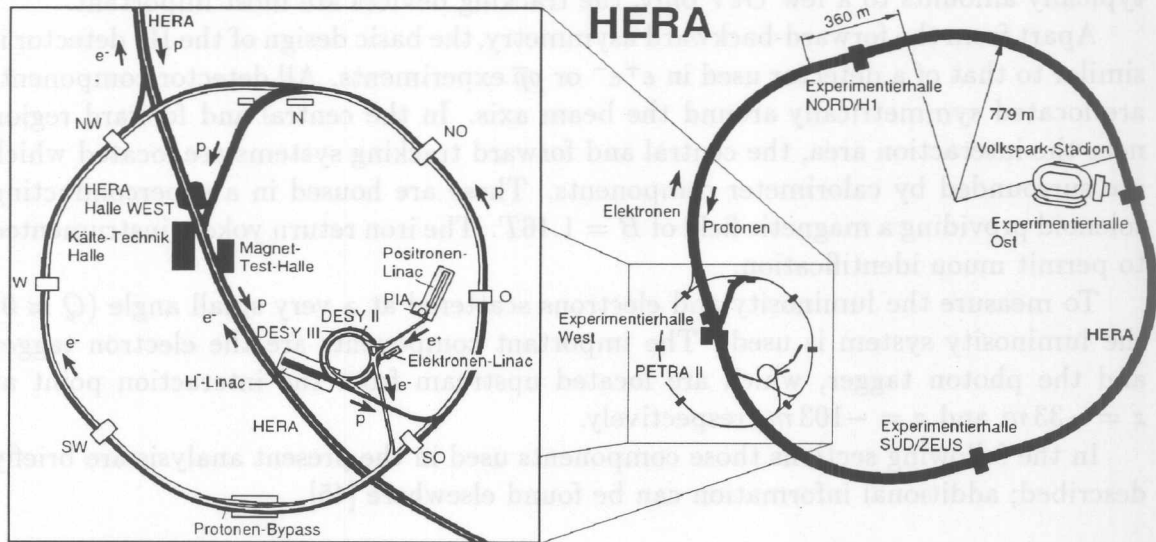


Figure 3.1: The experimental site of HERA

The longitudinal cut through the H1 detector in fig. 3.3 shows its main components. The combination of calorimeters and tracking devices allows to investigate most of the processes induced by the *ep* collisions at HERA. The large energy imbalance of the colliding beams (27.6 GeV electrons on 820 GeV protons) and the resulting event topologies where most of the final state particles are emitted with rather small angles in forward direction (proton direction) requires an asymmetric detector.

Depending on the physics processes under investigation, different demands have to be met. The analysis of deep-inelastic-scattering processes (DIS) for instance has to rely on very accurate energy flow measurements. In this case calorimeters with fine granularity, good energy resolution and a nearly overall hermeticity are needed. For the analysis of γp interactions however, where the deposited energy in the calorimeters

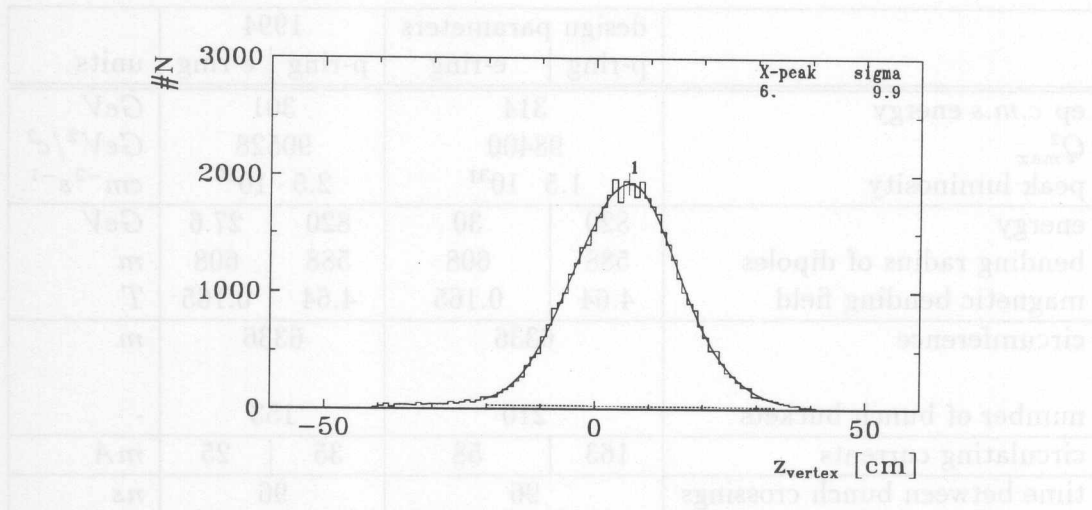


Figure 3.2: The z -vertex distribution as measured by H1

typically amounts to a few GeV only, the tracking devices are most important.

Apart from the forward-backward asymmetry, the basic design of the H1 detector is similar to that of a detector used in e^+e^- or $p\bar{p}$ experiments. All detector components are located symmetrically around the beam axis. In the central and forward region near the interaction area, the central and forward tracking systems are located which are surrounded by calorimeter components. These are housed in a superconducting solenoid providing a magnetic field of $B = 1.16T$. The iron return yoke is instrumented to permit muon identification.

To measure the luminosity and electrons scattered at a very small angle ($Q \approx 0$) the luminosity system is used. The important components are the electron tagger and the photon tagger, which are located upstream from the interaction point at $z = -33m$ and $z = -103m$, respectively.

In the following sections those components used in the present analysis are briefly described; additional information can be found elsewhere [45].

3.3 The central tracking chambers

The central tracking system consists of two jet chambers $CJC1$ and $CJC2$, two multiwire proportional chambers CIP and COP and the central z chambers CIZ and COZ . The basic principle of all components is that of a simple drift chamber [43, 44, 45]. The task of the central jet chamber is the measurement of the track-hit coordinates (r/φ and z) and the energy loss dE/dx . The combination of all information eventually allows to determine the transverse and the total momentum; in specific cases even the identification of charged particles is possible using dE/dx .

The central multiwire proportional chambers are mainly used to trigger events with small transverse energy flow and low multiplicity, which are not seen by the calorimeter triggers due to their high energy thresholds. The purpose of the central z chambers is to improve the z measurement provided by the CJC . The alignment of the different chambers is shown in figure 3.4.

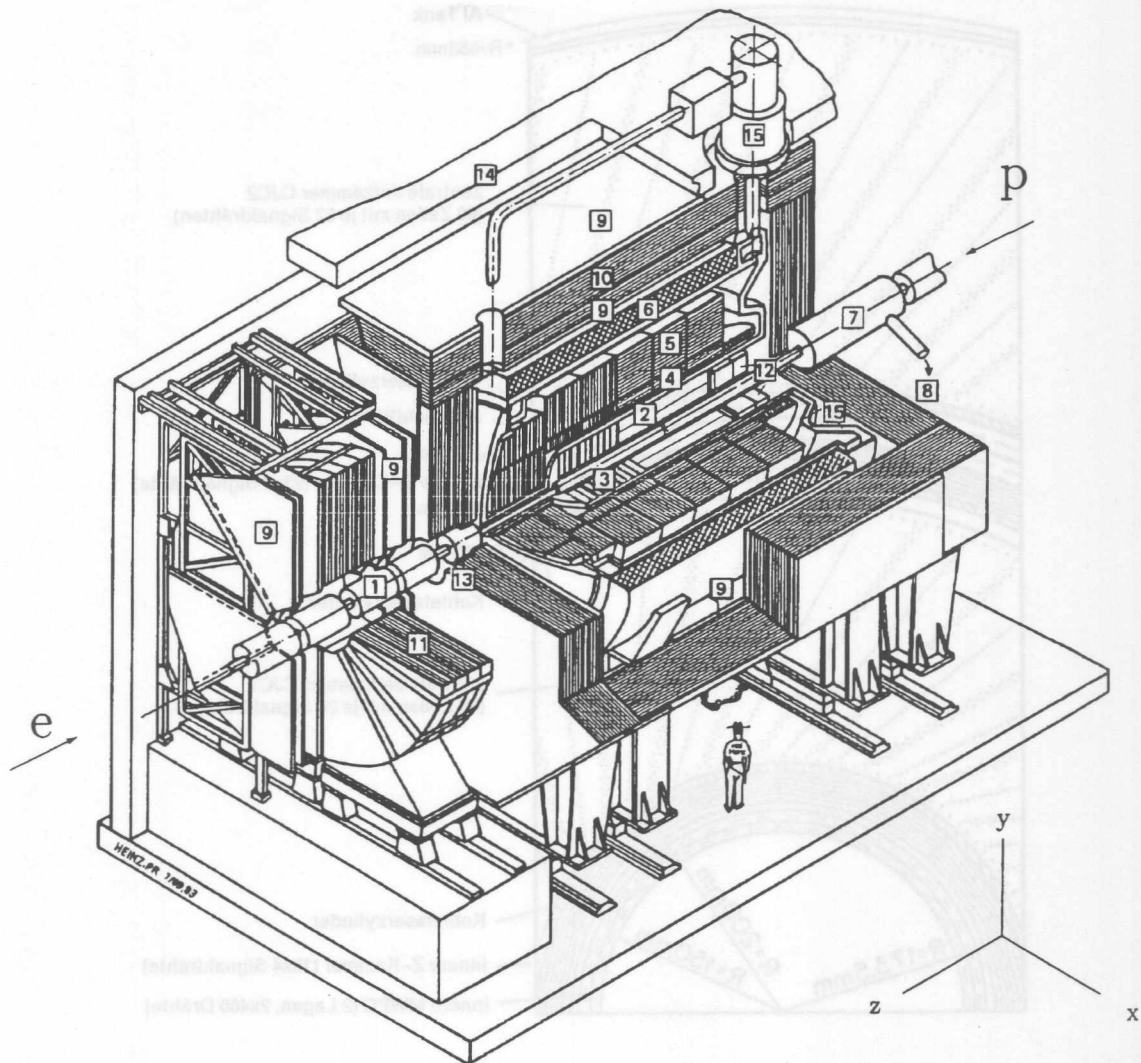


Figure 3.3: *The H1 experiment.*

(1): beam pipe and beam magnets, (2): central tracking chambers, (3): forward tracking chambers and transition radiators, (4)+(5): liquid argon calorimeter (electromagnetic calorimeter (4), hadronic calorimeter (5)), (6): superconducting coil, (7): compensating magnet, (8): helium cryogenics, (9): muon chambers, (10): instrumented iron, (11): muon toroid, (12): warm electromagnetic calorimeter, (13): plug calorimeter, (14): concrete shielding, (15): liquid argon cryostat

3.3.1 The central jet chamber

The central jet chamber (*CJC*) consists of two independent drift chambers *CJC1* and *CJC2*. The inner cylinder of *CJC1* consists of 30 drift cells with 24 sense wires each, the outer cylinder of *CJC2* of 60 drift cells with 32 sense wires each. All sense, potential and cathode wires are parallel to the beam axis, their layout is shown in figure 3.4.

To improve the r/φ resolution, the drift cells are tilted at 30° with respect to the radial direction. Since the detector is operated in a magnetic field, the electrons and

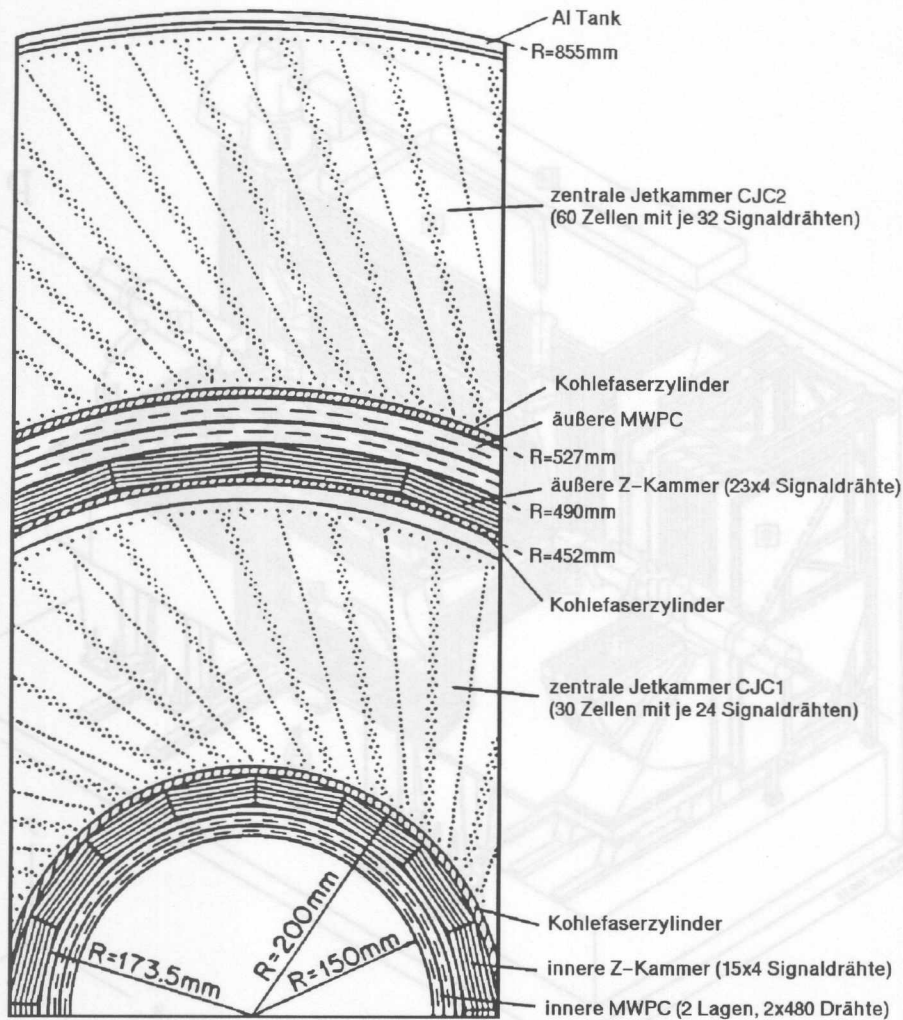


Figure 3.4: Alignment of the different tracking chambers

ions which are produced by particles traversing the drift chamber volume are forced by the Lorentz force to move on a circular path. This leads, on a macroscopic scale, to a constant angle α_L (known as the Lorentz angle) between the drift direction and the electric field between the sense- and cathode-wire plane. For particles coming from the primary interaction vertex, which have a relatively high transverse momentum, this angle is compensated by the tilt of the sense wire planes and the drift direction is perpendicular to the direction of the particle. This is usually one of the important requirements for a good r/φ resolution. In addition, it makes it much easier to resolve the so-called left-right ambiguities occurring during reconstruction, when track segments from adjacent cells are combined to form a track.

To resolve left-right ambiguities with respect to the sense wire plane within a cell, the sense wires are staggered by $\pm 150 \mu\text{m}$ against the nominal plane. Due to the electrostatic forces between the wires, this staggering increases; in the central region of the *CJC*, at $z = 0$, the effective staggering in *CJC1* is $\pm 250 \mu\text{m}$ and in *CJC2* $\pm 250 \mu\text{m}$ [46]. The sense wires are separated by pairs of potential wires which reduce the cross-talk between neighboring wires and the surface field of the wires by about 50%. The latter should prevent the chamber from a fast aging process. As

the nominal position of a specific sense wire between four potential wires is further given by a minimum of the electric field, the sense wire is in a condition of stable equilibrium.

Both chambers are operated under a slight overpressure of $1500 \pm 500 \mu\text{bar}$ with respect to the atmospheric pressure; during the data taking in 1994 they were filled with the flammable gas mixture Argon/Ethane (50/50).

3.3.2 The H1 calorimeter

The calorimeter system of the H1 detector consists of three different components: the LAr in the central region, the PLUG in the very forward region and the BEMC in the backward region. The largest one is the liquid argon calorimeter (LAr) covering the polar range from 4° to 155° . It consists of two components in order to identify both electromagnetic and hadronic showers. The fine segmentation with about 45 000 separate cells further allows a very good spatial resolution. The energy resolution of the electromagnetic calorimeter varies between 10% and $13\%\sqrt{E}$. The resolution of the hadronic part is of the order of $50\%\sqrt{E}$.

Hadrons emitted under a very small angle in the forward direction might substantially contribute to the transverse energy flow and are measured with the PLUG. With the angular acceptance being $0.6^\circ < \theta < 3^\circ$, it nearly closes the gap to the LAr. The PLUG consists of a copper silicon sandwich and has a resolution of $100\%\sqrt{E}$.

In the backward hemisphere ($151^\circ < \theta < 177^\circ$) an electromagnetic lead scintillator sandwich (BEMC) is used to close the gap between the beam pipe and the LAr. The main task of this component is the reconstruction of the scattered electron. The energy resolution is approximately $10\%\sqrt{E}$.

3.3.3 The luminosity system

The luminosity measurement at H1 is based on the electromagnetic Bethe-Heitler process $ep \rightarrow e'p\gamma$, which can be calculated within QED. For its identification, the scattered electron is measured in coincidence with the photon with two separate calorimeters at $z = -33\text{ m}$ and $z = -108\text{ m}$ (see fig. 3.5). The scattered electron is deflected by the magnets of the electron ring and detected in the electron-tagger (ET); the photon, moving collinearly with the incident electron, is detected in the photon-tagger (PD). The resolution of both calorimeters is of the order of $10\%\sqrt{E}$.

To estimate the background from interactions between electrons and the residual gas in the beam pipe or the beam wall itself, $eA \rightarrow e'A\gamma$, the pilot bunches are used, and the luminosity is calculated as

$$L = \frac{R_{tot} - (I_{tot}/I_0)R_0}{\sigma_{vis}}$$

where R_{tot} is the total rate of bremsstrahlung events, R_0 the rate in the pilot bunches and I_{tot}/I_0 the ratio of the corresponding beam currents; σ_{vis} is that part of the calculated cross section $ep \rightarrow e'p\gamma$ visible with the apparatus.

Besides the measurement of the luminosity, the luminosity system allows the selection of photoproduction events with $Q^2 < 0.01\text{ GeV}^2$. The trigger requirement for these events is given by the presence of a signal in the electron tagger and the absence of a signal in the γ -tagger (section 3.4.1). The reconstructed ETAG signal is also used to calculate the kinematic variable y (see eq. 1.1).

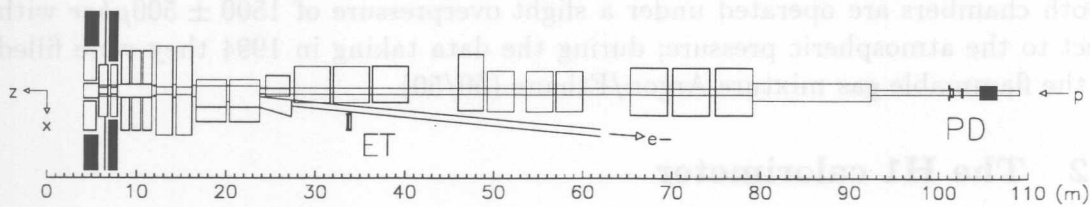


Figure 3.5: The luminosity system of H1

3.4 The H1 trigger

The main purpose of the H1 trigger is to select only those events which were caused by actual ep interactions. Due to the large background and the very short time interval between two bunch crossings, a trigger consisting of four successive levels, L1 to L4, was designed. The minimal dead time that can be achieved corresponds to about 10%; the level L1 is dead time free. At level L1, the central trigger logics (CTL) is used to form a very fast trigger decision. Because of delay times and long response times of some detector components, it takes typically $2 \mu\text{s}$ to form a L1-trigger decision, -much longer than the time interval between two bunch crossings. To avoid dead time at this level, a so-called pipeline system is used for intermediate data storage. In case of a positive L1-trigger decision these pipelines are stopped and the read-out starts. In the future, the trigger levels L2 and L3 will allow to stop the read-out again after $20 \mu\text{s}$ and some $100 \mu\text{s}$.

The fourth trigger level, L4, the so-called *filter farm*, is part of the central data acquisition (CDAQ). Since the complete information on the event is available, parts of the standard reconstruction program and special filter algorithms are used to obtain a L4-trigger decision. The filter farm reduces the event rate down to $5 - 10 \text{ Hz}$. A further reduction of the data sample is achieved during the event classification and selection during the *off-line* analysis. Figure 3.6 gives an overview on the data flow in the H1 experiment.

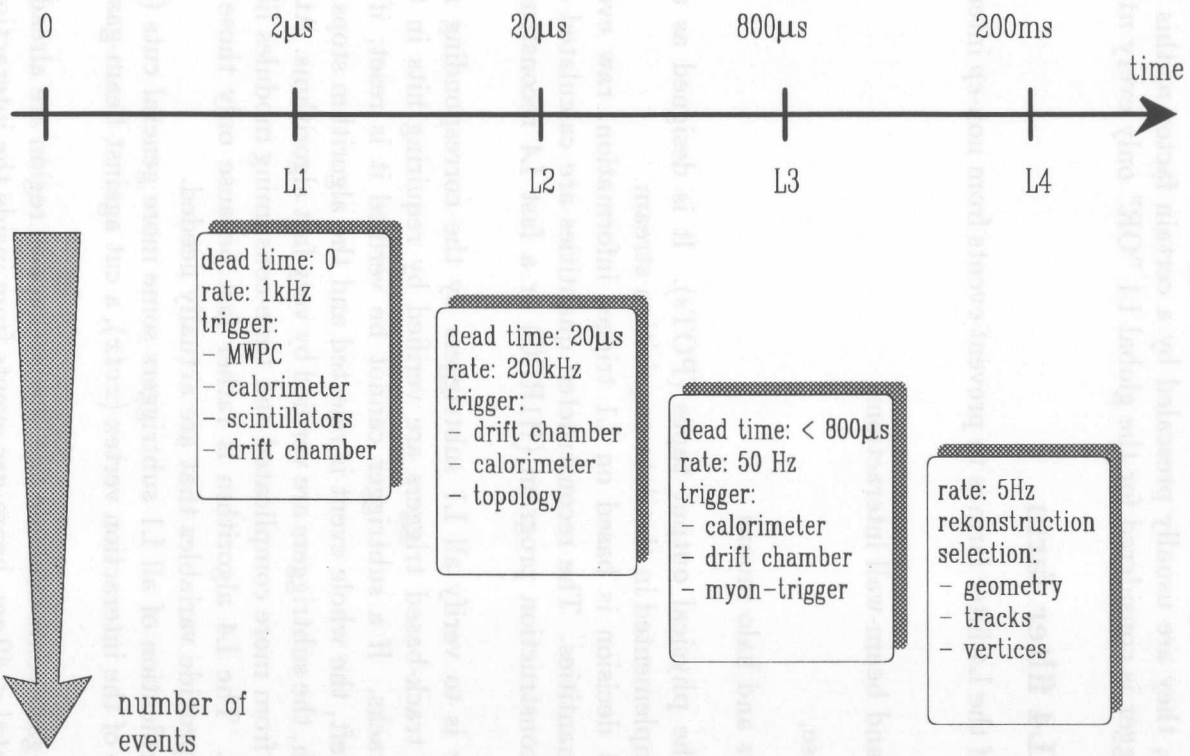


Figure 3.6: Overview on the data reduction at the H1 trigger

3.4.1 The central trigger logic (CTL)

The central trigger logic is one of the most important parts of the whole trigger system; here the decision is made whether an event is accepted at L1 or not. For this purpose, the various detector components can provide up to 128 different trigger elements which are "OR"ed or "AND"ed to form the so-called subtriggers. The final L1 decision is based on a global "OR" of all subtriggers. Since some subtriggers have a very high rate, they are usually prescaled by a certain factor n ; this means that a prescaled subtrigger is considered for the global L1 "OR" only every n th time.

3.4.2 The L4 filter farm

The main task of the L4 filter farm is to prevent events from non- ep interactions, such as

- beam-gas and beam-wall interactions,
- trigger noise,
- cosmic rays and halo muons

from going to the physical output tapes (POTs). It is designed as a fast, online software filter implemented in the data-acquisition stream.

The final L4 decision is based on L1 trigger information, raw event data and reconstructed quantities. The reconstructed quantities are calculated either by the standard H1 reconstruction program (H1REC) or a fast L4 reconstruction module (H1L4) [47].

The strategy is to verify all L1 subtriggers by the corresponding reconstructed quantities, e.g. track-based triggers are verified by requiring hits in the *CJC* and reconstructed tracks. If a subtrigger cannot be verified it is reset; if no other L1 subtriggers are left, the whole event is rejected and the algorithm stops.

To begin with, the subtriggers are verified by very fast algorithms. At a later stage, the information from more complicated and time-consuming modules like H1REC or H1L4 is needed. The L4 algorithm is rather fast because only those modules are executed which provide variables that are actually needed.

After the verification of all L1 subtriggers some more general cuts (e.g. a cut on the z coordinate of the interaction vertex ($zvtx$), a cut against beam-gas interactions) are applied.

While beam-gas events from outside the interaction region are already rejected by a $zvtx$ -cut of $|zvtx| < 40$ cm, beam-gas events from inside the interaction region need a special treatment. These events are characterized by a large longitudinal energy flow with

$$\frac{\sum p_z}{\sum p} \approx 1.0$$

and a very small inelasticity

$$y_{JB} = \frac{\sum E_i - p_{i,z}}{2 \cdot E_e} \approx 0.0$$

when calculated by the Jacquet-Blondel method.

On the filter farm, the cut on these two variables is defined by an ellipse in the $(y_{JB}, \sum p_z / \sum p)$ plane:

$$R_{\text{beam gas}} = \left(\frac{y_{JB}}{0.06} \right)^2 + \left(\frac{1 - \frac{\sum p_z}{\sum p}}{0.15} \right)^2 < 1.$$

To calculate y_{JB} and $\sum p_z / \sum p$, cell energies from the liquid argon calorimeter (LAr), clusters from the backward electromagnetic calorimeter (BEMC) and tracks reconstructed with H1L4 are used. Some double counting of energies at this reconstruction level leads to a slightly overestimated value of y_{JB} , which makes the cut actually looser than it is defined.

On average, about 70% of all events passing L1 were rejected by the L4 filter farm during the data taking in 1994. More detailed information on the L4 filter farm and its implementation in 1994 can be found in [47, 48].

3.5 The H1 reconstruction

The main goal of the reconstruction is to yield a parameterization of all data provided by the various detector components which allows the precise determination of the energy or the momentum of the measured particles; for identified particles this is the basis to obtain 4-vectors. For this purpose the specific energy loss along a reconstructed track can be measured in the *CJC*. The calorimeter components allow at least a distinction between hadrons and electrons (photons) based on the different shower profiles.

The primary interaction vertex (event vertex) is determined by fitting all reconstructed tracks to a common starting point.

Apart from some aspects related to track reconstruction and particle identification with the *CJC*, the following sections explain the reconstruction of secondary vertices used for the V^0 analysis.

3.5.1 Track reconstruction with the central jet chamber

Already during the *online* analysis on the L4 filter farm, the drift time t_{drift} and the corresponding charge integrals Q^+ and Q^- are calculated from the digitized drift chamber signals (*QT analysis*). Q^+ and Q^- allow both the determination of the specific energy loss and the calculation of the z coordinate using the relation $z \propto (Q^+ - Q^-)/(Q^+ + Q^-)$.

Given the drift velocity and the drift time, the drift length l_{drift} can be determined by $l_{\text{drift}} = (t_{\text{drift}} - T_0) v_{\text{drift}}$ which allows to calculate the distance between the particle trajectory and the signal wire or the space coordinate r_i, φ_i, z_i , respectively. The term T_0 is used to correct for the individual event time. The drift time itself is derived from the leading edge of the drift chamber signal, meaning that only those electrons arriving first at the signal wire are considered (*first-electron method* [49]).

The task of the track finding algorithm is to select all those reconstructed signals which can be associated to a track and provide a suitable parameterization. The track parameters chosen for this purpose are the following:

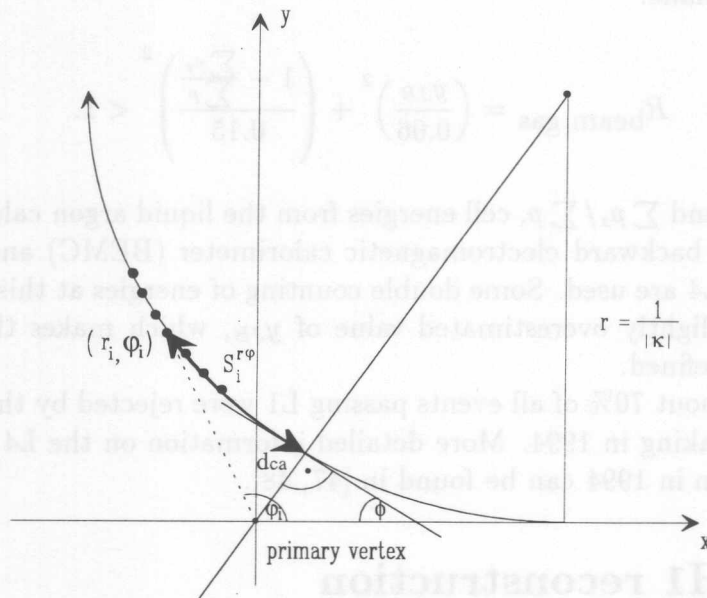


Figure 3.7: Definition of the 5 track parameters

κ	inverse radius $1/r$ of the track (signed)
d_{ca}	distance of closest approach to the z axis (signed)
ϕ	angle between the x axis and the tangent to the track at the point of closest approach
z_0	z coordinate at the point of closest approach
Θ	polar angle in the r/z plane at the point of closest approach

Fig. 3.7 and 3.8 illustrate the definitions of the track parameters and the sign conventions for κ .

The first three parameters follow from a circle fit to the associated space points in the r/φ plane

$$\frac{1}{2}\kappa(r_i^2 + d_{ca}^2) + (1 - \kappa d_{ca})r_i \sin(\phi - \varphi_i) - d_{ca} = 0,$$

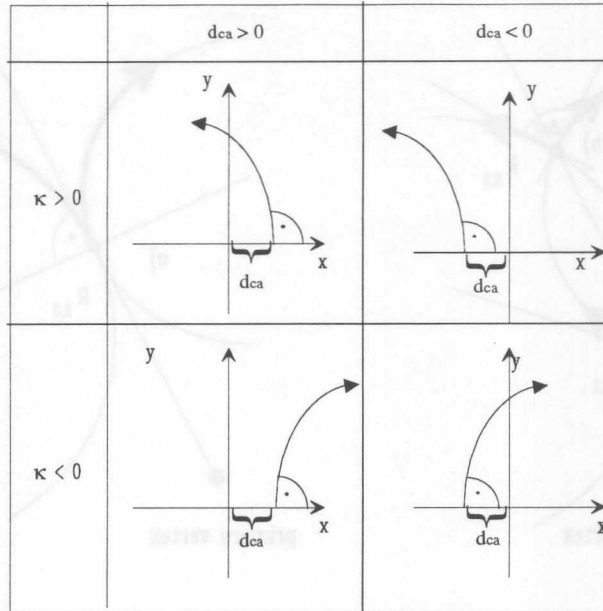
z_0 and dz/dS , with S being the track length, are determined by means of a linear regression

$$z_0 = z_i + S_i^{r\phi} \left(\frac{dz}{dS} \right)$$

where $S_i^{r\phi}$ corresponds to the r/φ projection of the track length between the point of closest approach and the point i . The term dz/dS describes the slope of the track in the r/z plane and is related to the polar angle by

$$\theta = \arctan \left(\frac{1}{\frac{dz}{dS}} \right).$$

With the present calibration, the spatial resolution that can be achieved with the *CJC* is $170 \mu\text{m}$ in the r/φ plane and about 2 cm along the z axis. Besides the wire-dependent corrections, the quality of the r/φ resolution is mainly affected by the T_0 ,

Figure 3.8: Sign conventions for κ and d_{ca}

the drift velocity v_{drift} and the Lorentz angle α_L . Due to the tilted cells of the *CJC*, incorrect parameters lead to “breaks” at the cathode wire plane and “kinks” at the signal wire plane.

3.5.2 Reconstruction of V^0 decays

Usually K_S^0 s are identified by their decay into two charged pions. In the present analysis these pions are measured with the *CJC* only¹. As the mean decay length is $c\tau = 2.675\text{ cm}$ for kaons, a large amount of secondary vertices are significantly separated from the primary interaction vertex.

The secondary vertex is determined by fitting two oppositely charged tracks to a common vertex [50]. The necessary quality criteria a track pair has to fulfill in order to be accepted as a candidate and the fit procedure itself, are discussed in the next section.

Since during the fit no assumption is made about the mass of the associated particles, it can be used to reconstruct other two-body decays, for instance $\Lambda \rightarrow p\pi$ and γ conversions. Due to their topology, all these decays are usually called V^0 decays.

Selection of track pairs

The basic set of track pairs is formed by all possible combinations of oppositely charged tracks measured with the *CJC*. To begin with, for each track, the vector \vec{c}_i to the circle center of the particle trajectory is calculated from the track parameters. Under the assumption that both particles originate from a secondary vertex, these circles should either have two intersection points or one tangential point. In the first case, it is

¹Actually, the z coordinate is mostly determined by the *CIZ* and/or the *COZ* whenever there is a successful link between *CJC* and one of these chambers.

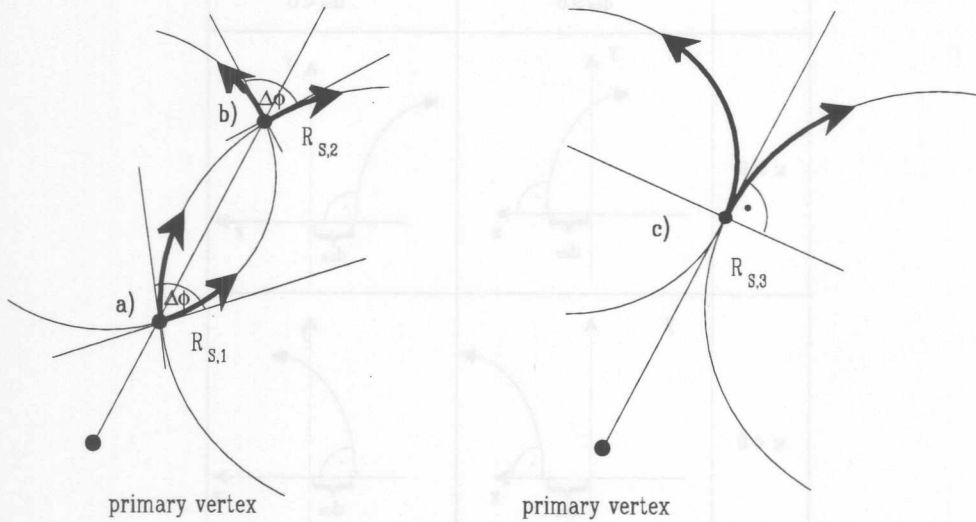


Figure 3.9: Different topologies of the K_S^0 decay. a)+b): Both circles intersect yielding in-bending and out-bending track pairs. c) There is only a tangential point, both tracks diverge.

possible to distinguish between *in-bending* and *out-bending* track pairs/ V^0 topologies (see fig. 3.9).

Momentum conservation at the secondary vertex leads to the constraint

$$\vec{p}_{trans,0} = \vec{p}_{trans,1} + \vec{p}_{trans,2}$$

where $\vec{p}_{trans,0}$ is the transverse momentum of the kaon and $\vec{p}_{trans,1}$ and $\vec{p}_{trans,2}$ are the transverse momenta of the associated pions. Furthermore the transverse momentum $\vec{p}_{trans,0}$ of the decaying particle has to be perpendicular to the vector $\vec{c} = \vec{c}_1 - \vec{c}_2$ connecting the two circle centers and the relation

$$\vec{p}_{trans,0} \vec{c} = (\vec{c}_1 - \vec{c}_2)(\vec{p}_{trans,1} + \vec{p}_{trans,2}) = 0 \quad (3.1)$$

has to hold (see fig. 3.10).

Since tracks from a V^0 decay should start at the same point in space, only those pairs with

- $\Delta b = |b_1 - b_2| < 20 \text{ cm}$

are accepted (b_i corresponds to the radius of the first measured space point, i.e. the start radius of the track). This loose cut guarantees that even decays having a very small decay angle $\Delta\phi$ in the r/φ plane are accepted. For such decays, both tracks are nearly parallel shortly after the decay; due to the limited double-track resolution, it may happen that only one track is completely reconstructed down to the primary vertex.

After this preselection, the radial distance R_S between the primary vertex and the corresponding intersection point(s) of the two circles is calculated. If there are no intersection points but the radial distance between the two circles is smaller than 1 cm , a tangential point $R_{tang} = R_{S,3}$ is assumed on the connecting line of both circles; this is done in order to take into account the finite resolution of the track parameters.

Further simple cuts reject all solutions R_S with:

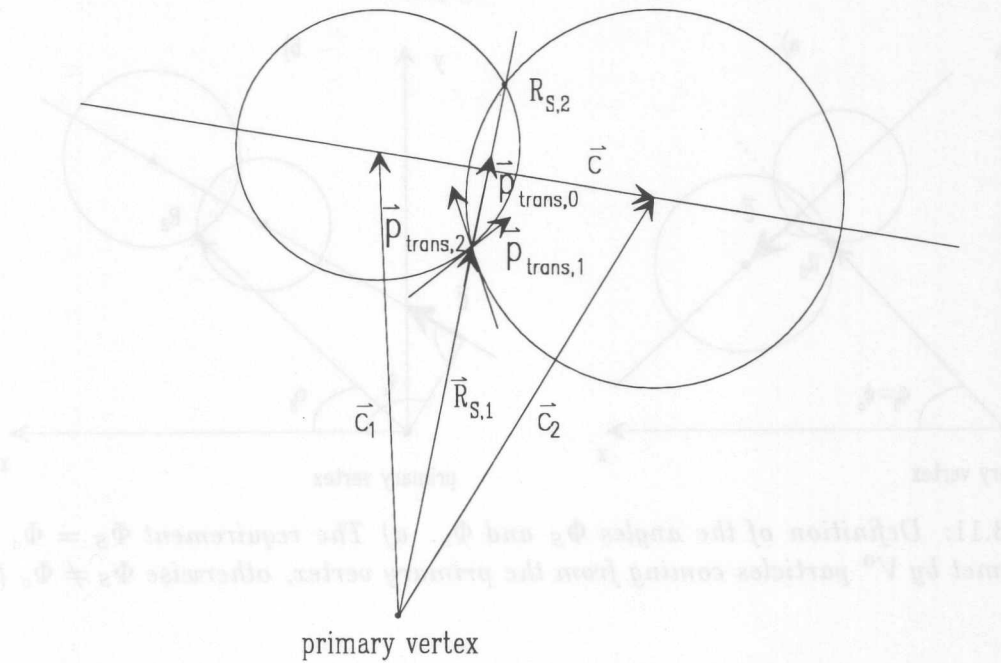


Figure 3.10: Geometry and used variables during the track pair selection

- $R_S < 0.2 \text{ cm}$ (the V^0 candidate must have a minimal decay length)
- $R_S > 80 \text{ cm}$ (these are probably unphysical solutions because the decay radius is nearly outside the active volume of *CJC2*)
- $R_S < \min(b_1, b_2) + 2 \text{ cm}$ (the start radii of the tracks and the corresponding decay radius have to agree within certain limits)

Eventually the condition given by eq. 3.1 is tested. For V^0 candidates coming from the primary vertex, the angle Φ_S at the kinematic decay radius R_S has to agree with the angle Φ_c of the direction cosine of the connecting line \vec{c} (see fig. 3.11). So far all cuts have been entirely motivated by the geometry of a V^0 decay. All track pairs and the associated decay points are kept for further analysis.

The V^0 fit

The aim of the V^0 fit is to test whether the selected track pair and the corresponding kinematic vertex are compatible with the hypothesis of a V^0 coming from the primary vertex (which is assumed to be the case, if the fit was successful and the corresponding χ^2 is reasonable). During the fit, all track parameters and coordinates of the decay point are varied in such a way that, in case of a successful fit, momentum conservation holds at the secondary vertex.

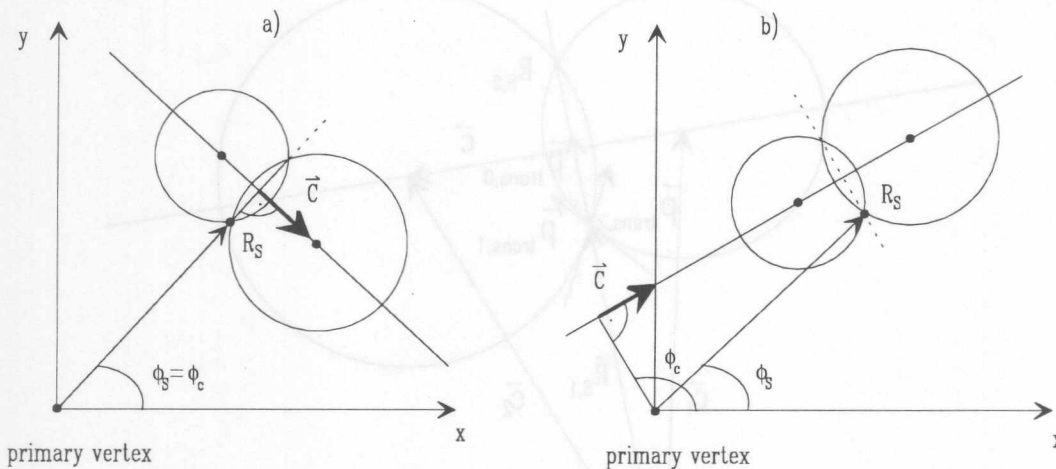


Figure 3.11: Definition of the angles Φ_S and Φ_c . a) The requirement $\Phi_S = \Phi_c$ can only be met by V^0 particles coming from the primary vertex, otherwise $\Phi_S \neq \Phi_c$ (b).

In the current version of the V^0 fit, as it is implemented in the standard H1 reconstruction program (H1REC), there are actually two fits.

To begin with, a fit working in the r/φ plane only is performed. The constraints at this level are given by

1. $\Delta\Phi = |\Phi_1 - \Phi_2| = 0.0$ at radius R_S
2. $\Phi(\vec{p}_{trans,1} + \vec{p}_{trans,2}) = \Phi_0$ Φ_0 is the direction of the V^0 particle in the r/φ plane

After a successful fit in the r/φ plane, some loose quality cuts on the parameters of the fitted tracks are applied.

In the second fit, the additional information on the z coordinates of the hits belonging to a track is used. At this level, hits which are not compatible with a V^0 hypothesis are rejected.

Eventually, only those V^0 candidates are kept where for both tracks more than 40% of the hits survived the z fit.

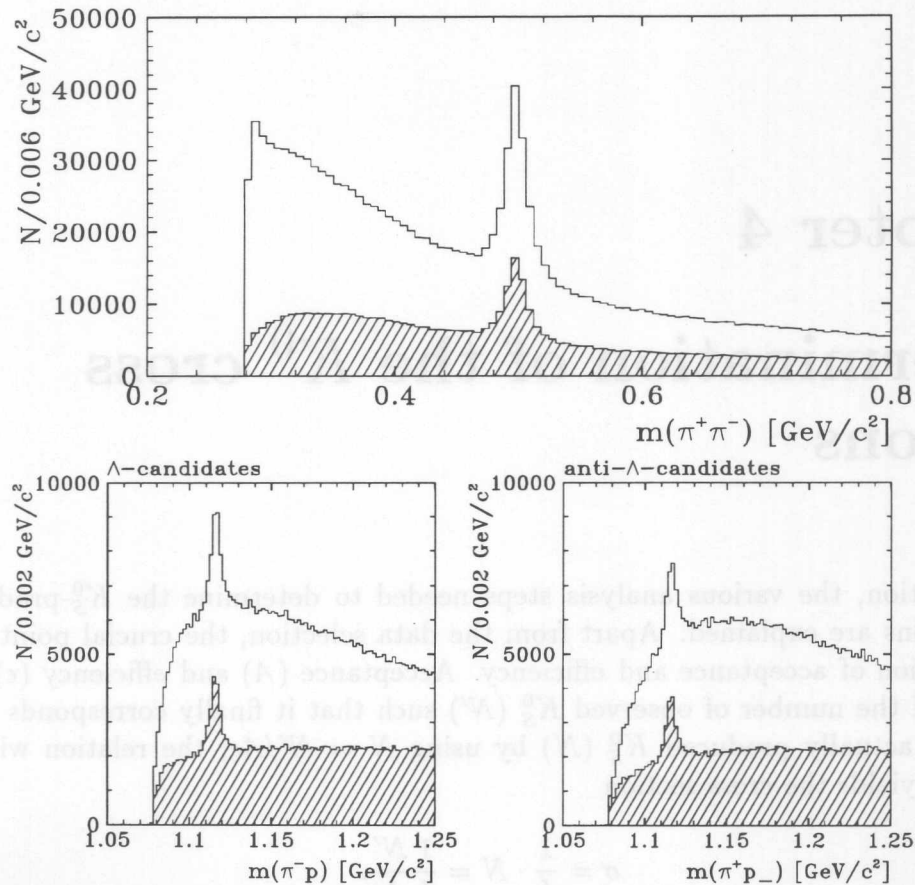


Figure 3.12: Reconstruction of K_S^0 and Λ decays with the H1 detector. The histograms show the invariant mass distributions for the three mass hypotheses K_S^0 (top), Λ and $\bar{\Lambda}$ (bottom) before any selection cuts, the expected signals are clearly visible. In the shaded histograms only candidates with $|\eta| < 1.3$ and $0.5 < p_t < 5.0 \text{ GeV}/c$ were considered; this corresponds to the kinematic range which can be investigated with the CJC.

V^0 reconstruction

After a successful V^0 fit, it is straightforward to reconstruct the corresponding particle. One simply has to calculate the invariant mass m_{xx} of the fitted particles. In case of the reconstruction of a K_S^0 , the hypothesis is that both particles are pions having a mass of $m = 139.6 \text{ MeV}/c^2$. From the relation $E_{1,2} = \sqrt{\vec{p}_{1,2}^2 + m_\pi^2}$ it follows that

$$m_{\pi\pi} = \sqrt{2m_\pi^2 + 2(E_1 E_2 - \vec{p}_1 \vec{p}_2)}$$

Histogramming these values, the K_S^0 signal becomes clearly visible in the expected mass region of 0.5 GeV , the spectrum starting at the kinematic threshold of $m_{\pi\pi}^{\text{min}} = 2m_\pi$. The same procedure holds for the reconstruction of Λ and $\bar{\Lambda}$ decays ($m_\Lambda = 1.115 \text{ GeV}/c^2$), see fig. 3.12.

Chapter 4

Determination of the K^0 cross sections

In this section, the various analysis steps needed to determine the K_S^0 -production cross sections are explained. Apart from the data selection, the crucial point is the determination of acceptance and efficiency. Acceptance (A) and efficiency (ϵ) allow a scaling of the number of observed K_S^0 (N') such that it finally corresponds to the number of actually produced K_S^0 (N) by using $N = N'/A\epsilon$; the relation with the luminosity yields the cross section

$$\sigma = \frac{1}{L} \cdot N = \frac{1}{L} \frac{N'}{A\epsilon}.$$

The determination of the acceptance is mainly related to the question whether a specific process like a K_S^0 decay can be detected at all with the detector components used for the analysis ($A = \prod A_i$).

By the various contributions to the efficiency ($\epsilon = \prod \epsilon_i$), the losses occurring during data-taking, processing and off-line analysis are estimated. One could, for example, think of particles passing the acceptance region of the detector which are not perfectly registered. Furthermore, not all measured signals yield reconstructed objects like tracks for instance. In contrast to these losses, which are due to the operating conditions and the set-up of the experiment, the losses occurring during the off-line analysis are due to cuts or selections made to improve the signal(s) itself. This is done for example by applying selection criteria against events coming from beam-gas or beam-wall interactions or by cuts improving the signal-to-background ratio in the K_S^0 signal.

Unfortunately, it is usually not possible to factorize acceptance and efficiency completely and one has to study products of both. The philosophy of the present analysis is to derive most of the correction factors from data in order to be as much independent as possible from any models used in Monte Carlo. Monte Carlos with detailed detector simulation are merely used for some cross-checks and to obtain some minor corrections.

Since acceptances and efficiencies are the starting point for the measurement of differential cross sections, they are discussed in detail in the following sections.

4.1 The data sample

The whole analysis is based on data available on the data summary tapes of the sixth reprocessing (DST6) which were taken in fall 1994. The corresponding run ranges, 87586-89912 and 90101-90419, refer to the period after the *CJC*-readout problem was fixed¹, and the integrated luminosity of $\approx 1.42 \text{ nb}^{-1}$ corresponds to about 50% of the total integrated luminosity delivered in 1994.

It should be mentioned that for the DSTs only those runs are accepted which are classified as "good" or "medium"; this H1-internal classification ensures that the main detector components were operational and the beam conditions stable. Nevertheless, it can happen that during a run some components are temporarily not fully operational, like the high voltage of one of the two *CJCs*. These events are rejected during the analysis and the total integrated luminosity corrected accordingly. Eventually the analysis is restricted to events from the so called CLASS19 sample, which have a signal in the electron tagger and meet some additional requirements explained in section 4.3.

The trigger chosen for this analysis is subtrigger 83 (tr83), which is a combination of ETAG- and DCR Φ -subtrigger elements (see section 4.2.1 and 4.2.2), and of course only those runs are selected where this trigger was enabled². The reduction of the whole data sample by the selections explained above is summarized in table 4.1.

Selection	# of events	comments	
"G/M"-runs on DST6	4 736 782	basic data quality criteria	
<i>CJC</i> -HV	4 588 958	high voltage of <i>CJC</i> on and lumi cross checks	
CLASS 19	2 045 401	selection of <i>tagged</i> minimum bias events	
tr83	-enabled -active	2 044 940 1 410 721	trigger: ETAG*DCR Φ
V^0 candidates	815 440	events contain at least one successfully fitted V^0 candidate	

Table 4.1: Event selection for the V^0 analysis

4.2 Event selection on L1

A suitable trigger should have a high efficiency for the process under study while reducing background, in this case events from beam-wall and beam-pipe interactions, significantly. The requirements for a trigger to select events from γp interactions that contain K_S^0 decays are determined by the fact that these events usually have a low

¹During the first period of data taking in 1994 there were problems with the read-out of some drift cells of the *CJC*.

²The term *enabled* means that this trigger element is considered for the global L1 "OR" (see section 3.4.1); the trigger element is *active* if the trigger element is set.

particle multiplicity and small transverse energy flow and are therefore rather similar to the ones originating from non- ep interactions.

4.2.1 Acceptance and efficiency of the electron tagger

To create a sample of photoproduction events only those events are selected where the scattered electron is detected in the electron tagger and the trigger element $ETAG$ is set. Due to the geometry of the electron tagger, the accessible kinematic range is limited both in y and Q^2 , because the electrons can only be detected for a certain range of the scattering angle θ and energy E'_e . The dependence on the two kinematic variables y_e and Q^2 is given by

$$Q^2 \approx 4E_e E'_e \sin^2 \frac{\theta}{2}$$

and

$$y_e \approx 1 - \frac{E'_e}{E_e}.$$

As the acceptance $A(y, Q^2)$ of the electron tagger is rather sensitive to the HERA electron beam optics, particularly to the horizontal beam tilt θ_x and to the horizontal offset Δx , it has to be determined whenever run-conditions change. The procedure used is based on a detailed Monte Carlo simulation of the HERA beam optics and the luminosity system, which allows a tuning of the MC to the data by varying θ_x and Δx [51].

The acceptance has been studied in the kinematic range $0.3 < y_e < 0.7$ (where it is expected to be larger than 20%) and integrated over Q^2 , the dependence on this variable in the range up to 0.01 GeV^2 being negligible. In order to exclude unreliable energy measurements from regions close to the detector boundaries, a fiducial cut of $|x_{ETAG}| < 6.5 \text{ cm}$ on the x-coordinate of the reconstructed energy has been applied. The efficiency of the $ETAG$ trigger element depends on the energy and is close to 100% in the kinematic range of interest, because the corresponding energies are well above the threshold of 4 GeV (see fig. 4.1). As the $ETAG$ -trigger element is set only when there is no signal in the photon detector, some γp events are lost, namely those which are in coincidence with an event from a bremsstrahlung process and therefore have a signal in the photon detector. These losses are of the order of 1 to 2% and included in the correction due to the $ETAG$ acceptance.

To account for the losses introduced by the $ETAG$ acceptance, each event is weighted with a factor defined by

$$w = 1/A_{Q^2}(y).$$

This procedure ensures that the y dependence of the K^0 cross sections is treated correctly.

At the L1-trigger level, the $ETAG$ trigger element is always combined with various other trigger elements. The ones of interest for the present analysis are discussed in the next section.

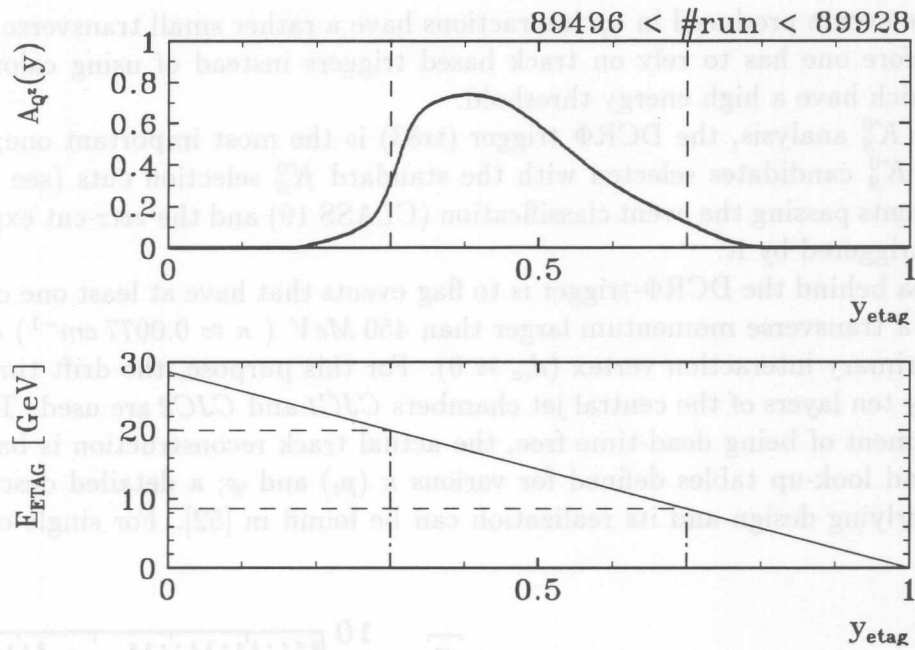


Figure 4.1: Acceptance of the electron tagger for a selected run period; in addition the corresponding energy range of the scattered electron is shown.

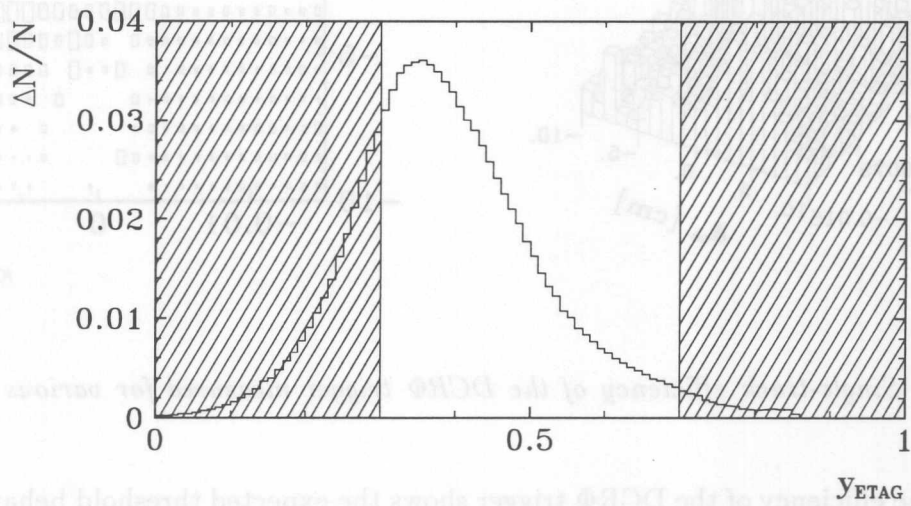


Figure 4.2: y distribution using the reconstructed energy in the electron tagger; in the analysis only events with $0.3 < y_e < 0.7$ from the not-hatched area are used.

4.2.2 Acceptance and efficiency of the DCR Φ trigger

Most of the events produced in γp interactions have a rather small transverse energy flow, therefore one has to rely on track based triggers instead of using calorimeter triggers which have a high energy threshold.

For the K_S^0 analysis, the DCR Φ trigger (tr83) is the most important one; about 90% of all K_S^0 candidates selected with the standard K_S^0 selection cuts (see section 4.5.3) in events passing the event classification (CLASS 19) and the $z vtx$ -cut explained below are triggered by it.

The idea behind the DCR Φ -trigger is to flag events that have at least one charged track with a transverse momentum larger than 450 MeV ($\kappa \approx 0.0077 \text{ cm}^{-1}$) coming from the primary interaction vertex ($d_{ca} \approx 0$). For this purpose, the drift time data provided by ten layers of the central jet chambers *CJC1* and *CJC2* are used. To meet the requirement of being dead-time free, the actual track reconstruction is based on ten thousand look-up tables defined for various κ (p_t) and φ ; a detailed description of the underlying design and its realization can be found in [52]. For single charged

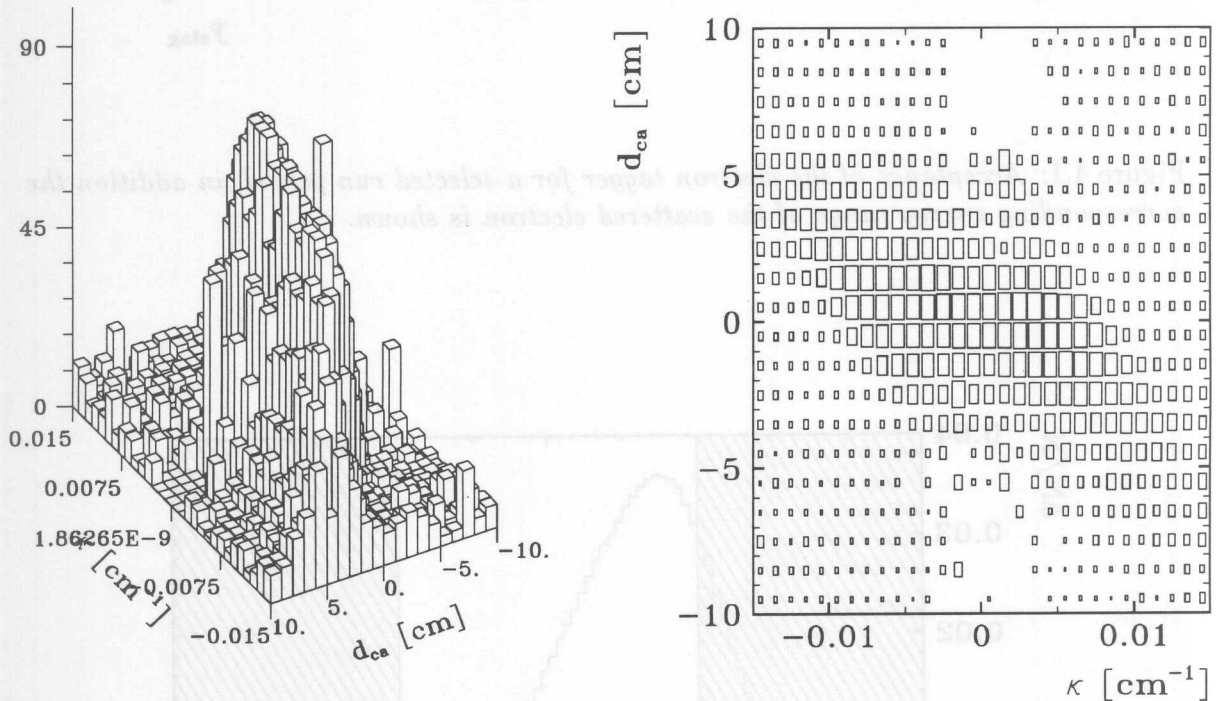


Figure 4.3: Single-track efficiency of the DCR Φ trigger measured for various κ and d_{ca} [53]

particles, the efficiency of the DCR Φ trigger shows the expected threshold behavior at around $400 \text{ MeV}/c$ as well as an asymmetry in the dependence on d_{ca} for positive and negative tracks (fig. 4.3). In highly efficient regions ($|d_{ca}| < 2 \text{ cm}$, $p_t > 500 \text{ MeV}/c$) the single track trigger efficiency is of the order of 85%, while the remaining inefficiencies are due to jet chamber inefficiencies and timing problems of the DCR Φ trigger. To avoid any additional inefficiencies from tracks which cannot reach *CJC2*, the z -vertex of each event is restricted to a range of $\pm 30 \text{ cm}$ around the mean z -position of the

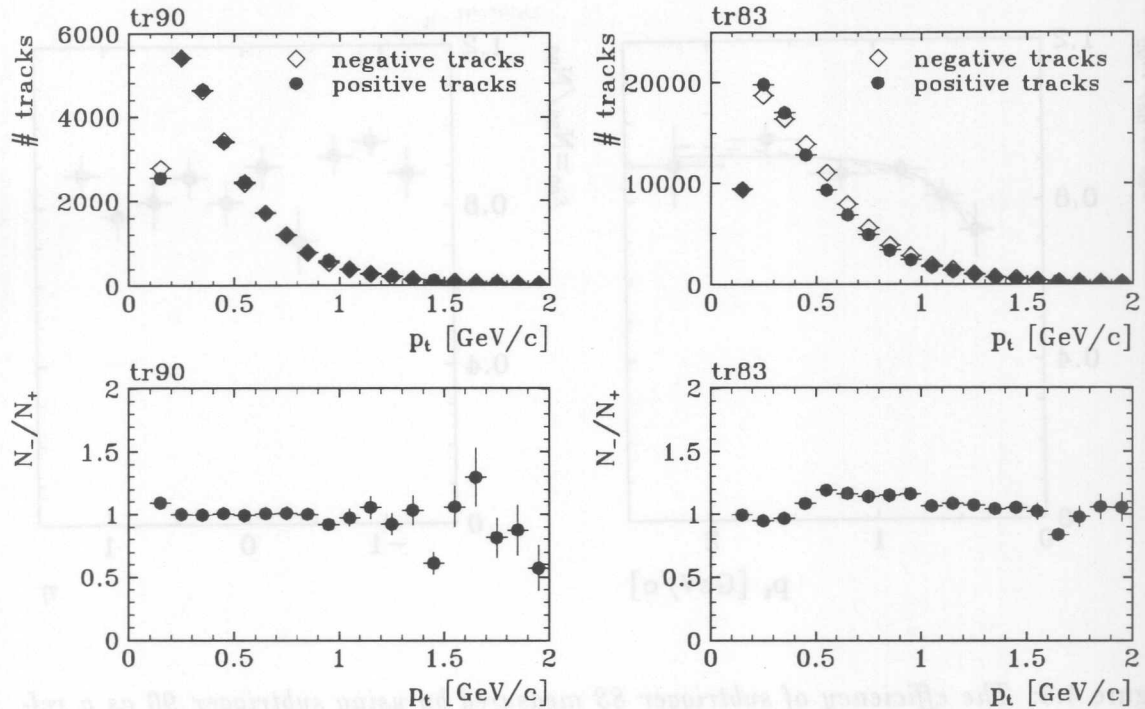


Figure 4.4: Uncorrected charged particle spectra in the low- p_t range and the corresponding ratios between negative and positive particles (both for tr83 and tr90)

interaction vertex. In addition, this cut reduces background from non- ep interactions.

During the data taking in 1994, the setup chosen for the DCR Φ trigger required at least one validated negative track mask corresponding to at least one negative track with $p_t > 400$ MeV/c. This is reflected in the charged particle spectrum of tracks fitted to the primary vertex, showing a significant excess of negative particles compared to positive ones for p_t around 500 MeV/c (see fig. 4.4). To prove that this is not an effect introduced by an inefficiency or miscalibration of the CJC , this spectrum is compared to the one obtained from an event sample selected with a non-track-based reference trigger (fig. 4.4), which shows no evidence of any charge asymmetry (apart from the low p_t range, where it is known that the reconstruction efficiency for positive tracks is slightly worse). It should be mentioned that for both spectra, the tracks had to pass the basic track cuts discussed in section 4.4.2.

The reference trigger used (subtrigger 90, tr90), is a combination of the ETAG-trigger element and a trigger element provided by the time-of-flight system (ToF signal, which is caused by hadrons coming from photon fragmentation). This trigger is unbiased and has an efficiency close to 100%. Because of a very high rate, tr90 was prescaled by a factor of 1001 most of the time and run with a lower prescale factor of 8 – 17 only for about two weeks. Since most of the events triggered by tr90 have no tracks in the central region, these data can only be used for monitoring purposes. To estimate the trigger efficiency for K_S^0 , the η and/or p_t -dependent ratios between K_S^0 selected by tr90 and those which are in addition triggered by the DCR Φ -trigger are

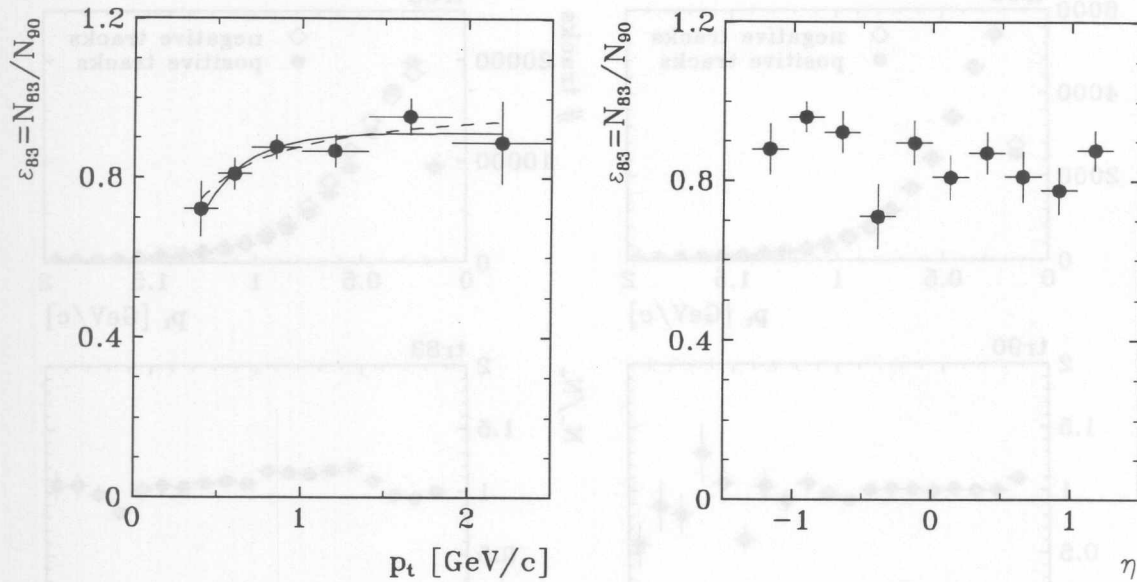


Figure 4.5: The efficiency of subtrigger 83 measured by using subtrigger 90 as a reference trigger. The p_t dependence is parameterized by two functions $\epsilon_{tr83}^1(p_t)$ (dashed) and $\epsilon_{tr83}^2(p_t)$ (solid).

calculated:

$$\epsilon = \frac{N_{K_S^0}(tr83 * tr90)}{N_{K_S^0}(tr90)}$$

The results, summarized in figure 4.5, show a clear indication for a p_t dependence of the trigger efficiency, which was fitted by two functions of the form

$$\epsilon_{tr83}^1(p_t) = a_1 \frac{p_t}{p_t + b_1} \quad \text{and} \quad \epsilon_{tr83}^2(p_t) = a_2 - \exp(-b_2 p_t)$$

with $a_1 = 1.0154$, $b_1 = 0.1505$ and $a_2 = 0.9180$, $b_2 = 3.7504$. For the determination of the cross sections, the parameterization given by ϵ_{tr83}^2 is used. The systematic uncertainty introduced by the difference of the two parameterizations is estimated by a comparison of the two cross sections obtained by applying ϵ_{tr83}^1 and ϵ_{tr83}^2 (see section 4.8.1) and is less than 6%.

Within statistical errors, no η dependence is observed. The effect of having more negative than positive tracks around $p_t \approx 500$ MeV is also taken into account by this method.

An alternative approach for correcting trigger inefficiencies relies on the single-track trigger efficiencies, which are used to define a weight for each event triggered by tr83. Working under the assumption that the mean multiplicity of the events of interest is larger than 1, –which should hold for events containing K_S^0 decays–, the trigger efficiency should always be larger than any efficiency of a single track in that specific event; this implies that the efficiency ϵ_{tr83} is given by

$$\epsilon_{tr83} = 1 - \prod_i (1 - \epsilon_{tracks}^i)$$

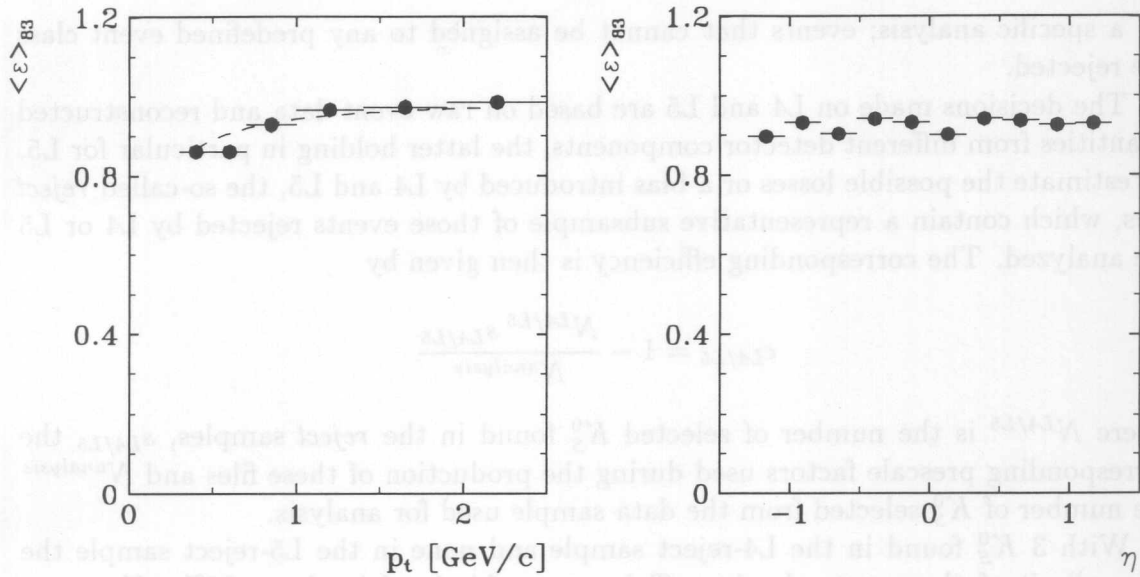


Figure 4.6: The mean efficiency $\langle \epsilon \rangle_{83}$ of trigger 83 using event weights

The mean trigger efficiency $\langle \epsilon \rangle_{83}$ for selecting K_S^0 is then defined by the ratio of the number of reconstructed K_S^0 and the corresponding number of weighted K_S^0 :

$$\langle \epsilon \rangle_{83} = \frac{N_{K_S^0}}{N_{K_S^0}^{\text{weighted}}}.$$

This is a very straightforward method, applicable to any event of interest, which has the advantage of avoiding problems arising from low statistics (e.g. of the reference trigger tr90). Unfortunately, the results of both methods disagree to a certain extent; the efficiency calculated from the event weights is systematically higher (fig. 4.6) than the efficiency estimated by using the reference trigger (fig. 4.5), and the reasons for these discrepancies are difficult to trace back. There are, for example, events where for none of the reconstructed tracks a single track efficiency can be assigned –usually because the momentum is too low– and no event weight can be calculated, which would lead to underestimate the trigger efficiency. On the other hand, this could also be an indication that the trigger introduces a bias towards events having a larger transverse energy or multiplicity in such a way that the remaining sample to which the weighting procedure is applied is no longer representative of the original one. The trigger efficiency used in this analysis is the one estimated by using tr90 as a reference trigger.

4.3 Event selection on L4 and L5

Apart from the losses occurring at the L1-trigger level, which are mainly related to the hardware performance of the detector components involved, there might be additional losses caused by the L4-filter farm and the event classification (L5). As explained in section 3.4, the main goal of the L4 filter farm is to reject events originating from non- ep interactions, while the event classification tries to flag events that are of interest

for a specific analysis; events that cannot be assigned to any predefined event class are rejected.

The decisions made on L4 and L5 are based on raw event data and reconstructed quantities from different detector components, the latter holding in particular for L5. To estimate the possible losses or a bias introduced by L4 and L5, the so-called *reject* files, which contain a representative subsample of those events rejected by L4 or L5 are analyzed. The corresponding efficiency is then given by

$$\epsilon_{L4/L5} = 1 - \frac{N^{L4/L5} s_{L4/L5}}{N^{analysis}}$$

where $N^{L4/L5}$ is the number of selected K_S^0 found in the *reject* samples, $s_{L4/L5}$ the corresponding prescale factors used during the production of these files and $N^{analysis}$ the number of K_S^0 selected from the data sample used for analysis.

With 3 K_S^0 found in the L4-reject sample and none in the L5-reject sample the upper limit of the event selection efficiency at this level is about 96%. However, since these events might originate from a non-*ep* interaction this correction will not be applied to the final results but merely taken into account as a contribution to the overall systematic uncertainty.

Since the ideas behind the rejection of non-*ep* events have already been discussed in section 3.4.2, the following section gives only a short description of CLASS19.

CLASS19 events

The event class CLASS19 chosen for the present analysis contains so-called *tagged minimum bias photo production* events.

To begin with, the beam-gas cut described in section 3.4.2 is refined. An event is classified as a beam-gas interaction if one of the following holds:

$$R_{\text{beam-gas}} = \left(\frac{y_{JB}}{0.12} \right)^2 + \left(\frac{1 - \frac{\sum p_z}{\sum p}}{0.18} \right)^2 < 1,$$

or

$$y_{JB} < 0.02 \text{ and } \sum p_z / \sum p > 0.0$$

where y_{JB} is the inelasticity calculated using the Jacquet-Blondel method and $\sum p_z$ and $\sum p$ are the sums over the longitudinal and total momenta. To calculate these sums, information from the calorimeter and from the tracker have been used. In addition

$$\sum E^{\text{tracks}} - \sum p_z^{\text{tracks}} < 1.8 \text{ GeV}$$

is required and the cut on the energy threshold of the electron tagger is tightened by

$$E_{\text{ETAG}} > 8 \text{ GeV}.$$

All events must have at least one track in the forward or central tracker and a reconstructed event vertex.

Furthermore, CLASS19 contains also all events triggered by tr90 passing the aforementioned energy threshold on the ETAG-energy; this allowed to use tr90 as a reference trigger as shown in section 4.2.2.

4.4 The track efficiency

A good understanding of the single track reconstruction efficiency is essential for any analysis dealing with charged particles. It becomes even more important for the reconstruction of exclusive decay channels, one of the simplest being the K_S^0 decay. Two aspects have to be considered: on the one hand inefficiencies solely introduced by the reconstruction program, and on the other hand inefficiencies related to the hardware performance of the central jet chamber in 1994. In addition to introducing some basic track selection cuts which are needed to guarantee the quality of the tracks, these two aspects are discussed in the following sections. It will become obvious that it is impossible to disentangle them completely.

4.4.1 Single track reconstruction efficiency

Even in areas where the *CJC* is fully operational inefficiencies can occur. Usually these are related to the reconstruction program and the precision of the values used for the Lorentz angle, drift time and wire dependent corrections, etc. (cf. section 3.5). To estimate these losses a visual scan was performed using about 400 tracks from randomly chosen events of the selected data sample. As non-reconstructed tracks are visible as groups of *unused* hits, the goal for each event was to look for such groups. A comparison with the curvature of a reference track allowed to estimate the momentum of a "non-reconstructed" track.

In this scan only three track candidates were found which seemed to fulfill the abovementioned criteria and the reconstruction efficiency is estimated to be $\geq 99\%$. This result is compatible with an independent study [54] where the track reconstruction efficiency is determined to be $(98 \pm 3 \pm 3)\%$. Given the statistics, both results are independent of p_t . As a K_S^0 is formed by two charged tracks, the K^0 reconstruction efficiency is: $\epsilon_{rec} = \epsilon_{track}^2$. For this analysis ϵ_{track} is assumed to be 98% with a systematic uncertainty of 2%.

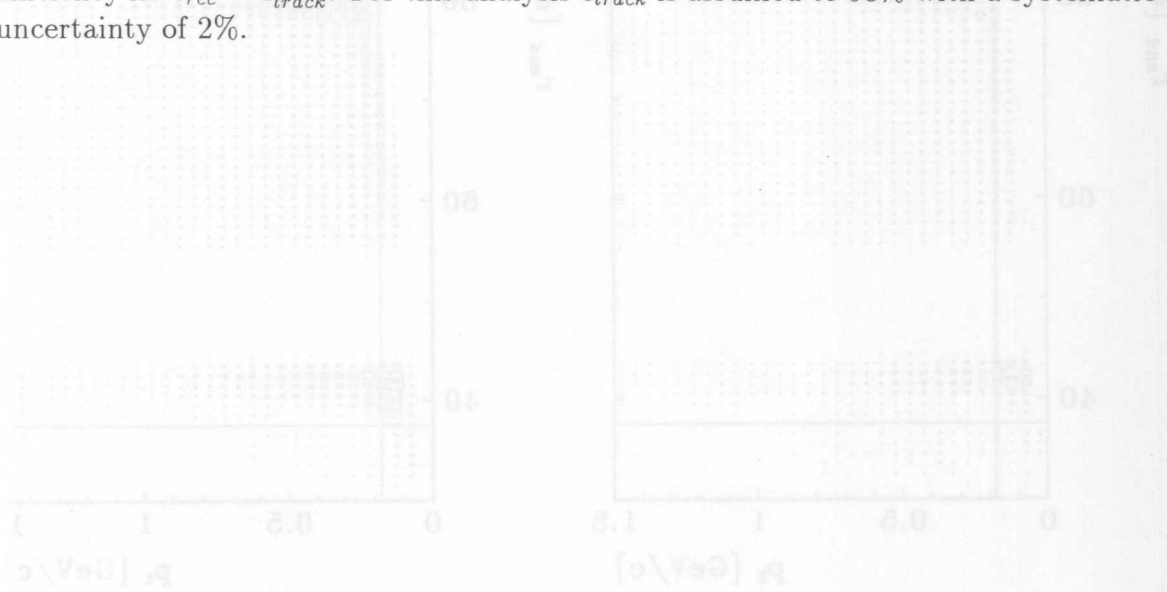


Figure 4.2: ϵ_{rec} vs p_t for tracks fitted to a secondary vertex; the lines indicate the basic track selection cuts.

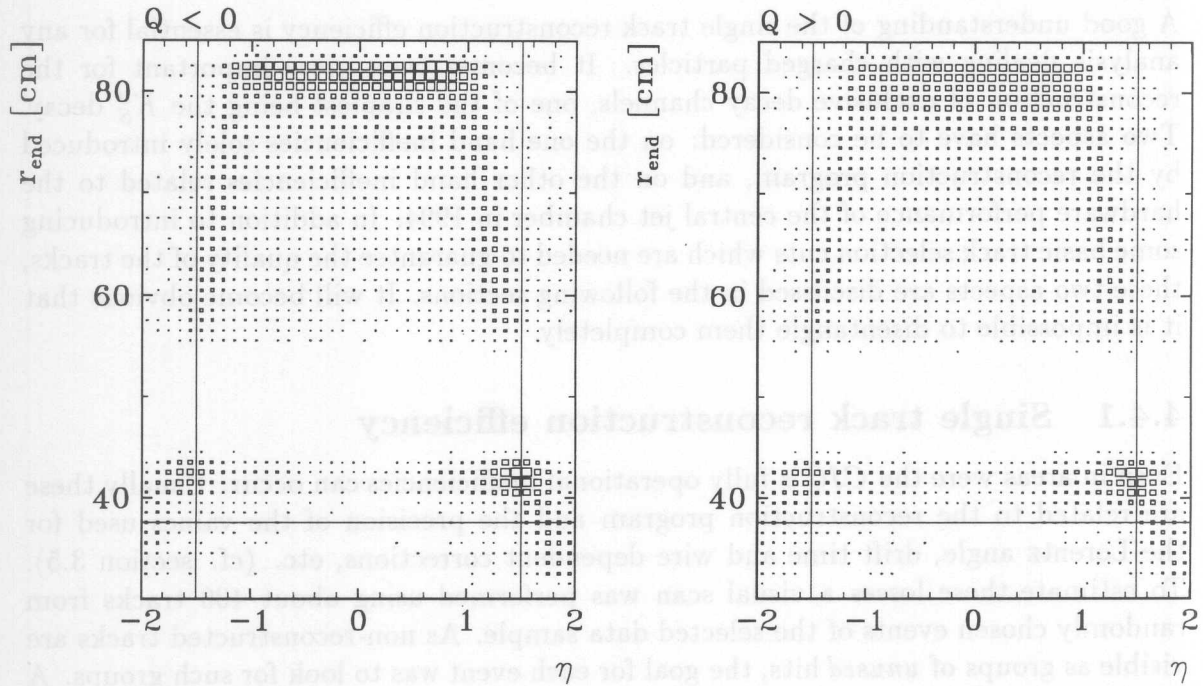


Figure 4.7: η vs. r_{end} for tracks fitted to a secondary vertex; the lines indicate the basic track selection cuts.

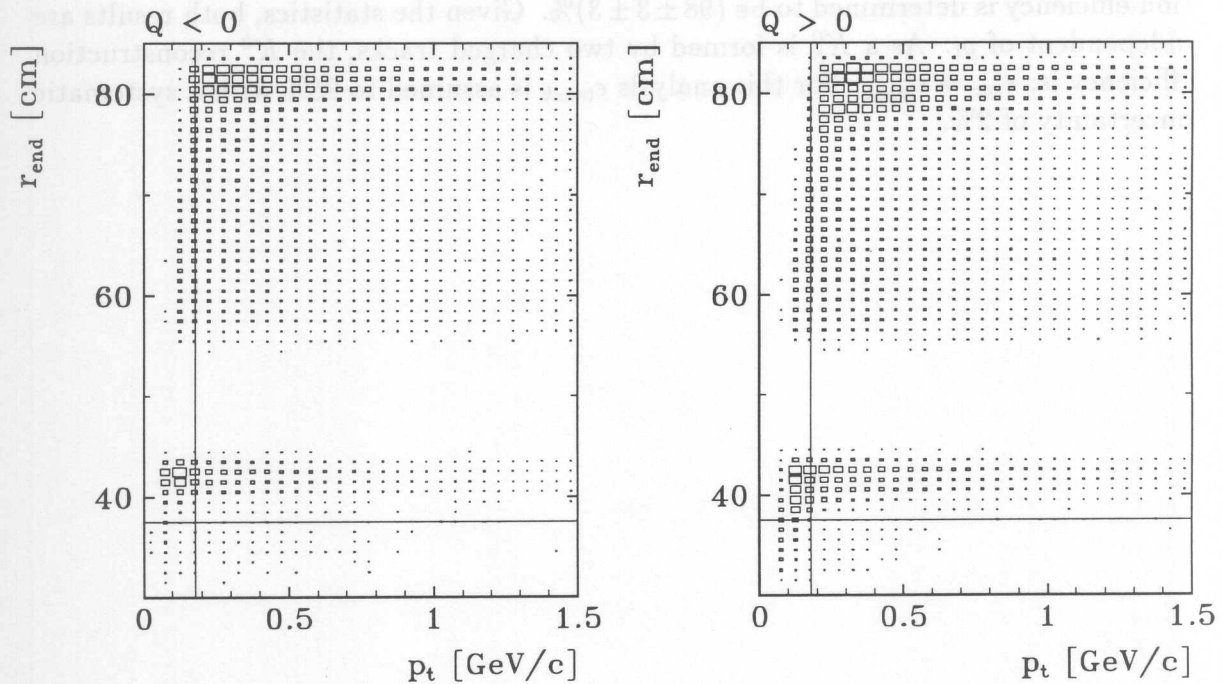


Figure 4.8: p_t vs. r_{end} for tracks fitted to a secondary vertex; the lines indicate the basic track selection cuts.

4.4.2 Basic track selection cuts

The aim of the basic track selection (see table 4.2) is to select tracks for which the expected reconstruction efficiency is close to 100% and certain quality criteria are fulfilled. The polar angular range of the tracks is restricted by applying a cut on the corresponding pseudorapidity of $|\eta| < 1.5$. This guarantees that most tracks reach $CJC2^3$ (see fig. 4.7). The studies shown in the previous sections further suggest a cut on the transverse momentum of $p_t > 0.18 \text{ GeV}$.

Additional cuts are related to the start point, r_{beg} , and the end point, r_{end} , of the reconstructed track as well as the radial track length given by $r_\Delta = r_{end} - r_{beg}$. The cut on the start radius, $r_{beg} < 30 \text{ cm}$, aims at rejecting track elements of split or broken tracks originating from the same particle, while the cut on the end radius, $r_{end} > 37.0 \text{ cm}$, is a simple quality cut; its correlation with p_t is shown in figure 4.8. This cut is even tightened by the additional requirement of $\Delta r > 10 \text{ cm}$, which is already applied during the V^0 selection. It should be mentioned that there is an obvious difference between positive and negative tracks, which decreases with increasing p_t , and which is very likely due to the asymmetric design of the chamber and inefficient cells in CJC (see below).

Track parameter	unit	cut
transverse momentum	[GeV/c]	$p_t > 0.18$
pseudorapidity		$ \eta < 1.50$
radial track length in CJC	[cm]	$\Delta r > 10.0$
start radius	[cm]	$r_{beg} < 30.0$
end radius	[cm]	$r_{end} > 37.5$

Table 4.2: Basic track selection cuts

4.4.3 Performance of the CJC in 1994

Because of HV-problems with several cathode wire planes of $CJC2$, the efficiency of the central jet chamber was reduced in some areas and in addition some wires were switched off (see fig. 4.9). That this hardware failure actually affects the track efficiency is easily seen from the non-flat φ distributions of reconstructed charged particles. Apart from a gap at $\varphi \approx 150^\circ$, which is caused by a dead region in $CJC1$ and to which the positive tracks are more sensitive, there are additional structures in the φ distribution (fig. 4.10). Though they are less pronounced, they can potentially introduce a bias and, surprisingly, the η distributions from different φ ranges also show differences (fig. 4.11). To avoid any bias from the V^0 finder, these plots refer to tracks fitted to the primary vertex. The implications for the actual K_S^0 analysis are discussed in detail in section 4.5.6.

A reduced HV along a cathode wire plane leads to a reduced drift velocity in the corresponding cell. In case the calibration module of the CJC , which in principle is able to determine such cell-dependent correction factors, fails to compensate for this

³In principle this holds only for tracks coming from the primary vertex and is also related to the actual z-position of the primary vertex.

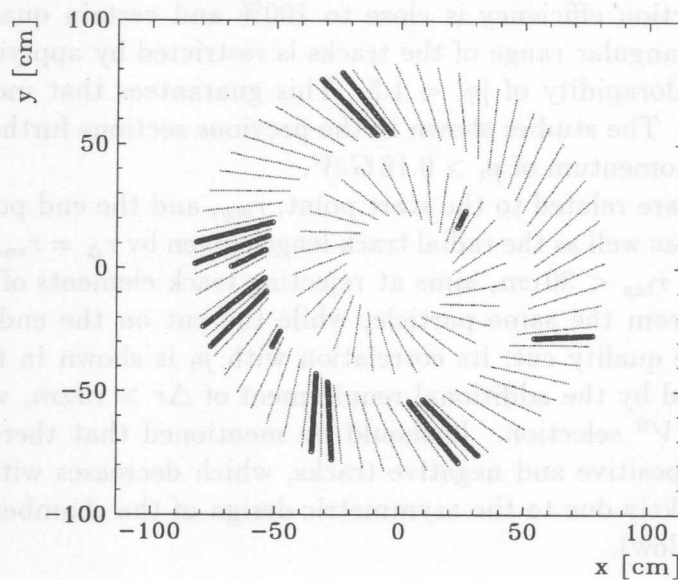


Figure 4.9: Position of the inefficient regions of the CJC in 1994. The affected wires are marked by circles; the dotted lines represent the cell boundaries.

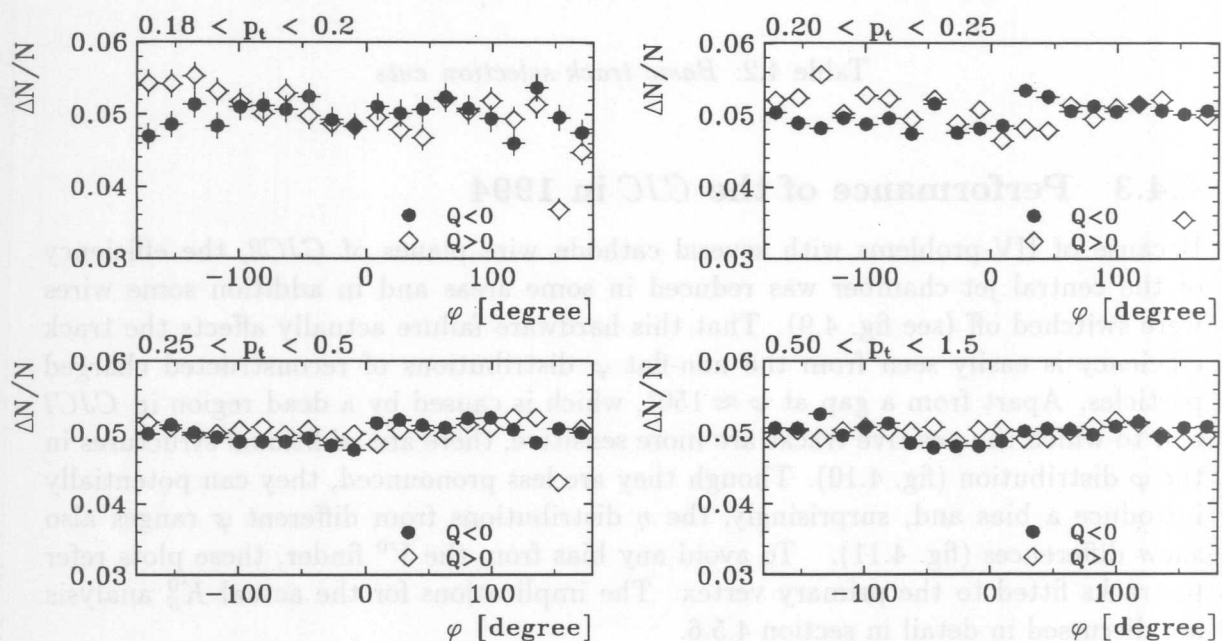


Figure 4.10: φ distributions of vertex fitted tracks for various p_t ranges. Besides the inefficient region at $\varphi \approx 150^\circ$, where mainly positive tracks are lost, there are additional "structures".

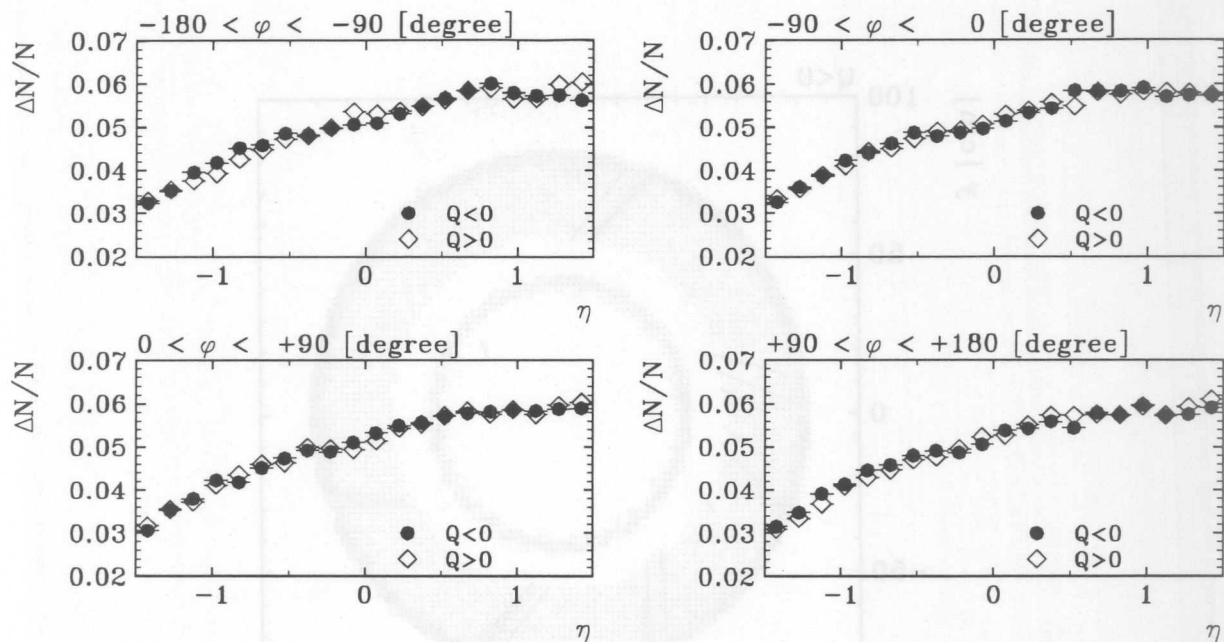


Figure 4.11: η distribution of vertex fitted tracks for various φ ranges (all tracks had to pass the basic selection cuts). Obviously the φ -dependent efficiency affects also the η distribution.

effect, the calculated drift lengths and therefore the (x, y) -positions of the particle trajectory are displaced.

Although the measurement of hits originating from *sick* sectors is probably poor, these hits were used during the track reconstruction. This situation suggests to classify the tracks as follows:

1. Tracks that traverse only fully operational regions. These tracks should have no problems and any inefficiencies should completely be related to the track reconstruction program.
2. Tracks that cross or enter a sick region. Here it is possible to distinguish further between
 - a) tracks where the reconstruction stopped just at the boundary of a sick cell and
 - b) tracks where the reconstruction program manages to make use of hits measured in *sick* areas.

Tracks mentioned under 2b) are suspected of being badly measured, meaning that the calculated track parameters and associated errors are somehow distorted.

Due to the asymmetric design of the *CJC*, it is clear that positive tracks which follow the tilt of the cells are affected differently than negative ones, particularly at low p_t (see fig. 4.12).

In the central region, about 50% of all charged tracks are potentially affected by the *sick* sectors (see fig. 4.13, fig. 4.14). To estimate this, the geometric model of the

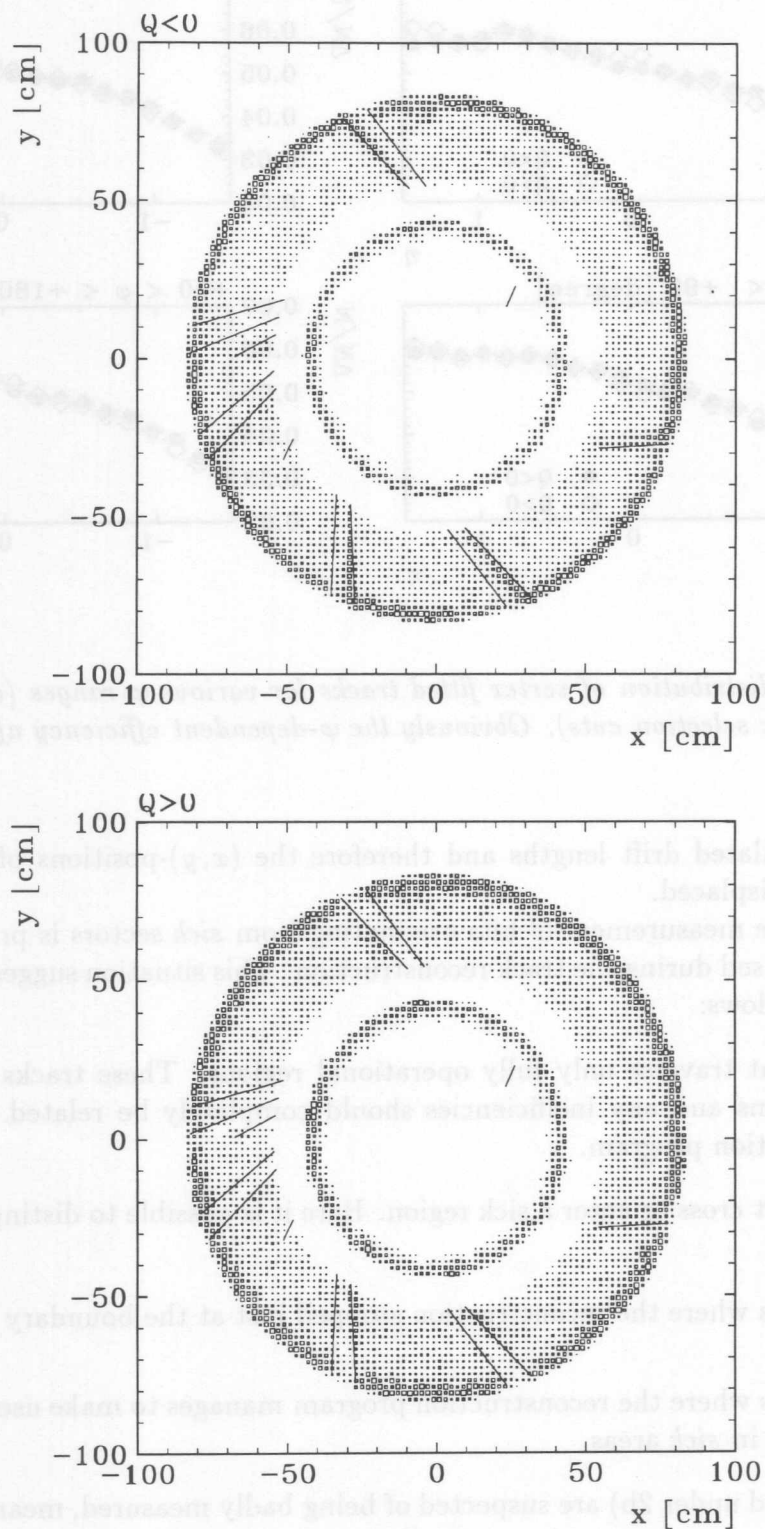


Figure 4.12: (x, y) -coordinates at r_{end} of tracks fitted to a secondary vertex, in addition the sense wire planes of the sick areas are shown. Obviously a lot more negative tracks enter CJC2 and stop close to the boundaries of a sick cell than positive tracks which more likely stop in CJC1.

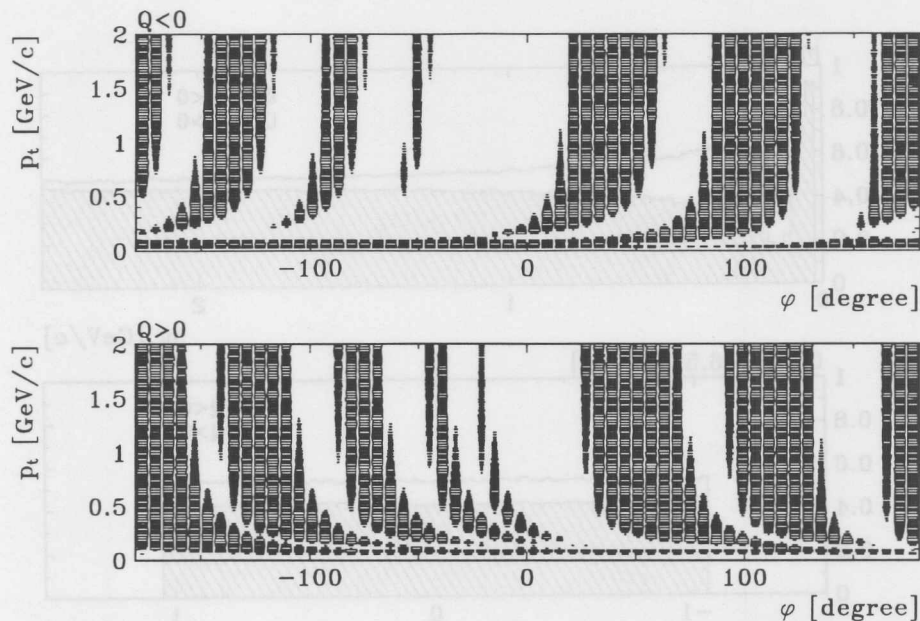


Figure 4.13: Geometric acceptance of charged particles in an inefficient CJC. The "empty" regions correspond to the (φ, p_t) ranges, where the trajectory would traverse one of the sick regions.

CJC implemented in the K_S^0 generator described in the following section was used. For each (η, p_t) -bin, positive and negative particles were generated using the five track parameters described in chapter 3.5.1. These tracks were forced to originate from a primary vertex with the (x, y) -coordinate at $(-0.5, 0.45)$ cm and the distribution of the z_0 -coordinate given by the event-vertex distribution. After extrapolating them into the active volume of the CJC, the tracks were rejected if they traversed one of the inefficient regions of the chamber.

To simplify the procedure, the areas around $\varphi = 0$ are merged into one single inefficient region; this is equivalent to calculating the geometric acceptance of the CJC for tracks traversing the good regions only.

The results of this simulation are summarized in figures 4.13 and 4.14. As expected there is no η dependence in the very central region of $|\eta| < 1.0$, while the gaps caused by the sick areas show a strong dependence on p_t (or κ), ϕ and the charge. Averaged over $|\eta| < 1.0$ the probability of a negative track to pass good regions only is much lower than for a positive track, particularly in the low- p_t range.

4.5 K_S^0 -reconstruction efficiency

In this analysis the K_S^0 -reconstruction efficiency is factorized as follows

$$\epsilon_{V^0} = \epsilon_{geo} \cdot \epsilon_{V^0 \text{ finder}} = \epsilon_{CJC} \cdot \epsilon_{BG} \cdot \epsilon_{V^0 \text{ finder}}$$

The factor $\epsilon_{geo} = \epsilon_{geo}(p_t, \eta)$ describes the geometric acceptance of the CJC (ϵ_{CJC}) including the efficiency of all cuts which have been used to improve the signal-to-background ratio (ϵ_{BG}). As these factors provide the dominant contributions to the

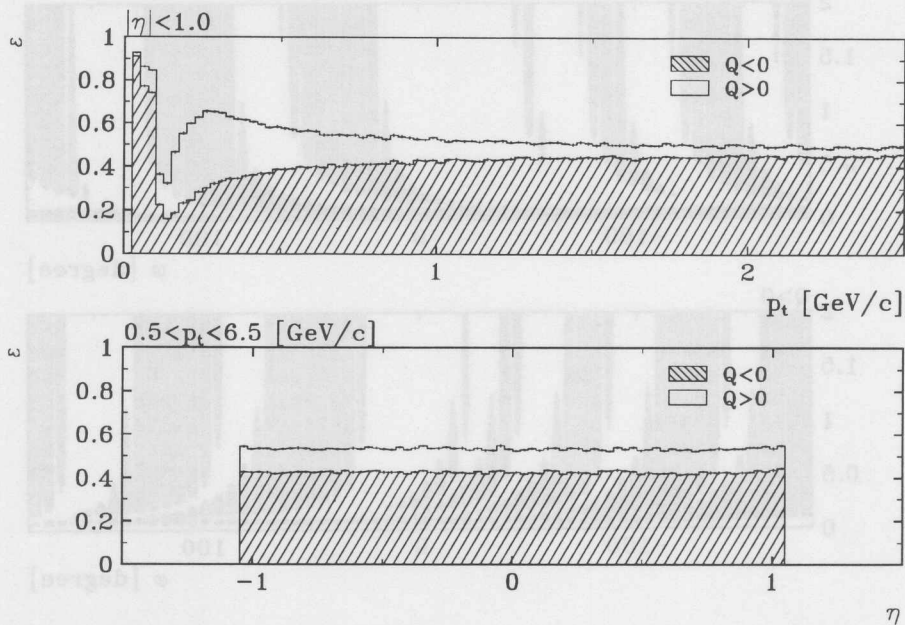


Figure 4.14: η - and p_t -dependent track efficiency in case the track trajectory is forced to cross fully efficient regions only.

V^0 -efficiency, they have been derived using a fast K_S^0 generator based on a geometric model of the *CJC*. This allowed the calculation of p_t - and η -dependent weights with high statistical accuracy.

As already mentioned in the previous section, some regions of the *CJC* were not fully operational during the data taking in 1994. The strategy to estimate the systematic effects introduced by tracks reconstructed in these regions is also based on this model.

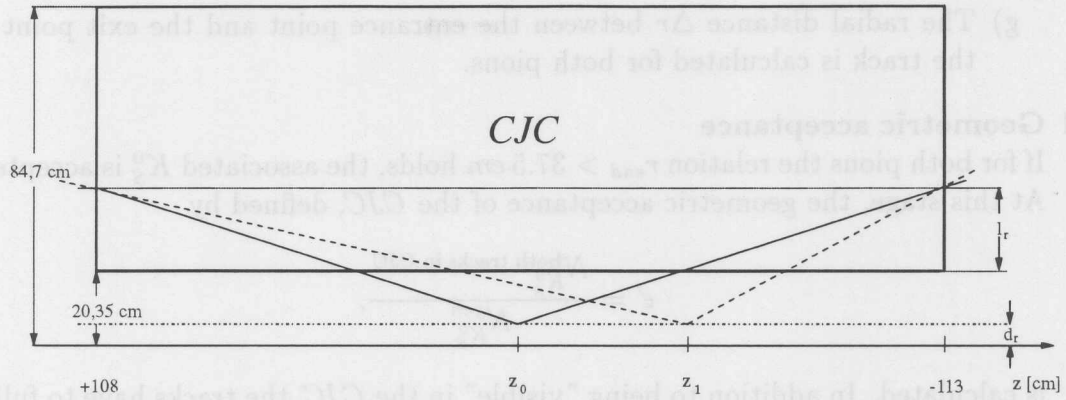
The efficiency of the V^0 -finder itself is the only correction whose determination relies on a full Monte Carlo simulation; but this correction is expected to be rather small.

4.5.1 The K_S^0 generator for the *CJC*

To determine the acceptance of the *CJC* and the losses induced by the cuts applied to improve the signal-to-background ratio, a geometric model has been used. The advantage of this geometric approach, where resolution effects of the detector components and losses due to reconstruction inefficiencies are ignored, is the possibility to investigate the p_t and η dependence of ϵ_{geo} simultaneously with very high statistics. In this approach, only the topology of single K_S^0 decays is simulated.

The alternative approach, using a full MC-simulation, usually suffers from poor statistics, so that the efficiencies can only be given as a function of either η or p_t , while the dependence on the second variable is lost. This implies that the efficiency calculation can be slightly dependent on the underlying physical model and therefore yields reliable results only when the input distributions are already close to the data distributions.

In the geometric model, the *CJC* is treated as one cylindrical volume ($CJC =$

Figure 4.15: *The geometric model of the CJC*

$CJC1 + CJC2$) with the boundaries given by the active volume (see figure 4.15). The procedure to generate a K_S^0 decay and to calculate p_t - and η -dependent efficiencies is as follows:

I Initialization

- a) define (p_t/η) -grid
(default: $0.5 < p_t < 6.5$, $\Delta p = 0.1 \text{ GeV}/c$, $|\eta| < 1.5$, $\Delta\eta = 0.1$)
- b) fix number of K_S^0 generated per point on the grid
(default: 5000)

II K_S^0 generation

- a) Assuming an isotropic decay angle distribution (corresponding to a flat distribution of $\cos\theta^*$, a K_S^0 is forced to decay randomly in its center of mass system into a $\pi^-\pi^+$. This yields $p_{\perp}^{*1,2}$ and $p_{\parallel}^{*1,2}$; in addition an angle $\varphi^* \in [0, 2\pi]$ is chosen that describes the rotation of the decay plane with respect to the $K_S^0 - z$ -plane.
- b) Depending on the actual (p_t^i, η^i) a radial decay length is chosen according to the distribution given by eq. 2.1 ($p = p_t \sin\theta$, $d = d_r \sin\theta$).
- c) The coordinates of the secondary vertex are calculated from the decay length, the pseudorapidity and the primary vertex. The z -distribution of the primary vertex is assumed to be Gaussian with $\sigma_z = 10 \text{ cm}$ and $z_0 = 4 \text{ cm}$ derived from data (see fig. 3.2). The (x, y) -coordinate is forced to be at $(-0.5, 0.5) \text{ cm}$, corresponding to the average x - and y -coordinates of the primary vertex.
- d) Applying a Lorentz transformation (see eq. 2.3, 2.4), the momentum components $p_{\perp}^{1,2}$ and $p_{\parallel}^{1,2}$ in the laboratory frame are calculated and their Cartesian components (p_x, p_y, p_z) determined.
- e) From the 4-vectors of the pions and the coordinates of the secondary vertex the track parameterizations as explained in section 3.5.1 are calculated.
- f) Both tracks are extrapolated along a helix from the secondary vertex into the CJC volume.

- g) The radial distance Δr between the entrance point and the exit point of the track is calculated for both pions.

III Geometric acceptance

If for both pions the relation $r_{end} > 37.5 \text{ cm}$ holds, the associated K_S^0 is accepted. At this stage, the geometric acceptance of the *CJC*, defined by

$$\epsilon' = \frac{N_{K_S^0}^{\text{both tracks in CJC}}}{N_{K_S^0}^{\text{gen}}},$$

is calculated. In addition to being "visible" in the *CJC*, the tracks have to fulfill the basic track cuts described in section 4.4.2.

IV Efficiency of the K_S^0 selection cuts

In addition to calculating the geometric acceptance, the efficiency ϵ_{BG} of cuts used to improve the signal-to-background ratio can be studied. The only restriction is given by the fact that all cuts have to rely on the 4-vectors and the associated track parameters of the particles. Any quality cut making use of errors calculated during the vertex fit cannot be taken into account.

V Acceptance of the fully operational *CJC*

To study a possible bias introduced by the sick areas, the geometric model is refined. In addition to Δr and r_{end} , the radial length r_{sick} between the entrance and exit point to a sick area of the *CJC* is calculated. This allows to restrict the analysis to those K_S^0 which were reconstructed using the information from fully operational areas only ($r_{sick} = r_{sick}^1 + r_{sick}^2 = 0$) and to calculate the corresponding acceptance ϵ_{geo}^{good} . The additional losses are of the order of 60% and slightly p_t dependent; there is no indication for any η dependence in the central region. Of course one can also calculate the acceptance ϵ_{geo}^{sick} for both pions in sick areas or define an upper limit on r_{sick} where this could even be φ or charge dependent.

For $p_t \in [p_t^i, p_t^{i+1}]$ and $\eta \in [\eta^i, \eta^{i+1}]$ the efficiency ϵ_{geo} is obtained from a two-dimensional linear interpolation on the "efficiency grid" which allows to define a weight for each reconstructed K_S^0 by

$$w_{geo} = \frac{1}{\epsilon_{geo}}.$$

4.5.2 The geometric acceptance of the *CJC*

The geometric acceptance surface for K_S^0 decays as defined in the previous section is shown in figure 4.16. Obviously there is no dependence on η , except near the acceptance limit, for K_S^0 s produced in the central region of the *CJC*, while the dependence on p_t is very pronounced, specifically at low p_t . By applying basic track cuts, between 20% and 60% of all K_S^0 are lost.

The effects of these cuts on the K_S^0 signal are summarized in figure 4.17. As expected, the major losses arise from the cut on the transverse momentum. For all plots only K_S^0 with $|\eta| < 1.3$ and $0.5 < p_t < 5.0 \text{ GeV}/c$ were considered; this corresponds to the kinematic range investigated in the present analysis.

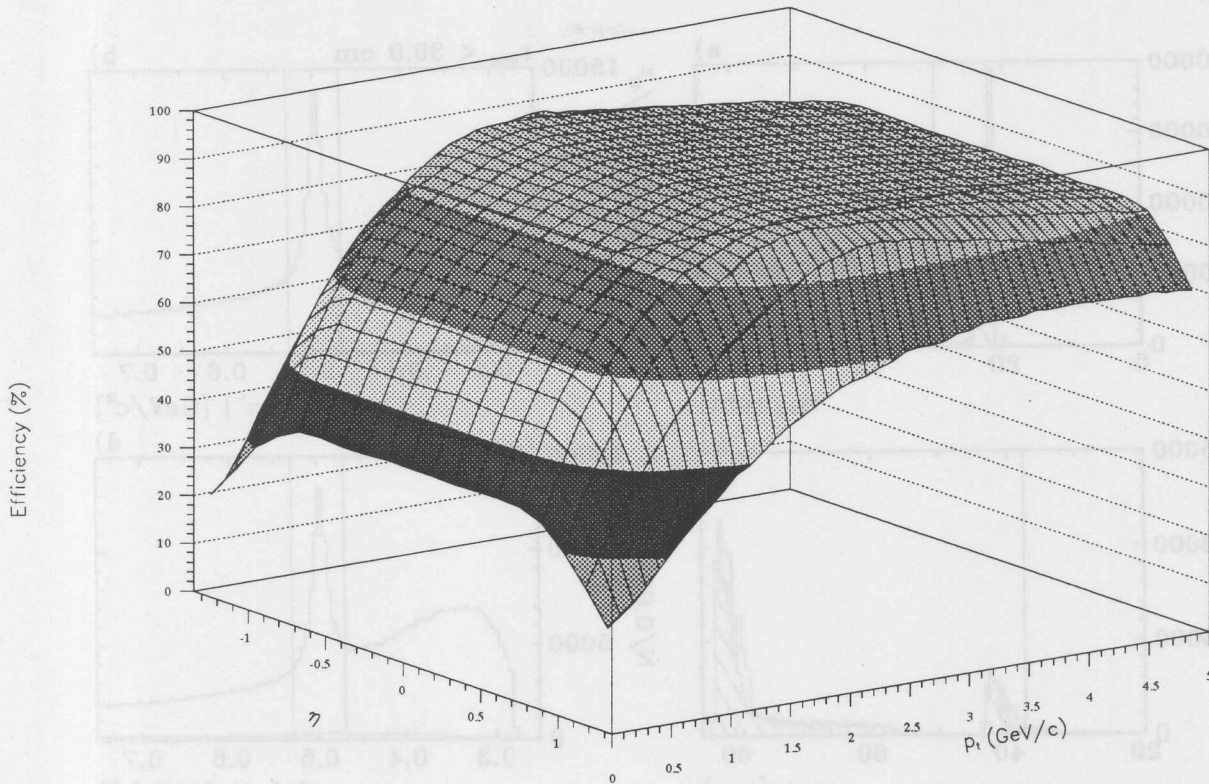


Figure 4.16: Acceptance surface obtained by applying basic track cuts

4.5.3 Improving the signal-to-background ratio

In addition to the basic track cuts, which ensure that corrections due to reconstruction inefficiencies remain small, one has to apply further cuts to improve the signal-to-background ratio, which at the same time ensure that the V^0 -finder efficiency is very high (see section 4.5.7).

The cuts used in the present analysis are listed in table 4.3 and will be discussed in the following sections.

	variable	unit	K_S^0
tracks	see table 4.4.2		
topology	radial decay length	d_r	[cm]
	momentum component perpendicular to direction of V^0 (in CMS)	p_\perp	[GeV/c]
	topological angle	Ψ	[degree]
			$ \Psi - 90^\circ > 20^\circ$
V^0	transverse momentum	p_t^0	[GeV/c]
	pseudorapidity	$ \eta $	
			> 0.5
			< 1.3

Table 4.3: Cuts used for the K_S^0 selection

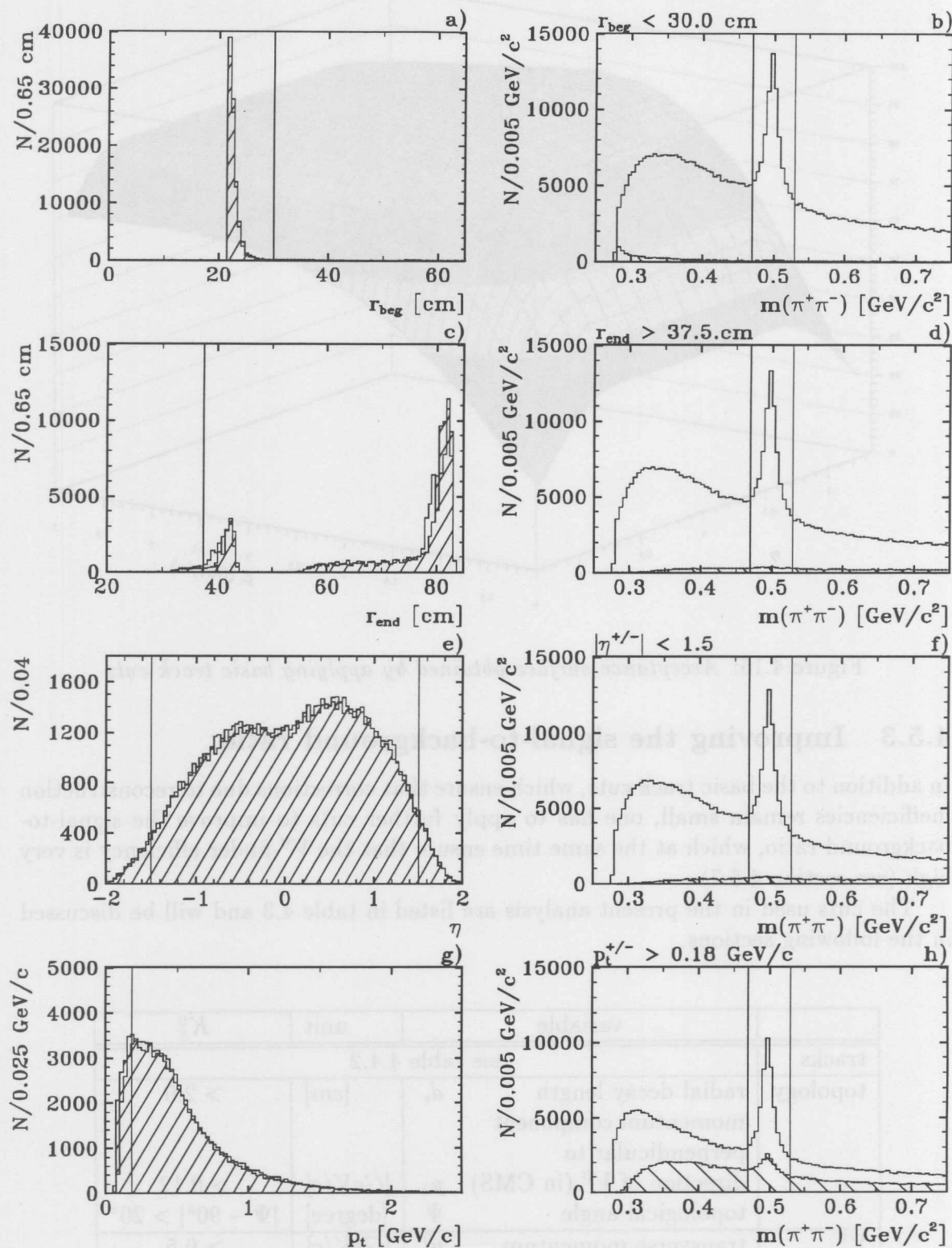


Figure 4.17: Basic track selection. Shown are the effects due to successive cuts on the start and end radius of a track as well as on η and p_t . The distributions of the track parameters are shown for positive (hatched) and negative particles (non-hatched) separately; only those tracks were considered, where the associated K_S^0 was in the indicated mass-window. The hatched invariant mass distributions show the K_S^0 s rejected by the additional basic track cut, such that the non-hatched distribution of figure (h) eventually is formed by K_S^0 used in this analysis.

- Cut on the radial decay length d_r

For the analysis only V^0 candidates with a reconstructed radial decay length of $2\text{ cm} < d_r < 18\text{ cm}$ are considered.

The main purpose of the lower cut is to reduce the combinatorial background from combinations formed by tracks coming directly from the primary vertex. As relation 2.1 shows, this cut causes additional losses, specifically in the low- p_t range.

With the upper limit of the radial decay length set to 18 cm , both tracks have to start right at the beginning of $CJCI$, this corresponds to the requirement made during the visual scan to determine the single-track efficiency (section 4.4.1). Furthermore, the kinematic region, where the V^0 -finder efficiency starts to decrease, has been excluded.

The effect of various cuts on d_r is summarized for the K_S^0 analysis in figures 4.18 and 4.19.

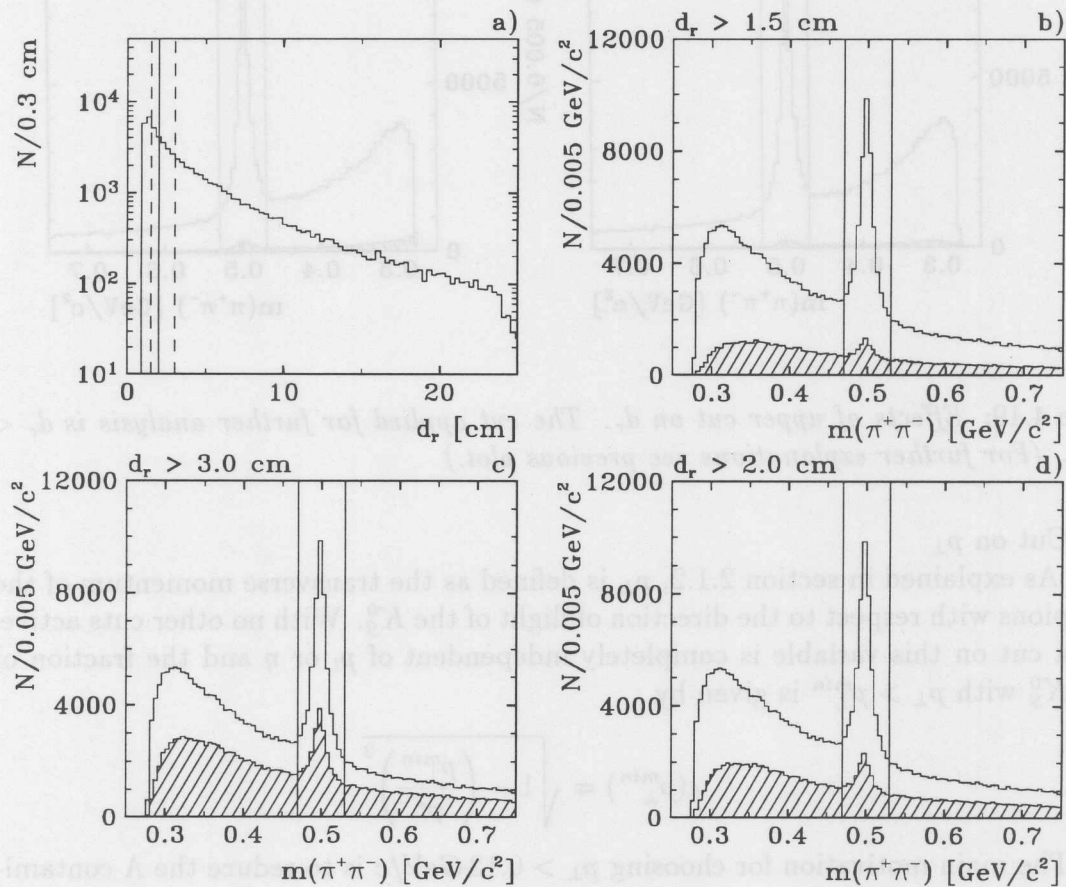


Figure 4.18: Effects of a lower cut on d_r . Shown are the distributions of the radial decay length d_r after applying basic track selection cuts (a) and the corresponding invariant mass spectra for three different cuts (b-d). To the radial decay length distribution only those K_S^0 with $\Delta m = |m_{\pi\pi} - m_{K_S^0}| < 0.030\text{ GeV}/c^2$ contribute. The non-hatched distributions show the mass spectra before applying any cut on d_r , the hatched distributions are formed by the rejected K^0 candidates. The cut applied in this analysis is $d_r > 2\text{ cm}$.

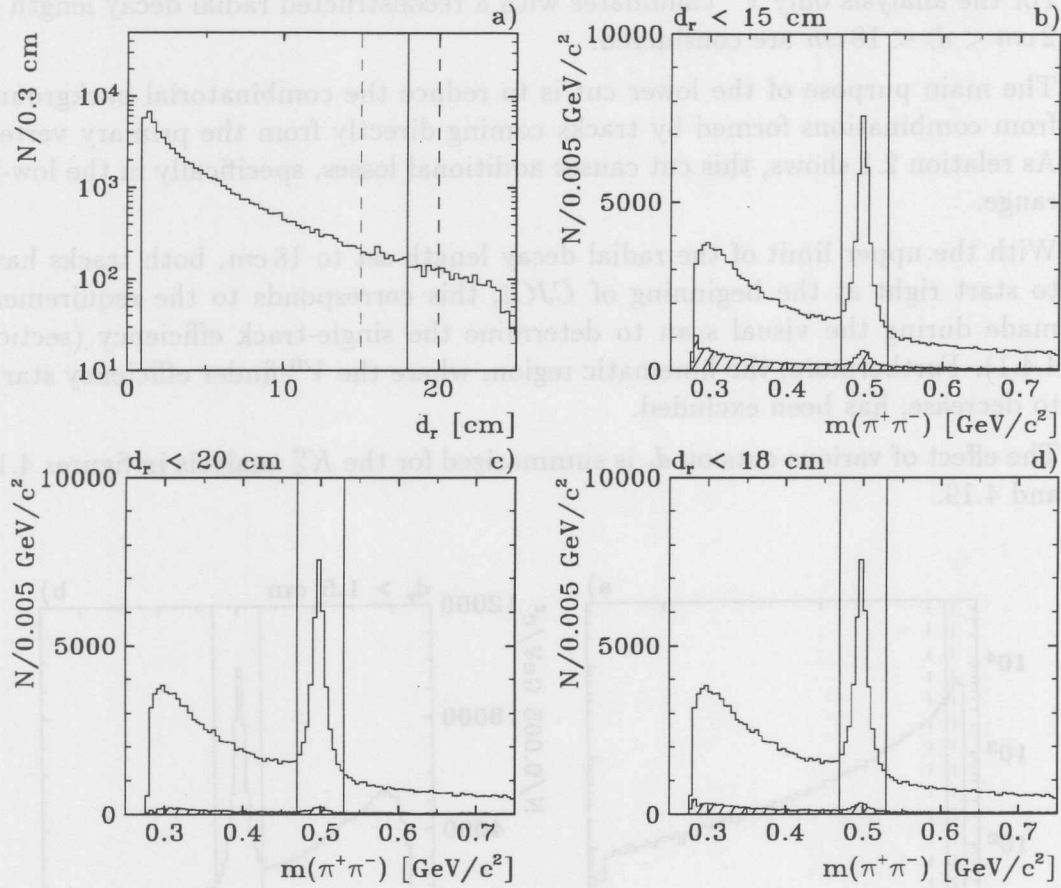


Figure 4.19: Effects of upper cut on d_r . The cut applied for further analysis is $d_r < 18$ cm. (For further explanations see previous plot.)

- Cut on p_{\perp}

As explained in section 2.1.2, p_{\perp} is defined as the transverse momentum of the pions with respect to the direction of flight of the K_S^0 . With no other cuts active, a cut on this variable is completely independent of p_t or η and the fraction of K_S^0 with $p_{\perp} > p_{\perp}^{min}$ is given by

$$\epsilon(p_{\perp}^{min}) = \sqrt{1 - \left(\frac{p_{\perp}^{min}}{p^*}\right)^2}$$

The main motivation for choosing $p_{\perp} > 0.12$ GeV/c is to reduce the Λ contamination in the K_S^0 signal (see fig 4.20), since for true Λ s the relation $p_{\perp} < p_{\Lambda}^* = 0.1005$ GeV/c has to hold (see fig. 4.21):

$$p_{\Lambda}^* = \sqrt{E_{\pi}^{*2} - m_{\pi}^2} = \sqrt{E_p^{*2} - m_p^2} = 0.1005 \text{ GeV}/c$$

with

$$E_{\pi}^* = \frac{m_{\Lambda}^2 - m_p^2 + m_{\pi}^2}{2m_{\Lambda}}$$

$$E_p^* = \frac{m_{\Lambda}^2 - m_{\pi}^2 + m_p^2}{2m_{\Lambda}}$$

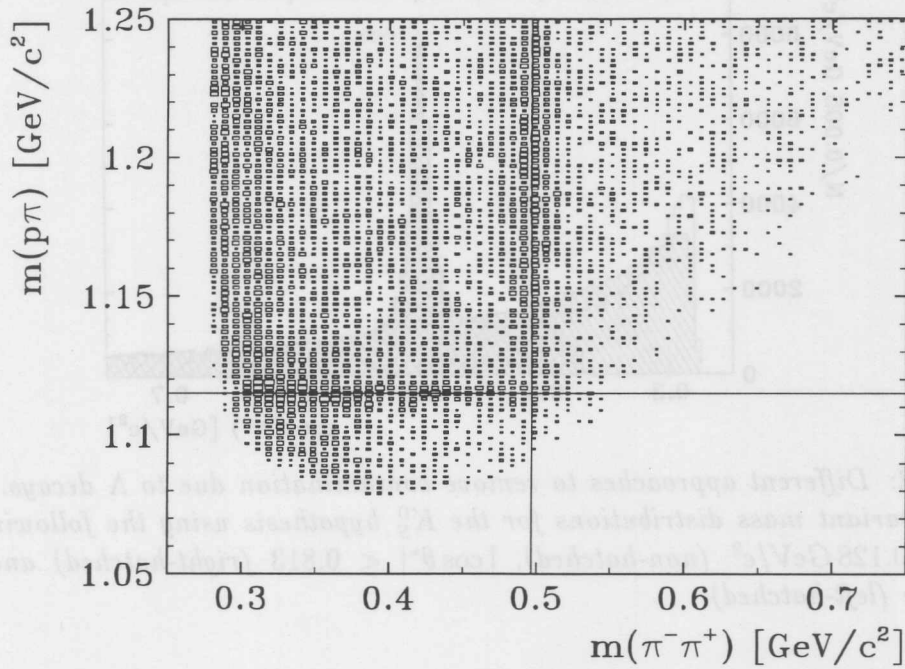


Figure 4.20: Λ -mass hypothesis vs. K_S^0 -mass hypothesis. In the kinematic range, where the two lines representing the Λ and K_S^0 mass intersect, it is not possible to resolve the ambiguity between the Λ - and K_S^0 -mass hypothesis.

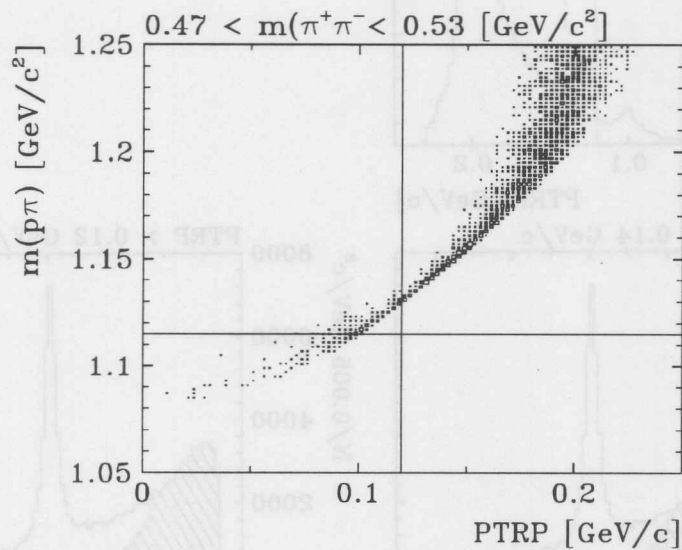


Figure 4.21: Λ -mass hypothesis vs. p_{\perp} (PTRP) for K_S^0 candidates with $\Delta m = |m_{\pi\pi} - m_{K_S^0}| < 0.030 \text{ GeV}/c^2$

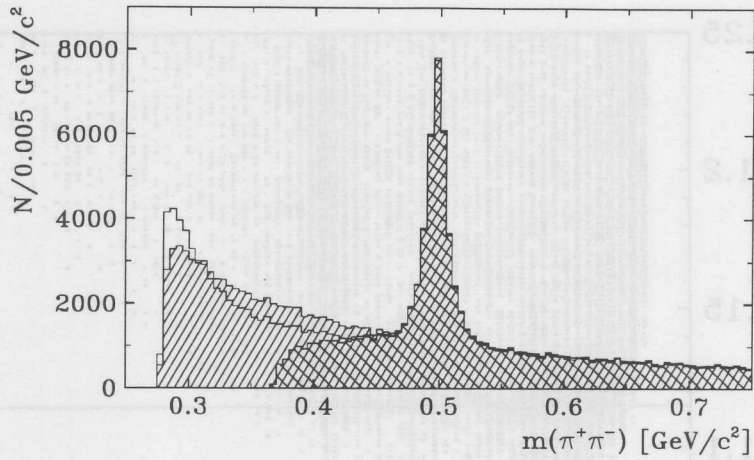


Figure 4.22: Different approaches to remove contamination due to Λ decays. Shown are the invariant mass distributions for the K_S^0 hypothesis using the following cuts: $m(p\pi) > 0.128 \text{ GeV}/c^2$ (non-hatched), $|\cos\theta^*| < 0.813$ (right-hatched) and $p_\perp > 0.12 \text{ GeV}/c$ (left-hatched).

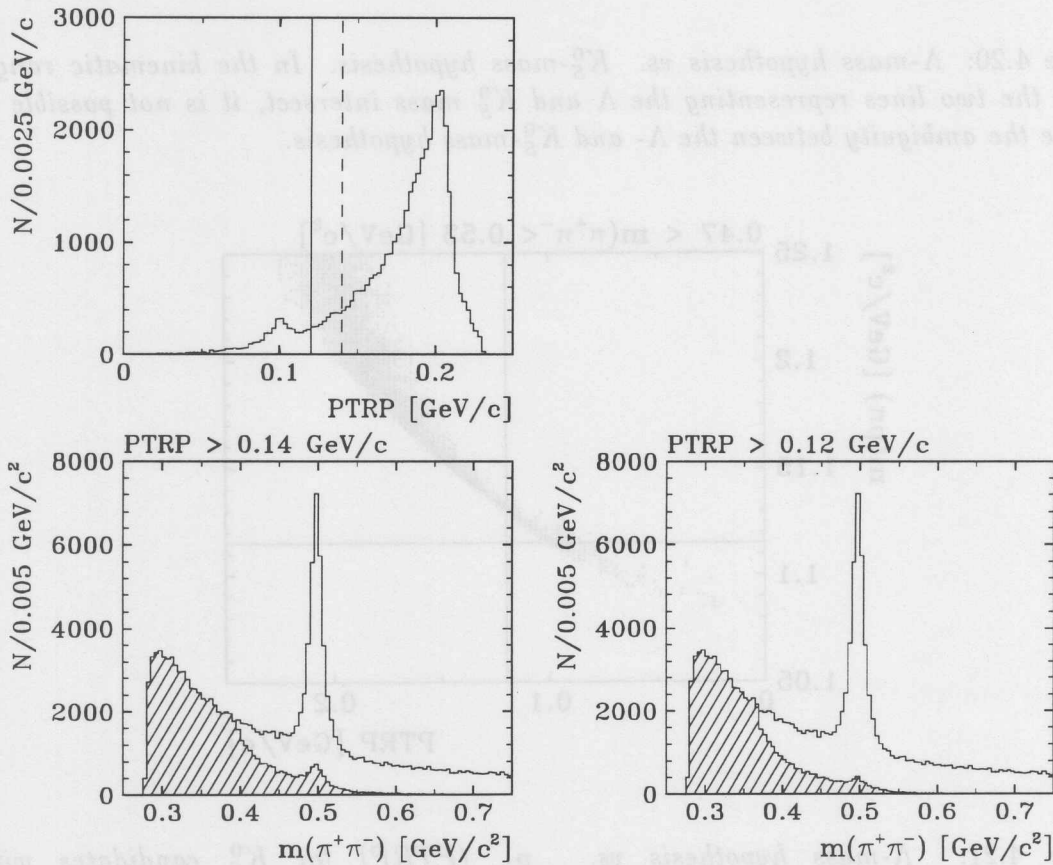
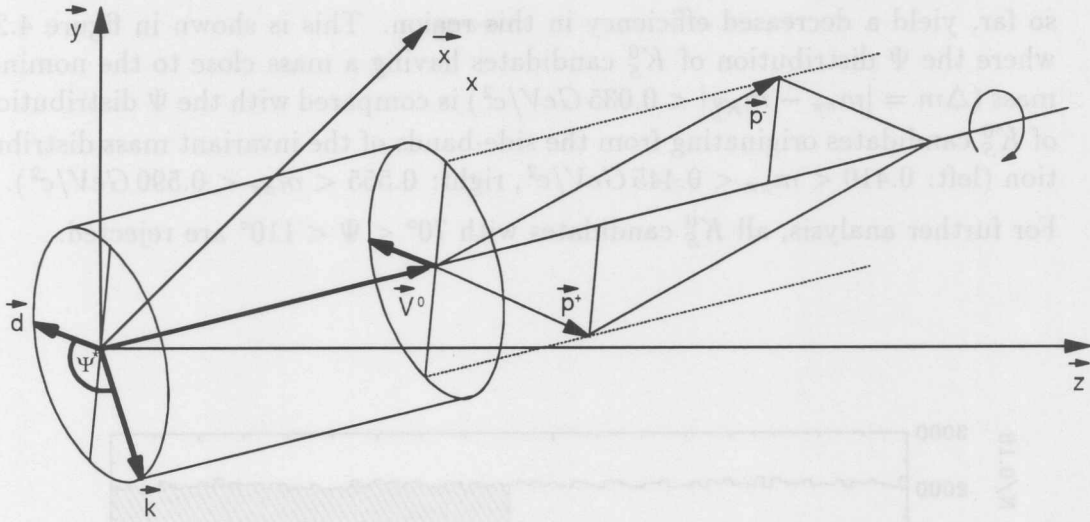


Figure 4.23: Effects of a cut on p_\perp (PTRP). Shown are the distributions of the transverse momentum with respect to the direction of flight of the K_S^0 (top) and the corresponding invariant mass spectra for two different cuts (bottom). The cut applied in this analysis is $p_\perp > 0.12 \text{ GeV}/c$. The contamination from Λ decays before applying the cut is visible in the p_\perp distribution at the expected value of $p_\Lambda^* = p_\perp \approx 0.1 \text{ GeV}/c$.

Figure 4.24: Definition of the topological angle Ψ

where m_Λ , m_p and m_π are the particle masses. Other methods to remove or reduce the contamination due to Λ decays are based on cuts on the Λ -mass hypothesis itself or the angle θ^* , which is closely related to p_\perp by

$$\cos \theta^* = \sqrt{1 - (p_\perp/p_K^*)^2}.$$

For $p_t = 0.12 \text{ GeV}/c$, which is the cut applied in the K_S^0 selection, $\cos \theta^* \approx 0.813$.

As can be seen from figure 4.21, a cut of $p_\perp > 0.12 \text{ GeV}/c$ is equivalent to rejecting all K_S^0 candidates with a $\Lambda/\bar{\Lambda}$ -mass hypothesis of $m_{p\pi} \leq 0.128 \text{ GeV}^2$.

The impact on the K_S^0 signal (i.e. losses, improvement of the signal-to-background ratio) is negligible however (fig. 4.22); the effects on the invariant mass distribution of the K_S^0 candidates are shown in figure 4.23.

- Cut on the topological angle Ψ

The topological angle is defined by

$$\begin{aligned} \Psi &= \arccos(\vec{d}_n \cdot \vec{k}_n) && \text{with} && (4.1) \\ \vec{d} &= \vec{p}^\dagger \times \vec{p}^\ddagger && \text{and} && \\ \vec{k} &= (\vec{V}^0 \times \vec{z}) \times \vec{V}^0 \end{aligned}$$

where \vec{d} describes the plane of the secondary particles and \vec{k} the production plane of the K_S^0 (see fig. 4.24). Due to the magnetic field, a K_S^0 with $\Psi < 90^\circ$ corresponds to a topology where the decay particles are *in-bending*, while for $\Psi > 90^\circ$ both particles are *out-bending* (see fig. 3.9). (In previous experiments, these topologies were also known as *cowboys* and *seagulls/seamen*). Before applying any cuts, the Ψ distribution for K_S^0 is flat while the cuts discussed so far cause losses in the region around $\Psi \approx 90^\circ$ (see fig. 4.25).

The motivation for a cut on Ψ is given by the fact that the combinatorial background increases significantly at $\Psi \approx 90^\circ$ while the V^0 selection cuts discussed

so far, yield a decreased efficiency in this region. This is shown in figure 4.26 where the Ψ distribution of K_S^0 candidates having a mass close to the nominal mass ($\Delta m = |m_{\pi\pi} - m_{K_S^0}| < 0.035 \text{ GeV}/c^2$) is compared with the Ψ distribution of K_S^0 candidates originating from the side-bands of the invariant mass distribution (left: $0.410 < m_{\pi\pi} < 0.445 \text{ GeV}/c^2$, right: $0.555 < m_{\pi\pi} < 0.590 \text{ GeV}/c^2$).

For further analysis, all K_S^0 candidates with $70^\circ < \Psi < 110^\circ$ are rejected.

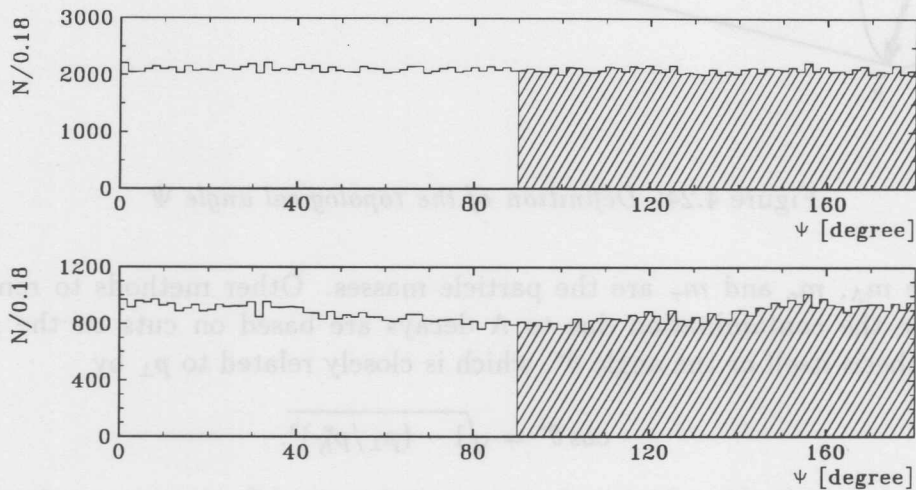


Figure 4.25: Shape of the Ψ distribution as predicted by the geometric model. The upper figure corresponds to the raw distribution averaged over all p_t and η ranges before applying any cuts, the lower refers to the one after applying the so far explained cuts, i.e. basic track selection, cut on d_r and p_\perp .

All cuts discussed above can be derived from the given track-parameters or the corresponding 4-vectors and are straightforward to implement in the geometric model. As it turns out they are more effective for high- p_t - V^0 s than for low- p_t ones. The additional losses caused by the selection cuts are of the order of 50%. Finally the overall acceptance surface, including the track quality cuts used for the geometric acceptance, is shown in fig. 4.28. As the corrections become very large for small p_t , the analysis is restricted to the range of $p_t > 0.5 \text{ GeV}/c$ and $|\eta| < 1.3$, where the variation of the efficiency is very small.

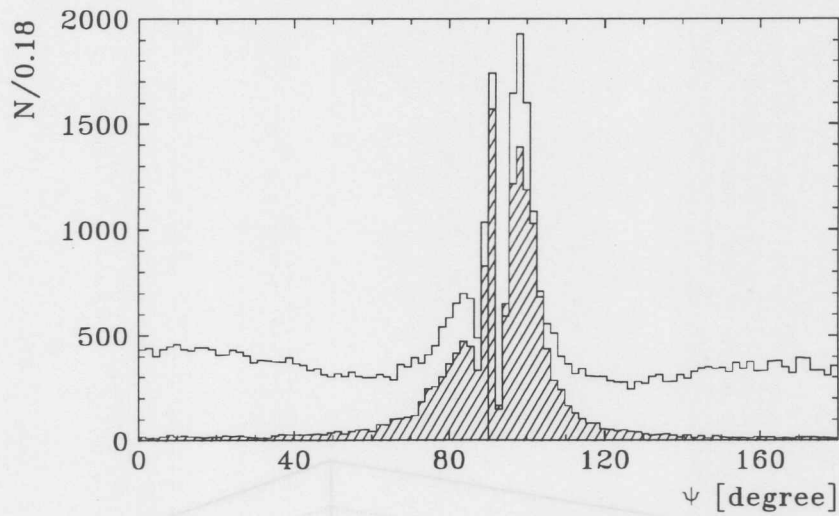


Figure 4.26: Shape of the Ψ distribution in data after applying cuts. The non-hatched distribution is formed by K_S^0 with $\Delta m = |m_{\pi\pi} - m_{K_S^0}| < 0.035 \text{ GeV}/c^2$, the hatched distribution by mass combinations from the right and left side-bands.

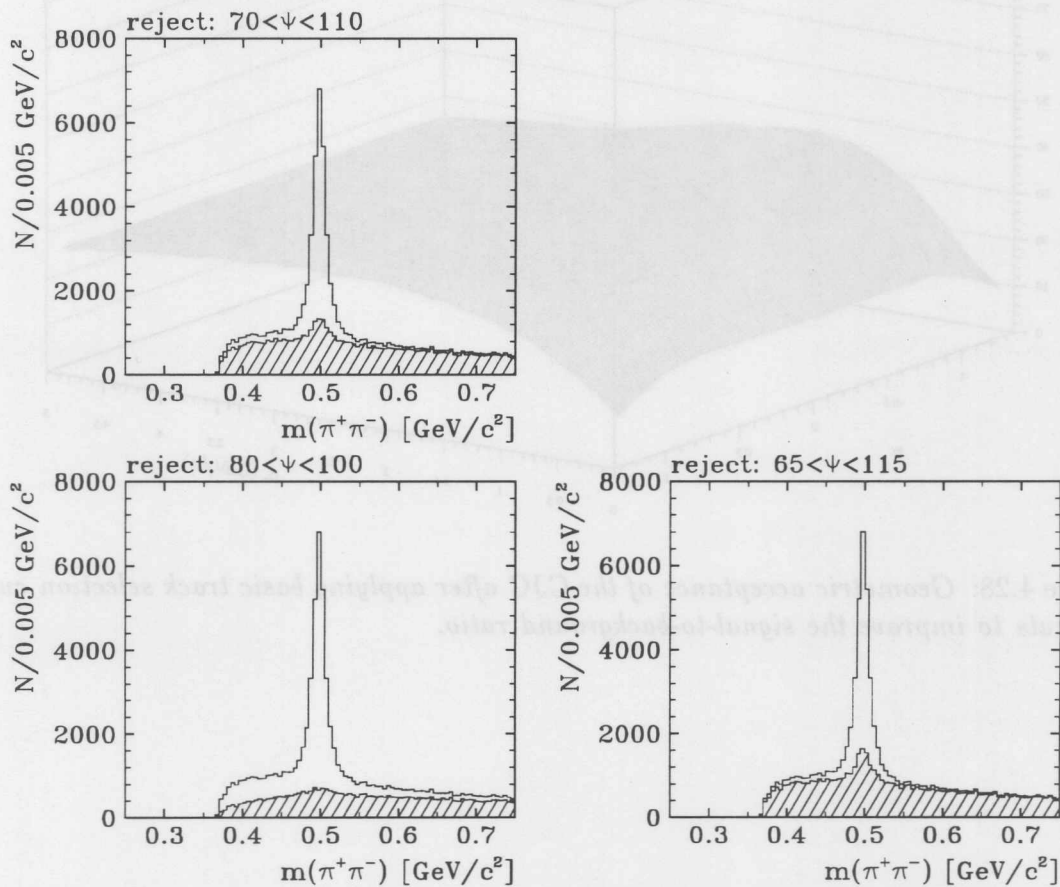


Figure 4.27: Effects of cuts on the topological angle Ψ . Shown are the effects that three different cuts on the topological angle Ψ have on the invariant mass spectrum of the K_S^0 candidates. The hatched distributions show the rejected K_S^0 candidates. For further analysis all K_S^0 candidates with $70^\circ < \Psi < 110^\circ$ rejected.

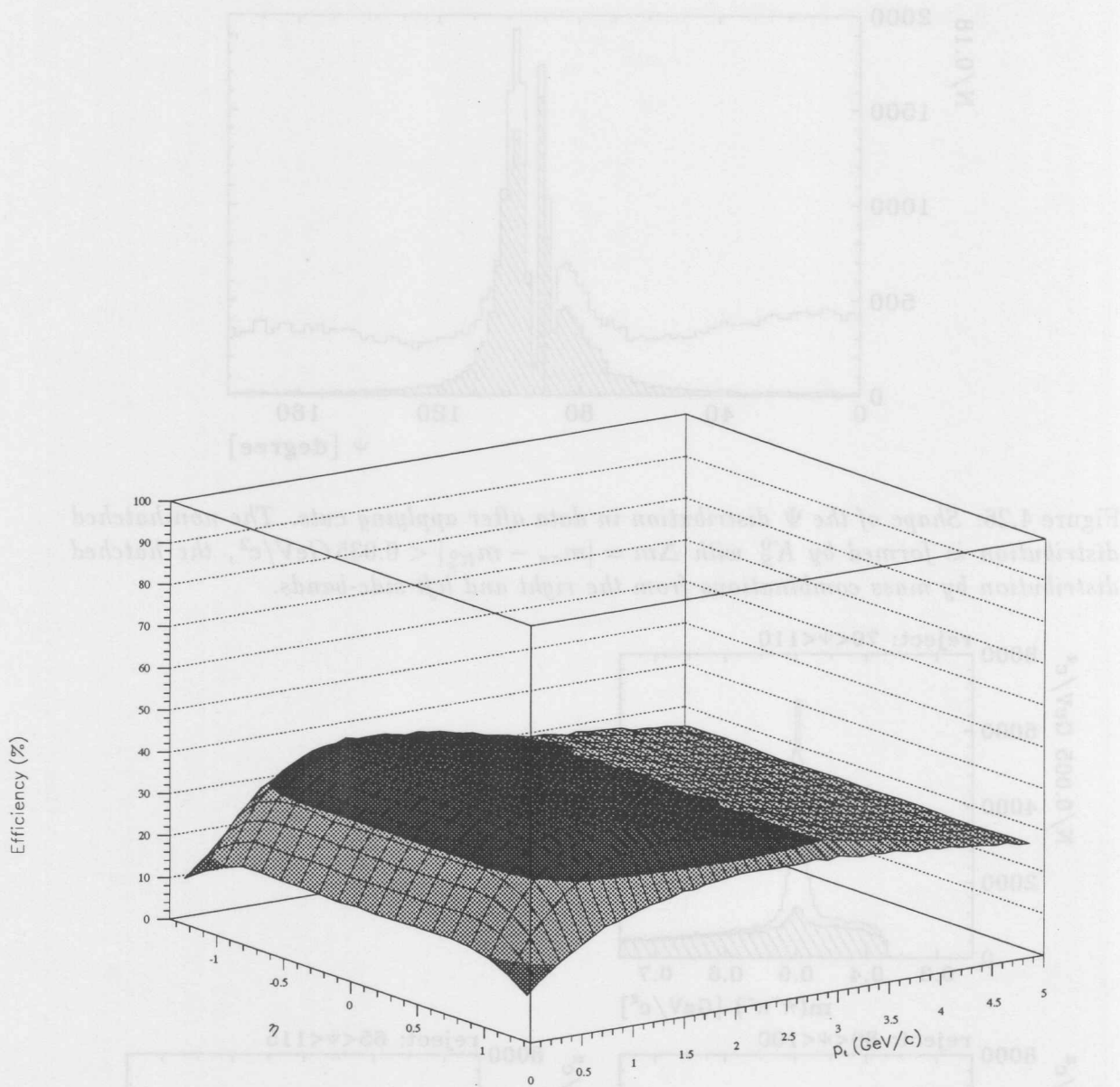


Figure 4.28: Geometric acceptance of the CJC after applying basic track selection cuts and cuts to improve the signal-to-background ratio.

4.5.4 The misalignment of the CJC

Since the CJC consists of two independent chambers and has a complex structure introduced by the tilt of the drift cells against the radial direction, a precise measurement of the particle momenta can only be guaranteed if the chambers are correctly aligned, or if a possible misalignment is taken into account during the reconstruction; furthermore, the chambers have to be properly calibrated.

In the charged particle analysis based on the 94-data [61] it was observed that the momenta of positive tracks are systematically shifted to higher values, this effect increasing with p_t .

Since there is no reason to assume that this effect is limited to vertex fitted tracks, there might be an impact on the K_S^0 analysis, particularly in the high- p_t range under study. To estimate a possible bias, an additional upper cut on the transverse momentum of the associated pions was introduced and the corresponding geometric acceptances calculated. By applying an upper cut to both pions at the same time, the accessible kinematic range of the K_S^0 is limited to $p_{t,max}^0 \leq 2 \cdot p_{t,cut}^{pion}$; therefore this cut was applied to one pion only: first to the positive pion then to the negative pion.

Comparing the number of K_S^0 s corrected for geometric acceptance with various upper cuts on the transverse momentum of the pions, no significant variation was observed. The misalignment of the CJC has, therefore, a negligible impact in the kinematic range under study.

4.5.5 The K_S^0 signal and the determination of the signal-to-background ratio

After applying all cuts discussed so far, the number of K_S^0 in the kinematic range $|\eta| < 1.3$ and $0.5 < p_t < 5.0 \text{ GeV}/c$ is $N_{K^0} = 21781 \pm 163$, and the corresponding signal-to-background ratio within a range of $\pm 50 \text{ MeV}/c^2$ around the nominal peak position is $S/B \approx 7.2$ (see fig. 4.29, left). The position of the mass peak at $m_{\pi^+\pi^-} = 0.49752 \pm 0.00007 \text{ GeV}/c^2$ is in rather good agreement with the published mean value [55].

For the calculation of differential cross sections, the number of K_S^0 produced in a certain kinematic range, defined for example by p_t , η or y_{rap} , has to be determined. In the present analysis two different approaches were used: on the one hand a simple side-band subtraction, and on the other hand a fit to the corresponding invariant mass spectrum of K_S^0 candidates.

To apply the side-band subtraction method, the K_S^0 s were divided into three subsamples defined by different mass windows with $\Delta m^{\text{peak}} = 2\Delta m^{\text{left}} = 2\Delta m^{\text{right}}$. The first sample contains all K_S^0 candidates from a mass region close to the peak ($m_{\pi\pi} \in [0.465, 0.535]$), while the others are taken from the left and right part of the spectrum ($m_{\pi\pi}^{\text{left}} \in [0.555, 0.59]$ and $m_{\pi\pi}^{\text{right}} \in [0.41, 0.445]$).

Since the background is small, the "true" K_S^0 spectrum is simply determined from the difference between the *peak* distribution and the sum of the two side-band distributions.

In the second method, the K_S^0 signal for each point of the spectrum is investigated separately and analyzed by fitting an appropriate function to it. As the remaining background is low, it was described by a first order polynomial (straight line), while for the actual K_S^0 signal a superposition of two Gaussians yielded the best results.

The superposition of two Gaussians is motivated by the fact that the mass resolutions for the two topologies (*in-bending* and *out-bending*) differ significantly (see fig. 4.29, right), while the peak position is nearly the same. This is utilized to reduce the number of degrees of freedom of the fit by forcing the two Gaussians to have the same mean value; in addition, the relative contributions of the topologies are fixed according to the actual number of reconstructed *in-bending* and *out-bending* K_S^0 s in a given mass-window around the peak. The results of both methods are compatible within statistical errors.

In principle the K^0 -mass resolution is given by the width of the K^0 signal. Taking into account K^0 from the whole kinematic range under study the resolution is $\sigma^{in} = 5.74 \pm 0.08 \text{ MeV}/c^2$ for the *in-bending* topology and $\sigma^{out} = 14.55 \pm 0.18 \text{ MeV}/c^2$ for the *out-bending* topology.

A more detailed analysis shows that there is an indication that both the peak position and the width of the mass peak are slightly dependent on p_t and η ; for this analysis, these effects are neglected.

4.5.6 Inefficiencies related to the *CJC* performance

Some problems of the track reconstruction related to the sick areas in the *CJC* have been discussed in section 4.4.3. In this section, special emphasis is put on the K_S^0 -reconstruction.

Since the corrections rely on high-precision efficiencies derived from a geometric model rather than a full MC-simulation limited by poor statistics, they can only be trusted if there are no other systematic effects which are not modeled (or cannot be modeled).

Concerning the inefficiencies of the *CJC*, the following questions need to be answered:

1. Do the sick areas only lead to a φ -dependent decrease in efficiency resulting from tracks being simply lost? This could be taken into account by applying a correction factor which "fills the dips" of the corresponding φ distribution.
2. Are there additional effects which somehow bias the track properties in such a way that the measurement of a K_S^0 formed by pions crossing the sick areas is unreliable⁴?

In this case, a simple scale factor to fill the dips of the φ distribution would not be appropriate.

Estimate of the actual losses

In principle one could try to estimate the number of K_S^0 s lost from the φ distribution shown in figure 4.30. In this figure the φ distributions of *in-bending* and *out-bending* K_S^0 are shown separately because the *out-bending* topology is more sensitive to inefficiencies in the *CJC*⁵ than the *in-bending* one. To determine the losses one can assume that there are φ -regions where the losses of the *in-bending* topology are negligible.

⁴Of course not all K_S^0 s with a pion trajectory crossing a sick area must have problems because quite often the corresponding tracks stop before entering the cell.

⁵This also explains why the Ψ distribution of figure 4.26 is not symmetric around 90° .

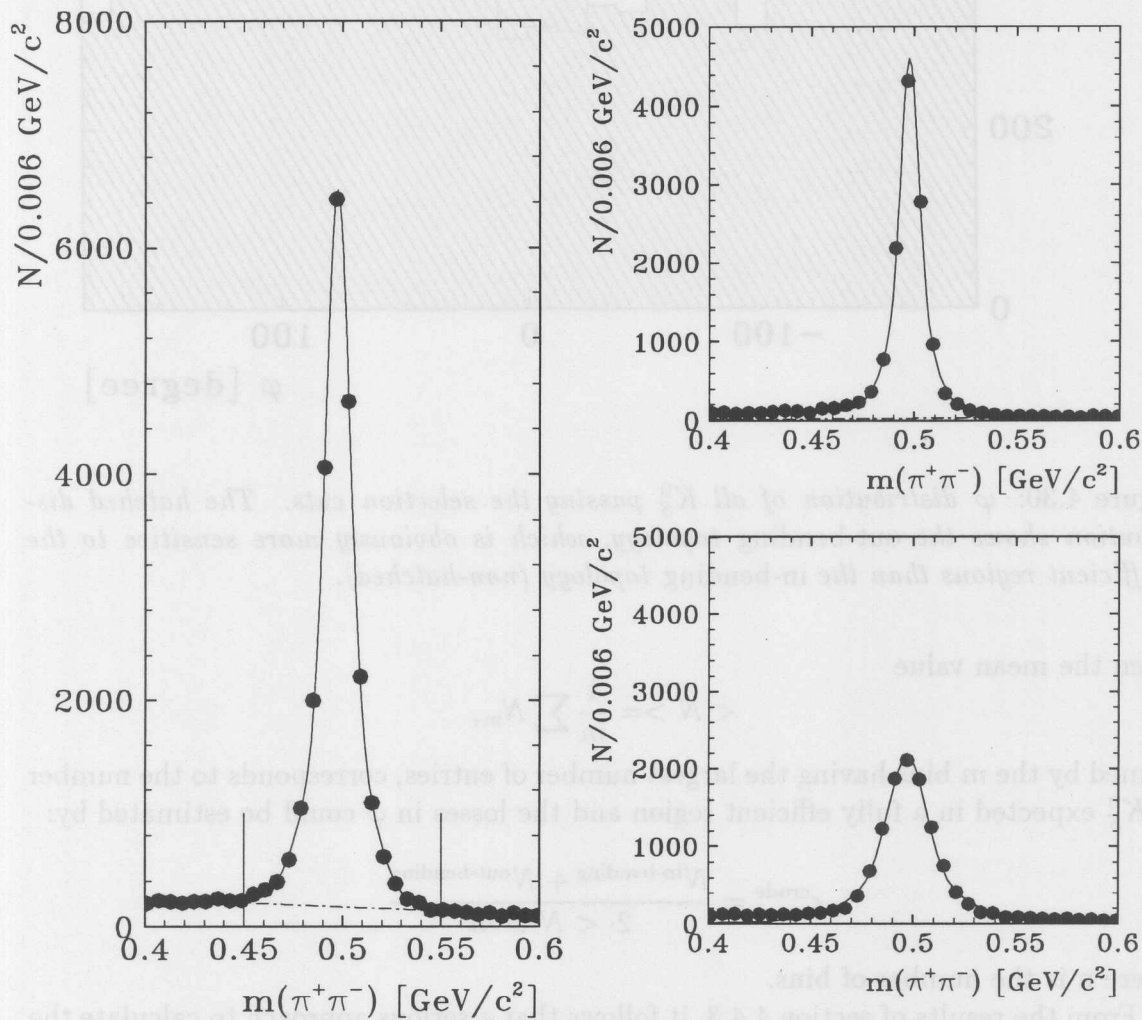


Figure 4.29: The final K_S^0 signals. On the left the final K_S^0 signal after applying all cuts discussed so far (\bullet) and the corresponding fit are shown ; on the right the K_S^0 signals of the in-bending (top right) and the out-bending (bottom right) topology are shown separately.

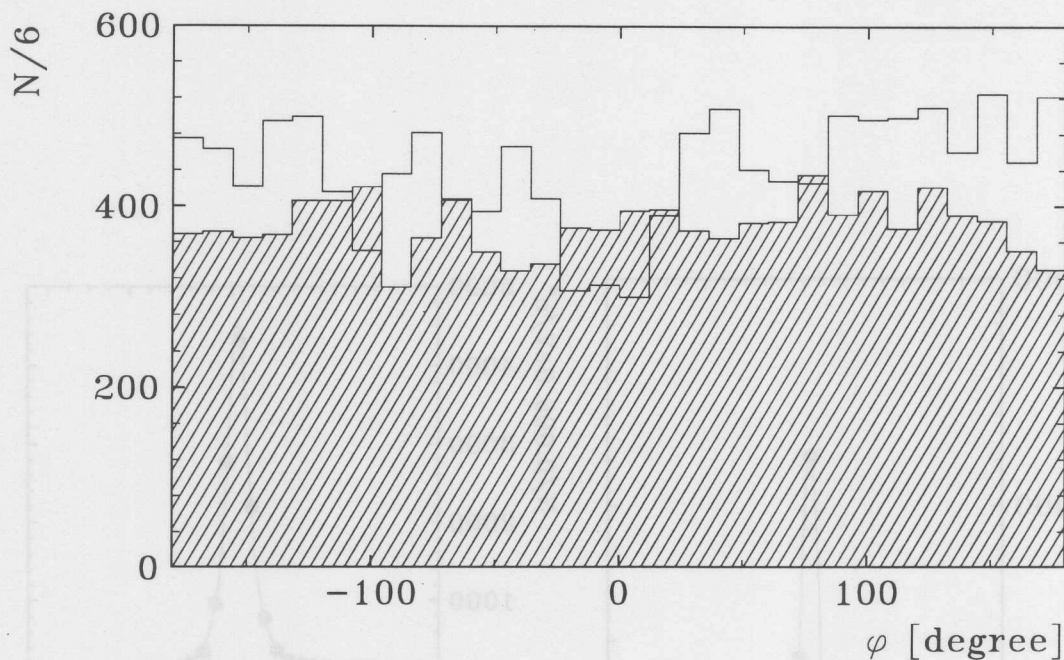


Figure 4.30: φ distribution of all K_S^0 passing the selection cuts. The hatched distribution shows the out-bending topology, which is obviously more sensitive to the inefficient regions than the in-bending topology (non-hatched).

Then the mean value

$$\langle N \rangle = \frac{1}{m} \sum N_m,$$

formed by the m bins having the largest number of entries, corresponds to the number of K_S^0 expected in a fully efficient region and the losses in φ could be estimated by:

$$\epsilon_\varphi^{\text{crude}} = \frac{N^{\text{in-bending}} + N^{\text{out-bending}}}{2 \cdot \langle N \rangle \cdot n}$$

where n is the number of bins.

From the results of section 4.4.3, it follows that a serious approach to calculate the losses should at least depend on p_t (either the p_t of the two pions, which is difficult to carry out, or the p_t of the K_S^0 averaging over $p_t^{\pi,1}$ and $p_t^{\pi,2}$). There is no obvious reason to introduce an η dependence (see fig. 4.14).

Since there are some systematic η -dependent effects which are not fully understood so far this is a misleading assumption.

The sick areas and the η distribution

From the geometric model, no η -dependent effects are expected, but a comparison between the distributions shown in figure 4.31 suggests that this is wrong for data. This figure shows the η distributions of three different K_S^0 -samples: 1) all K_S^0 s, 2) K_S^0 s with both pions in good regions and 3) K_S^0 s with both pions in sick regions. All distributions have been corrected with their corresponding geometric acceptance (ϵ_{geo} , $\epsilon_{geo}^{\text{good}}$ and $\epsilon_{geo}^{\text{sick}}$) and should in principle be identical. The obvious discrepancies

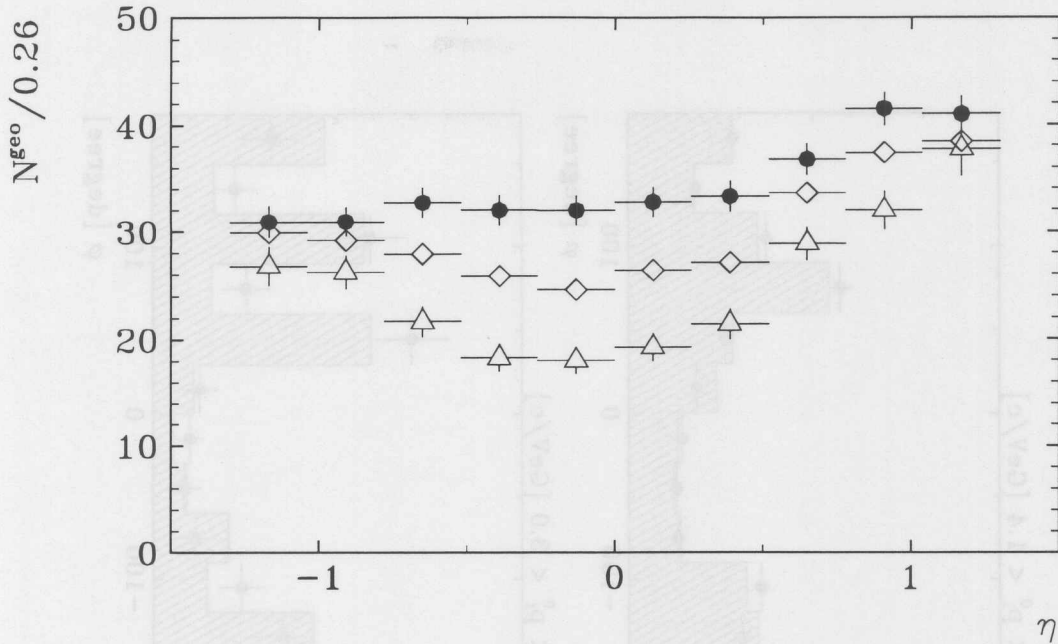


Figure 4.31: η distributions for various K_S^0 samples (corrected for geometric acceptance, \bullet : both π in good regions, \triangle : both π in bad regions, \diamond : all K_S^0). Obviously there are systematic effects in the central region which the geometric model is unable to correct for.

are therefore an indication of additional inefficiencies related to the sick areas which are not included in the geometric model. The straightforward solution to avoid any systematic uncertainties would be to restrict the analysis to the first sample. For this sample a good agreement between data and the predictions from the geometric model exists, and it is reasonable to conclude that there are no further hidden biases.

To compare data with predictions from the model, the flat p_t and η distributions used as input were weighted according to a (p_t, η) distribution generated with the standard version of PYTHIA5.7 (see section 1.5.2). Of particular interest are of course the φ distributions obtained by excluding K_S^0 s whose decay particles cross sick areas (fig. 4.32 and 4.33). The good agreement between data and model are also an evidence of a high efficiency of the V^0 finder for this specific sub-sample.

Unfortunately this sub-sample contains only about 35% of the whole K_S^0 -sample, and the rejected sample probably also includes a large amount of good K_S^0 s, namely those formed by pions where the reconstructed track(s) stop at the boundary of a sick cell or even in *CJC1*.

Attempts to recover some statistics

Before actually rejecting 65% of the whole K_S^0 -sample in order to minimize the systematic uncertainties around $\eta \approx 0$, some approaches were tested to recover statistics and to correct for this η -dependent inefficiency, respectively.

- Based on the hypothesis that the quality of a track is related to the radial distance r_{sick} between entering and leaving a sick area, one could try to define

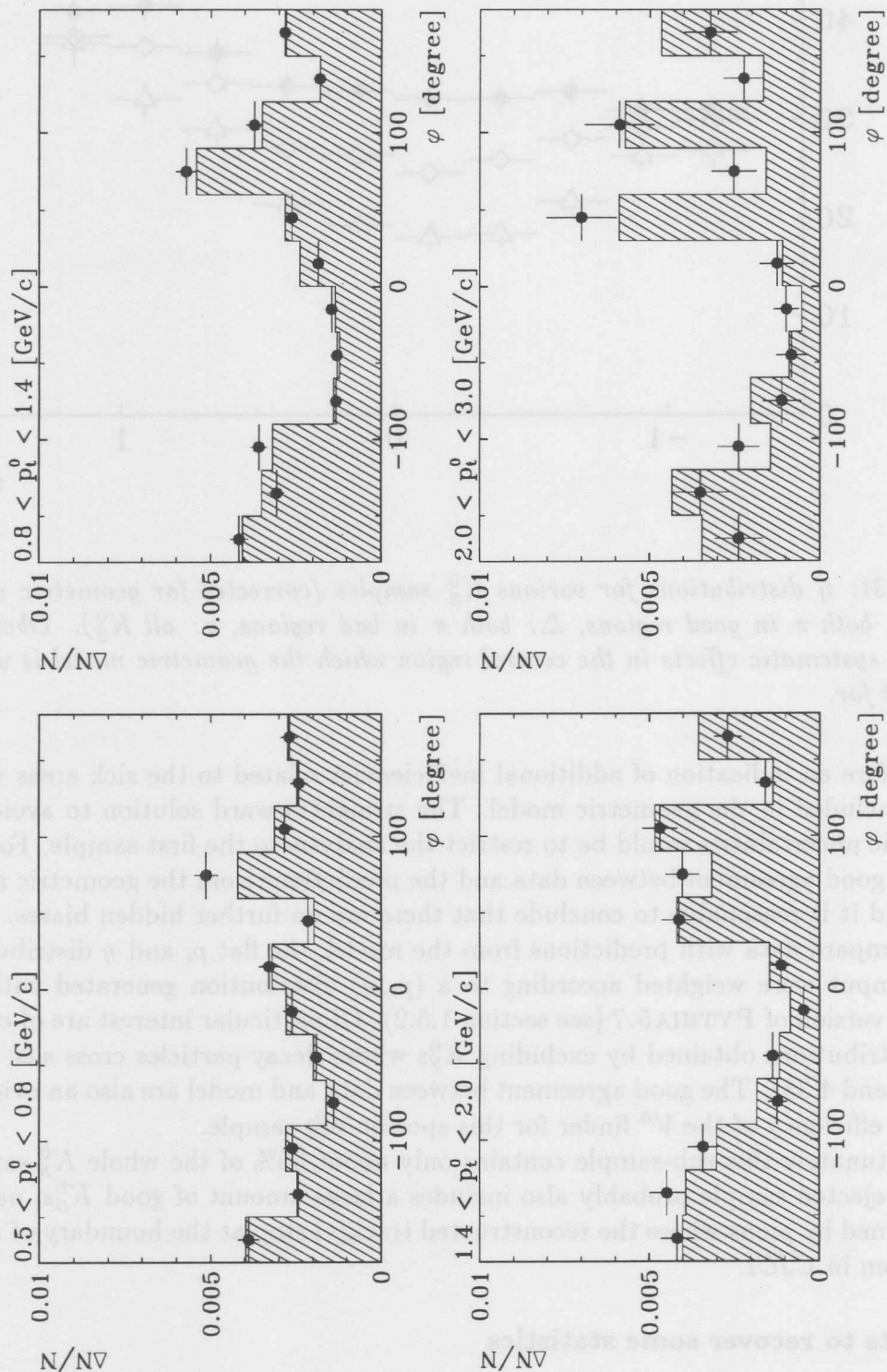


Figure 4.32: *Out-bending topology: p_t -dependent φ distributions obtained by accepting only those K_S^0 with both pions in fully efficient regions of the CJC (histogram: prediction of the geometrical model, \bullet : data).*

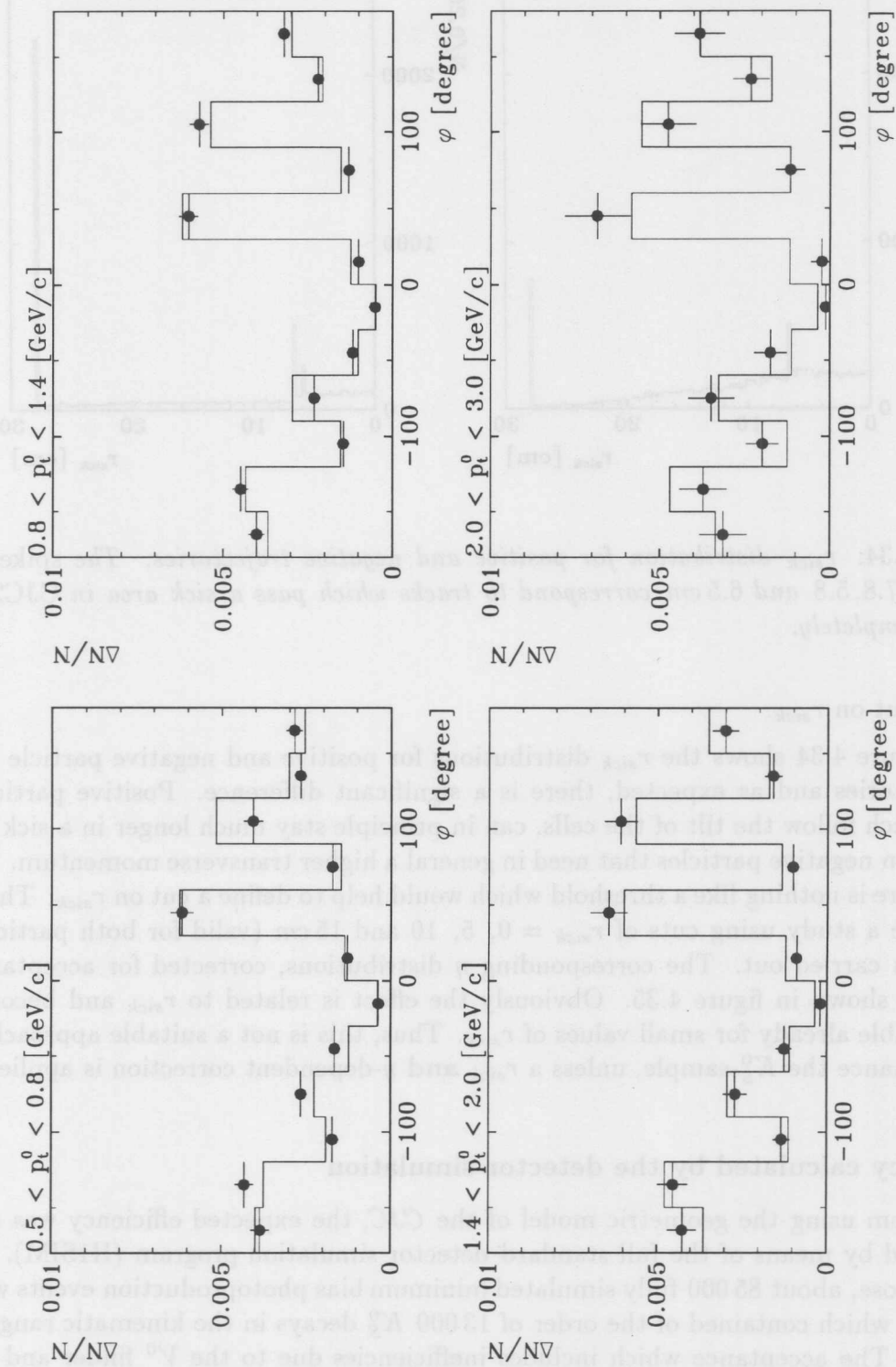


Figure 4.33: *In-bending topology*: p_t -dependent φ distributions obtained by accepting only those K_S^0 with both pions in fully efficient regions of the CJC (histogram: prediction of the geometrical model, \bullet : data).

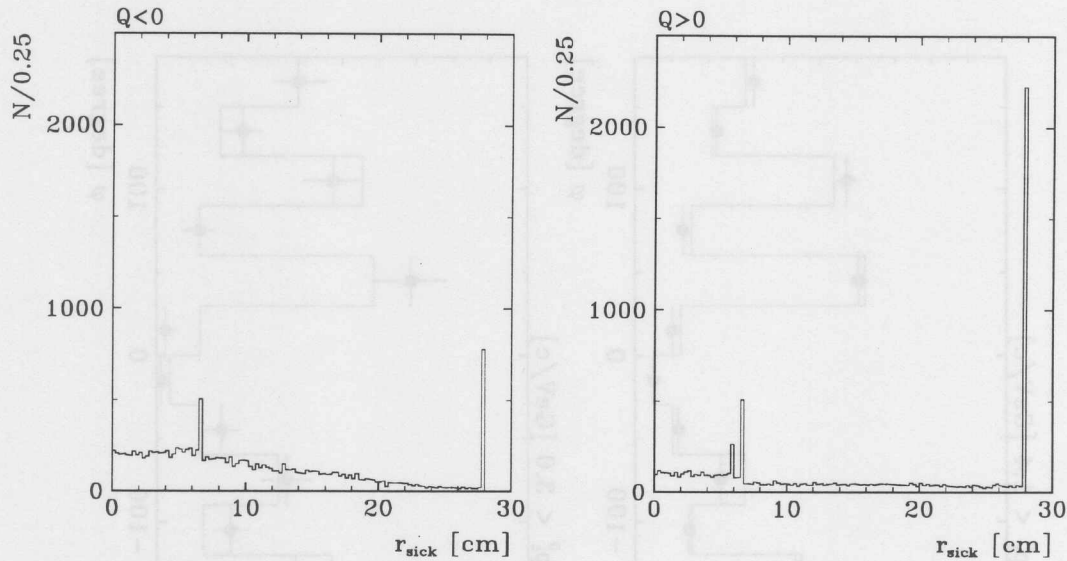


Figure 4.34: r_{sick} distribution for positive and negative trajectories. The spikes at $r_{sick} = 27.8, 5.8$ and 6.5 cm correspond to tracks which pass a sick area in CJC2 or CJC1 completely.

a cut on r_{sick} .

Figure 4.34 shows the r_{sick} distributions for positive and negative particle trajectories and as expected, there is a significant difference. Positive particles, which follow the tilt of the cells, can in principle stay much longer in a sick cell than negative particles that need in general a higher transverse momentum. But there is nothing like a threshold which would help to define a cut on r_{sick} . Therefore a study using cuts of $r_{sick} = 0, 5, 10$ and 15 cm (valid for both particles) was carried out. The corresponding η distributions, corrected for acceptance, are shown in figure 4.35. Obviously the effect is related to r_{sick} and becomes visible already for small values of r_{sick} . Thus, this is not a suitable approach to enhance the K_S^0 -sample, unless a r_{sick} and η -dependent correction is applied.

Efficiency calculated by the detector simulation

Apart from using the geometric model of the *CJC*, the expected efficiency was also calculated by means of the full standard detector simulation program (H1SIM). For this purpose, about 85 000 fully simulated minimum bias photoproduction events were analyzed which contained of the order of 13 000 K_S^0 decays in the kinematic range of interest. The acceptance which includes inefficiencies due to the V^0 finder and the track reconstruction (though these are expected to be negligible in the kinematic range under study!), is given by

$$\epsilon_{MC} = \frac{N_{K_S^0}^{rec}}{N_{K_S^0}^{gen}}$$

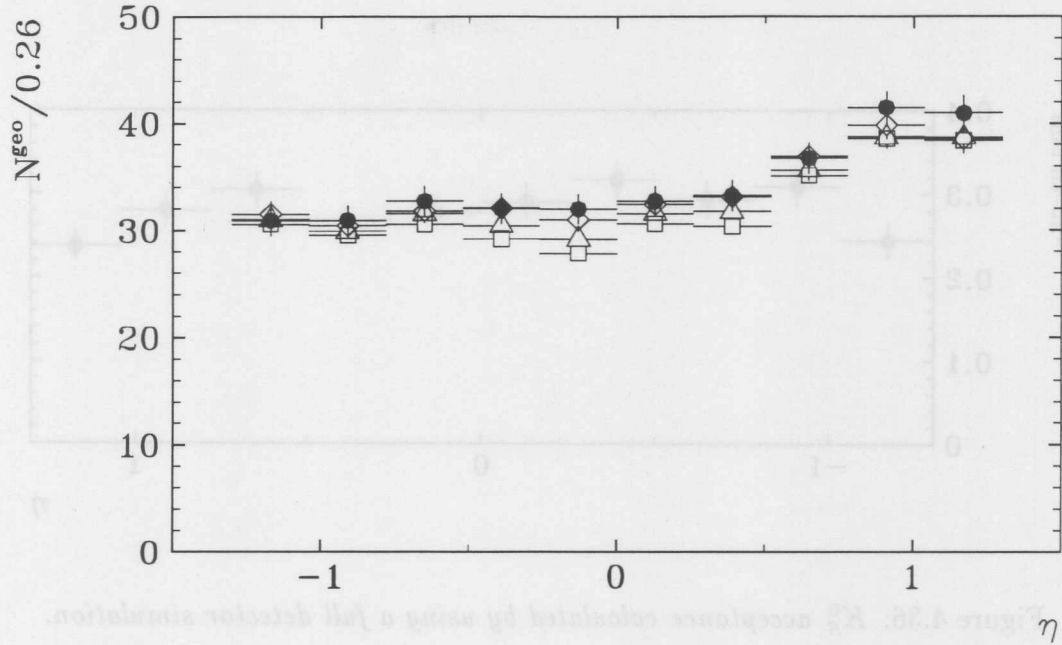


Figure 4.35: η distributions for various K_S^0 samples, selected with a cut on r_{sick} (see text). ●: both π in good regions only, ◇: $r_{sick} < 5$ cm, △: $r_{sick} < 10$ cm, □: $r_{sick} < 15$ cm

where $N_{K_S^0}^{gen}$ is the number of generated decays in the specific kinematic range and $N_{K_S^0}^{rec}$ the number of reconstructed decays⁶ (see fig. 4.36). Eventually the following two η distributions are compared (fig. 4.37):

- the η spectrum derived from the full sample corrected with the efficiency derived from the full detector simulation
- the η spectrum derived from the reduced sub-sample corrected with the efficiency calculated using the geometric model.

Since there is a significant discrepancy between the two distributions, particularly at $\eta \approx -0.25$, the simulation of the H1 detector does not reproduce all effects related to the sick areas of the CJC^7 . This is not surprising since the inefficient regions of the CJC are taken into account by merely reducing the single hit efficiency, but no effects like shifted (x, y) -coordinates due to wrong drift velocities, etc. are considered.

Conclusion

The predictions concerning the K_S^0 -efficiency/acceptance from the detector simulation introduce some systematic uncertainties and furthermore the statistic accuracy is very low, therefore it is not used in the present analysis.

⁶In this analysis no migration effects between adjacent bins are considered.

⁷As can be seen from a comparison between the η distribution based on the full sample corrected with efficiencies from the geometric model (see fig. 4.31) and the aforementioned Monte Carlo η distribution, some effects are taken into account

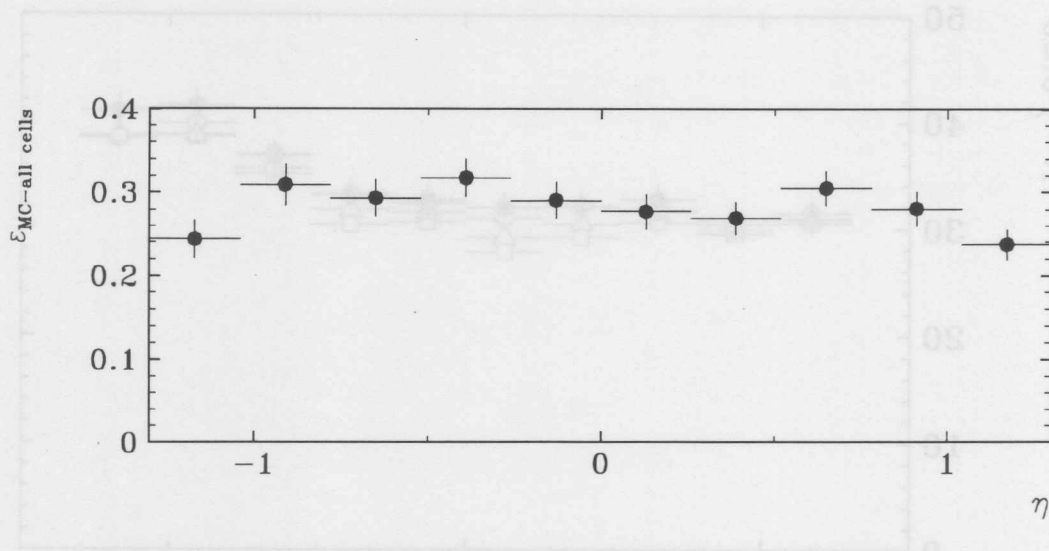


Figure 4.36: K_S^0 acceptance calculated by using a full detector simulation.

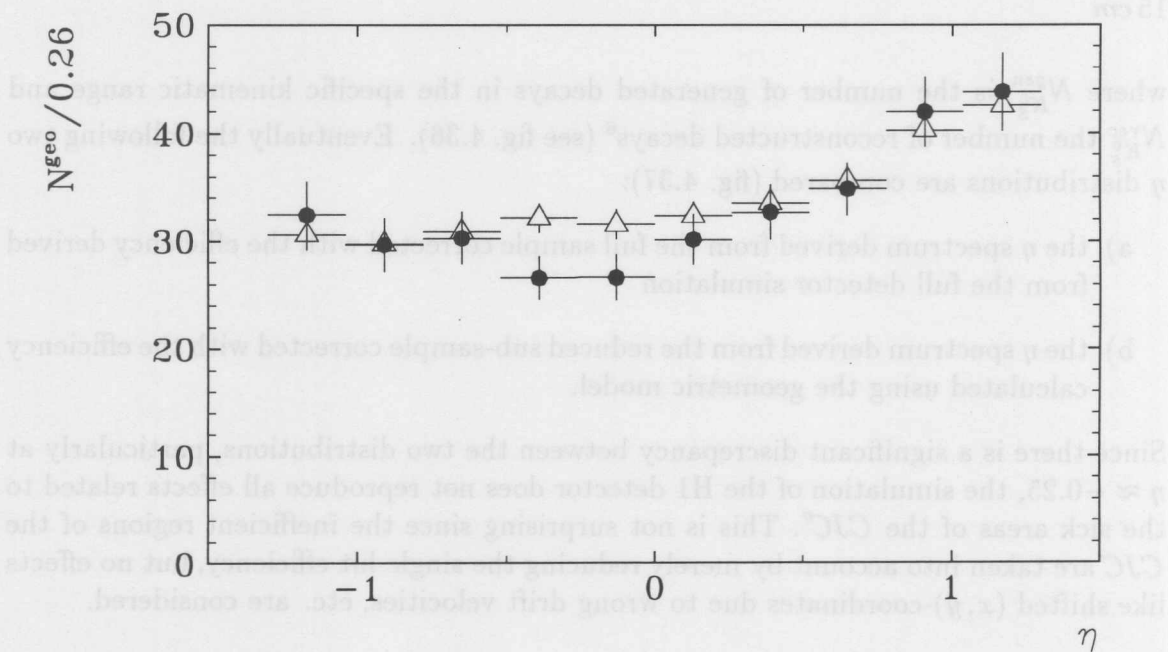


Figure 4.37: Comparison between H1SIM and the geometric model: the first η distribution (●) is based on the full sample and corrected with the corresponding efficiency derived from a full simulation of the H1 detector. For the second distribution (△) only those K_S^0 were accepted where both pions are measured in fully efficient regions of the CJC, the corresponding acceptance correction being calculated using the geometric model (no scaling for luminosity, etc. is applied).

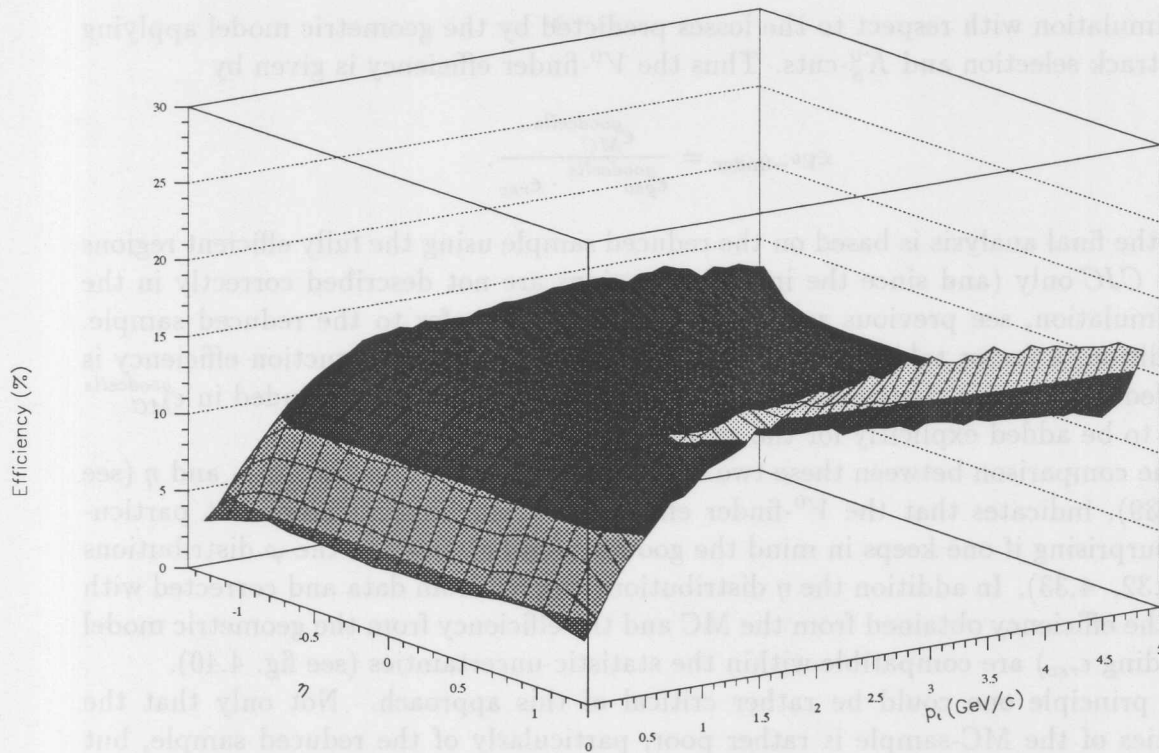


Figure 4.38: Geometric acceptance of the CJC for selected K_S^0 in fully efficient regions.

The geometric model allows the determination of the geometric acceptance with high statistic accuracy but only for regions of the CJC where the efficiency is high and well understood. Since there were inefficient regions during the data-taking in 1994, data from these regions were not considered for the present analysis. To correct for losses caused by the *sick* areas of the CJC and to recover the sample some studies were performed. Obviously the amount of losses is dependent on various variables like the transverse momentum, the radial distance the track is measured in the inefficient region and its charge. Therefore no attempt to correct for these inefficiencies using a multi-dimensional correction factor was made. One possibility to avoid problems caused by tracks measured in sick regions would be to re-run the CJC -reconstruction module using only hits which were measured in fully efficient regions. In this case one would have to study the difference between *short* and *long* tracks. Unfortunately it was not possible to reprocess all the data taken in 1994 for this specific analysis. The geometric acceptance for the remaining sample is therefore rather small, see fig. 4.38.

4.5.7 V^0 -finder efficiency

During the selection of the final K_S^0 candidates, the reconstruction of the module of the V^0 finder makes explicitly use of the single hit information. Therefore it is not possible to test its efficiency with the geometric model which uses track parameters and 4-vectors only and it has to be estimated by studies on a full MC-simulation.

The idea is to define the V^0 -finder efficiency by the additional losses occurring in the

MC-simulation with respect to the losses predicted by the geometric model applying basic track selection and K_S^0 -cuts. Thus the V^0 -finder efficiency is given by

$$\epsilon_{V^0\text{-finder}} = \frac{\epsilon_{MC}^{goodcells}}{\epsilon_{geo}^{goodcells} \cdot \epsilon_{rec}}$$

Since the final analysis is based on the reduced sample using the fully efficient regions of the CJC only (and since the inefficient regions are not described correctly in the MC-simulation, see previous section) both efficiencies refer to the reduced sample. In addition, a factor taking into account the single track reconstruction efficiency is included. While this contribution to the (in)efficiency is already included in $\epsilon_{MC}^{goodcells}$ it has to be added explicitly for the geometric model.

The comparison between these two efficiencies, both as a function of p_t and η (see fig. 4.39), indicates that the V^0 -finder efficiency is very high. This is not particularly surprising if one keeps in mind the good agreement between the φ distributions (fig. 4.32, 4.33). In addition the η distributions derived from data and corrected with both the efficiency obtained from the MC and the efficiency from the geometric model (including ϵ_{rec}) are compatible within the statistic uncertainties (see fig. 4.40).

In principle one could be rather critical of this approach. Not only that the statistics of the MC-sample is rather poor, particularly of the reduced sample, but one also has to average over one of the two variables, p_t or η , under study. To do this it is no longer possible to use "flat" input distributions for the geometric model, but they have to be weighted according to some MC-predictions (in this case PYTHIA5.7 was used) which of course introduces some bias.

Though there might be an indication for a small inefficiency of the V^0 -finder (particularly in the low p_t range) this is not taken into account by applying an additional correction factor but just by assigning a global systematic uncertainty of 6%.

For future analysis on K_S^0 - (or even Λ -) related topics it would be desirable to have

- a much better understanding of the CJC in order to
 - model any inefficiencies of the CJC correctly in the detector simulation
 - and/or to handle data from inefficient regions more appropriately, maybe by rejecting them at all
- higher statistics of fully simulated events

or simply a fully efficient CJC (but even then a better understanding of some remaining effects would be necessary!).

4.6 The luminosity measurement

In the H1 experiment, the measurement of the luminosity is based on the Bethe-Heitler process; there are several methods for its measurement [56]. They vary in accuracy and are used for different purposes, e.g. a fast online monitoring and the off-line determination of the luminosity used for physics analysis.

The run-dependent results of the off-line analysis are available in the H1 database. In addition, one has to correct for the loss of luminosity caused by events that are rejected because some of the subdetectors had problems.

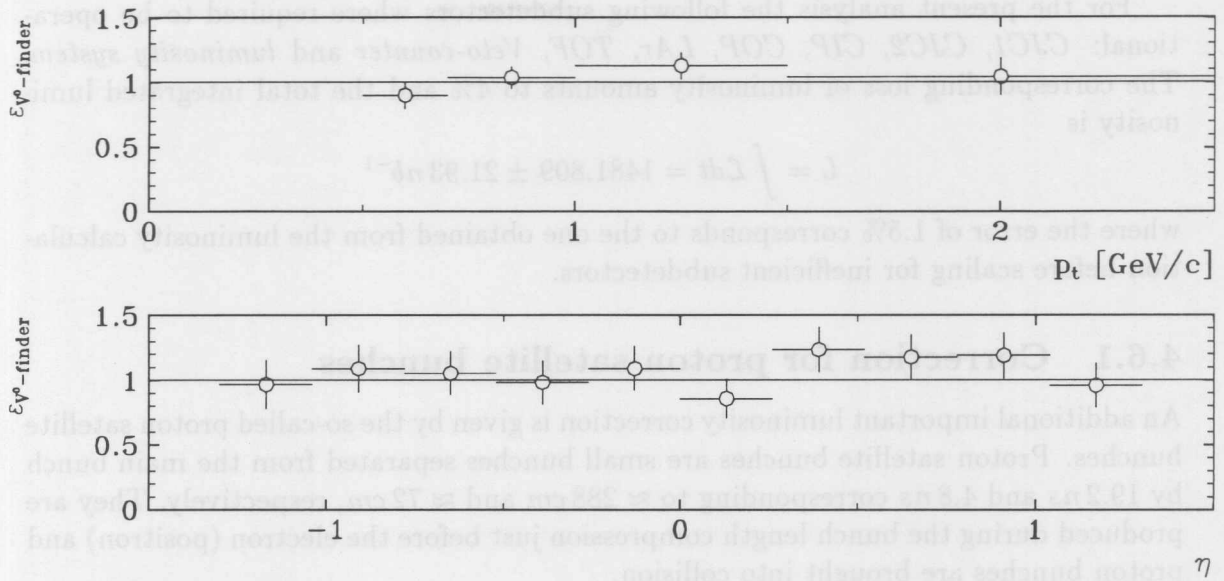


Figure 4.39: The V^0 -finder efficiency $\epsilon_{V^0\text{-finder}}$ both as a function of p_t and η (since there is hardly no statistics in the MC-sample for $p_t > 2.5$, the kinematic range under study is given by $|\eta| < 1.3$ and $0.5 < p_t < 2.5$ GeV/c).

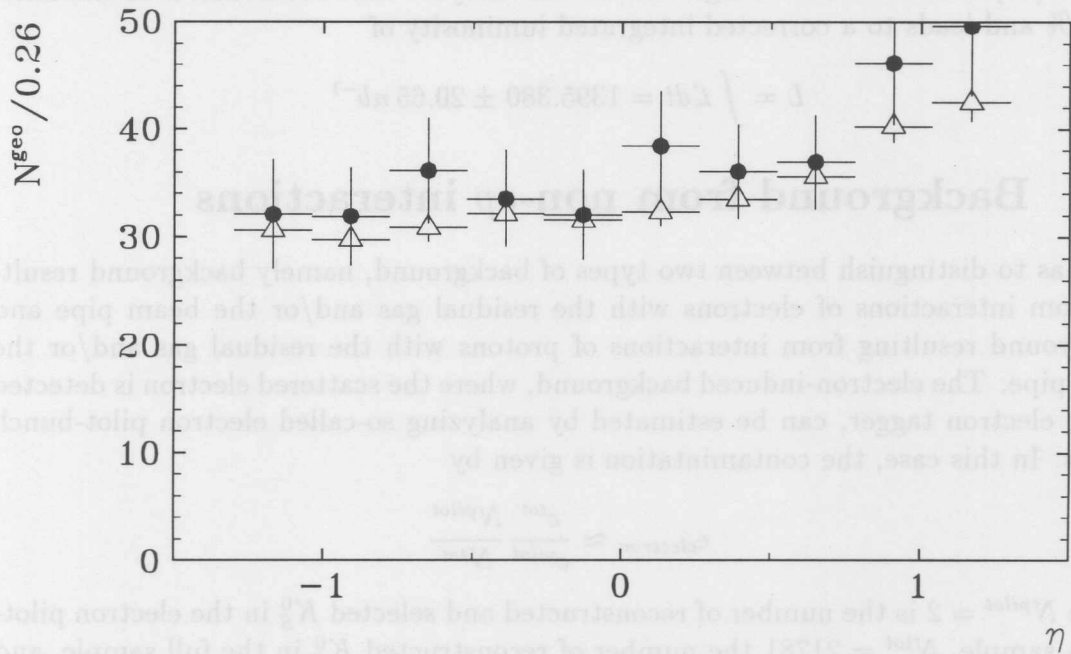


Figure 4.40: Comparison between H1SIM and the geometric model: both η distributions are based on the reduced sample. The first one (●) is corrected with the corresponding efficiency derived from a full simulation of the H1 detector, for the second distribution (△) the corresponding acceptance correction was calculated using the geometric model.

For the present analysis the following subdetectors were required to be operational: *CJC1*, *CJC2*, *CIP*, *COP*, *LAr*, *TOF*, *Veto-counter* and *luminosity system*. The corresponding loss of luminosity amounts to 4% and the total integrated luminosity is

$$L = \int \mathcal{L} dt = 1481.809 \pm 21.93 \text{ nb}^{-1}$$

where the error of 1.5% corresponds to the one obtained from the luminosity calculation before scaling for inefficient subdetectors.

4.6.1 Correction for proton satellite bunches

An additional important luminosity correction is given by the so-called proton satellite bunches. Proton satellite bunches are small bunches separated from the main bunch by 19.2 ns and 4.8 ns corresponding to $\approx 288 \text{ cm}$ and $\approx 72 \text{ cm}$, respectively. They are produced during the bunch length compression just before the electron (positron) and proton bunches are brought into collision.

The necessity for a correction arises from the fact that (bremsstrahlung) events caused by satellite bunches contribute to the luminosity measurement, which is sensitive to all bremsstrahlung events with a z -vertex position of $\pm 5.8 \text{ m}$ around the nominal interaction point (IP), while for physics analysis usually only a restricted region of $\pm 30 \text{ cm}$ around the IP is chosen.

Since the data taking in 1994 it is possible to calculate run-dependent correction factors [57] for the z -vertex range used in the analysis. The correction is of the order of 4.1% and leads to a corrected integrated luminosity of

$$L = \int \mathcal{L} dt = 1395.380 \pm 20.65 \text{ nb}^{-1}$$

4.7 Background from non- ep interactions

One has to distinguish between two types of background, namely background resulting from interactions of electrons with the residual gas and/or the beam pipe and background resulting from interactions of protons with the residual gas and/or the beam pipe. The electron-induced background, where the scattered electron is detected in the electron tagger, can be estimated by analyzing so-called electron pilot-bunch events. In this case, the contamination is given by

$$\epsilon_{\text{electron}} \approx \frac{c^{\text{tot}}}{c^{\text{pilot}}} \frac{N^{\text{pilot}}}{N^{\text{tot}}}$$

where $N^{\text{pilot}} = 2$ is the number of reconstructed and selected K_S^0 in the electron pilot-bunch sample, $N^{\text{tot}} = 21781$ the number of reconstructed K_S^0 in the full sample, and c^{tot} and c^{pilot} the corresponding currents in all and the non-colliding bunches. Since the ratios between the current in the non-colliding bunches and the total current were ≈ 12 for the entire run period, $\epsilon_{\text{electron}}$ is estimated to be $\approx 0.11\%$. This value is consistent with the result of $0.21 \pm 0.02\%$ of an independent study performed on the whole sample (CLASS19 triggered by tr83) [58]; thus, this kind of background can be neglected.

For proton-induced background the situation is somewhat different. Since this analysis is restricted to events with a scattered electron detected in the electron tagger,

version	btc		K_S^0 selection				
	p_t [GeV/c]	η	r_d^{low} [cm]	r_d^{up} [cm]	p_{\perp} [GeV/c]	Ψ^{low} [degree]	Ψ^{up} [degree]
0.	0.18	1.5	2.0	18.0	0.12	70.	110.
1	0.15						
2	0.2						
3		1.75					
4			1.5				
5			3.0				
6				15.0			
7				20.0			
8					0.14		
9						80.	100.
10						65.	115.
11	use of the alternative trigger efficiency function ϵ_{tr83}^1						

Table 4.4: Variation of cuts to study systematic effects: the first row corresponds to the final settings, in the rows below the changed parameters are given; the corresponding plots showing the effects on the actual invariant mass distribution of the K_S^0 candidates can be found in section 4.5.2 and 4.5.3 (btc: basic track selection).

the background cannot be estimated from the analysis of proton pilot-bunch events (by definition proton pilot-bunches do not have colliding partners!). Therefore, the proton-induced background was estimated by analyzing an independent reference trigger (tr86=ETAG) and was found to be of the order of $2.2 \pm 0.5\%$ [58].

4.8 Systematic uncertainties

In this section, special emphasis is put on the study of systematic uncertainties introduced by the K_S^0 selection (see section 4.5.3, 4.5.6) and some basic track cuts (section 4.4.2). At the end, a summary on the corrections applied is given.

4.8.1 Systematic uncertainties related to the K_S^0 selection

To study the systematic uncertainties introduced by the K_S^0 selection, all cuts applied have been varied within reasonable limits (see table 4.4). Then, after applying the corresponding (η, p_t) -dependent corrections from the geometric model and the additional corrections like trigger/ETAG-efficiency, luminosity, etc., the η -, p_t - and y_{rap} -dependent cross sections were calculated. They are defined as follows:

$$\begin{aligned} \frac{d\sigma}{d\eta} &= \frac{1}{L} \frac{dN_{K_S^0}^*}{d\eta} && \text{for various } p_t \text{ ranges} \\ \frac{d^2\sigma}{dp_t^2 d\eta} &= \frac{1}{L} \frac{1}{2p_t} \frac{1}{d\eta} \frac{dN_{K_S^0}^*}{dp_t} && \text{for } |\eta| < 1.3, \Delta\eta = 2.6 \\ \frac{d\sigma}{dy_{rap}} &= \frac{1}{L} \frac{dN_{K_S^0}^*}{dy_{rap}} && \text{for } 0.5 < p_t < 5.0 \text{ GeV}/c \end{aligned}$$

with L being the integrated luminosity and $N_{K_S^0}^*$ the corrected number of reconstructed K_S^0 . The final results are summarized in table 4.6 and 4.7; from the overall deviation of the η - and p_t -dependent cross sections the systematic uncertainty is estimated to be of the order of 10%. The standard parameterization used for the trigger efficiency is given by ϵ_{tr83}^2 (see section 4.3), the results by applying ϵ_{tr83}^1 are also included in the aforementioned tables.

4.8.2 Summary of systematic uncertainties

Table 4.5 summarizes all corrections applied during the present analysis together with the systematic uncertainties. Adding all contributions in quadrature, the overall systematic uncertainty is estimated to be of the order of 10%.

comment	method	efficiency	syst. uncertainty [%]
luminosity	offline calculation	1395.38 nb^{-1}	2.5
ETAG-acceptance	offline calculation (y dependent)	$0.2 < \epsilon < 0.78$	(see luminosity)
L1: tr83	reference trigger (tr90) (p_t dependent)	$0.83 < \epsilon < 0.95$	6.0
L4/L5: event selection	<i>reject</i> files	1.00	2.0
single track reconstruction	visual scan	0.98	2.0
geometric acceptance (and selection cuts)	geometric model (p_t dependent)	$0.07 < \epsilon < 0.14$	4.0
V^0 finder	comparison to H1SIM	1.00	5.0
background from non- ep interactions	pilot-bunch events	-	2.5

Table 4.5: Summary of corrections and systematic uncertainties.

version	p_t -ranges [GeV/c]				
	0.5 – 0.6	0.6 – 0.7	0.7 – 0.8	0.8 – 0.9	0.9 – 1.0
0	142.52 ± 6.37	96.95 ± 3.91	65.55 ± 2.67	46.07 ± 1.91	30.43 ± 1.38
1	138.73 ± 5.92	95.04 ± 3.73	66.34 ± 2.57	46.01 ± 1.85	29.97 ± 1.36
2	142.99 ± 6.77	95.40 ± 4.02	64.74 ± 2.73	45.42 ± 1.95	30.83 ± 1.42
3	138.57 ± 6.11	94.83 ± 3.78	64.82 ± 2.57	46.80 ± 1.86	30.28 ± 1.31
4	136.39 ± 5.98	91.74 ± 3.79	62.03 ± 2.60	44.78 ± 1.92	30.68 ± 1.43
5	138.43 ± 7.18	92.50 ± 4.18	66.30 ± 2.99	43.06 ± 1.92	30.59 ± 1.54
6	142.32 ± 6.37	96.97 ± 3.95	65.35 ± 2.69	46.41 ± 1.94	30.35 ± 1.40
7	141.67 ± 6.31	96.25 ± 3.89	64.96 ± 2.64	46.02 ± 1.90	30.53 ± 1.37
8	144.47 ± 6.33	97.87 ± 3.89	66.09 ± 2.79	47.37 ± 1.92	31.42 ± 1.45
9	137.52 ± 6.55	90.99 ± 3.95	64.94 ± 2.78	45.77 ± 2.04	30.87 ± 1.47
10	138.54 ± 6.24	96.50 ± 3.84	65.44 ± 2.68	46.24 ± 1.95	29.92 ± 1.38
11	141.27 ± 6.31	97.60 ± 3.95	66.48 ± 2.71	46.82 ± 1.94	30.89 ± 1.40

Table 4.6: $d\sigma/dp_t^2 d\eta$ for various K_S^0 -selection cuts.

version	η -ranges				
	-1.30 – -1.04	-1.04 – -0.78	-0.78 – -0.52	-0.52 – -0.26	-0.26 – 0.0
0	67.35 ± 3.53	68.56 ± 3.48	66.89 ± 3.26	72.75 ± 3.70	65.43 ± 3.17
1	68.00 ± 3.38	69.94 ± 3.41	66.71 ± 3.09	72.55 ± 3.61	66.38 ± 3.16
2	67.00 ± 3.61	65.92 ± 3.62	66.82 ± 3.38	72.66 ± 3.62	64.86 ± 3.28
3	69.53 ± 3.18	68.40 ± 3.49	66.49 ± 3.23	72.69 ± 3.64	65.14 ± 3.16
4	64.88 ± 3.42	67.20 ± 3.40	64.69 ± 3.11	70.07 ± 3.50	67.62 ± 3.24
5	67.18 ± 4.00	66.50 ± 3.58	65.67 ± 3.59	68.63 ± 4.03	63.18 ± 3.58
6	67.01 ± 3.57	66.68 ± 3.53	66.82 ± 3.29	72.58 ± 3.72	64.65 ± 3.16
7	67.39 ± 3.52	67.07 ± 3.47	65.94 ± 3.20	72.19 ± 3.64	65.70 ± 3.16
8	69.00 ± 3.62	68.37 ± 3.50	67.62 ± 3.28	74.72 ± 3.73	64.86 ± 3.17
9	65.84 ± 3.69	68.92 ± 3.78	65.58 ± 3.39	69.01 ± 3.36	66.83 ± 3.28
10	67.36 ± 3.58	65.93 ± 3.22	67.55 ± 3.27	69.39 ± 3.56	62.76 ± 3.20
11	67.55 ± 3.53	67.40 ± 3.50	67.12 ± 3.27	72.87 ± 3.70	65.40 ± 3.17

Table 4.7: $d\sigma/d\eta$ for various K_S^0 -selection cuts.

p_t -ranges [GeV/c]					
1.0 – 1.2	1.2 – 1.4	1.4 – 1.8	1.8 – 2.2	2.2 – 3.0	3.0 – 5.0
19.86 ± 0.71	10.26 ± 0.43	3.881 ± 0.165	1.448 ± 0.102	0.3377 ± 0.0300	0.0376 ± 0.0043
19.88 ± 0.70	10.12 ± 0.43	3.906 ± 0.166	1.462 ± 0.101	0.3375 ± 0.0300	0.0376 ± 0.0043
19.90 ± 0.73	10.10 ± 0.43	3.892 ± 0.166	1.448 ± 0.102	0.3375 ± 0.2300	0.0376 ± 0.0043
19.78 ± 0.69	10.18 ± 0.42	3.856 ± 0.163	1.468 ± 0.102	0.3366 ± 0.0299	0.0375 ± 0.0042
20.01 ± 0.75	10.14 ± 0.44	3.961 ± 0.178	1.541 ± 0.114	0.3579 ± 0.0309	0.0366 ± 0.0042
19.99 ± 0.75	9.73 ± 0.45	3.921 ± 0.179	1.383 ± 0.104	0.3364 ± 0.0319	0.0345 ± 0.0043
19.75 ± 0.72	10.26 ± 0.45	3.801 ± 0.168	1.429 ± 0.107	0.3300 ± 0.0318	0.0336 ± 0.0042
19.72 ± 0.70	10.25 ± 0.34	3.856 ± 0.162	1.441 ± 0.107	0.3340 ± 0.0285	0.0282 ± 0.0041
20.12 ± 0.73	10.15 ± 0.46	3.941 ± 0.175	1.416 ± 0.102	0.3340 ± 0.0319	0.0267 ± 0.0040
20.05 ± 0.73	10.12 ± 0.46	3.736 ± 0.172	1.532 ± 0.104	0.3709 ± 0.0299	0.0390 ± 0.0042
19.76 ± 0.71	10.24 ± 0.44	3.784 ± 0.167	1.420 ± 0.106	0.3167 ± 0.0290	0.0272 ± 0.0047
20.06 ± 0.71	10.27 ± 0.44	3.834 ± 0.163	1.409 ± 0.100	0.3236 ± 0.0288	0.0354 ± 0.0040

$d\sigma/dp_t^2 d\eta$ (cont.)

η -ranges				
0.0 – 0.26	0.26 – 0.52	0.52 – 0.78	0.78 – 1.04	1.04 – 1.30
72.28 ± 3.36	70.01 ± 3.33	78.33 ± 3.55	91.01 ± 3.95	90.20 ± 4.06
72.67 ± 3.25	70.12 ± 3.30	78.38 ± 3.36	88.17 ± 3.71	85.77 ± 3.81
72.97 ± 3.52	70.79 ± 3.44	78.42 ± 3.70	89.17 ± 4.07	89.16 ± 4.20
72.29 ± 3.37	71.09 ± 3.37	78.00 ± 3.53	87.32 ± 3.73	87.11 ± 3.70
69.72 ± 3.30	67.43 ± 3.19	77.72 ± 3.44	85.32 ± 3.82	88.10 ± 4.14
72.49 ± 3.76	67.67 ± 3.64	78.69 ± 3.84	91.58 ± 4.44	85.63 ± 4.20
72.57 ± 3.44	71.39 ± 3.44	77.81 ± 3.57	88.38 ± 3.91	88.78 ± 4.04
73.91 ± 3.39	70.92 ± 3.35	78.22 ± 3.54	88.61 ± 3.84	87.96 ± 3.95
72.37 ± 3.40	72.05 ± 3.41	79.47 ± 3.58	89.40 ± 3.91	92.04 ± 3.93
70.81 ± 3.45	66.76 ± 3.41	83.18 ± 3.77	89.00 ± 4.17	84.10 ± 4.29
70.98 ± 3.37	70.10 ± 3.43	77.37 ± 3.50	90.91 ± 3.88	89.10 ± 3.93
72.56 ± 3.36	70.11 ± 3.33	78.55 ± 3.56	91.25 ± 3.95	90.36 ± 4.06

$d\sigma/d\eta$ (cont.)

4.9 Fully corrected cross sections

In the following sections the results of the cross section measurements are summarized; unless stated otherwise, all results correspond to K^0 production, that is $2K_S^0$. In addition to the results shown in section 4.8, the p_t dependence of $d\sigma/d\eta$ is presented for four different ranges of p_t .

To allow a more direct comparison to other processes, e.g. deep inelastic scattering, a Lorentz transformation into the center of mass of the γp system has been performed, yielding the cross sections as functions of p_t and y_{rap}^* ; since the γp system moves collinearly to the z axis, the transverse momentum is not affected by the Lorentz transformation. The variable y_{rap} (see eq. 2.7) in the laboratory frame is related to y_{rap}^* by

$$y_{rap}^* = y_{rap} - \ln(\gamma_{\gamma p} + \gamma_{\gamma p}\beta_{\gamma p}) \quad (4.2)$$

with

$$\gamma_{\gamma p} = \frac{E_{\gamma p}}{M_{\gamma p}} = \frac{E_p + E_\gamma}{W} = \frac{E_p + yE_e}{2\sqrt{yE_eE_p}}$$

and

$$\beta_{\gamma p} = \frac{p_{\gamma p}}{E_{\gamma p}} = \frac{E_p - E_\gamma}{E_p + E_\gamma} = \frac{E_p - yE_e}{E_p + yE_e}.$$

On average, a transformation into the center-of-mass system is equivalent to shifting the y_{rap} distribution by ≈ -2 (see fig. 4.41). The accessible kinematic range in y^* is, apart from the y -dependent Lorentz boost, determined by the η cut applied in the laboratory frame due to the limited acceptance of the *CJC*. The accessible y^* ranges are shown for various p_t and y in fig. 4.42. It follows that for $-2.8 < y^* < -1.3$, the η cut is ineffective while for y^* outside this region the η cut applied in the laboratory frame causes losses and has to be taken into account. In particular, this has to be kept in mind for any comparison with the cross section $d^2\sigma/dp_t^2 dy^*$ which is given for $-3.2 < y^* < 1.0$ and $|\eta| < 1.3$. Furthermore, these losses are responsible for the decrease of $d\sigma/dy^*$ at around -3 and -1, respectively, as shown in fig. 4.47. To get a cross section which is independent on the η cut one could restrict the y^* range to $-2.8 < y^* < -1.3$.

In addition to the ep cross sections, the photoproduction cross sections are given. They are related to each other by the flux factor $F(y, Q^2)$ (see section 1.2) and for the kinematic range under study, the flux factor is given by $F(y, Q^2) = 0.0136$. The total K^0 cross section integrated over the full kinematic range under study is given in table 4.8.

kinematic range	K^0 cross section [nb]	
	ep	γp
$0.5 < p_t < 5.0 \text{ GeV}, \eta < 1.3$	389.32 ± 27.26	28626.48 ± 2004.42
$0.5 < p_t < 5.0 \text{ GeV}, \eta < 1.3, -3.2 < y_{rap}^* < -1$	356.62 ± 24.96	26222.06 ± 1834.92

Table 4.8: The total K^0 cross section.

The errors quoted in the following tables are the statistical errors only, the overall systematic uncertainty is of the order of 10% (see section 4.8.2).

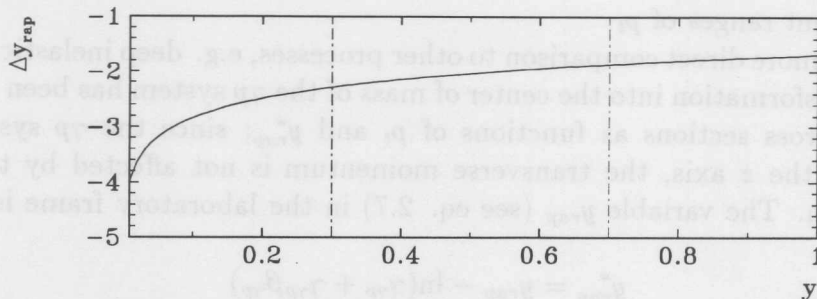


Figure 4.41: The shift $\Delta y_{rap} = y_{rap}^* - y_{rap}$ of the rapidity distributions as a function of the scaling variable y .

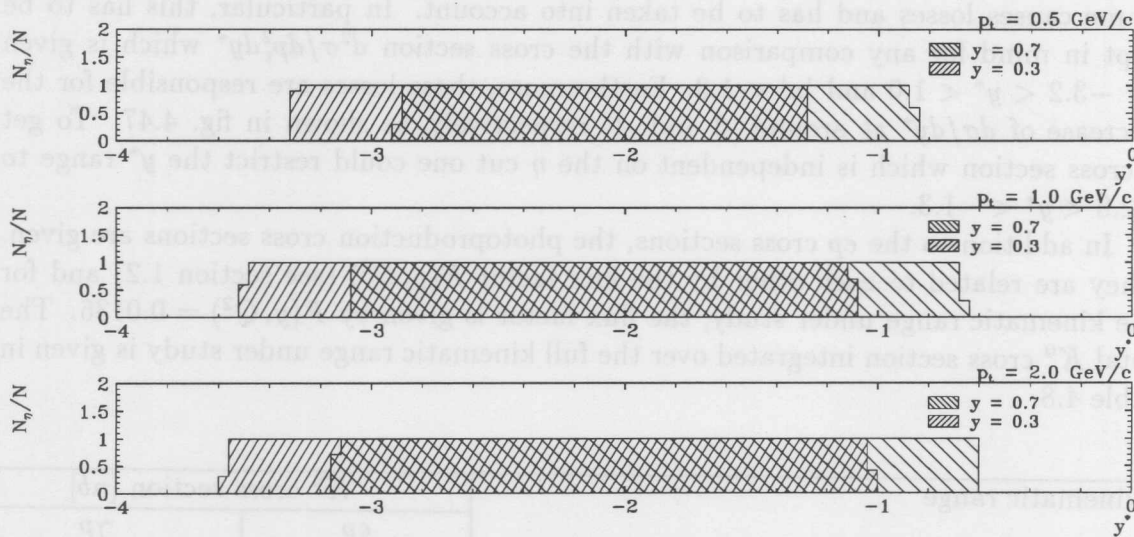
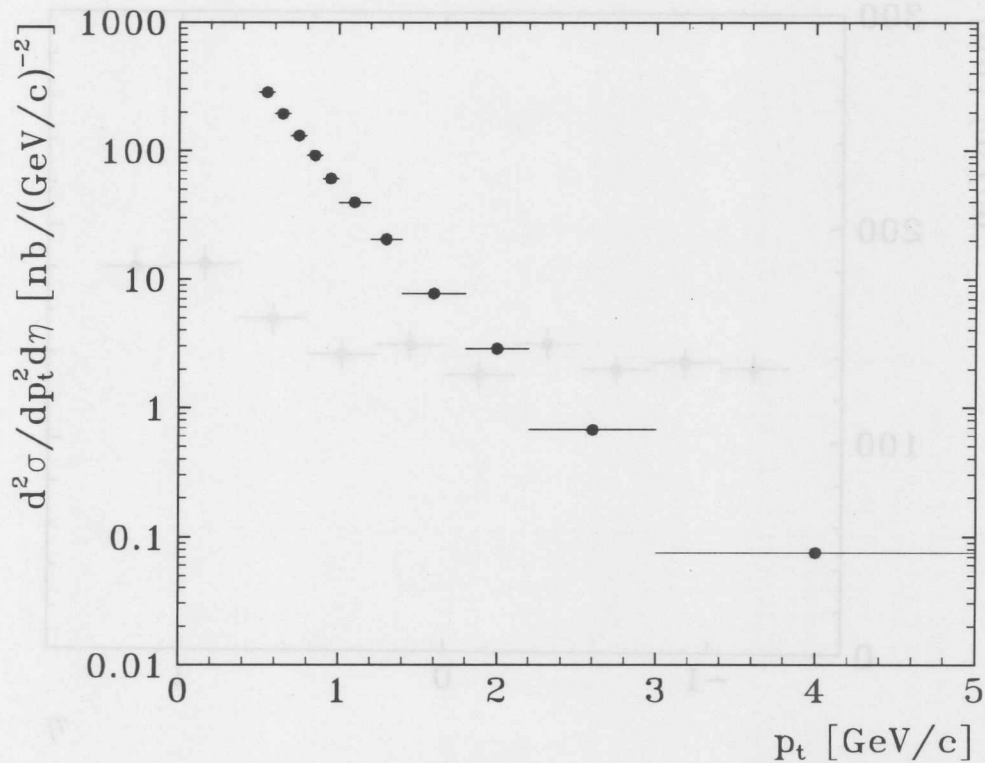


Figure 4.42: The impact of an η cut of $|\eta| < 1.3$ on the accessible y^* range in the center of mass of the γp system.

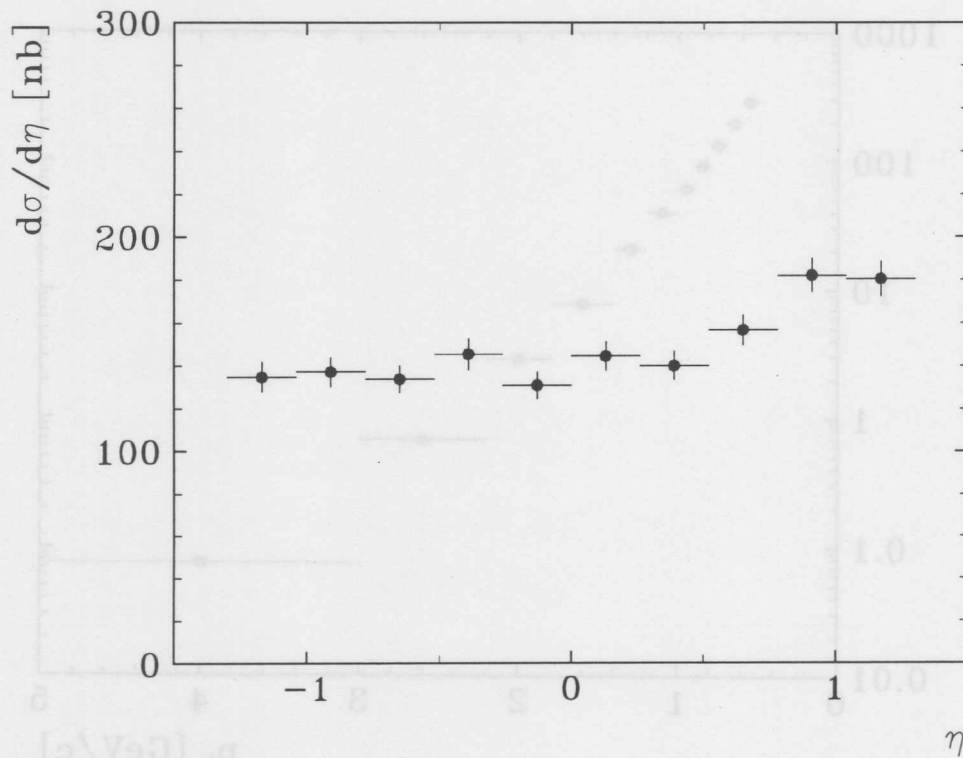
4.9.1 $d^2\sigma/dp_t^2 d\eta$ for $|\eta| < 1.3$

p_t range [GeV/c]	ep		γp	
	$\frac{d^2\sigma}{dp_t^2 d\eta} [\text{nb}/(\text{GeV}/c)^2]$		$\frac{d^2\sigma}{dp_t^2 d\eta} [\text{nb}/(\text{GeV}/c)^2]$	
0.5 – 0.6	285.04	± 12.74	20959.60	± 936.80
0.6 – 0.7	193.30	± 7.82	14213.80	± 575.00
0.7 – 0.8	131.10	± 5.34	9640.20	± 392.60
0.8 – 0.9	92.14	± 3.82	6779.20	± 281.00
0.9 – 1.0	60.86	± 2.76	4475.20	± 203.00
1.0 – 1.2	39.72	± 1.42	2894.20	± 104.40
1.2 – 1.4	20.52	± 0.86	1508.80	± 63.20
1.4 – 1.8	7.76	± 0.33	570.80	± 24.20
1.8 – 2.2	2.90	± 0.20	213.00	± 15.00
2.2 – 3.0	0.68	± 0.06	49.66	± 4.42
3.0 – 5.0	0.075	± 0.009	5.58	± 0.64

Table 4.9: $d^2\sigma/dp_t^2 d\eta$ for $|\eta| < 1.3$.Figure 4.43: $d^2\sigma/dp_t^2 d\eta$ for $|\eta| < 1.3$.

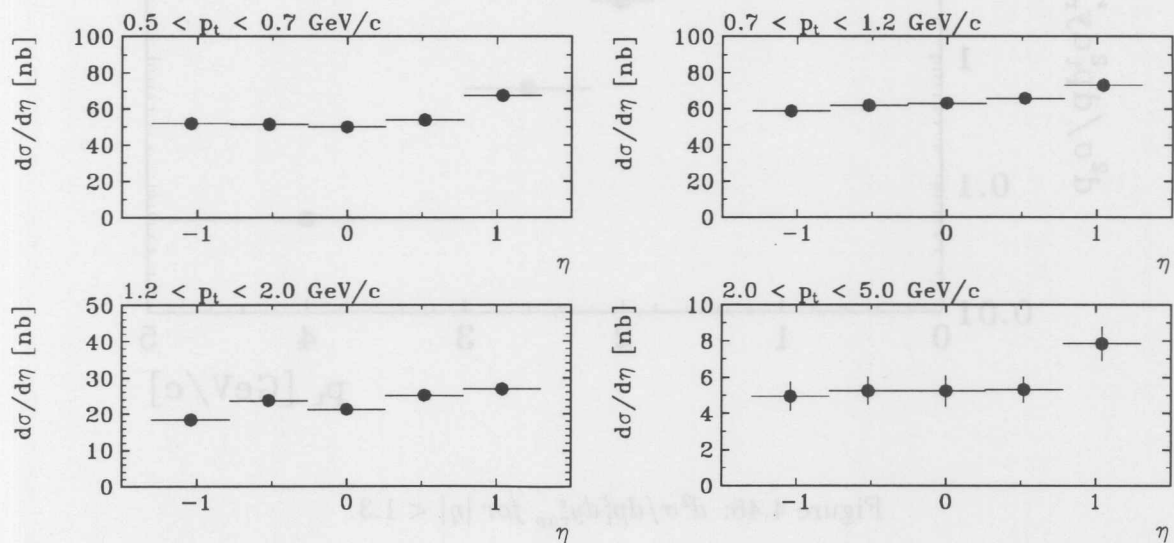
4.9.2 $d\sigma/d\eta$ for $0.5 < p_t < 5.0 \text{ GeV}/c$

η range			ep		γp	
			$\frac{d\sigma}{d\eta} [\text{nb}]$		$\frac{d\sigma}{d\eta} [\text{nb}]$	
-1.30	—	-1.04	134.70	\pm 7.06	9904.80	\pm 519.20
-1.04	—	-0.78	137.12	\pm 6.96	10082.80	\pm 511.80
-0.78	—	-0.52	133.78	\pm 6.52	9957.20	\pm 479.40
-0.52	—	-0.26	145.50	\pm 7.40	10759.00	\pm 544.20
-0.26	—	0.00	130.86	\pm 6.34	9622.40	\pm 466.20
0.00	—	0.26	144.56	\pm 6.72	10629.80	\pm 548.20
0.26	—	0.52	140.02	\pm 6.66	10296.00	\pm 489.80
0.52	—	0.78	156.66	\pm 7.10	11519.60	\pm 522.00
0.78	—	1.04	182.02	\pm 7.90	13384.40	\pm 581.00
1.04	—	1.30	180.40	\pm 8.12	13265.20	\pm 597.00

Table 4.10: $d\sigma/d\eta$ for $0.5 < p_t < 5.0 \text{ GeV}/c$.Figure 4.44: $d\sigma/d\eta$ for $0.5 < p_t < 5.0 \text{ GeV}/c$.

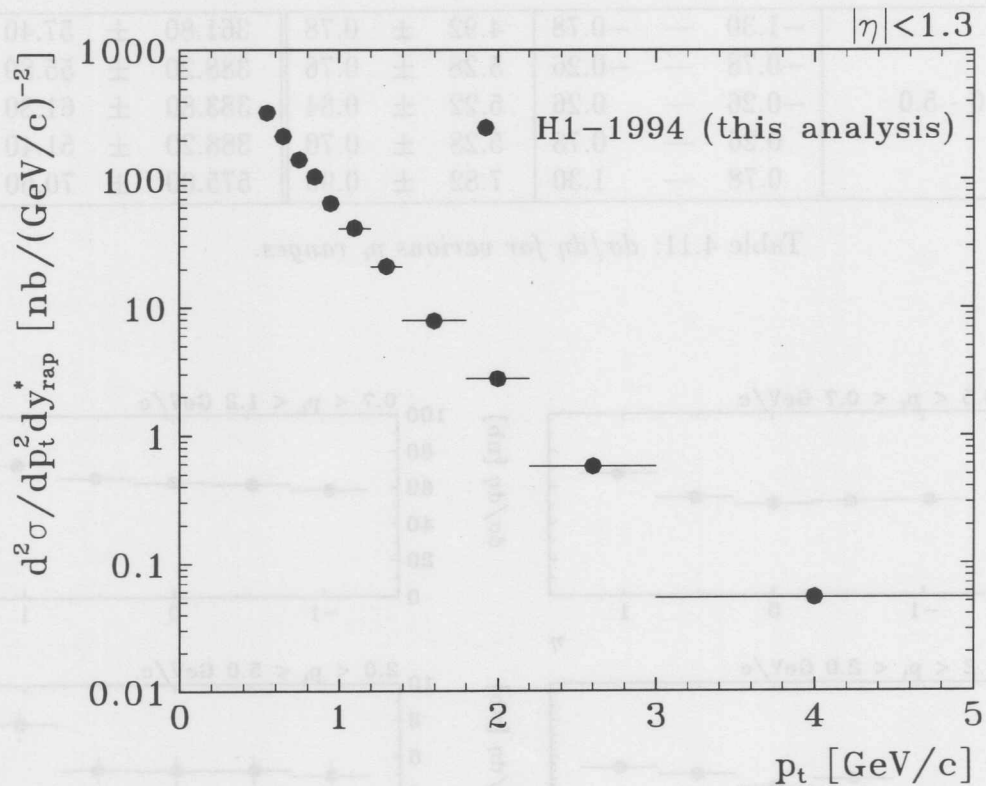
4.9.3 $d\sigma/d\eta$ for various p_t ranges

p_t range [GeV/c]	η range	ep		γp	
		$d\sigma/d\eta$ [nb]		$\frac{d\sigma}{d\eta}$ [nb]	
0.5 - 0.7	-1.30 — -0.78	51.68	± 4.08	3800.20	± 300.00
	-0.78 — -0.26	51.04	± 4.10	3753.20	± 301.40
	-0.26 — 0.26	49.82	± 3.62	3663.40	± 398.20
	0.26 — 0.78	53.48	± 3.90	3932.60	± 286.80
	0.78 — 1.30	67.18	± 4.46	4940.00	± 328.00
0.7 - 1.2	-1.30 — -0.78	58.54	± 2.92	4304.60	± 214.80
	-0.78 — -0.26	61.68	± 2.90	4535.40	± 213.20
	-0.26 — 0.26	62.94	± 2.96	4628.20	± 217.60
	0.26 — 0.78	65.92	± 3.04	4847.20	± 223.60
	0.78 — 1.30	72.98	± 3.28	5366.40	± 241.20
1.2 - 2.0	-1.30 — -0.78	18.24	± 1.38	1341.20	± 101.40
	-0.78 — -0.26	23.64	± 1.56	1738.40	± 114.80
	-0.26 — 0.26	21.14	± 1.40	1554.40	± 103.00
	0.26 — 0.78	25.08	± 1.54	1844.20	± 113.20
	0.78 — 1.30	26.98	± 1.74	1984.00	± 128.00
2.0 - 5.0	-1.30 — -0.78	4.92	± 0.78	361.80	± 57.40
	-0.78 — -0.26	5.28	± 0.76	388.20	± 55.80
	-0.26 — 0.26	5.22	± 0.84	383.80	± 61.80
	0.26 — 0.78	5.28	± 0.70	388.20	± 51.40
	0.78 — 1.30	7.82	± 0.96	575.00	± 70.60

Table 4.11: $d\sigma/d\eta$ for various p_t ranges.Figure 4.45: $d\sigma/d\eta$ for various p_t ranges.

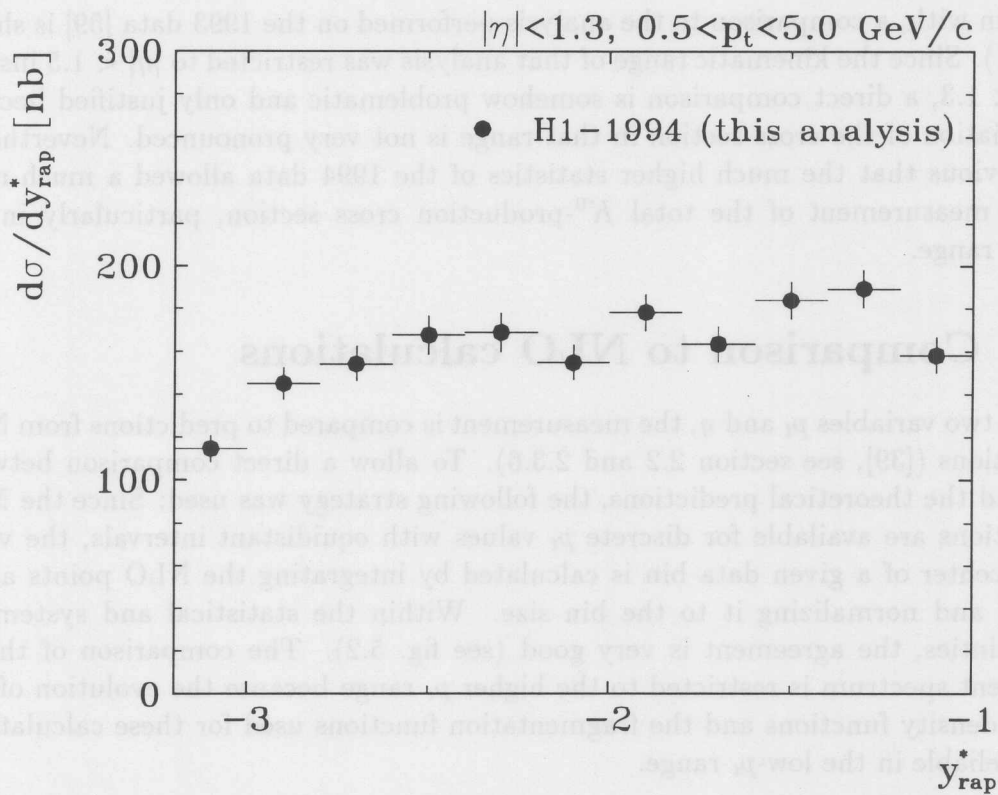
4.9.4 $d^2\sigma/dp_t^2 dy_{rap}^*$ for $|\eta| < 1.3$

p_t range [GeV/c]	ep		γp	
	$\frac{d^2\sigma}{dp_t^2 dy_{rap}^*} [\text{nb}/(\text{GeV}/c)^2]$		$\frac{d^2\sigma}{dp_t^2 dy_{rap}^*} [\text{nb}/(\text{GeV}/c)^2]$	
0.5 – 0.6	327.97	± 14.64	24116.80	± 1076.60
0.6 – 0.7	215.64	± 8.72	15856.60	± 641.00
0.7 – 0.8	142.06	± 5.92	10446.40	± 435.00
0.8 – 0.9	104.31	± 4.28	7670.40	± 314.80
0.9 – 1.0	64.94	± 3.02	4775.00	± 222.20
1.0 – 0.2	41.81	± 1.56	3074.60	± 114.80
1.2 – 1.4	20.94	± 0.93	1539.60	± 68.40
1.4 – 1.8	7.90	± 0.35	579.40	± 25.80
1.8 – 2.2	2.77	± 0.20	203.60	± 14.80
2.2 – 3.0	0.58	± 0.06	42.50	± 4.26
3.0 – 5.0	0.054	± 0.007	3.98	± 0.52

Table 4.12: $d^2\sigma/dp_t^2 dy_{rap}^*$ for $|\eta| < 1.3$ Figure 4.46: $d^2\sigma/dp_t^2 dy_{rap}^*$ for $|\eta| < 1.3$.

4.9.5 $d\sigma/dy_{rap}^*$ for $0.5 < p_t < 5.0 \text{ GeV}/c$ and $|\eta| < 1.3$

y_{rap}^* range	ep		γp	
	$d\sigma/dy_{rap}^* [nb]$		$d\sigma/dy_{rap}^* [nb]$	
-3.20 — -3.00	114.46	± 6.30	8416.60	± 463.20
-3.00 — -2.80	145.02	± 7.64	10663.60	± 561.80
-2.80 — -2.60	154.22	± 8.08	11340.20	± 594.20
-2.60 — -2.40	167.62	± 9.04	12325.60	± 664.80
-2.40 — -2.20	168.92	± 8.92	12421.20	± 656.00
-2.20 — -2.00	154.98	± 8.26	11396.00	± 607.20
-2.00 — -1.80	178.30	± 8.64	13110.80	± 635.40
-1.80 — -1.60	163.52	± 8.28	12024.00	± 608.80
-1.60 — -1.40	183.94	± 8.72	13525.60	± 641.20
-1.40 — -1.20	189.38	± 8.88	13925.60	± 53.00
-1.20 — -1.00	158.26	± 8.28	11637.20	± 608.80

Table 4.13: $d\sigma/dy_{rap}^*$ for $0.5 < p_t < 5.0 \text{ GeV}/c$ and $|\eta| < 1.3$.Figure 4.47: $d\sigma/dy_{rap}^*$ for $0.5 < p_t < 5.0 \text{ GeV}/c$.

Chapter 5

Discussion of results

In this section the results on the differential cross sections are compared both to Monte Carlo predictions and to next-to-leading-order calculations (NLO). In addition, the measurement of the K/π ratio and possible lines of investigation beyond those followed here are discussed.

5.1 Comparison to the 1993 measurement

To begin with, a comparison to the analysis performed on the 1993 data [59] is shown (fig. 5.1). Since the kinematic range of that analysis was restricted to $|\eta| < 1.5$ instead of $|\eta| < 1.3$, a direct comparison is somehow problematic and only justified because the variation of the cross section in that range is not very pronounced. Nevertheless it is obvious that the much higher statistics of the 1994 data allowed a much more precise measurement of the total K^0 -production cross section, particularly in the high- p_t range.

5.2 Comparison to NLO calculations

For the two variables p_t and η , the measurement is compared to predictions from NLO calculations ([39], see section 2.2 and 2.3.6). To allow a direct comparison between data and the theoretical predictions, the following strategy was used: Since the NLO calculations are available for discrete p_t values with equidistant intervals, the value at the center of a given data bin is calculated by integrating the NLO points along the bin and normalizing it to the bin size. Within the statistical and systematic uncertainties, the agreement is very good (see fig. 5.2). The comparison of the η -dependent spectrum is restricted to the higher p_t range because the evolution of the parton density functions and the fragmentation functions used for these calculations is not reliable in the low- p_t range.

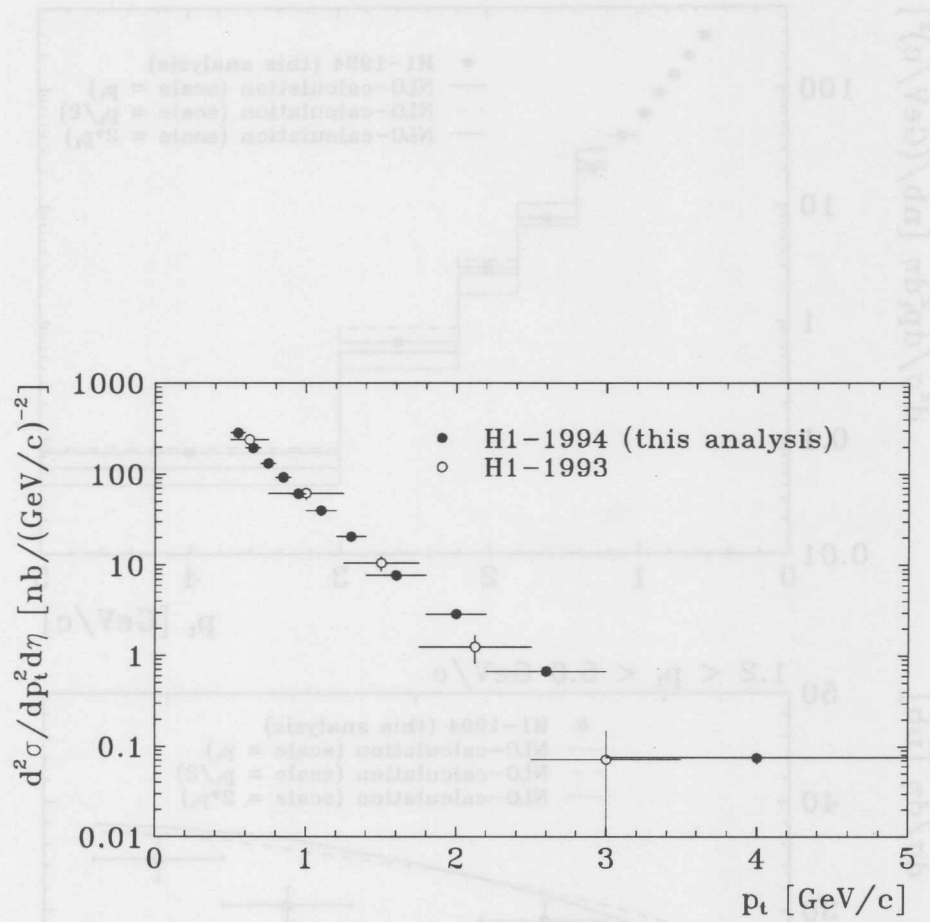


Figure 5.1: Comparison between the 1993 [59] and the 1994 analysis.

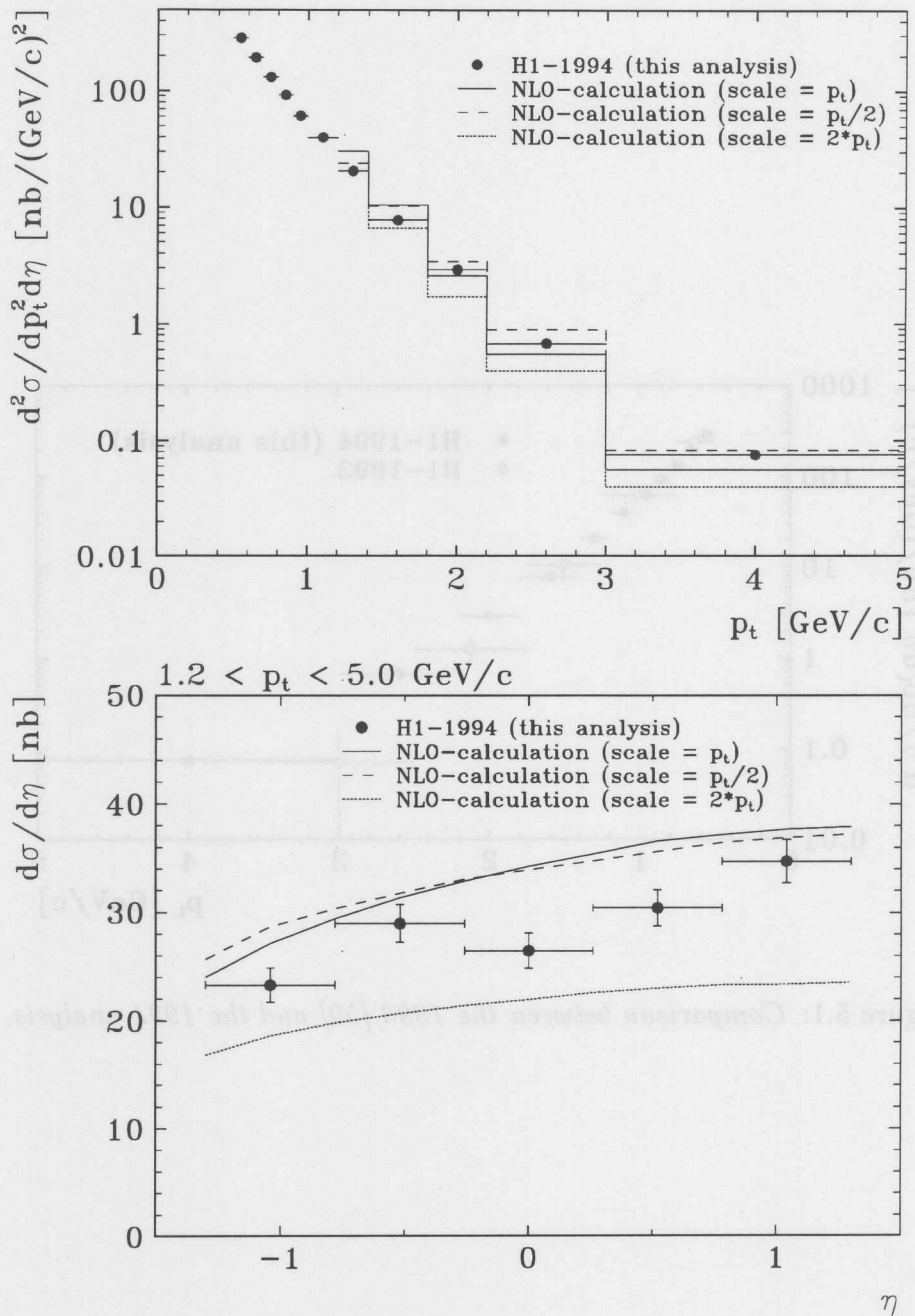


Figure 5.2: Comparison between data and NLO calculation. Top: $d\sigma/d\eta$ for $0.5 < p_t < 5.0 \text{ GeV}/c$, bottom: $d\sigma/d\eta$ for $0.5 < p_t < 5.0 \text{ GeV}/c$.

5.3 Comparison to QCD-based generators

5.3.1 PYTHIA 5.7

To compare the measurements with predictions from PYTHIA 5.7 in combination with JETSET 7.4, three different values of the strangeness suppression factor λ were chosen ($\lambda = 0.0$, $\lambda = 0.2$ and $\lambda = 0.3$). It is observed that the slope of the predicted p_t distribution is slightly different from what is seen in data (see fig. 5.3); the K^0 yield seems to be overestimated in the low- p_t range and slightly underestimated in the high- p_t range, this being valid both for $\lambda = 0.2$ and $\lambda = 0.3$.

The prediction for $\lambda = 0.0$ illustrates that at higher p_t strangeness from other sources than the fragmentation process yields a significant contribution.

The comparison of the η distributions shows that the shape is reasonably reproduced by the PYTHIA prediction; however, there might be a slight discrepancy in the region of large η where the increase of the cross section seems to be more significant in data than in Monte Carlo. It seems that the data favor the lower strangeness suppression factor of $\lambda = 0.2$ but within the statistical and systematic uncertainties $\lambda = 0.3$ is not excluded. In addition one has to keep in mind the conceptual problems related to a determination of λ as discussed in section 2.3.3.

Furthermore, the comparison of the corresponding distributions in the center of mass of the γp system are shown in fig. 5.4. For all comparisons so far, multiple interactions were enabled at the generator level (see section 2.3.2). A scenario without multiple interactions as shown in fig. 5.5 cannot describe the significant increase of the K^0 -production cross section as it is observed in the forward direction. The data seem to be in much better agreement with a model including multiple interactions.

5.3.2 PHOJET

Similar to the previous section, the experimental measurements have been compared with predictions from the PHOJET generator in combination with JETSET (both, for $\lambda = 0.2$ and $\lambda = 0.3$). Though the two generators, PHOJET and PYTHIA, are based on different approaches, their predictions are compatible.

As can be seen from figure fig. 5.6, the K^0 yield seems to be slightly overestimated in the low- p_t range and, in addition, there might be a slight discrepancy in the region of large η between data and the PHOJET prediction. Like in PYTHIA, changing λ leads roughly only to a scaling of the cross section.



Figure 5.3: Comparison between data and PYTHIA prediction including multiple interactions. Top: $d\sigma/dp_t$ for $|\eta| < 1.3$. Bottom: $d\sigma/dp_t$ for $0.5 < \eta < 0.9$ GeV/c.

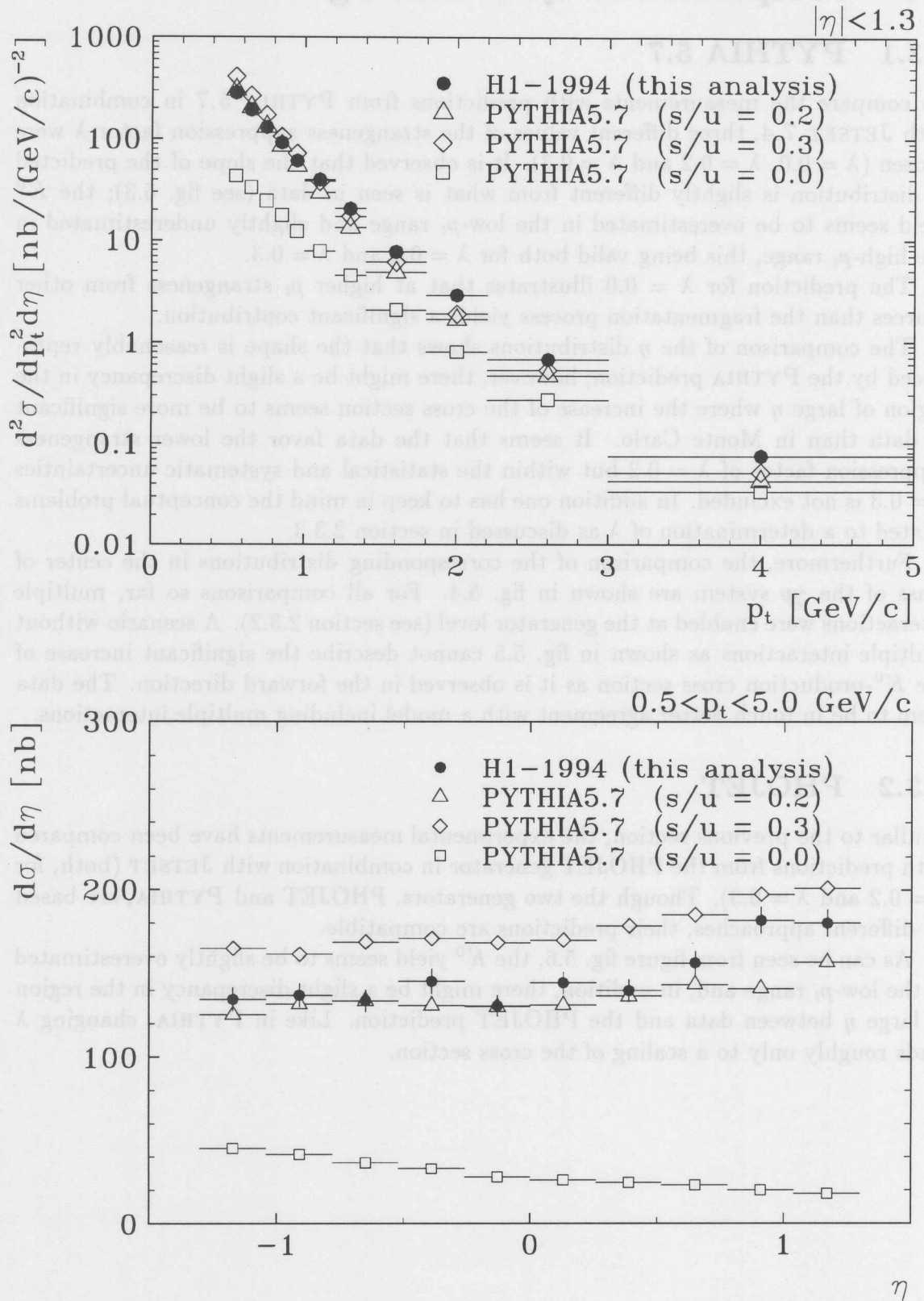


Figure 5.3: Comparison between data and PYTHIA prediction including multiple interactions.

Top: $d^2\sigma/dp_t^2 d\eta$ for $|\eta| < 1.3$,

Bottom: $d\sigma/d\eta$ for $0.5 < p_t < 5.0$ GeV/c.

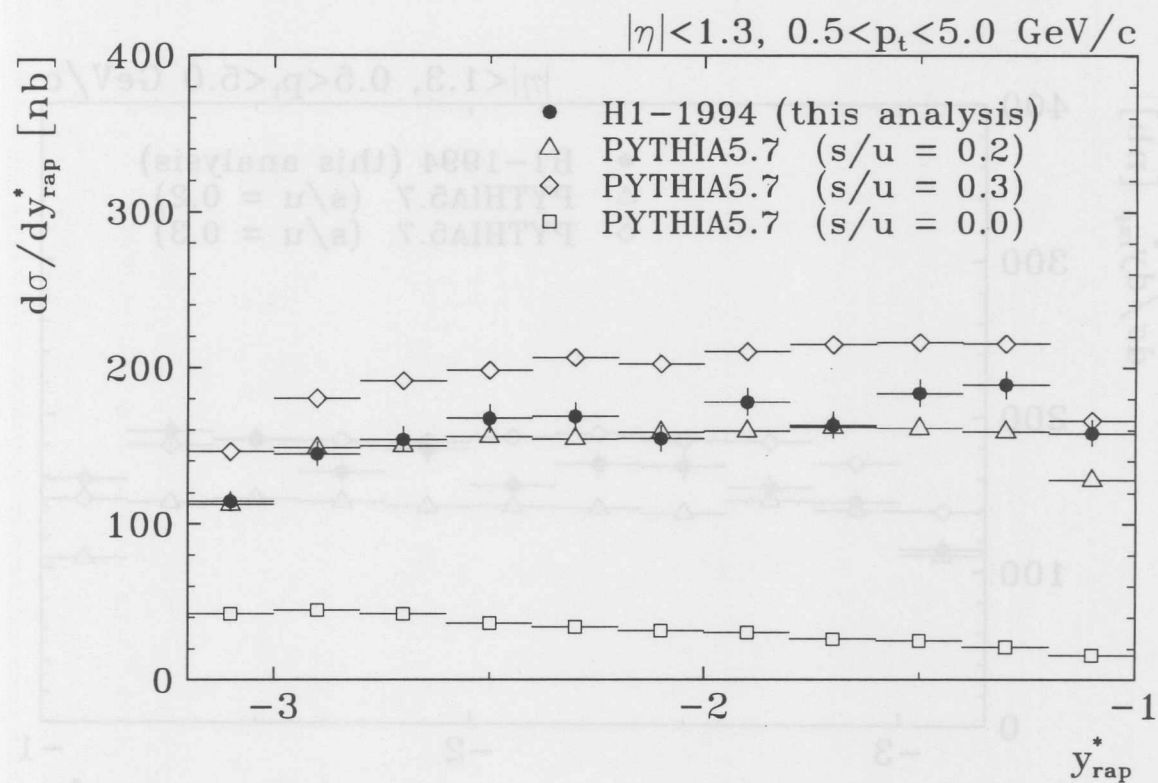
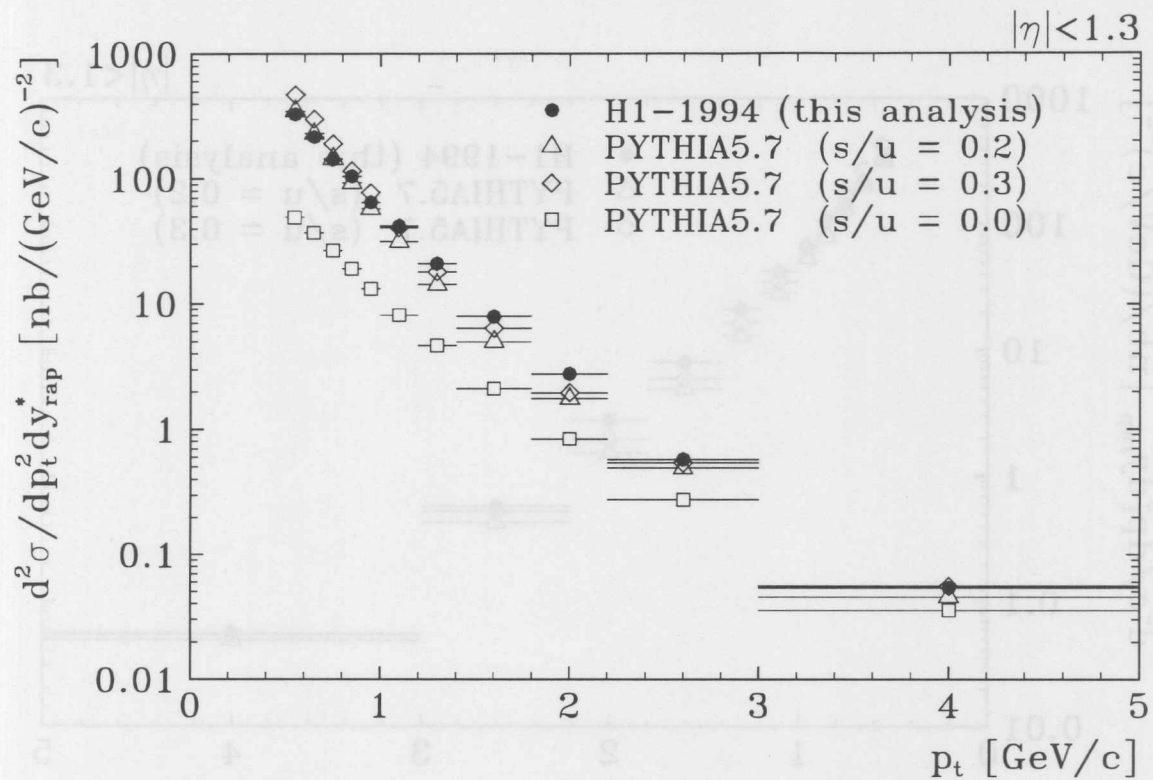


Figure 5.4: Comparison between data and PYTHIA prediction including multiple interactions.

Top: $d^2\sigma/dp_t^2 dy^*$ for $|\eta| < 1.3$

Bottom: $d\sigma/dy^*$ for $|\eta| < 1.3$ and $0.5 < p_t < 5.0 \text{ GeV/c}$.

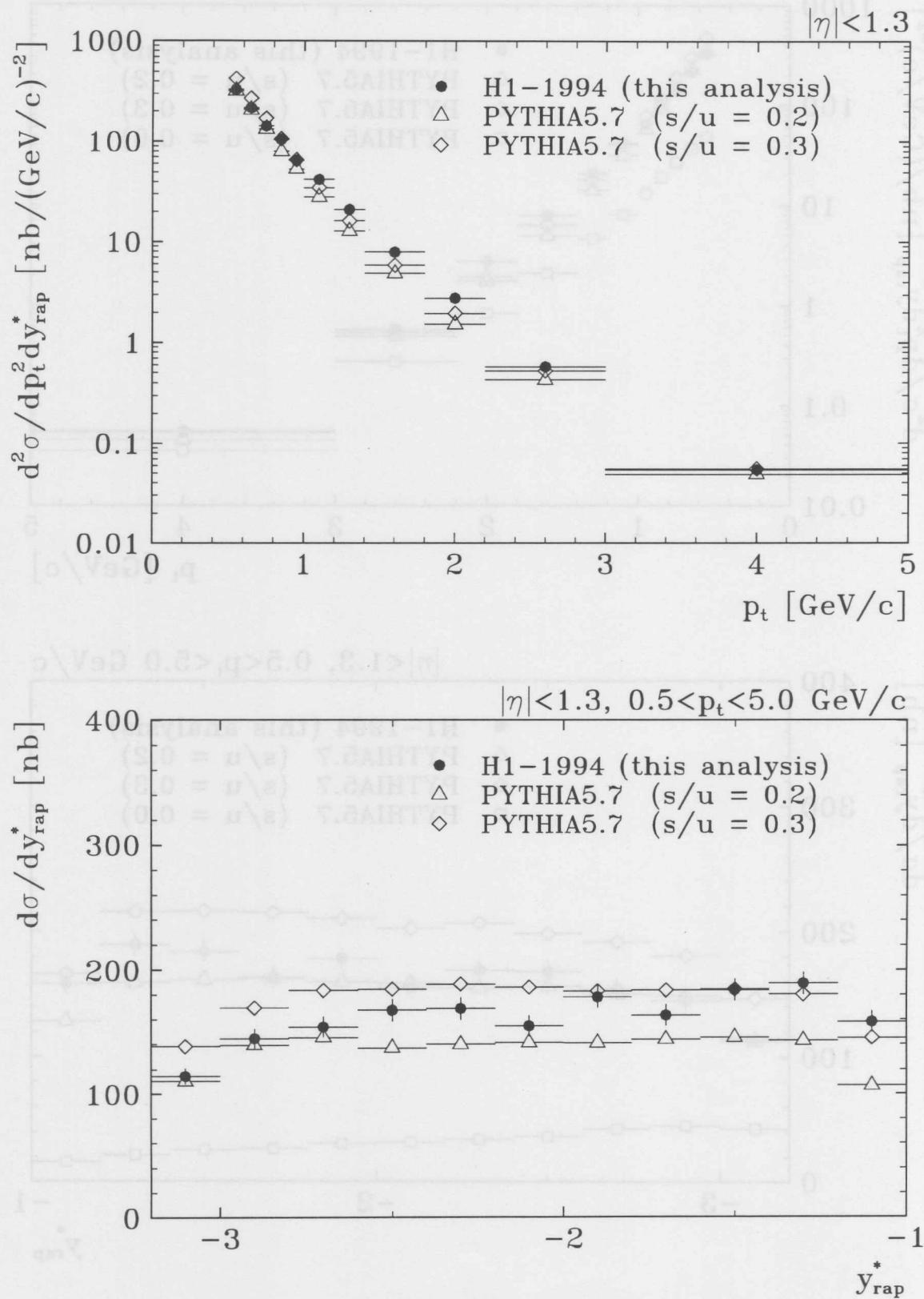


Figure 5.5: Comparison between data and PYTHIA without multiple interactions.

Top: $d^2\sigma/dp_t^2 dy_{rap}^*$ for $|\eta| < 1.3$ Bottom: $d\sigma/dy_{rap}^*$ for $|\eta| < 1.3$ and $0.5 < p_t < 5.0 \text{ GeV}/c$

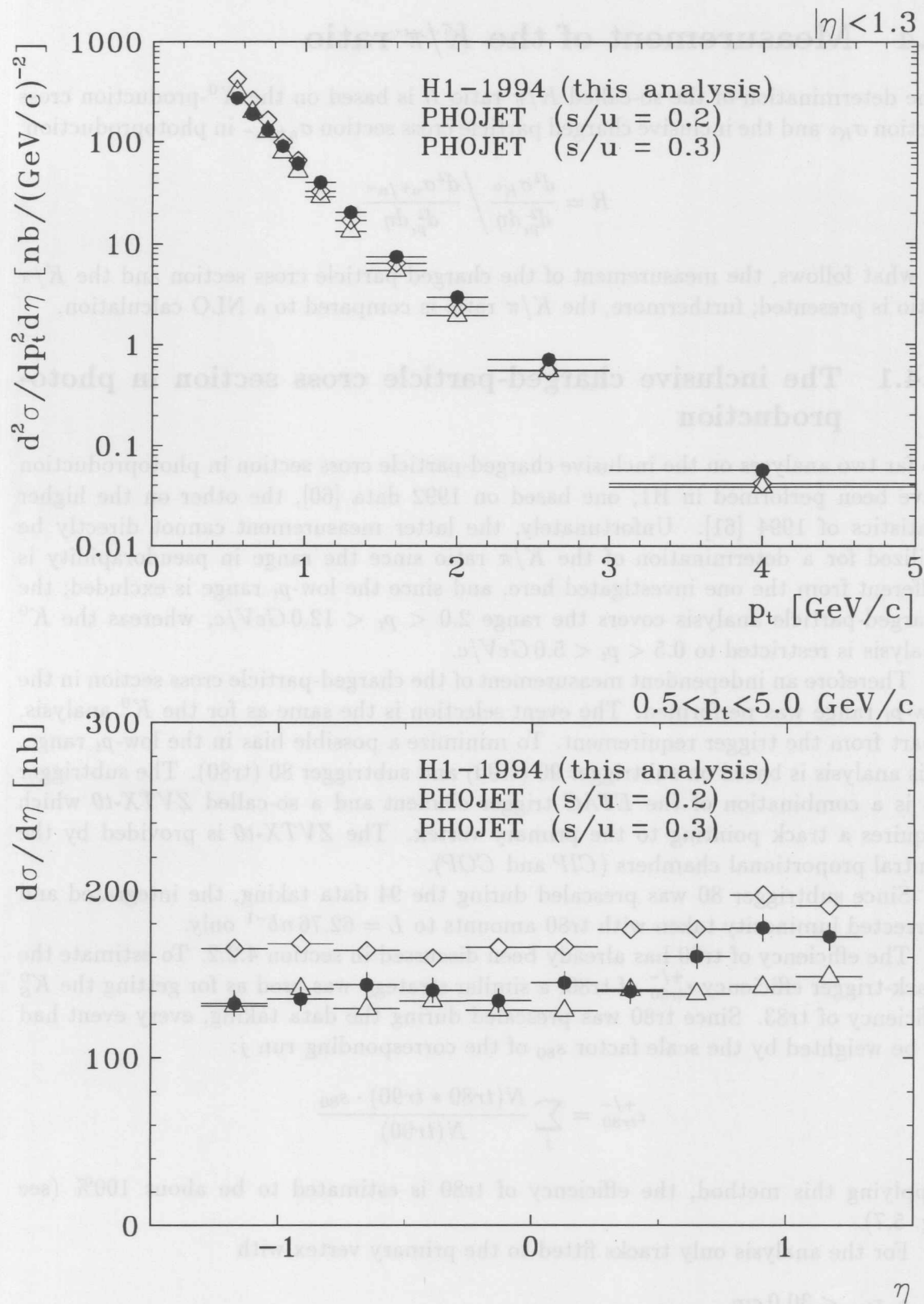


Figure 5.6: Comparison between data and PHOJET prediction.

Top: $d^2\sigma/dp_t^2 d\eta$ for $|\eta| < 1.3$

Bottom: $d\sigma/d\eta$ for $0.5 < p_t < 5.0 \text{ GeV}/c$

5.4 Measurement of the K/π ratio

The determination of the so-called K/π ratio R is based on the K^0 -production cross section σ_{K^0} and the inclusive charged particle cross section σ_{n^+/n^-} in photoproduction:

$$R = \frac{d^2\sigma_{K^0}}{d_{p_t}^2 d\eta} \bigg/ \frac{d^2\sigma_{n^+/n^-}}{d_{p_t}^2 d\eta}.$$

In what follows, the measurement of the charged particle cross section and the K/π ratio is presented; furthermore, the K/π ratio is compared to a NLO calculation.

5.4.1 The inclusive charged-particle cross section in photoproduction

So far two analyses on the inclusive charged-particle cross section in photoproduction have been performed in H1; one based on 1992 data [60], the other on the higher statistics of 1994 [61]. Unfortunately, the latter measurement cannot directly be utilized for a determination of the K/π ratio since the range in pseudorapidity is different from the one investigated here, and since the low- p_t range is excluded; the charged-particle analysis covers the range $2.0 < p_t < 12.0 \text{ GeV}/c$, whereas the K^0 analysis is restricted to $0.5 < p_t < 5.0 \text{ GeV}/c$.

Therefore an independent measurement of the charged-particle cross section in the low- p_t range was performed. The event selection is the same as for the K^0 analysis, apart from the trigger requirement. To minimize a possible bias in the low- p_t range, this analysis is based on subtrigger 90 (tr90) and subtrigger 80 (tr80). The subtrigger 80 is a combination of the *ETAG* trigger element and a so-called *ZVTX-t0* which requires a track pointing to the primary vertex. The *ZVTX-t0* is provided by the central proportional chambers (*CIP* and *COP*).

Since subtrigger 80 was prescaled during the 94 data taking, the integrated and corrected luminosity taken with tr80 amounts to $L = 62.76 \text{ nb}^{-1}$ only.

The efficiency of tr90 has already been discussed in section 4.2.2. To estimate the track-trigger efficiency $\epsilon_{tr80}^{+/-}$ of tr80, a similar strategy was used as for getting the K_S^0 efficiency of tr83. Since tr80 was prescaled during the data taking, every event had to be weighted by the scale factor s_{80} of the corresponding run j :

$$\epsilon_{tr80}^{+/-} = \sum_j \frac{N(tr80 * tr90) \cdot s_{80}}{N(tr90)}$$

Applying this method, the efficiency of tr80 is estimated to be about 100% (see fig. 5.7).

For the analysis only tracks fitted to the primary vertex with

- $r_{beg} < 30.0 \text{ cm}$
- $|\eta| < 1.3$ and
- $l_r < 10 \text{ cm}$

were considered. Since the reconstruction efficiency for these tracks is almost 100% ([61], visual scan), no correction for reconstruction inefficiencies is applied.

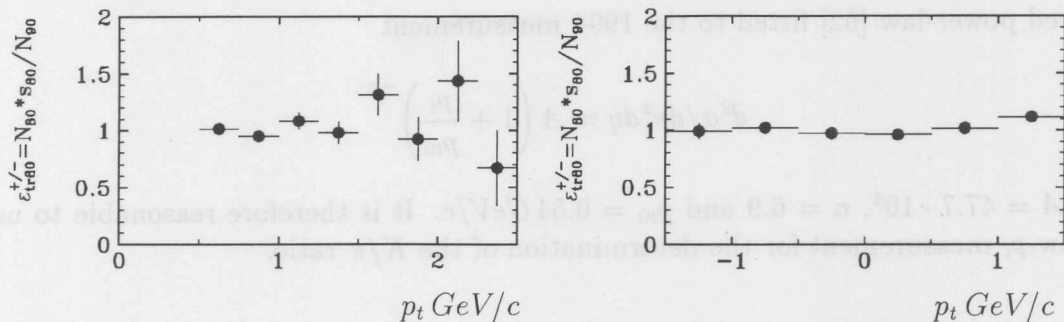


Figure 5.7: Efficiency of subtrigger 80 for charged particles (estimated by using *tr90* as an independent reference trigger).

To avoid any bias from the sick areas (see section 4.5.6), only those tracks are selected which traverse fully efficient regions; the losses are corrected for the geometric acceptance. The remaining correction is the ETAG acceptance and has been discussed in detail in section 4.2.1. The contamination due to tracks which originate from a K^0 decaying very close to the primary vertex can be seen from fig. 5.8 and is negligible, at least if the transverse momentum of one of the tracks is larger than $0.5 \text{ GeV}/c$. With this strategy, it is easy to estimate the charged particle cross section in the

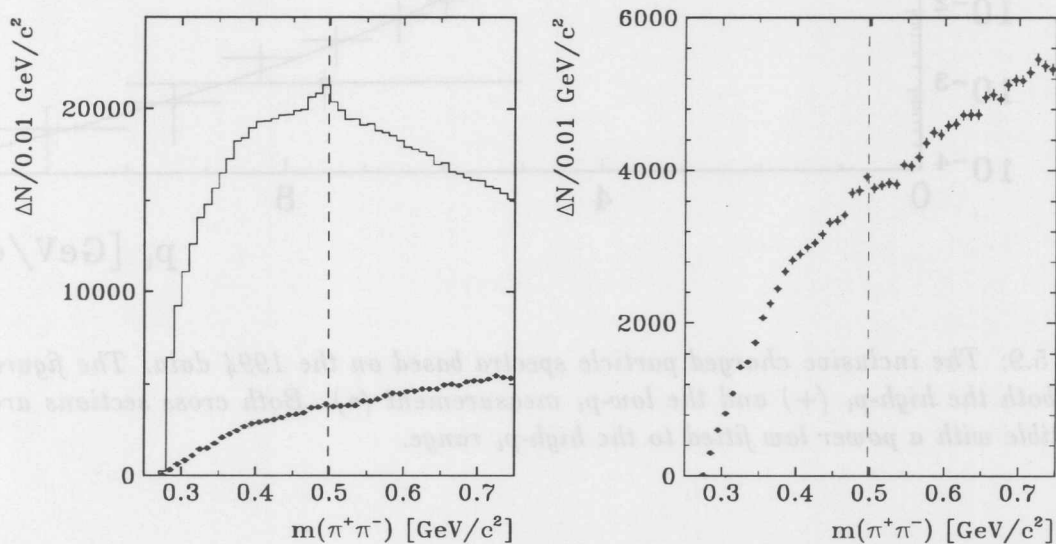


Figure 5.8: K_S^0 signal formed by tracks fitted to the primary vertex (histogram: both tracks have to pass the basic track selection cuts, \bullet : at least one track has to have a p_t larger than $0.5 \text{ GeV}/c$).

low- p_t range. Fig. 5.9 shows the high- p_t analysis together with the results of the aforementioned low- p_t analysis which in this case was restricted to $|\eta| < 1.0$. In the overlapping region between 2 and $3 \text{ GeV}/c$ the two measurements are in very good agreement. Furthermore, the low- p_t results follow the prediction from the QCD-

inspired power-law [62] fitted to the 1994 measurement

$$d^2\sigma/dp_t^2 d\eta = A \left(1 + \frac{p_t}{p_{t0}}\right)^{-n}$$

with $A = 47.7 \cdot 10^4$, $n = 6.9$ and $p_{t0} = 0.54 \text{ GeV}/c$. It is therefore reasonable to use the low- p_t measurement for the determination of the K/π ratio.

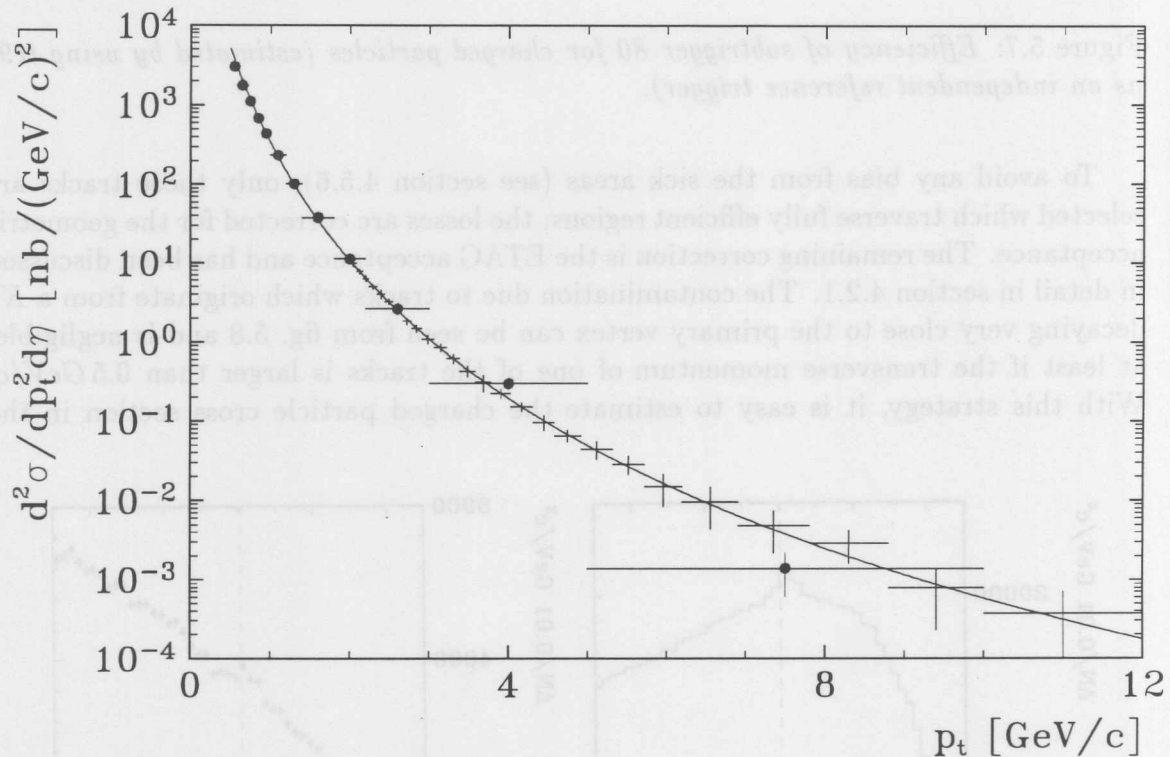


Figure 5.9: The inclusive charged particle spectra based on the 1994 data. The figure shows both the high- p_t (+) and the low- p_t measurement (•). Both cross sections are compatible with a power law fitted to the high- p_t range.

5.4.2 The K/π ratio

Based on the measurement of the K^0 -production cross section (see table 4.6) and the low- p_t charged particle spectrum discussed in the previous section the K/π ratio as shown in fig. 5.10 is determined. It is compared with a prediction from a NLO calculation [63] which is in reasonable agreement with the experimental measurement. Since the starting scale of the parameterization of the fragmentation functions is $\sqrt{2} \text{ GeV}$ an increasing discrepancy for $p_t < 1.4 \text{ GeV}/c$ is not surprising; the "dip" occurring at around $3 \text{ GeV}/c$ is ascribed to the charm threshold.

For the measurement, only the statistical errors are shown, the systematic uncertainty is estimated to be of the order of 15%. For this estimate the systematic uncertainty of the charged particle cross section measurement was assumed to be as large as the one of the K^0 cross section measurement.

As has been discussed in section 2.3.3, it is not possible to relate this ratio directly to the strangeness suppression factor as it is used for instance in JETSET.

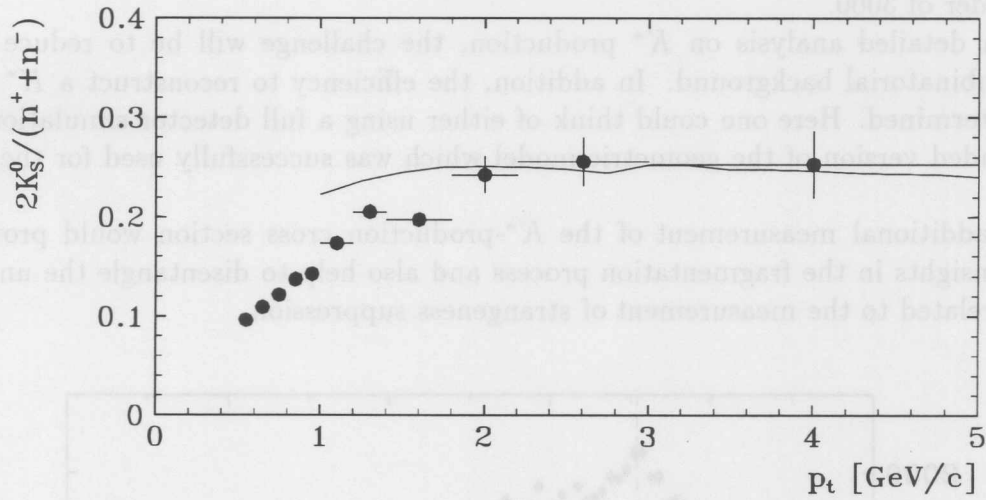


Figure 5.10: The K/π ratio. The measurement (\bullet) is compared to a NLO calculation ($-$)[63].

5.5 Outlook

Higher statistics and a better understanding of the *CJC* will open a new field for further studies on strangeness production. In the following sections some additional aspects of strangeness production will be discussed.

5.5.1 Reconstruction of K^* decays

In section 2.3.5 it has been shown that about 50% of all K^0 in the hadronic final state are expected to come from K^* decays. Therefore it should be possible to reconstruct these decays in the channel $K^{*\pm} \rightarrow K^0\pi^\pm$ just by forming the $(K_S^0\pi^\pm)$ invariant mass. Using tracks fitted to the primary vertex that fulfill the basic track selection criteria explained in section 4.4.2, the K^* signal is clearly visible in the expected mass region around $m_{K^0\pi} = 982 \text{ GeV}/c^2$ (see fig. 5.11). Without any further cuts to improve the signal-to-background ratio the number of reconstructed K^* decays is estimated to be of the order of 3000.

For a detailed analysis on K^* production, the challenge will be to reduce the high combinatorial background. In addition, the efficiency to reconstruct a K^* has to be determined. Here one could think of either using a full detector simulation or an expanded version of the geometric model which was successfully used for the K^0 analysis.

The additional measurement of the K^* -production cross section would provide further insights in the fragmentation process and also help to disentangle the uncertainties related to the measurement of strangeness suppression.

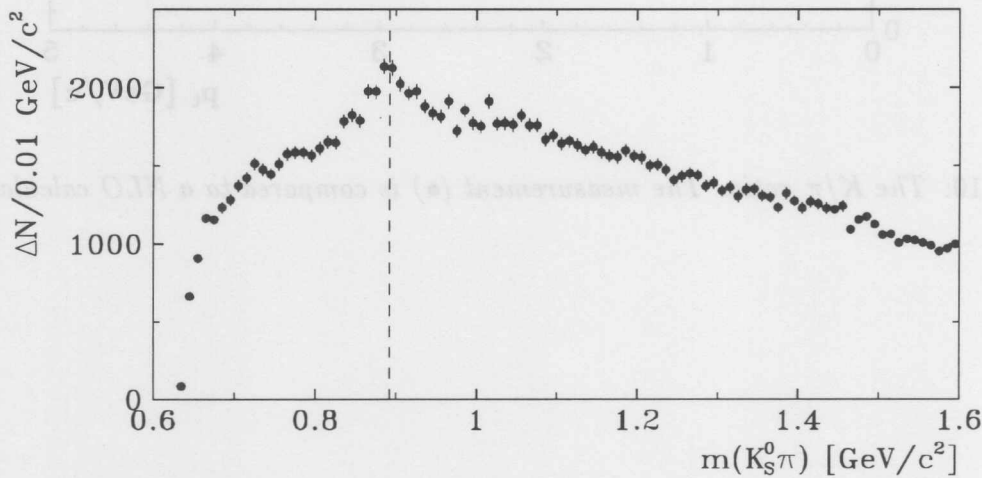


Figure 5.11: The uncorrected K^* signal using selected K^0 -candidates and vertex fitted tracks passing the basic track selection cuts (e.g. $p_t > 0.18 \text{ GeV}/c$, $|\eta| < 1.3$).

5.5.2 Λ production

Since during the secondary vertex fit (see section 3.5.2) no assumption is made on the mass of the decaying particles, these vertices can also be used to reconstruct other two-body decays like $\Lambda \rightarrow p\pi^-$ and $\bar{\Lambda} \rightarrow \bar{p}\pi^+$. Some kinematic relations of the Λ decay are given in section 4.5.3, where the Λ decay was viewed as a contamination to the K_S^0 sample.

The cuts chosen for a preliminary selection of Λ and $\bar{\Lambda}$ decays are given in table 5.1. With these cuts¹, there are approximately 7000 reconstructed Λ s and $\bar{\Lambda}$ s. The width of both signals is about $\sigma_\Lambda = 0.003 \text{ GeV}/c^2$ (see fig. 5.12) and the positions of the mass peaks ($m_\Lambda = 1.11541 \text{ GeV}/c^2$, $m_{\bar{\Lambda}} = 1.11585 \text{ GeV}/c^2$) are in good agreement with the published mean values [55].

	variable	unit	$\Lambda/\bar{\Lambda}$
tracks	see table 4.4.2		
topology	radial decay length	d_r	[cm]
	momentum component perpendicular to direction of V^0 (in CMS)	p_\perp	[GeV/c]
	topological angle	Ψ	[degree]
	momentum asymmetry	A	
V^0	transverse momentum	p_t^0	[GeV/c]
	pseudorapidity	$ \eta $	

Table 5.1: Preliminary cuts used for the $\Lambda/\bar{\Lambda}$ -selection

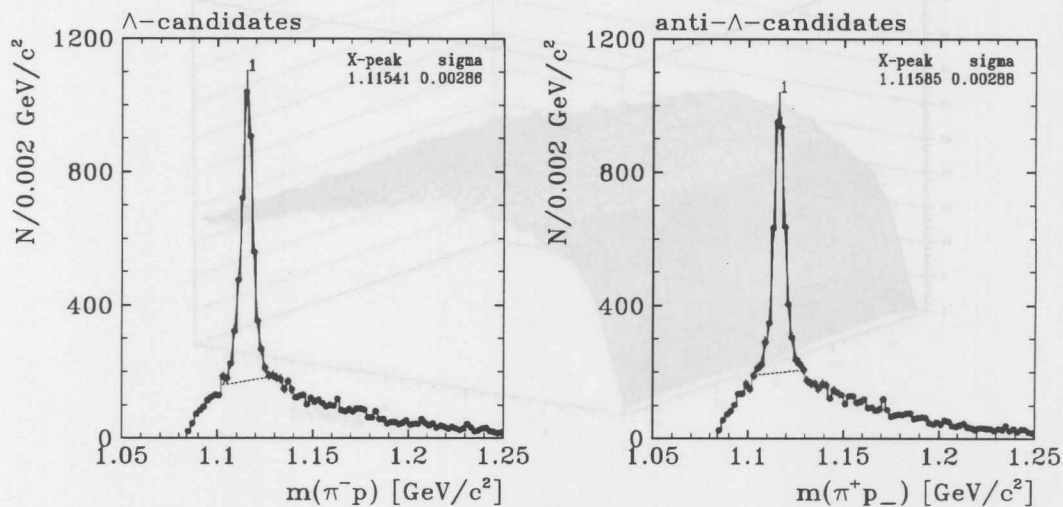


Figure 5.12: The uncorrected Λ and $\bar{\Lambda}$ signals.

¹At this stage of analysis, the full *CJC* is taken into account.

Similar to the K^0 analysis, there are two kinds of cuts: On the one hand cuts that are related to the tracks associated to the Λ (see section 4.4.2 for the basic track cuts), and on the other hand cuts that are related to the topology of a Λ decay.

The large mass difference between the two daughter particles, the pion and the proton, leads to an asymmetry in the corresponding transverse momenta (the proton having higher momentum). This fact can be used to reduce the combinatorial background by imposing an upper limit on the asymmetry $A = (p_t^\pi - p_t^p)/(p_t^\pi + p_t^p)$.

It should be mentioned that the cuts given in table 5.1 can be improved, but more detailed studies were beyond the scope of this analysis. It would be of advantage to decrease the cut on the transverse momentum given by the basic track selection cuts from $0.18 \text{ GeV}/c$ to e.g. $0.15 \text{ GeV}/c$, in order to recover a significant number of $\Lambda/\bar{\Lambda}$ -candidates.

As long as all cuts used for the selection of Λ and $\bar{\Lambda}$ candidates can be related to the 4-vectors of the associated particles, it is possible to use the geometric model for the calculation of the geometric acceptance. For a fully efficient *CJC*, the acceptance is of the order of 15 – 20% both for Λ s and $\bar{\Lambda}$ s (see fig. 5.13); if the analysis is restricted to those decays where the pion and the proton are reconstructed in fully efficient regions only, the acceptance decreases dramatically and is of course different for Λ s and $\bar{\Lambda}$ s.

If one attempts to extract the corrections obtained from data, one of the main problems will arise during the calculation of the trigger efficiency, since for studies based on a reference trigger the statistics is very limited.

Nevertheless, more statistics or a new analysis of the 94-data taking will certainly allow a measurement of the Λ and $\bar{\Lambda}$ production cross sections.

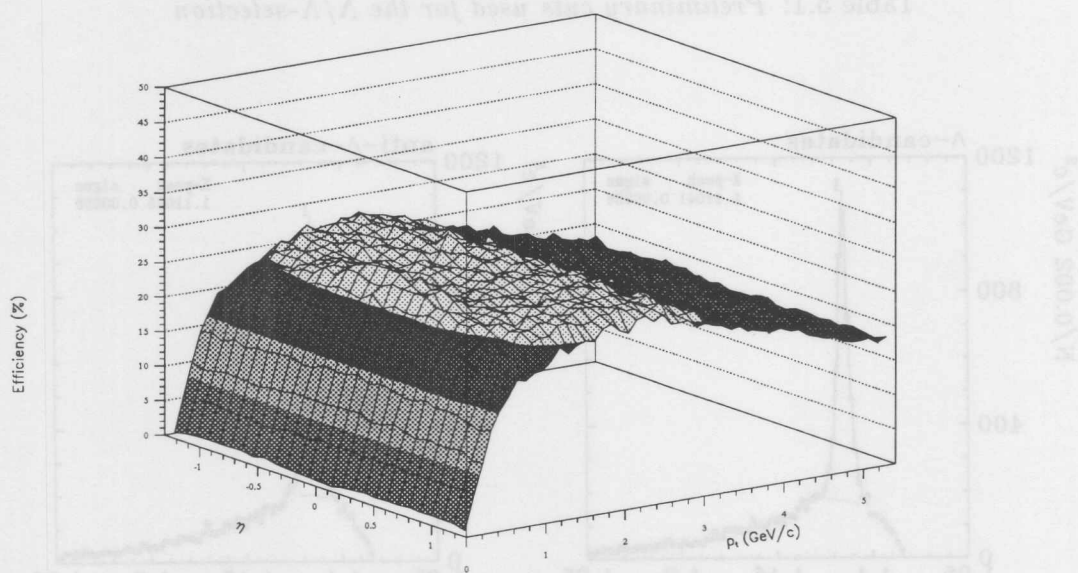


Figure 5.13: The geometric acceptance for Λ and $\bar{\Lambda}$ decays taking the full *CJC* into account and using preliminary selection cuts.

5.5.3 The energy dependence of the K^0 -production cross section

The energy spread of the photons resulting from the process $e \rightarrow e'\gamma$ at the electron vertex (see section 1.2) offers the unique opportunity to study γp interactions at various energies without changing the experimental setup. For tagged photoproduction events the accessible energy of the γp system ranges from ≈ 160 to ≈ 250 GeV and is related to the ETAG acceptance and the chosen y range (see section 1.1 and 4.2.1).

In section 1.2 it has been shown that the measurement of the total γp cross section is in reasonable agreement with the Regge-motivated parameterization [4]

$$\sigma_{\gamma p}^{tot} = X_{\gamma p} s^{\epsilon_{DL}} + Y_{\gamma p} s^{-\eta}. \quad (5.1)$$

The first term in this parameterization, with $\epsilon_{DL} = 0.08$, corresponds to Pomeron exchange; the second term, arising from ρ, ω, f and a exchange, becomes very small for large s and will be neglected in what follows.

Furthermore, it has been observed in hadron-hadron collision [64] and in events with virtual photon-proton interactions [65] that the cross sections for events which are tagged by a large momentum transfer (e.g. a hadronic jet or a high- p_t particle) rises more steeply than the total interaction cross section [66].

This leads to the question whether a similar behavior is observed when a subsample of γp events is tagged by asking for a specific particle, for instance a K_S^0 , in the final state.

As a first step in the direction of a more detailed analysis on this subject, the following approach was chosen. As a reference sample, all CLASS19 events triggered by tr83 are used; however, one has to bear in mind that this sample is not representative of the aforementioned total γp sample. Then various subsamples of this CLASS19 sample are tagged by asking for at least

- one K_S^0 or
- one $\Lambda/\bar{\Lambda}$ or
- one charged particle

in the given kinematic range² $0.5 < p_t < 5.0$ GeV/c and $|\eta| < 1.3$. The W distributions of the CLASS19 sample and the tagged sample are now used to define the W dependent ratio:

$$R_{tag/CL19}(W) = \left(\frac{1}{N_{tag}} \frac{dN_{tag}}{dW} \right) / \left(\frac{1}{N_{CL19}} \frac{dN_{CL19}}{dW} \right)$$

where dN_{tag}/dW is the number of tagged events and dN_{CL19}/dW is the number of reference events for a given W interval; furthermore, each W distribution is normalized to the total number of events in each sample such that the mean value of R should be one.

²Since this analysis requires large statistics, the full K_S^0 and $\Lambda/\bar{\Lambda}$ samples were used (i.e. no cells were skipped).

In a more detailed analysis it would be necessary to study the fully corrected ratio given by:

$$R_{tag/CL19}^{corr}(W) \propto \frac{\frac{1}{dW} \sum_{tag} \frac{1}{\epsilon_{ETAG}(W)} \cdot \frac{1}{A_{tag}(p_t, \eta)}}{\frac{1}{dW} \sum_{CL19} \frac{1}{\epsilon_{ETAG}(W)} \cdot \frac{1}{A_{CL19}(p_t, \eta)}} = \frac{\sum_{tag} \frac{1}{A_{tag}(p_t, \eta)}}{\sum_{CL19} \frac{1}{A_{CL19}(p_t, \eta)}},$$

where $\epsilon_{ETAG}(W)$ is the ETAG acceptance; A_{tag} is given by the efficiency and acceptance resulting, e.g. from the *CJC* and the trigger, and A_{CL19} the one corresponding to the CLASS19 reference sample. Since the ETAG acceptance is assumed to be independent of the hadronic final state, it cancels for a given W bin in the ratio. A possible W dependence of A_{tag} has been studied by applying for each event, tagged by asking for at least one K_S^0 , an acceptance factor obtained from the geometric model and the corresponding trigger efficiency. To treat events with more than one reconstructed K_S^0 in the specified kinematic range correctly, $A_{K_S^0/tag}$ was defined as:

$$A_{K_S^0/tag} = \epsilon_{tr83}(p_t) \cdot \left(1 - \prod_{K_S^0} (1 - \epsilon_{geo}(p_t, \eta))\right).$$

As can be seen from fig. 5.14, at this stage of the analysis there is no indication for a significant W dependence of $A_{K_S^0/tag}$ since this would lead to a different slope of the ratio.

To quantify the slopes, the assumption is made that the production cross section of each sample is proportional to $W^{2\epsilon}$ (see eq. 5.1) such that each ratio can be described by a function

$$r \propto \frac{W^{\epsilon_{tag}}}{W^{\epsilon_{CL19}}} = W^{2(\epsilon_{tag} - \epsilon_{CL19})} = W^{2\Delta}.$$

In figure 5.15 the W -dependent ratios of all three tagged subsamples are shown; the results for Δ are summarized in table 5.2.

tag ($0.5 < p_t < 5 \text{ GeV}/c, \eta < 1.3$)	Δ
Λ/Λ	0.25205 ± 0.04615
K_S^0	0.16407 ± 0.03296
charged particles	0.12094 ± 0.00890

Table 5.2: Slope values Δ for the W -dependent ratios (see text).

It is observed that the cross sections of the tagged subsamples rise faster with W than the total cross section (which is approximated by the CLASS19 sample triggered by tr83). However, since the statistical errors are rather large and the systematic uncertainties have not yet been fully investigated, it is not possible to draw any conclusion as to whether there is a difference between event samples tagged by a K_S^0 , a Λ or simply an unidentified charged particle with a certain p_t in the hadronic final state. It could well be the case that the rise of the cross section is only related to the p_t of the particle, independent of its mass or flavour.

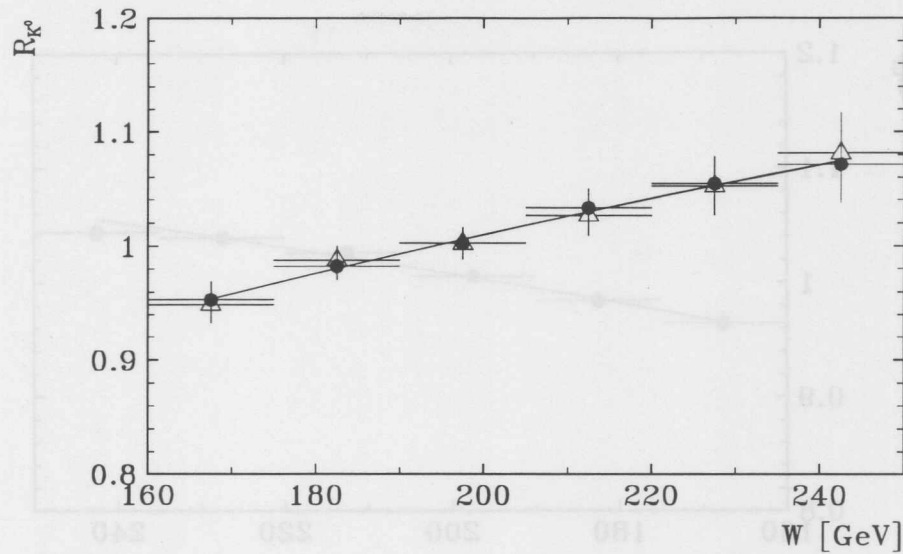


Figure 5.14: W dependence of the ratio $R_{K^0_{S^0}/CL19}(W) = R_{K^0}$ obtained by applying no correction (●) and by weighting each event to account for acceptance and efficiency effects (△).

It should be mentioned that a more detailed analysis on the p_t dependence of the slope has already been performed by tagging p_t -dependent subsamples using the highest- p_t particle found in an event [67]. With the limited statistics of the K^0_S and Λ samples a p_t dependence could not be investigated.

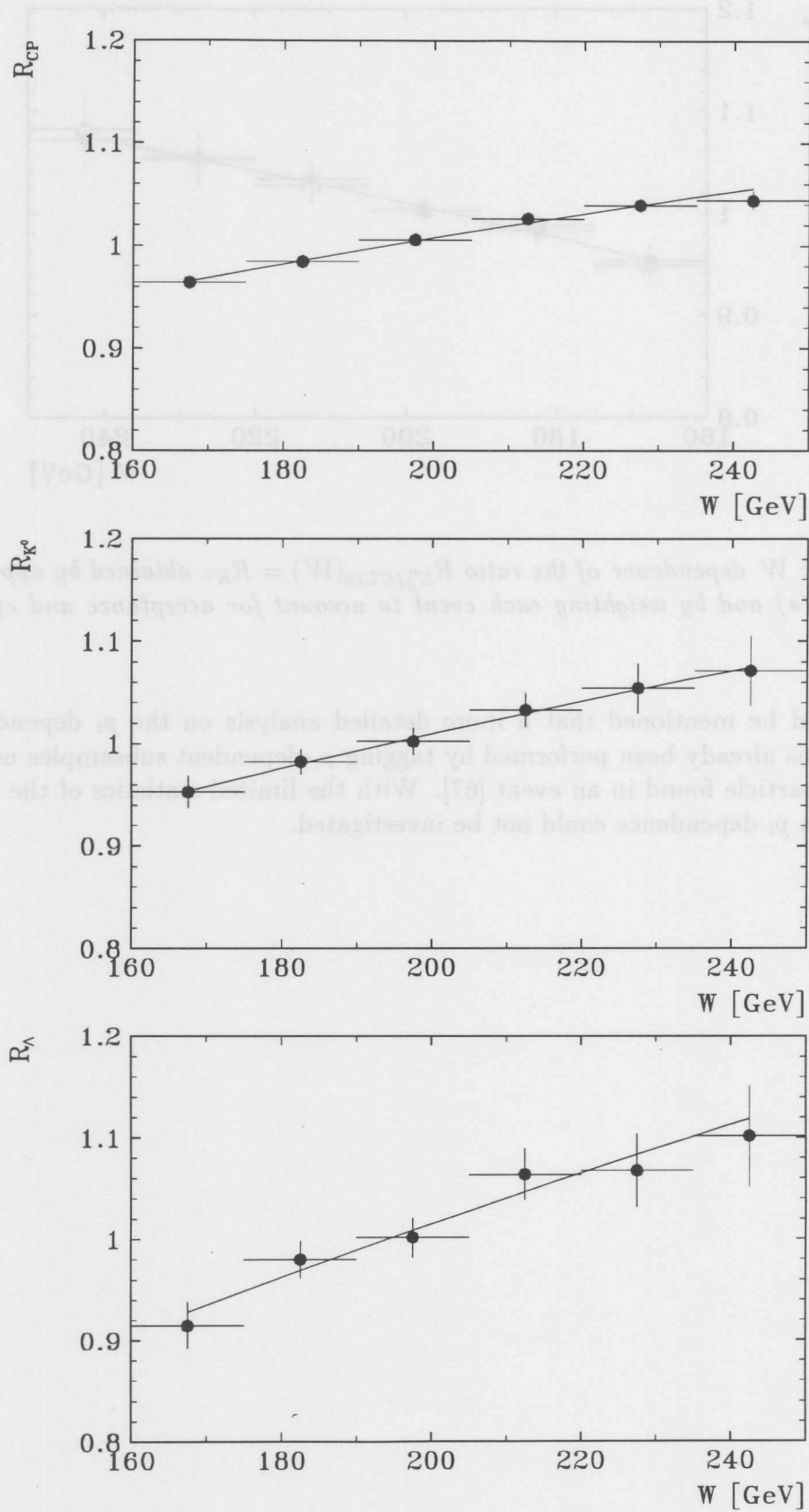


Figure 5.15: W dependence of the ratio $R_{tag/CL19}(W)$ for various subsamples. The subsamples are tagged by asking for at least one specific particle in the kinematic range of $0.5 < p_t < 5 \text{ GeV}/c$ and $|\eta| < 1.3$; the particles have to be either identified as $\Lambda/\bar{\Lambda}s$ (bottom), K_S^0s (middle) or simply charged particles (top).

It is instructive to plot the prediction of PYTHIA; for this purpose, a sample of minimum bias photoproduction events was simulated. Similar to the data analysis, two subsamples of events containing a least one K_S^0 or one Λ , respectively, in the specified kinematic range were tagged and the corresponding W spectrum related to the W spectrum of the full sample. Figure 5.16 shows the W dependent ratios as predicted by PYTHIA ($\Delta_{K^0} = 0.2086 \pm 0.0255$, $\Delta_{\Lambda} = 0.3489 \pm 0.0430$). The fact that the slopes observed in data are systematically smaller than the ones predicted by the Monte Carlo could be attributed to the fact that the reference samples are not the same; the requirement of a trigger, which is of course not taken into account for the generator studies, might for instance bias the reference sample used in the data analysis.

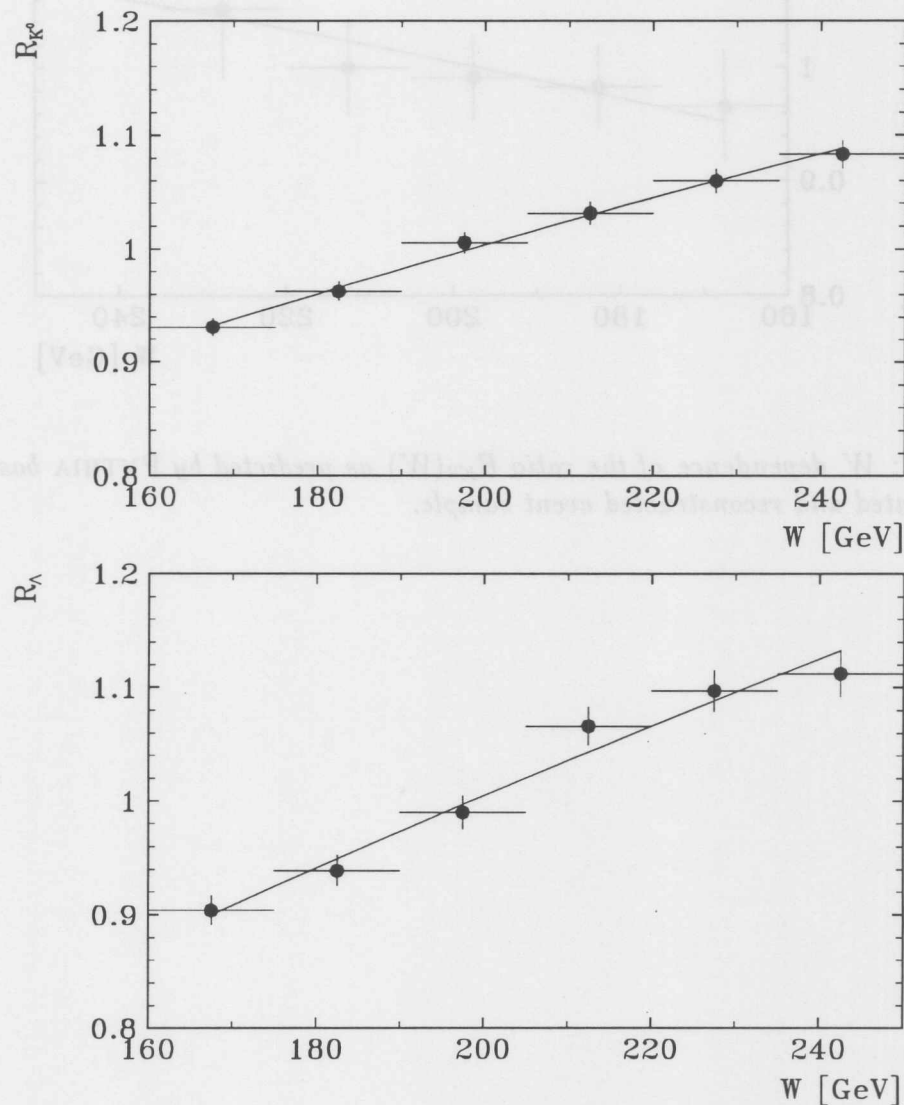


Figure 5.16: W dependence of the ratios $R_{K^0}(W)$ and $R_{\Lambda}(W)$ as predicted by PYTHIA. For the event tagging the same kinematic cuts were applied on the K_S^0 and the Λ as for the data sample; the W distribution of the tagged sample is related to the the W distribution of the total generated sample.

In addition to the generator studies, the effect was also studied using a sample of simulated and reconstructed Monte Carlo events (see fig. 5.17). Since the statistics of these events was rather limited, less tight cuts had to be chosen in order to select the K_S^0 . Nevertheless, the slope is clearly visible; it is therefore reasonable to conclude that the observed slope in data is not a detector artifact.

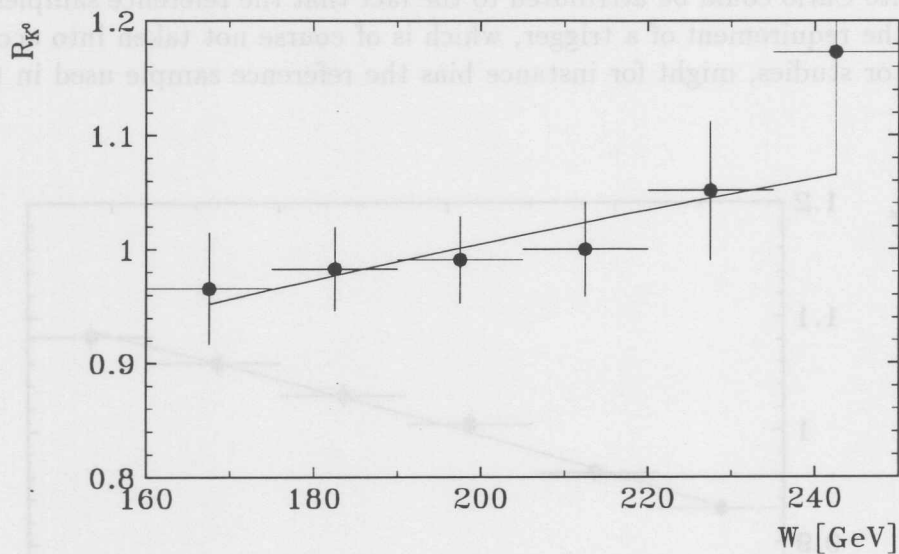


Figure 5.17: W dependence of the ratio $R_{K^0}(W)$ as predicted by PYTHIA based on a fully simulated and reconstructed event sample.

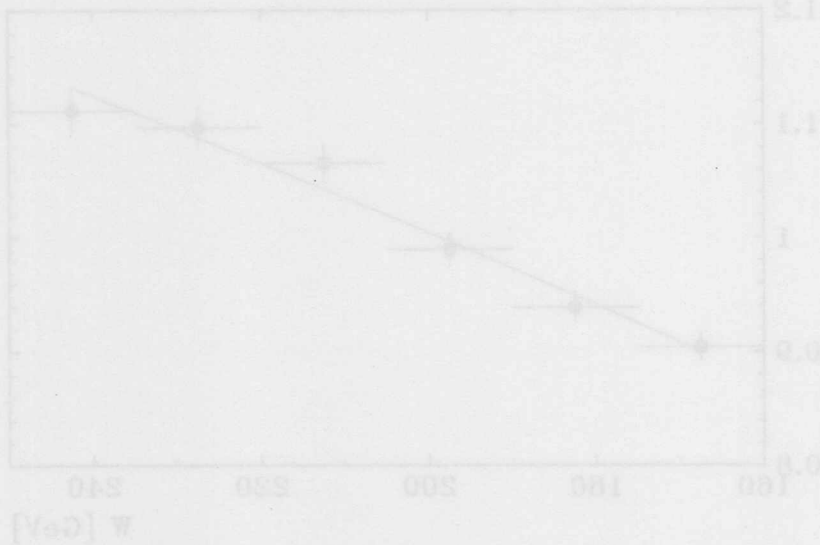


Figure 5.18: W dependence of the ratio $R_{K^0}(W)$ and $R_{K^+}(W)$ as predicted by PYTHIA. For the event tagging the same kinematic cuts were applied on the K_S^0 and the K^+ as for the data sample, the W distribution of the tagged sample is related to the W distribution of the total generated sample.

Chapter 6

Summary

In this study, strangeness production has been investigated in γp interactions at a center-of-mass energy of $W \approx 160 - 240 \text{ GeV}$. The differential K_S^0 -production cross section has been measured both as a function of the transverse momentum p_t and the pseudorapidity η in the kinematic range $0.5 < p_t < 5.0 \text{ GeV}/c$ and $|\eta| < 1.3$. Due to the higher integrated luminosity this analysis allowed a much more precise measurement than previous analyses.

Furthermore, the dependence on the rapidity y^* as measured in the center of mass of the γp system has been determined; this should make it possible to compare these γp results to those from processes such as DIS for instance.

Since the majority of K^0 is expected to come from fragmentation processes, the experimental results were compared with two Monte Carlo predictions, PYTHIA and PHOJET, using JETSET to describe the fragmentation phase.

Concerning the p_t dependence, both Monte Carlo predictions seem to overestimate the K^0 yield in the low- p_t range, while an underestimate in the high p_t range is not considered as being significant. Within the given systematic and statistic uncertainties, the shape of the η distribution is reasonably reproduced in both cases; however, there might be a slight discrepancy in the forward region. Qualitatively the data seem to be in better agreement with a lower strangeness suppression factor of $\lambda = 0.2$ but bearing in mind the discrepancy between MC and data, particularly in the low p_t range, and the systematic uncertainties $\lambda = 0.3$ is not excluded.

Apart from Monte Carlo predictions based on leading order QCD calculations, the results were compared to theoretical NLO calculations using fragmentation functions derived from fits to $p\bar{p}$ and e^+e^- collider experiments. Within the statistical and systematic uncertainties the experimental results are in good agreement with the NLO calculations.

To have an additional handle on the strangeness suppression factor λ , the K/π ratio, approximated by the ratio of the inclusive K^0 and charged-particle cross sections, has been measured. For this purpose, the charged-particle spectrum based on high p_t tracks [61] has been extended to the low- p_t range where in the overlap region the two analyses are in very good agreement. The interpretation of the ratio with regard to the strangeness suppression factor λ is non-trivial and would need further input from additional studies on strangeness production.

The prospects of future analyses on strangeness productions such as the measurement of $\Lambda/\bar{\Lambda}$ and K^* -productions cross sections and the energy dependence of the K^0 production have been discussed.

List of Figures

1.1	Kinematics of deep-inelastic electron-proton scattering	7
1.2	W in photoproduction as a function of y	8
1.3	Total photoproduction cross section as a function of $W_{\gamma p}$	9
1.4	Feynman diagram of photon-gluon fusion (PGF)	10
1.5	Feynman diagram of QCD-Compton scattering	11
1.6	The various states of the photon	11
1.7	Processes of the anomalous photon	12
1.8	Corrections of the order $\mathcal{O}(\alpha_s)$ to boson-gluon fusion	13
1.9	Contributions of the various subprocesses to $b\bar{b}$ production	14
2.1	Quark-flow diagram of the K_S^0 decay	17
2.2	Decay length distribution for various momenta	18
2.3	Kinematic variables associated with the K_S^0 decay	18
2.4	p_{\perp} distribution for the K_S^0 decay	19
2.5	Parameters and functions involved in the cross section calculation	20
2.6	The model of string fragmentation (1)	22
2.7	The model of string fragmentation (2)	22
2.8	The model of independent fragmentation	24
2.9	The expected K^0 -production cross section for various λ	26
2.10	Prediction for the K/π ratio for various λ	26
2.11	Composition of the hadronic final state from fragmentation (1)	28
2.12	Composition of the hadronic final state from fragmentation (2)	28
2.13	Stable particles in the kinematic range $\eta < 1.3, 0.5 < p_t < 5.0 \text{ GeV}/c$ (1)	29
2.14	Stable particles in the kinematic range $\eta < 1.3, 0.5 < p_t < 5.0 \text{ GeV}/c$ (2)	29
2.15	η distributions of K^0 produced in γp interactions	31
2.16	p_t distributions of K^0 produced in γp interactions	32
2.17	Fragmentation functions from NLO calculations	33
2.18	Parton density distributions of the proton and the photon	35
2.19	Distribution of the scaling variables x_{γ} and x_p	36
3.1	The experimental site of HERA	38
3.2	The z-vertex distribution	39
3.3	The H1 experiment	40
3.4	Alignment of the different tracking chambers	41
3.5	The luminosity system of H1	43
3.6	Overview on the data reduction at the H1 trigger	44
3.7	Definition of the 5 track parameters	47
3.8	Sign conventions for κ and d_{ca}	48
3.9	Different topologies of the K_S^0 decay	49

3.10	Geometry and used variables during the track pair selection (1)	50
3.11	Geometry and used variables during the track pair selection (2)	51
3.12	Reconstruction of K_S^0 and Λ decays with the H1 detector	52
4.1	Acceptance of the electron tagger	56
4.2	y distribution from the electron tagger	56
4.3	Single-track efficiency of the DCR Φ trigger	57
4.4	Uncorrected charged particle spectra in the low- p_t range	58
4.5	The efficiency of subtrigger 83	59
4.6	The mean efficiency $\langle \epsilon \rangle_{83}$ of trigger 83 using event weights	60
4.7	η vs. r_{end} for tracks fitted to a secondary vertex	63
4.8	p_t vs. r_{end} for tracks fitted to a secondary vertex	63
4.9	Position of the inefficient regions of the <i>CJC</i> in 1994	65
4.10	φ distributions of vertex fitted tracks	65
4.11	η distribution for various φ ranges	66
4.12	(x, y) -coordinates at the end of the track	67
4.13	Geometric acceptance of charged particles in an inefficient <i>CJC</i>	68
4.14	η - and p_t -dependent track efficiency in an inefficient <i>CJC</i>	69
4.15	The geometric model of the <i>CJC</i>	70
4.16	Acceptance surface obtained by applying basic track cuts	72
4.17	Basic track selection: losses of the K_S^0 signal	73
4.18	Effects of a lower cut on d_r	74
4.19	Effects of upper cut on d_r	75
4.20	Λ -mass hypothesis vs. K_S^0 -mass hypothesis	76
4.21	Λ -mass hypothesis vs. p_{\perp}	76
4.22	Different approaches to remove Λ contamination	77
4.23	Effect of a cut on p_{\perp}	77
4.24	Definition of the topological angle Ψ	78
4.25	Shape of the Ψ distribution as predicted by the geometric model	79
4.26	Shape of the Ψ distribution in data after applying cuts	80
4.27	Effects of cuts on the topological angle Ψ	80
4.28	Geometric acceptance of the <i>CJC</i> (2)	81
4.29	The final K_S^0 signals	84
4.30	φ distribution of all K_S^0 passing the selection cuts	85
4.31	Corrected η distributions for various K_S^0 samples (1)	86
4.32	φ distributions: comparison between data and geometric model (1)	87
4.33	φ distributions: comparison between data and geometric model (2)	88
4.34	r_{sick} distribution for positive and negative trajectories	89
4.35	Corrected η distributions for various K_S^0 samples (2)	90
4.36	K_S^0 acceptance calculated by using a full detector simulation	91
4.37	Comparison between H1SIM and the geometric model (1)	91
4.38	Geometric acceptance of the <i>CJC</i> (3)	92
4.39	The V^0 -finder efficiency both as a function of p_t and η	94
4.40	Comparison between H1SIM and the geometric model (3)	94
4.41	The relation between Δy_{rap} and y	101
4.42	The impact of an η cut on the y^* distribution	101
4.43	$d^2\sigma/dp_t^2 d\eta$ for $ \eta < 1.3$	102
4.44	$d\sigma/d\eta$ for $0.5 < p_t < 5.0 \text{ GeV}/c$	103

4.45 $d\sigma/d\eta$ for various p_t ranges 104

4.46 $d^2\sigma/dp_t^2 dy_{rap}^*$ for $|\eta| < 1.3$ 105

4.47 $d\sigma/dy_{rap}^*$ for $0.5 < p_t < 5.0 GeV/c$ 106

5.1 Comparison between the 1993 and the 1994 analysis 108

5.2 Comparison between data and NLO calculation. 109

5.3 Comparison between data and PYTHIA prediction ($d^2\sigma/dp_t^2 d\eta$ and $d\sigma/d\eta$) 111

5.4 Comparison between data and PYTHIA prediction ($d^2\sigma/dp_t^2 dy^*$ and $d\sigma/dy^*$ 112

5.5 Comparison between data and PYTHIA without MI ($d^2\sigma/dp_t^2 dy^*$ and $d\sigma/dy^*$) 113

5.6 Comparison between data and PHOJET ($d^2\sigma/dp_t^2 dy^*$ and $d\sigma/dy^*$) . . 114

5.7 Efficiency of subtrigger 80 for charged particles 116

5.8 K_S^0 signal formed by tracks fitted to the primary vertex 116

5.9 The inclusive charged particle spectrum 117

5.10 The K/π ratio 118

5.11 The uncorrected K^* signal 119

5.12 The uncorrected Λ and $\bar{\Lambda}$ signals 120

5.13 The geometric acceptance for Λ and $\bar{\Lambda}$ decays 121

5.14 W dependence of the ratio $R_{K_S^0/CL19}(W)$ 124

5.15 W dependence of the ratio $R_{tag/CL19}(W)$ for various subsamples 125

5.16 W dependence of the ratios $R_{K^0}(W)$ and $R_{\Lambda}(W)$ as predicted by PYTHIA 126

5.17 W dependence of the ratio $R_{K^0}(W)$ as predicted by PYTHIA based on a fully simulated and reconstructed event sample 127

List of Tables

2.1	Isospin doublet of the pseudo scalar K mesons	16
3.1	Parameters of the ep collider HERA	38
4.1	Event selection for the V^0 analysis	54
4.2	Basic track selection cuts	64
4.3	Cuts used for the K_S^0 selection	72
4.4	Variation of cuts to study systematic effects	96
4.5	Summary of corrections and systematic uncertainties	97
4.6	$d\sigma/dp_t^2 d\eta$ for various K_S^0 -selection cuts	98
4.7	$d\sigma/d\eta$ for various K_S^0 -selection cuts	98
4.8	The total K^0 cross section	100
4.9	$d^2\sigma/dp_t^2 d\eta$ for $ \eta < 1.3$	102
4.10	$d\sigma/d\eta$ for $0.5 < p_t < 5.0 \text{ GeV}/c$	103
4.11	$d\sigma/d\eta$ for various p_t ranges	104
4.12	$d^2\sigma/dp_t^2 dy_{rap}^*$ for $ \eta < 1.3$	105
4.13	$d\sigma/dy_{rap}^*$ for $0.5 < p_t < 5.0 \text{ GeV}/c$ and $ \eta < 1.3$	106
5.1	Preliminary cuts used for the $\Lambda/\bar{\Lambda}$ -selection	120
5.2	Slope values Δ for the W -dependent ratios	123

Bibliography

- [1] H1-Collaboration, Phys. Lett. **B299** 374, (1992)
- [2] C. F. Weizsäcker, Z. Phys. **88**, 612 (1934)
E. J. Williams, Phys. Rev. **45**, 729 (1934)
- [3] A. I. Lebedev,
Proceedings des HERA Workshops „*Physics at HERA*“; Bd.1, 613 (1991)
- [4] A. Donnachie, P. V. Landshoff, Phys. Lett. **B296**, 227 (1992)
- [5] H1-Collaboration, DESY 95-162, (1995), acc. by Z. Phys
- [6] ZEUS-Collaboration, Z. Phys. **C63** 391, (1994)
- [7] H. Abramovich et al., Phys. Lett. **B269** 465, (1991)
- [8] CDF-Collaboration, Phys. Rev. **D50** 5550, (1994)
- [9] G. A. Schuler, T. Sjöstrand, Nucl. Phys. **B407** 539 (1993)
- [10] A. Ali et al., Proceedings of the Workshop *Physics at HERA*, Hamburg, October 29-30, 1991, edited by W. Buchmüller and G. Ingelman
R. van Woudenberg et al., Proceedings of the Workshop *Physics at HERA*, Hamburg, October 29-30, 1991, edited by W. Buchmüller and G. Ingelman
H. Jung et al., Proceedings of the Workshop *Physics at HERA*, Hamburg, October 29-30, 1991, edited by W. Buchmüller and G. Ingelman
- [11] T. H. Bauer et al., Rev. of Mod. Phys., Vol. 50, no. 2, 261, (1978)
- [12] J. F. Gilman, Ann. Rev. Nucl. Part. Phys. **40**, 213 (1990)
- [13] R. K. Ellis, Z. Kunst Nucl. Phys. **B303**, 653 (1988)
- [14] R. Engel, A. Rostovtsev, *PHOJET - A Monte Carlo Event Generator for Photoproduction*,
H1-01/95-420, (1995)
- [15] T. Sjöstrand, *PYTHIA5.7 and JETSET7.5, Physics and Manual*,
CERN-TH.7112/93
T. Sjöstrand current updates to PYTHIA5.7
- [16] I. Abt, *Manual to IJRAY, a Monte Carlo generator shell to produce ep events for H1*, H1-05/93-290

- [17] A. Capella et al., Phys. Rev. **236** 227, (1994)
- [18] P. Aurenche et al., Phys. Rev. **D45** 92, (1992)
F. W. Bopp, Phys. Rev. **D49** 3236, (1994)
F. W. Bopp, Comp. Phys. Commun. **83** 107, (1994)
- [19] H. Plathow-Besch, Comp. Phys. Commun. **75** 396, (1993)
H. Plathow-Besch, *PDFLIB - Users Manual*, CERN-W5051
- [20] R. Engel, *private communication*
- [21] R. K. Ellis, P. Nason, Nucl. Phys. **B374**, 551 (1989)
- [22] B. A. Kniehl, G. Kramer, DESY 94-009, (1994)
- [23] T. Sjostrand, Computer Phys. Commun. **82**, 74 (1994)
- [24] B. Anderson, G. Gustafson, B. Söderberg, Z. Phys. **C20**, 317 (1983)
- [25] C. Peterson, et al., Phys. Rev. **D27**, 105 (1983)
- [26] R. D. Field, R. P. Feynman, Nucl. Phys. **B136** 1 (1978)
- [27] B. Andersson et al., Z. Phys. **C1**, 105 (1979)
B. Andersson et al., Z. Phys. **C3**, 223 (1980)
B. Andersson et al., Z. Phys. **C6**, 235 (1980)
- [28] P. Hoyer et al., Nucl. Phys. **B161** 349 (1979)
A. Ali et al., Nucl. Phys. **B168** 409 (1980)
A. Ali et al., Phys. Lett. **B93** 155 (1980)
- [29] B. R. Webber, Nucl. Phys. **B238**, 492 (1984)
- [30] B. Andersson et al., Z. Phys. **C20**, 317 (1983)
- [31] M. Bengtsson, T. Sjöstrand, Z. Phys. **C37**, 465 (1988)
- [32] C. Peterson et al., Phys. Rev. **D27**, 105 (1983)
- [33] A. Casher et al., Phys. Rev. **D20**, 179 (1979)
- [34] W. Hofmann, Ann. Rev. Nucl. Part. Sci. **38** 279, (1988)
- [35] OPAL-collaboration, Z. Phys. **C56** 521, (1992)
- [36] A. Breakstone et al., Phys. Lett. **B135** 264, (1991)
- [37] G. D. Lafferty, Phys. Lett. **B353** 541, (1995)
- [38] W. Hofmann, Nucl. Phys. **A479** 337c, (1988)
- [39] J. Binnewies, B. A. Kniehl, G. Kramer,
Neutral-Kaon Production in e^+e^- , ep and $p\bar{p}$ collisions at Next-to-Leading Order, DESY-95-114, FERMILAB-PUB-95/154-T, MPI/PhT/95-54, (1995)

- [40] W. Glück, E. Reya, A. Vogt, *Z. Phys.* **C53** 651, (1992)
- [41] S. Nussinov, *Phys. Rev. Lett.* **35** 1313, (1977)
- [42] G. Wolf, *Hera Physics, Machine and Experiments*, DESY 86-089 (1986)
- [43] H1-Collaboration, *Technical Proposal for the H1 Detector*, DESY, *internal report*, PRC-86/02 (1986)
- [44] H1-Collaboration, *Technical Progress Report*, DESY, *internal report*, PRC-87/01 (1987).
- [45] H1-Collaboration, *The H1 Detector at HERA*, DESY 93-103 (1993).
- [46] C. Niebuhr, *private communication*
- [47] R. Prosi, *Pedestrian's Guide to the L4 Filter Farm*, H1-11/94-412 (1994)
- [48] R. Prosi, *The L4 Filter Farm Selection Algorithm*, H1-95/03-433 (1995)
- [49] P. Steffen, *private communication*
- [50] V. Blobel, *private communication*
- [51] S. Levonian, *H1LUMI-A Fast Simulation Package for the H1 Luminosity System*, H1-04/93-287 (1993)
- [52] J. Riedelberger, *The H1 Trigger with Emphasis on Tracking Triggers*, contr. paper to 5th International Conference on Advanced Technology and Particle Physics, Como 1994, also H1-01/95-419
- [53] J. Riedelberger, *private communication*
- [54] C. Grab, *private communication*
- [55] Particle Data Group, *Phys. Rev.* **D50** 1173 (1994)
- [56] H1 Collaboration, *Experimental Study of Hard Photon Radiation Processes at HERA*, DESY-95-024 (1995)
- [57] S. Levonian, A. Panitch, *Treatment of the Proton Satellite Bunches in 1994 Data* H1-09/95-454 (1995)
- [58] S. Levonian, *private communication*
- [59] F. Linsel, *Erzeugung von K^0 -Mesonen in der Photoproduktion bei einer Schwerpunktsenergie von 190 GeV am HERA Speicherring*, Dissertation Universität Hamburg, DESY FH1T-95-03 (internal report)
- [60] H1 Collaboration, I. Abt et al., *Phys. Lett.* **B328** 176 (1994)
- [61] W. Hoprich, *diploma thesis*, Heidelberg (1994)
- [62] R. Hagedorn, *Riv. Nuovo Cim.* **6** 1 (1983)

- [63] B. A. Kniehl, *private communication*
- [64] UA1 Collaboration, C. Albajar et al., Nucl. Phys. **B309** 261 (1990)
- [65] H1 Collaboration, T. Ahmed et al., Phys. Lett. **B358** 412 (1995)
- [66] A. Rostovtsev, contribution to 2nd Rencontres du Vietnam (1995)
- [67] A. Rostovtsev, *talk given at the H1 collaboration meeting, Heidelberg (1995), private communication*

Acknowledgments

It's done! - and I would like to thank all those who made it possible!

First of all, I am indebted to Prof. V. Blobel for his encouragement to continue this work and for the time he spent on valuable discussions whenever asked for. I was glad to have his support while doing this analysis.

Furthermore, without the continuous support and motivation by Dr. Silhacene Aïd this analysis would probably not be what it is now I am very grateful for endless discussions, technical support and for his careful reading of the manuscript.

I wish to thank all members of the H1 Photoproduction and Diffractive groups and the pleasant working atmosphere they created. Dr. A. Rostovtsev and Dr. S. Levonian contributed some valuable ideas during the finishing of this analysis, the same holds for Prof. J. Dainton, particularly some of his questions were very helpful.

For interesting discussions and help I would like to thank Dr. Carsten Niebuhr, Dr. Frank Linsel, who did a similar analysis on K_S^0 and David Milstead who is analyzing K_S^0 in DIS.

I am very grateful to Prof. G. Kramer, Dr. Bernd Kniehl and Janko Binnewies for their interest in my work and providing helpful advice and lots of NLO calculations custom-made to my analysis.

Apart from those engaged in H1 and physics in general I would like to thank all of my family for their patience and support during the last time.